An Investigation of Corrosion Mechanisms of Constructional Alloys in Supercritical Water Oxidation (SCWO) Systems

by

Hojong Kim

B.S. Materials Science and Engineering
Seoul National University, 2000

Submitted to the Department of Materials Science and Engineering
in partial fulfillment of the requirements for the degree of
Doctor of Philosophy
at the
Massachusetts Institute of Technology
June 2004

Author: _____

Department of Materials Science and Engineering
April 8, 2004

Certified by: _____

Ronald M. Latanision
Professor of Materials Science and Engineering
Thesis Supervisor

Certified by: _____

Ronald G. Ballinger
Professor of Nuclear Engineering and Materials Science and Engineering
Thesis Supervisor

Certified by: _____

Donald R. Sadoway
Professor of Materials Science and Engineering
Thesis Committee Member

Accepted by: _____

Carl V. Thompson II
Stavros Salapatas Professor of Materials Science and Engineering
Chair, Departmental Committee on Graduate Students

An Investigation of Corrosion Mechanisms of Constructional Alloys in Supercritical Water Oxidation (SCWO) Systems

by

Hojong Kim

Submitted to the Department of Materials Science and Engineering
on May 7, 2004 in partial fulfillment of the requirements for the degree of
Doctor of Philosophy

Abstract

Supercritical water oxidation (SCWO) is a technology that can effectively destroy aqueous organic waste above the critical point of pure water. These waste feed streams are very aggressive and pose material performance issues. As potential alloys in construction of SCWO systems, nickel-base alloys are tested.

Corrosion in aqueous feed streams of ambient pH values of 2, 1 and 7 is studied both at supercritical (~425°C) and subcritical (~300-360°C) temperatures with a constant pressure of 24.1MPa. Dealloying of Ni and Fe, and oxidation of Cr and Mo are observed at subcritical temperatures at a pH value of 2. At a pH value of 1, even chromium is selectively dissolved and only molybdenum forms a stable oxide at the subcritical temperature. At supercritical temperatures, normal thin oxidation occurs at both pH values of pH 2 and 7. In contrast, in the neutral pH solution, dealloying is not observed at any temperature. Stress corrosion cracking (SCC) in acidic feed streams is observed both at the supercritical and subcritical temperatures.

In order to understand the corrosion mechanisms, the chemistry of a feed stream, the formation of the dealloyed oxide layer, and the level of stress are investigated. The suppression of dealloying at supercritical temperatures comes from the low proton concentration associated with the low dissociation constant of HCl and water. However, the growth rate of the dealloyed oxide layer at subcritical temperatures is very fast, which is primarily due to the dealloying and the high diffusivity of the nickel in this defective oxide layer. SCC at subcritical temperatures results from the dealloyed oxide layer formation along the grain boundary as intrusions, which act as a precursor to the crack initiation and propagation. SCC at the supercritical temperature is thought to result from the direct chemical attack of associated HCl molecules. SCC is not observed in the neutral solution.

Thesis Supervisor: Ronald M. Latanision
Title: Professor of Materials Science and Engineering

Thesis Supervisor: Ronald G. Ballinger
Title: Professor of Nuclear Engineering and Materials Science and Engineering

Table of Contents

Chapter 5: Conclusions and Future work

Appendix

List of Figures

List of Tables

Acknowledgements

First thanks to my parents who were always supportive of my family with their special warmth. Many thanks to my wife, Jonghee, who has been my best friend. Also my lovely daughter, Youngdo, and son, Minsung made me happy with their beautiful smiles.

Thanks to Professor Ronald M. Latanision, who has been my thesis advisor and constant source of encouragement. Thanks to Professor Ronald G. Ballinger and Professor Donald R. Sadoway for their comments and insight in the discussion of my thesis. Special thanks to Dr. Bryce Mitton, who always worked with me during my experiments and helped me write my thesis in many ways. Thanks to Junghoon Lee, a graduate student in electrical engineering and computer science, for his brilliant help in Matlab programming. Finally, thanks to Eleanor Bonsaint for her kindness and attention with my family.

The work presented in this thesis was supported by the U.S. Army Research Office and the U.S. Department of Energy.

Thanks to everyone and everything near me. I could not have completed my graduate work, and for that matter anything in my life, without help from them.

Chapter 1: Introduction

1.1 Overview of SCWO

Supercritical water oxidation (SCWO) is a technology which can effectively destroy aqueous organic wastes above the critical point of water. Pure water has a critical point at 374°C and 22.1MPa. As the critical point is approached, the density of water changes rapidly as a function of changes in either temperature or pressure. In the supercritical region, the density is intermediate between that of liquid water (1 g/㎤) and low pressure vapor (<10^{-3} g/㎤). Typically, at SCWO conditions (T: ~550-650°C, P: ~250bar), water density is approximately 0.1g/㎤ and the properties of water are significantly different from the liquid water under ambient conditions. The dielectric constant of water drops from approximately 80 at room temperature to 2 at 450°C and the ionic dissociation constant decreases from 10^{-14} $(mol/Kg)^2$ at room temperature to 10^{-23} $(mol/Kg)^2$ at supercritical conditions. These changes result in supercritical water acting as a non-polar dense gas with solvation properties approaching those of a low-polarity organic. Under these conditions, hydrocarbons generally exhibit high solubility in supercritical water and, conversely, the solubility of inorganic salts is very low. These unique physical and solvation properties of supercritical water make it an effective medium for the decomposition of aqueous organic wastes such as chemical agents and aqueous municipal wastes. When organic compounds and oxygen are dissolved in water above its critical point, they are immediately brought into intimate molecular contact in a single homogeneous phase at high temperature. With no interphase transport limitations and due to sufficiently high temperatures, the kinetics of oxidation is fast and the oxidation reaction proceeds rapidly to completion with a residence time of one minute or less.

The oxidation products of hydrocarbons are CO_2 and H_2O. Heteroatomic groups such as Cl, F, P, or S are converted to inorganic compounds, usually acids, salts, or oxides in high oxidation states, which can be precipitated from the mixture along with other unwanted inorganics that may be present in the feed. In addition, Phosphorous is converted to phosphate and sulfur to sulfate. Nitrogen-containing compounds are oxidized to N_2(g) with some N_2O. Finally, due to a relatively low reactor temperature relative to the incineration process, neither NO_x nor SO_2 is formed.[1]

1.1.1 The SCWO process

Figure 1.1 represents a schematic diagram of a waste treatment system based on SCWO technology.[2, 3] In this process, aqueous organic waste in an aqueous medium

(1), which may be neutralized with a caustic solution (2) or have fuel (3) injected for startup is initially pressurized from atmospheric pressure to the pressure in the reaction vessel and pumped through a heat exchanger (4). This promotes rapid initiation of the oxidation reaction and helps to optimize the overall plant energy balance by better heat integration. At the head of the reactor (5), the organic waste stream is mixed with an oxidant of air or oxygen. In some cases, it may be advantageous to use oxidants such as hydrogen peroxide (H_2O_2) in preference to either air or oxygen. However, the commercial utility of this oxidant is limited due to its higher cost (approximately 30 to 40 times higher than oxygen). Mixing of the oxidant and organic waste streams with the hot reactor contents initiates the exothermic oxidation reaction, heating the reacting mixture to temperatures of 550°C to 650°C, accelerating reaction rates and reducing residence times for complete destruction of organic waste. This organic destruction, in the top zone of the reactor (6), occurs quickly with typical reactor residence times of one minute or less. Because salts have such a low solubility in supercritical water, their precipitation is rapid under almost shock-like conditions. The higher-density solid salts separate from the reacting phase and fall to the bottom of the reaction vessel (7) where they can be redissolved and removed as a concentrated brine (8) or collected as solids and removed periodically at a temperature of ~200°C. A small fraction of salt is entrained with the hot reactor overhead effluent (9). The primary effluent (9), gaseous products of reaction with the supercritical water, leaves the reactor at its top into a separator (10) where the gas (11) and liquid (12) are quenched and separated. While a portion of the liquid remains in the system and is recycled (13), the reactor effluent (other than that recycled), consisting of supercritical water, carbon dioxide, a small amount of entrained salt and possibly nitrogen, is first mixed with cold recycle fluid to redissolve the salt and then is further cooled to be discharged at atmospheric conditions (14). Excess thermal energy contained in the effluent can be used to generate steam for external consumption to produce electricity at high efficiency or for high-temperature industrial process heating needs. For larger-scale systems, energy recovery may potentially take the form of power generation by direct expansion of the reactor products through a supercritical steam turbine. Such a system would be capable of generating significant power in excess of that required for air compression or oxygen pumping and feed pumping. For very dilute aqueous wastes, it can be more economical to use a regenerative heat exchanger to preheat the waste (4) than to add supplemental fuel (3). The cooled effluent (9) from the process separates into a liquid water phase (12) and a gaseous phase (11), the latter containing primarily carbon dioxide along with oxygen, which is in excess of the stoichiometric requirements (and nitrogen when air is the oxidant). This separation is carried out in multiple stages in order

to minimize the erosion of valves as well as to maximize the separation due to phase equilibrium constraints. Because of the corrosive nature of supercritical brines and the fact that heavy metals are present in many waste streams, trace metal concentrations (e.g. Cr, Ni, An, Hg) will appear in aqueous effluent streams from the SCWO process. Consequently, a polishing step involving ion exchange or selective adsorption may be needed. This would be particularly important in applications where recycled process or portable water is required.[1-3]

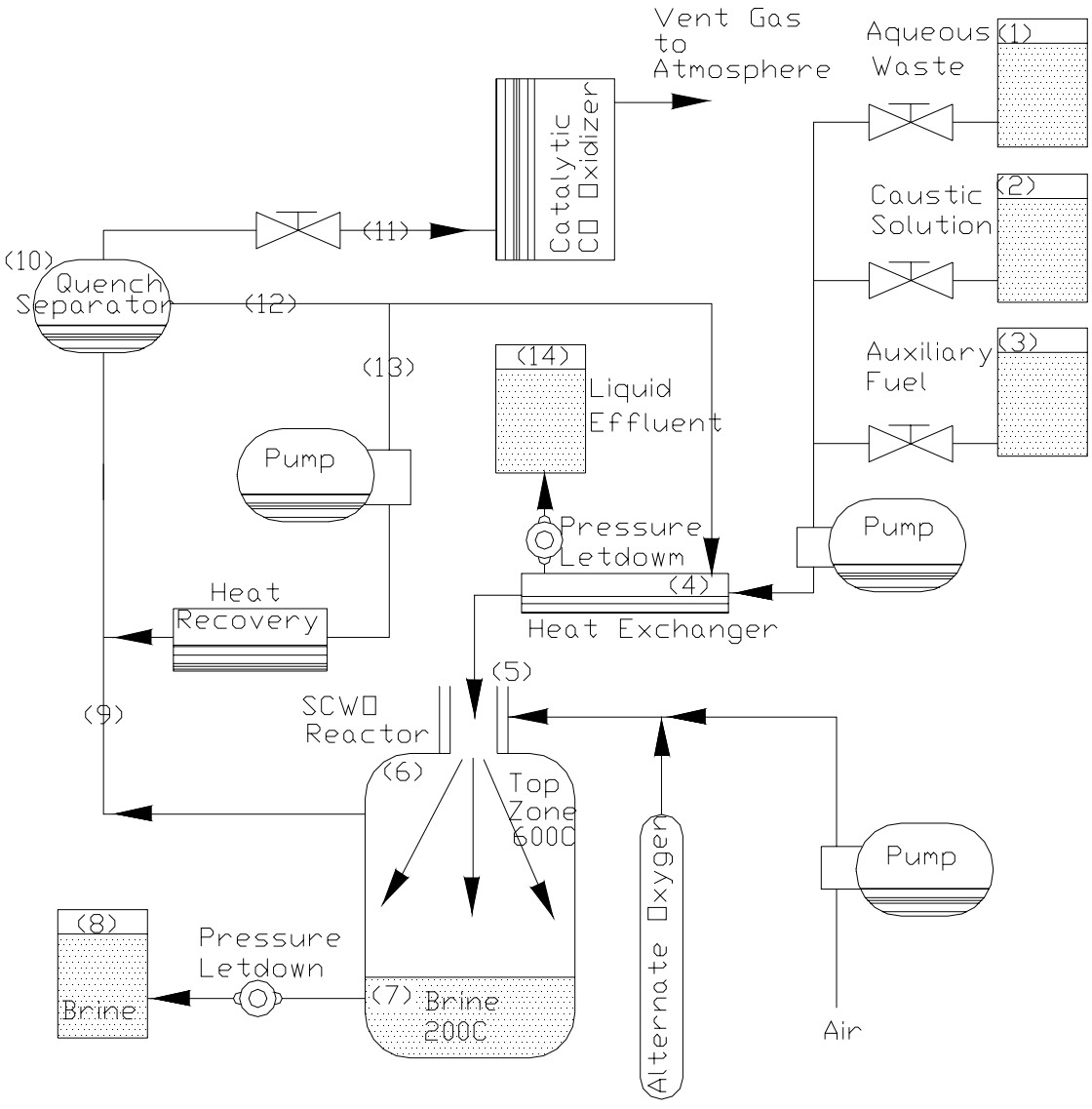

Figure 1.1 A schematic diagram of the SCWO process utilized by MODAR.

1.1.2 Applications and advantages of SCWO

The SCWO process can be applied to handling a wide range of wastes containing oxidizable components and has been shown to be well-suited to handling aqueous wastes with 1-20 wt% organics. The major applications of SCWO include the demilitarization of chemical agents and explosives, treatment of human waste, and remediation of mixed waste and contaminated soils. SCWO systems provide high destruction efficiencies for organics within short residence times. Typical destruction and removal efficiencies can exceed 99.9999% for normal operating conditions of 250 bar, 600℃, and residence times of one minute or less. A SCWO system is entirely self-contained, and also allows for capture and storage of reaction products for analysis and further treatment, if necessary. Under normal operating conditions, hydrocarbons are converted to carbon dioxide and water, and although the carbon dioxide is a greenhouse gas, it can be recovered at pressure and liquefied for reuse or sequestration. Finally, as a result of the relatively low operating temperature, NO_x and SO_2 compounds are not produced.[1, 3-5]

On the other hand, incineration is usually restricted for economic reasons to waste streams of relatively high organic concentrations. To achieve high destruction efficiencies for hazardous and toxic wastes, incineration is performed at temperatures as high as 900-1300℃, often with excess air. With aqueous wastes the energy required to vaporize and heat water to these temperatures is substantial. If the waste contains 25% organics or more, there is sufficient heating value in the waste to sustain the incineration process. However, with decreasing organic content, the supplemental fuel required to satisfy the energy balance becomes a major cost. Furthermore, incineration is also being regulated to restrict stack gas emission to the atmosphere. Extensive equipment must now be used downstream of the reaction system to remove NO_x, acid gases, and particulates from the stack gases before discharge. The cost of this equipment often exceeds that of the incineration itself.[1]

In the range of concentration of 1 –20 wt% organics, both wet air oxidation and SCWO have certain practical and potential economic advantages over controlled incineration treatment. In wet air oxidation, carried out typically at temperatures ranging from 200 to 300℃, destruction of toxic organic chemicals can be as high as 99.9% with adequate residence time but many materials such as chlorobenzenes are more resistant. Total chemical oxygen demand (COD) reduction is usually only 75-99% or lower, indicating that while the toxic compounds may undergo satisfactory destruction, certain intermediate products remain unoxidized. Because the wet air oxidation is not complete, the effluent from the process can contain appreciable concentrations of volatile organics and may require additional treatment such as bio-oxidation. SCWO typically achieves

greater than 99.99% reduction in total organic carbon, so SCWO offers a much more thorough treatment option than wet air oxidation.[1]

While incineration is the chief competitor to SCWO, there are also other waste treatment technologies. These include catalytic oxidation, molten metal treatment, electrochemical oxidation, flash photolysis, and microbial degradation. SCWO is particularly well suited to dilute aqueous wastes, which are too concentrated for absorptive remediation and too dilute for effective incineration or molten metal reforming.[5]

Supercritical light water cooled reactor

The use of supercritical light water as the coolant in a direct cycle nuclear reactor offers potentially very high efficiencies in the energy conversion cycle compared to contemporary nuclear or fossil energy conversion. Because the change of phase occurs in core, the need for steam separators and dryers typical of boiling water reactors (BWRs) or for steam generators as contemporary pressurized water reactors (PWRs) is eliminated. High efficiencies and plant simplification are extremely attractive attributes. However, little is known today about the most suitable materials of construction for supercritical water (SCW) nuclear reactors. Unlike fossil SCW systems, with which there is considerable operating experience, water radiolysis that produces oxygen, hydrogen peroxide, etc., has the potential to corrode the materials of construction of the pressure boundaries in nuclear SCW reactors.

1.1.3 Engineering issues in SCWO systems

Although SCWO is a technology which can effectively destroy civilian and military wastes by oxidation in water, the commercial development of SCWO has not yet been successful due to engineering issues of salt and solids management, reaction rates, and materials performance. The detailed nature of these engineering issues is reviewed in the literature.[1, 5] Due to its relation to problems of corrosion, the significance of inorganic salt formation is briefly addressed here. Many of the wastes for SCWO produce insoluble salts. Corrosion and metal atoms in the feed stream can produce insoluble oxides. While these oxides can be entrained by control of fluid velocity near process surfaces, the salts are sticky and adhere to the surface of the reactor. These sticky salts can hinder heat transfer, harbor corrosive agents, and block the process streams. Also, these entrained solids can cause erosion of the system.[5]

1.2 Corrosion problems in SCWO systems

While SCWO is capable of destroying toxic organic wastes, many of the wastes contain solvents or oils that are high in chlorine or other potentially corrosive precursors such as proton, fluorine, and sulfur. During destruction by SCWO, these can be oxidized to acidic products. In the case of chemical agents, the oxidation of Sarin (GB) produces a mix of hydrofluoric and phosphoric acids; the oxidation of VX results in sulfuric and phosphoric acids; and finally, the oxidation of mustard agent produces hydrochloric and sulfuric acids. Such acidic conditions result in significant corrosion of the process unit and corrosion may ultimately be the deciding factor in the commercial application of the SCWO technology. There has been an extensive research in an effort to find suitable materials for the construction of the SCWO systems. These potential materials include (1) iron-base alloys, (2) ceramics (3) noble metals (4) titanium-base alloys and (5) nickel-base alloys. Their preliminary test results are reviewed from the literature here.[3]

Iron-base alloys

In general, alloys such as 316L stainless steel are unlikely to be employed as a component of SCWO systems except for very innocuous feed streams; however, such alloys have generally been included as a baseline material. Although feed streams may be innocuous enough to permit the use of 316L stainless steel, processing would need to be restricted to low halogen, moderate pH influents. Within a restricted pH range and for an influent with minimal Cl, 316L may exhibit a reasonable performance and a uniform corrosion rate as low as 0.035 mmpy. However, even for a restricted Cl feed, stress corrosion cracking (SCC) may be observed at higher pH values (pH>12). When exposed to a sludge, to a maximum temperature of 425℃, 316L exhibited pitting and crevice corrosion in both the subcritical and supercritical temperature ranges. When exposed to a highly chlorinated organic feed stream (0.3 wt% chloride) at 600℃, weight loss data indicate a corrosion rate on the order of 50 mmpy and SCC for both stressed (u-bend) and non-stressed 316L samples. When a new Cr-Fe alloy, Ducrolloy (50 wt%Cr, 44 wt%Fe), tested in chlorinated acidic conditions, good corrosion resistance was observed for exposure times up to 400 hours. While these data apparently agree with the general concept that corrosion resistance improves with increasing Cr content, results are preliminary and need to be confirmed by further testing.

Ceramics

The problems associated with the corrosion of various alloys have prompted research into ceramic materials. However, results are not encouraging. With the possible exception of monolithic alumina and PSZ (partially stabilized zirconia), ceramics, generally, have exhibited poor resistance to chlorinated waste streams over a wide pH (2-12) and temperature range(350-500℃). The general behavior for the ceramic materials tested

(Al_2O_3, AlN, Sapphire, Si_3N_4 and ZrO_2) in both chlorinated and non-chlorinated acidic chemical agent simulant feeds was found to be very poor. In aqueous sulfuric acid feeds, zirconia ceramics also show poor resistance.

Noble metals

Although the use of noble metals or their alloys would significantly increase the cost of system fabrication, they have been viewed as a possible solution to severe corrosion problems for some very aggressive waste streams.

An experiment carried out in a non-neutralized chlorinated feed stream with low level additions of Zn, Pb and Ce to assess material suitability for SCWO included platinum and two platinum alloys (Pt-10Ir and Pt-30Rh). These materials were exposed for periods between 60 and 240 hours at two temperatures (400 and 610°C). At the higher temperature all three materials showed excellent corrosion resistance with rates on the order of 0.03-0.08 mmpy. At the lower temperature, corrosion rates for Pt, Pt-10Ir, and Pt-30Ir were 1.14, 2.34, and 4.83 mmpy respectively. While these rates may be acceptable for the normal engineering alloys, the high cost may restrict the application of these materials. While the corrosion resistance of Pt is good at higher temperatures, it shows high rates of degradation at subcritical temperatures in acidic chlorinated feed streams. For such feeds, this would cause a potentially troublesome transition between Pt liner and a second material. One experiment in which an Inconel 625 tube was coated with a 30㎛ gold layer exhibited intergranular SCC and failed within 34 hours. Conversely, under the same conditions, the uncoated tube did not fail even after 150 hours. Such behavior suggests that loss of liner integrity could lead to catastrophic failure as a result of enhanced and unexpected degradation of the pressure bearing wall.

Titanium-base alloys

Preliminary tests of Ti indicated poor resistance to the non-chlorinated acidic chemical agent simulant feeds. However, resistance to the chlorinated feed was found to be acceptable. When exposed to chlorinated feeds, titanium apparently exhibits a corrosion rate of less than 3.5 mmpy. Reportedly, Ti provides outstanding performance at the subcritical temperature and is as resistant as the Ni alloys at the supercritical temperatures. In addition, good performance (grade 9 and 12) is observed during exposure to sludge. It has been suggested to use titanium liners as the solution to the corrosion problem in chlorinated organic feed streams. However, it appears to be premature as other researchers have experienced problems with titanium and reported through-wall pitting of liners during destruction efficiency testing of a chlorinated waste. At elevated temperatures, potential problems with creep also need to be considered for this material. Further testing is required before a definitive conclusion can be made regarding the

applicability of titanium alloys to SCWO systems.

Nickel-base alloys

There have been more extensive tests and the database is larger for this class of alloy than for others because high-nickel alloys are frequently recommended for severe service applications. For this reason, nickel-base alloys have been utilized during fabrication for a number of bench-scale and pilot plant reactors. However, the current database suggests that these materials may not be able to handle very aggressive SCWO feed streams as they may exhibit both significant weight loss and localized corrosion including, pitting, stress corrosion cracking (SCC) and dealloying in aggressive environments.

In deionized water, at elevated temperatures (450 -500℃) the general trend, even after extended exposure (150-240 hours), is toward the formation of a potentially protective film for both Inconel 625 and C-276. Even for such innocuous feed streams, minor pitting and grain boundary carbide formation have been observed for Inconel 625.

Dealloying of Cr and Mo for Inconel 625, or Cr, Mo, and W for C-276, was recognized as a potential contributor to degradation within SCWO systems. Based on the effluent analysis, results suggested a loss of chromium for non-chlorinated feeds, while a selective dissolution of Ni was apparent for chlorinated feeds. Corroboration was subsequently provided by metallographic examination during analysis of a failed C-276 SCWO preheater tube, which revealed severe depletion of Ni for acidic chlorinated conditions. This analysis also indicated that the most severe corrosion was associated with a high subcritical temperature and that, at supercritical conditions, in the absence of salt precipitates, corrosion may actually be minimal for nickel-base alloys. At supercritical temperatures for an untreated acidic chlorinated feed, nickel-base alloys follow a general trend in which the corrosion rate decreases between 400 and 600℃.

1.3 Objectives of research

Corrosion of constructional materials is a major limiting factor in commercial development of SCWO systems. Although there has been an effort to identify suitable materials for SCWO systems, materials with suitable corrosion resistance are not developed and/or identified. As a continuing effort to identify the corrosion resistant materials for SCWO systems, commercial nickel-base alloys are selected as a part of candidate constructional materials. Using test facilities developed earlier[4, 6], these various materials are exposed to the acidic and neutral feed streams. The objectives of the research are summarized as follows.

Effects of alloying elements on corrosion resistance

Commercial nickel-base alloys with various compositions are tested to identify suitable materials and the effects of alloying elements.

Effects of chemical environment (acidic and neutral environments)

With feed streams of acidic and neutral solutions, the effect of the pH changes on the nickel-base alloys is investigated. Experiments with feed streams of a neutral solution (air saturated deionized water) are closely related to the application of supercritical light water cooled reactors.

Study of corrosion mechanisms

From these test results, the corrosion mechanisms of the nickel-base alloys are investigated in relation with the physical property changes of water over a wide temperature range (290-430℃). The dealloying of elements, the formation of oxide, and stress corrosion cracking (SCC) are discussed in both the supercritical and subcritical temperature ranges by considering the thermodynamics of a metal-water system, the kinetics of oxide growth, and a rudimentary stress analysis of the system.

Corrosion mitigation methodology

By understanding the corrosion mechanisms in SCWO systems, methodologies for corrosion mitigation are suggested and recommendations for further experiments are provided.

Bibliography

1. Tester, J.W., et al., *Supercritical Water Oxidation Technology - Process-Development and Fundamental Research.* ACS Symposium Series, 1993. **518**: p. 35-76.
2. Modell, M., *Standard Handbook of Hazardous Waste Treatment and Disposal*. 1989, New York: McGraw-Hill.
3. Mitton, D.B., J.H. Yoon, and R.M. Latanision, *An overview of Corrosion Phenomena in SCWO systems for Hazardous Waste Destruction.* Zairyo-to-Kankyo, 2000. **49**(3): p. 130-137.
4. Cline, J.A., *Experimental and Ab Initio Investigation into the Fundamentals of corrosion, in the Context of Supercritical Water Oxidation Systems*, in *Department of Chemical Engineering*. 2000, MIT.
5. Tester, J.W. and J.A. Cline, *Hydrolysis and Oxidation in Subcritical and Supercritical Water: Connecting Process Engineering Science to Molecular*

Interactions. Corrosion, 1999. **55**(11): p. 1088-1100.

6. Orzalli, J.C., *Preliminary Corrosion Studies of Candidate Materials for Supercritical Water Oxidation Reactor Systems,* in *Department of Materials Science and Engineering*. 1994, MIT: Cambridge.

Chapter 2: Background

Understanding the fundamental properties of water is essential in developing the corrosion mechanism in supercritical water environments. In this chapter, the properties of pure water over a wide temperature range at constant pressure of 25MPa and thermodynamics of a metal in an aqueous environment are presented.

2.1 Properties of water

2.1.1 Definition of supercritical water

A one-component fluid is defined to be supercritical when its temperature and pressure exceed its critical temperature and pressure, respectively. Supercritical water is a single-phase fluid when both its pressure and temperature are beyond its critical point. The phase behavior of pure water as a function of temperature and pressure is summarized in a phase diagram in Figure 2.1. When pressure and temperature are increased along the equilibrium line between the liquid and vapor, a critical point is reached where there is no distinction between the liquid and vapor phases. At this critical point, the meniscus separating the liquid phase and vapor phase disappears. The critical point is the last point

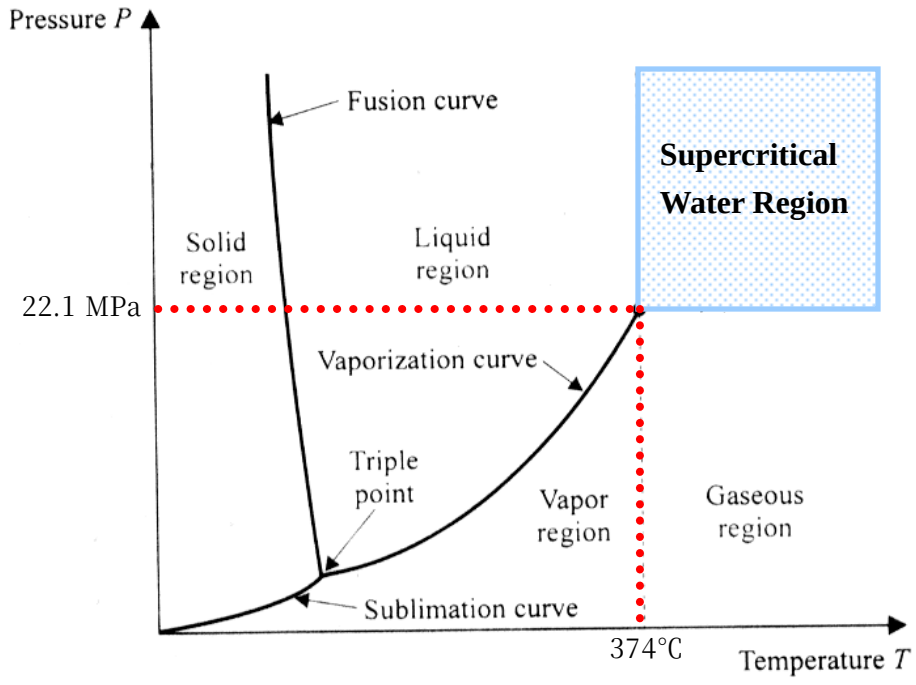

Figure 2.1 Phase diagram of pure water. The supercritical water region is superimposed on the diagram.[1]

in the two-phase region, and the only point in the one-phase region where the compressibility is infinite ($\beta_T = -1/V(\partial V/\partial P)_T \rightarrow \infty$). Above this critical point, water exists as a single-phase fluid, called supercritical water (SCW). Pure water has its critical point at 373.946℃, and 22.064MPa. In the supercritical region, a state of liquid-like density can transform into one of vapor-like density by tuning the pressure or the temperature, without appearance of an interface. The further from the critical point, the easier it is to gently manipulate the density by tuning pressure or temperature. In supercritical water, a range of intermediate-density states can be reached that are not available at subcritical temperatures and pressures.[2]

2.1.2 Physical Properties of water

The physical properties of pure water at the supercritical region are quite different from those of ambient water (25℃, 1atm). These properties of water have been investigated for many decades over a wide range of pressure and temperature due to their importance in technology. Further, thermodynamic and transport properties of pure water have been well tabulated in the literature over a wide range of temperatures and pressures.[3-5] As SCWO systems operate in a pressure range of 3500-4000psi (24.13-27.58MPa), the physical properties of pure water at constant pressure of 25MPa are reviewed in this section over a wide temperature range. As temperature increases at constant pressure, the density of water drops continuously and drops even more rapidly near the critical temperature as shown in Figure 2.2(a). The density of water above the critical temperature is a sensitive function of the pressure, and density change is interrelated with other properties of water such as the dielectric constant, hydrogen bonding network, and ionic dissociation constant.

Hydrogen bonding

The peculiar physical properties of water originate from the hydrogen bonding network of water molecules, which can be considered equivalent to an electrical dipole. When water is in the solid state, ice, the hydrogen bond network is complete. Structural research has shown that liquid water, under most conditions, is described as a somewhat broken-down, slightly expanded form of the ice lattice. More specifically, liquid water has a considerable degree of short-range order characteristics of the tetrahedral bonding in ice and partly retains the tetrahedral bonding and resulting network structure characteristic of the crystalline structure of ice.[6] As temperature increases at constant pressure, the hydrogen bonding network is reduced because of thermal randomization of water molecules. Although some researchers report that hydrogen bonding in supercritical

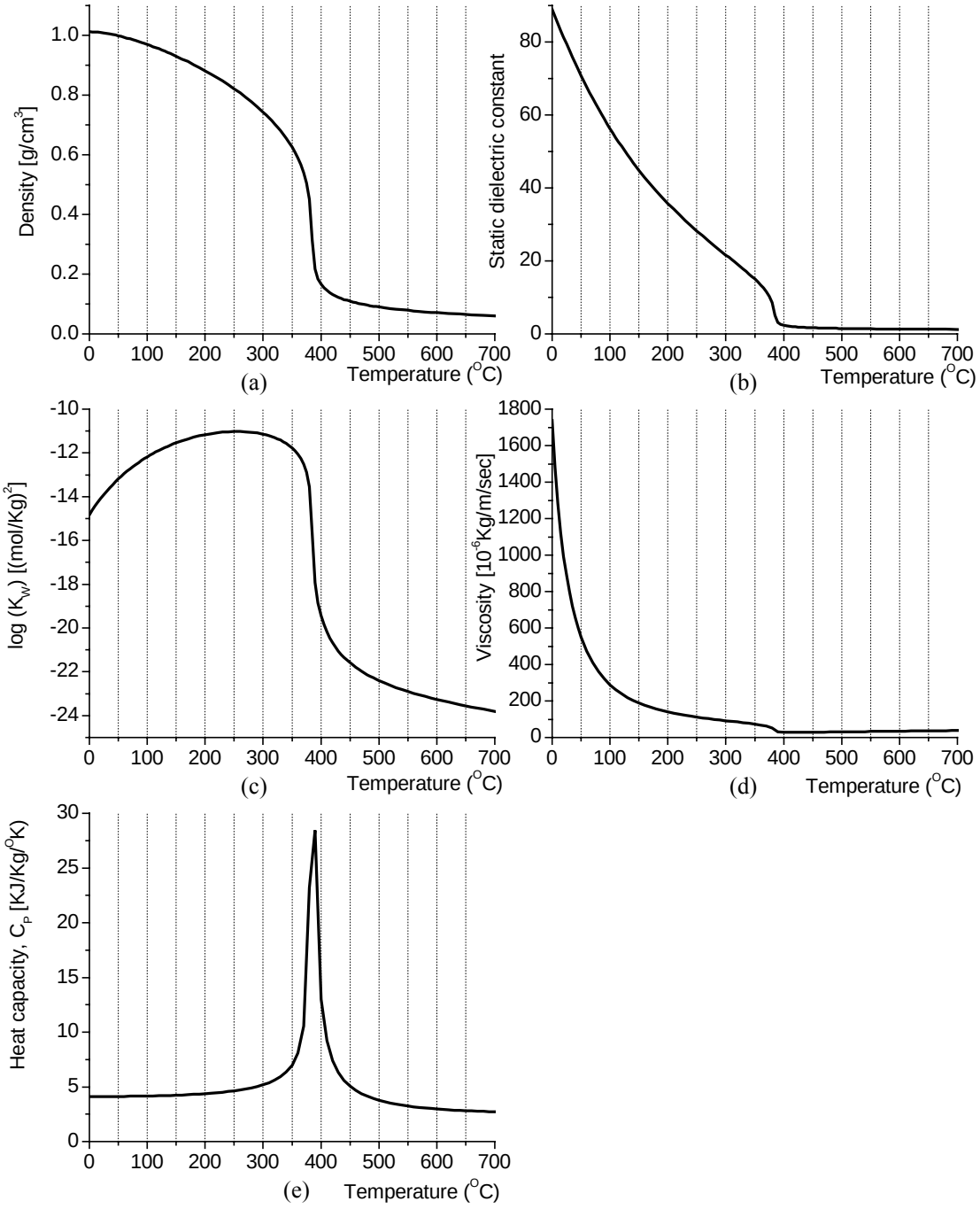

Figure 2.2 Physical properties of pure water at constant pressure of 25MPa as a function of temperature(℃). (a) Density (g/cm^3) (b) static dielectric constant (c) ionic dissociation constant (mol/Kg)^2 (d) viscosity (10^{-6}Kg/m/s) (e) heat capacity (KJ/Kg/K).

water completely disappears above 400℃ in neutron diffraction experiments[7, 8], it is generally accepted that hydrogen bonding persists even at a high supercritical temperature range[9-11].Nevertheless, the degree of hydrogen bonding is severely restricted above the critical point of water and only a small residual amount of hydrogen bonding is retained. The structure of water molecules is still under investigation by various experimental techniques such as NMR, Raman spectroscopy and diffraction techniques.

Static Dielectric constant

The high static dielectric constant of water under ambient conditions is related to both its molecular structure and hydrogen bonding. As the degree of hydrogen bonding is reduced at high temperature, the dielectric constant of water decreases as shown in Figure 2.2 (b). The static dielectric constant of pure water at 25MPa drops from around 80 at room temperature to 5-10 near the critical point, and to around 2 above 450℃. The decrease of the dielectric constant can be understood with the Kirkwood equation, which describes the dielectric constant of liquids containing associated dipoles.

$$\frac{(\varepsilon-1)(2\varepsilon+1)}{9\varepsilon}=\frac{4\pi n}{3}\left(\alpha_{deform}+\frac{\mu^2(1+g\overline{\cos\gamma})^2}{3kT}\right) \qquad (2.1)$$

where n is the number of dipoles per unit volume, α_{deform} is the deformation polarizability, which is a measure of how the molecules deform under electric fields and become induced dipoles, μ is dipole moment of a molecule, g is the number of nearest-neighbor water molecules linked with the central molecule, $\overline{\cos\gamma}$ is the average of the cosines of the angles between the dipole moment of the central water molecule and those of its bonded neighbors, k is the Boltzmann constant, and T is the absolute temperature. This equation takes into account the short-range interactions between polar molecules which lead to the formation of molecular groups orienting as a unit under the influence of electric fields. It also considers the actual local field, as distinct from the externally applied electric field, operating on the orienting entities. From this relation, it is clear that the association of dipoles arising from short-range forces is very important in determining the dielectric constant of a liquid. The linking together of dipoles increases g, the number of dipoles which are nearest neighbors to a reference dipole, and thus increases the dielectric constant[6]. As the water goes beyond its critical point, hydrogen bonding is substantially restricted in the supercritical region, and as a result, the dielectric constant decreases substantially.

Ionic dissociation constant of water

The ionic dissociation constant of pure water can be defined as the product of the hydrogen ion activity and hydroxide ion activity. This activity is defined in a unit of molal concentration for its convenience with a wide temperature change.

$$H_2O(l) \leftrightarrow H^+(aq) + OH^-(aq)$$

$$K_w = m_{H^+} m_{OH^-} \qquad (2.2)$$

where m_{H^+} and m_{OH^-} are the molality of H^+ and OH^- ions respectively, and K_w is the ionic dissociation constant of pure water, defined by equation (2.2) as 10^{-14} [(mol/kg)^2] under ambient conditions. This ionic product constant increases as temperature increases initially and then rapidly decreases near the critical point as shown in Figure 2.2 (c). The ionic dissociation constant of pure water drops to 10^{-18} in the near critical region, and finally to 10^{-23} under supercritical conditions. The decrease of ionic product constant and dielectric constant partly indicates that the ionic species are not preferred at the supercritical temperature range. A low ionic dissociation constant, dielectric constant and limited hydrogen bonding affect the solvation properties of supercritical water drastically.

Other than these properties, water also has a large heat capacity near its critical point, typically 2 to 6 times that of liquid water as shown in Figure 2.2(e) and its isothermal compressibility is very large. The viscosity of pure water also continuously decreases as temperature increases up to about 425℃ and slightly increases at higher temperatures (T>~425℃) as shown in Figure 2.2 (d).

2.1.3 Solvation properties of water

Water is usually considered to be a highly polar liquid solvent, characterized by a high, practically constant density (0.990-1.000 g/cm^3), a high dielectric constant (~80), a high degree of molecular association, and a low but definite degree of self-dissociation (K_w = 10^{-14}). However, the properties of water as a solvent undergo marked changes as the temperature and pressure vary. By observing water properties over a wide range of temperature, it is clear that ideas concerning the nature of water as a highly polar solvent are only tenable over a comparatively narrow range of low temperatures and pressures.

The properties of supercritical water are substantially different from those of liquid water under ambient conditions. In the region near the critical point of pure water, the density changes rapidly with both temperature and pressure, and is intermediate between that of liquid water and low-pressure water vapor. At typical operating conditions of

SCWO systems, the water density is approximately 0.1g/cm^3. The solvation characteristics of supercritical water can be understood by hydrogen bonding, the dielectric constant, and the ionic dissociation constant of water as described in the previous section. The properties of pure water are summarized in Table 2.1 under ambient conditions and supercritical conditions. A low dielectric constant and low ionic dissociation constant along with only a small residual amount of hydrogen bonding make supercritical water act as a non-polar dense gas and its solvation properties resemble those of a low-polarity organic. [12]

Table 2.1 Comparison of physical properties of pure water at room temperature and supercritical temperature.[12]

Property	Ambient water (25℃, 1atm)	Supercritical water (500℃, 25MPa)
Density (g/cm^3)	1	~0.1
Hydrogen bonding	Substantial	Small residual amount
Dielectric constant	78	~2
Ionic dissociation constant	10^{-14} (mol/Kg)^2	10^{-22} (mol/Kg)^2
Solubility of NaCl	26.4 wt%	~100 ppm
Solubility of Benzene	0.07 wt%	Complete miscibility

Near the critical point, the solubility of an organic compound in water correlates strongly with density and so is dependent on the system pressure in this region. Many organic compounds such as hydrocarbon are sparingly soluble in water at room temperature. However, the solubility of hydrocarbons increases as temperature increases. Above the critical point of the mixture, the hydrocarbons are completely miscible with supercritical water in all proportions and become a single-phase fluid. For example, the solubility of benzene at room temperature is around 0.07wt%. The solubility is increased to about 7 to 8 wt% and is fairly independent of pressure at 260℃, as shown in Figure 2.3. At 287℃, the solubility is somewhat pressure-dependent, and increases to about 18wt% at 20 to 25MPa. In this pressure range, the solubility rises to 35wt% at 295℃. Above the critical point of the benzene-water system (300℃), the mixture is supercritical, and as a result, there exists only a single phase. The benzene is completely miscible with supercritical water in all proportions.[12] Other hydrocarbons exhibit similar behavior to that of benzene and exhibit generally high solubility in supercritical water. The critical points of various hydrocarbon-water systems are listed in Table 2.2. For binary mixtures of a hydrocarbon-water system, the critical solution temperature is usually defined either

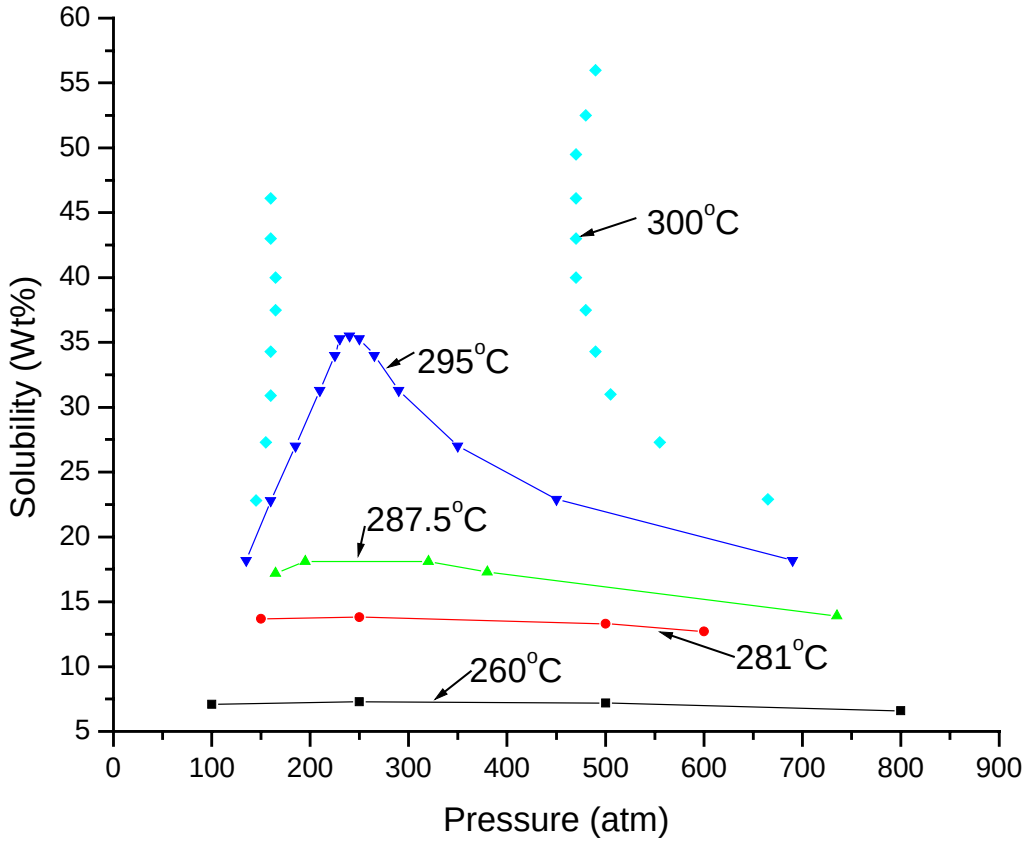

Figure 2.3 Solubility changes of benzene at various temperature and pressure ranges.[13]

Table 2.2 Critical solution temperatures for hydrocarbon-water systems[13]

Hydrocarbon	Critical solution temperature (℃)	Pressure (atm)
Benzene	297	240
n-Heptane	353	290
n-Pentane	351	340
2-Methyl pentane	352	310
Toluene	308	220

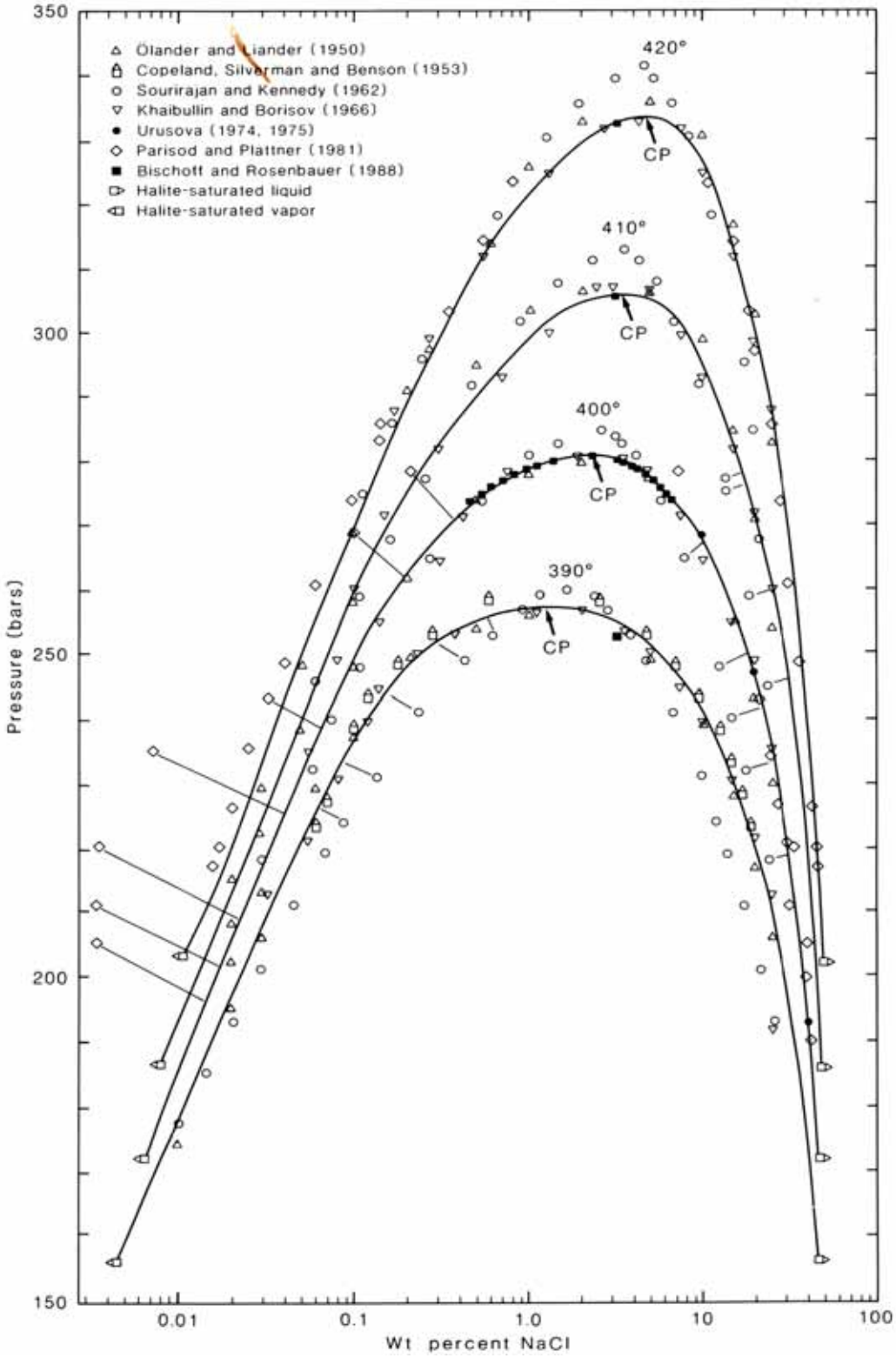

Figure 2.4 Experimental data for vapor-liquid isotherms of NaCl-H_2O from 390℃ to 420℃. CP: critical point. [14]

as the minimum temperature for mixing of two substances in all proportions as liquid; or it is the maximum temperature of a binary system for two liquid phases in equilibrium.[13, 15] Along with the solubility characteristics of hydrocarbons in supercritical water, permanent gases such as nitrogen, oxygen, hydrogen, carbon dioxide and air are completely miscible with supercritical water.[12, 16-18]

In contrast to the solvation property change of hydrocarbons, the solvation property of inorganic salt shows opposite characteristics. For example, the solubility of NaCl is about 26.4wt% under ambient conditions and is about 37wt% at 300℃ and about 120ppm at 550℃ and 25MPa. The solubility of NaCl near the critical point of water is shown in Figure 2.4. Other inorganic salts such as $CaCl_2$ and KCl show similar behavior as NaCl. Figure 2.4 shows that the solubility of NaCl in supercritical water decreases as temperature increases at constant pressure and is extremely low in the supercritical temperature range. If the influent contains a superfluous amount of NaCl at low temperatures, this mixture is separated into three phases consisting of a supercritical water phase, dense brine solution, and solid NaCl phase. These salts can be very sticky and can hinder heat transfer, harbor corrosive agents, and tend to aggregate and obstruct flow.[19] The solubility of several types of oxides such as CuO, Fe_3O_4 and$Mg(OH)_2$ also decreases as temperature increases, crossing the critical temperature at 250 bars[20].

2.2 Thermodynamics of a metal-water system

Corrosion in aqueous solutions has been found to involve electrons or charge transfer. A change in electrochemical potential or the electron activity or availability at a metal surface has a profound effect on the rates of corrosion reactions. Thus, corrosion reactions are said to be electrochemical. Thermodynamics gives an understanding of the energy changes involved in the electrochemical reactions of corrosion. These energy changes provide the driving force and control the spontaneous direction for a chemical reaction. Thus, thermodynamics shows how conditions may be adjusted to make corrosion impossible.[21]

Pourbaix (potential-pH, E-pH) diagrams are useful tools for summarizing the thermodynamic relationships in metal-water systems and, hence, for interpretating equilibrium electrochemical data and probable corrosion reactions. The Pourbaix diagram may be thought of as a map showing conditions of solution oxidizing power (potential) and acidity or alkalinity (pH) for the various possible phases that are stable in an aqueous electrochemical system. Although these thermodynamic principles are useful for revealing the reactions that are thermodynamically possible, their limitations are apparent. They refer to pure, defect-free, unstressed metals in pure water and do not indicate the

rate at which these reactions may take place. The actual extent or rate of corrosion is governed by kinetic laws.

The method to construct Pourbaix diagrams for major alloying elements such as Ni, Cr, Fe, and Mo for nickel-base alloys is presented at room temperature and high temperatures. For alloy systems, the Pourbaix diagrams of major alloying elements are frequently superposed. Apparently, these types of diagrams do not consider the interactions between constituent elements in an alloy.

2.2.1 Review of thermodynamic principles in aqueous media

Pourbaix diagrams are graphical representations of the domain of stability of metal ions, oxides, and other species in solution. The lines that show the limits between two domains express the value of the equilibrium potential between two species as a function of pH. They are computed from thermodynamic data, and standard chemical potentials by using the Nernst equation. The equilibrium potentials and pH values that set the limits between the various stability domains are determined from the chemical equilibria between the chemical species considered.

The change in electrode potential as a function of concentration is given by the Nernst equation for a general half-cell reaction as

$$aA + mH^+ + ne^- = bB + dH_2O$$

$$E = E^0 - \frac{RT}{nF}\ln\frac{(B)^b(H_2O)^d}{(A)^a(H^+)^m} \qquad (2.3)$$

where E is the electrode potential, E^0 is the standard electrode potential, R is the gas constant, T is the absolute temperature, n is the number of moles of electrons transferred in the half-cell reaction, F is Faraday constant, parentheses represent the activities of the species, and the stoichiometric coefficients of the species are represented as a, m, n, b, and d, respectively. The activity of each reactant and product is defined as unity for the standard state. For dilute or strongly dissociated solutes found in most instances of corrosion, activity is approximated by concentration. For solid materials, the solid is taken as the standard state of unit activity, and for gases, 1 atm pressure of the gas is taken as the standard state.[21] The standard electrode potential can be calculated using thermodynamic data by the relation given by

$$E^0 = -\frac{\Delta G^0}{nF} = -\frac{(b\mu_B^0 + d\mu_{H_2O}^0) - (a\mu_A^0 + m\mu_{H^+}^o)}{nF} \qquad (2.4)$$

where μ^0 is the chemical potential of the species in the standard state, and ΔG^0 is change in free energy when the half-cell reaction occurs under conditions in which the reactants and products are in their standard states. The chemical potential of hydrogen

ions in the standard state, $\mu^0_{H^+}$, is conventionally defined as zero as a reference. In considering aqueous metallic corrosion, there are three types of reactions to be considered in constructing the E-pH diagram:

1) Electrochemical reactions of pure charge transfer
2) Electrochemical reactions involving both electrons and H^+
3) Pure acid-base reactions

The example of pure nickel in aqueous media is chosen to illustrate these reactions.

Reactions of pure charge transfer

These electrochemical reactions involve only electrons and the reduced and oxidized species. They do not have protons (H^+) as reacting species, and consequently, are not influenced by pH. An example of a reaction of this type is:

$$Ni^{2+}(aq) + 2e^- = Ni$$

The equilibrium potential given by the Nernst equation (2.3) is:

$$E = E^0 + \frac{RT}{nF}\ln(Ni^{2+}) \qquad (2.5)$$

where E is the equilibrium potential for Ni^{2+}/Ni, E^0 is the standard potential for Ni^{2+}/Ni. The equilibrium potential, E depends on the activity of Ni^{2+} in the solution and the standard potential E^0 can be calculated from equation (2.4):

$$E^0 = -\frac{\Delta G^0}{nF} = \frac{\mu^0_{Ni^{2+}} - \mu^0_{Ni}}{2F} = \frac{\mu^0_{Ni^{2+}}}{2F} \qquad (2.6)$$

where μ^0 is the standard chemical potential of each species. The standard potential has a numeric value of –0.25 V at room temperature. As the reaction does not have protons as reacting particles, the electrochemical potential is independent of pH and only depends on the activity of Ni^{2+}.

Reactions involving both electrons and H^+

Metal can also react with water to form an oxide according to the electrochemical reaction:

$$NiO + 2H^+(aq) + 2e^- = Ni + H_2O$$

The corresponding Nernst equation and standard potential are given as:

$$E = E^0 + \frac{RT}{nF}\ln\frac{(NiO)(H^+)^2}{(Ni)(H_2O)} \qquad (2.7)$$

$$E^0 = \frac{\mu^0_{NiO} - \mu^0_{Ni} - \mu^0_{H_2O}}{2F}. \qquad (2.8)$$

As Ni is a stable element in its standard state, its chemical potential is zero. At 25℃, the standard potential for this reaction is 0.11 V. The NiO and Ni are solid phases, and they

are considered to be pure and so their activity is assumed to be 1. The activity of water in aqueous solution is also assumed to be 1. By changing the natural logarithm into a conventional logarithm, the Nernst equation becomes:

$$E = 0.11 + 0.03\log(H^+)^2 . \quad (2.9)$$

Because pH = -log(H^+) by definition, it is possible to simplify equation (2.9) to:

$$E = 0.11 - 0.06\,pH . \quad (2.10)$$

Pure acid-base reactions

When the equilibria between metal ions and oxide are considered, it is observed that the reaction does not have electron transfer. For Ni^{2+}/NiO, the reaction is

$$Ni^{2+} + H_2O \leftrightarrow NiO + 2H^+ .$$

As the reaction does not include electrons, it does not depend on the potential. From the chemical equilibrium reaction, we get

$$\Delta G^0 = -RT\ln K_{eq} \quad (2.11)$$

$$\log K_{eq} = \frac{\sum \nu_R \mu_R^0 - \sum \nu_P \mu_P^0}{2.3RT} \quad (2.12)$$

where K_{eq} is equilibrium reaction constant, ν_R is the stoichiometric coefficients of the reactants, and ν_P is the stoichiometric coefficients of the product. Then, for the Ni^{2+}/NiO reaction,

$$\log\frac{(NiO)(H^+)^2}{(Ni^{2+})(H_2O)} = \frac{\mu_{Ni^{2+}}^0 + \mu_{H_2O}^0 - \mu_{NiO}^0}{2.3RT} . \quad (2.13)$$

By assuming that (NiO) and (H_2O) both have activities of 1 and by replacing the chemical potential of each species at standard state, the equation (2.12) at room temperature can be written as

$$\log(Ni^{2+}) = 12.41 - 2\,pH . \quad (2.14)$$

Water E-pH construction

Because Pourbaix diagrams are traced for equilibrium reactions taking place in water, the water E-pH diagram always must be considered at the same time as the system under investigation. Water can be decomposed into oxygen and hydrogen, according to the following reactions:

$$2H^+ + 2e^- = H_2 \quad \text{and}$$

$$\tfrac{1}{2}O_2 + 2H^+ + 2e^- = H_2O .$$

The equilibrium potential for these two reactions are determined by using the Nernst

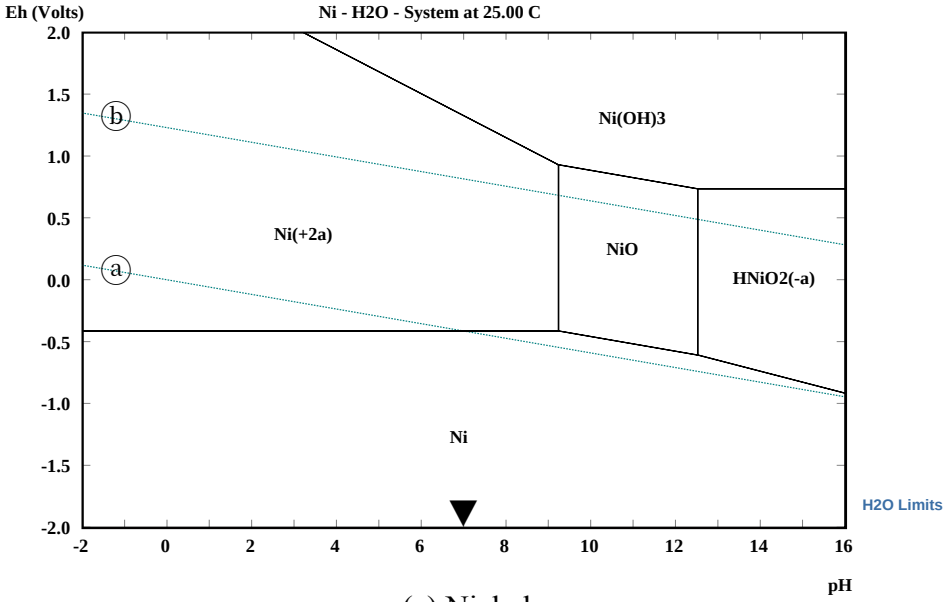

(a) Nickel

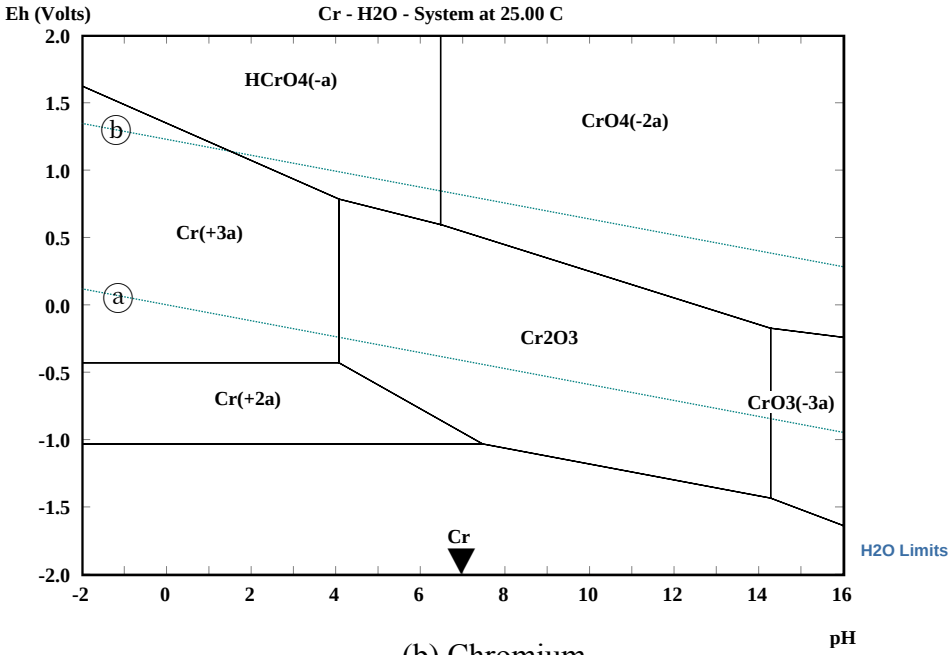

(b) Chromium

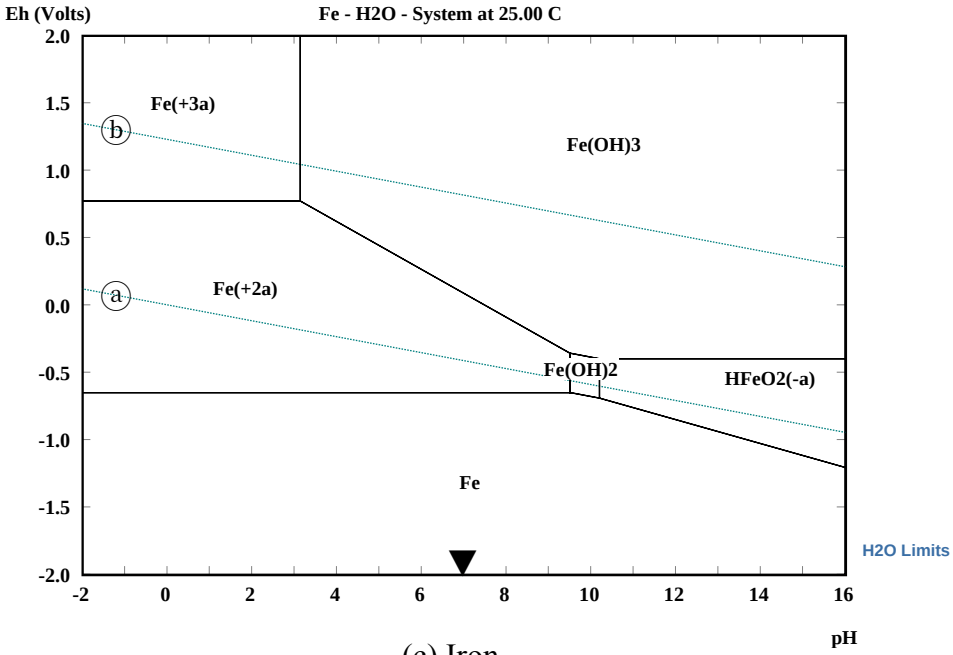

(c) Iron

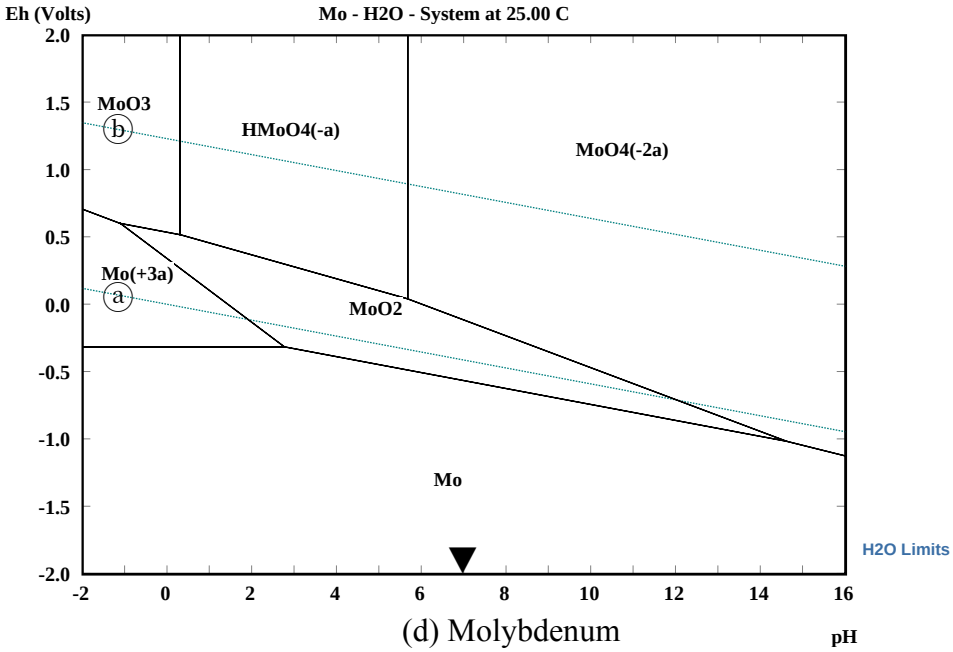

(d) Molybdenum

Figure 2.5 E-pH diagram for Ni, Cr, Fe and Mo at T=25℃ and P=1bar with an assigned molality of 10^{-6}. The stability line of water is indicated by ⓐ, ⓑ in each diagram. Neutral pH 7 is indicated by ▼.

equation (2.3) as

$$E_{H^+/H_2} = E^0_{H^+/H_2} + \frac{0.059}{2}\log\frac{(H^+)^2}{p_{H_2}}, \text{ and} \tag{2.15}$$

$$E_{O_2/H_2O} = E^0_{O_2/H_2O} + \frac{0.059}{2}\log\frac{(p_{O_2})^{1/2}(H^+)^2}{(H_2O)}. \tag{2.16}$$

Because $E^0_{H^+/H_2} = 0$, by convention, the above equation simplifies to

$$E_{H^+/H_2} = -0.059\,pH \quad \text{and} \tag{2.17}$$

$$E_{O_2/H_2O} = 1.23 - 0.059\,pH \tag{2.18}$$

assuming that the partial pressures of oxygen and hydrogen gases are in standard states of 1 atm and room temperature.

By considering all probable sets of reactions in the Water-Nickel system, we can draw the E-pH diagram. The E-pH diagrams for Ni, Cr, Fe and Mo at room temperature are demonstrated in Figure 2.5 with the assumption of the molal activity of dissolved species as 10^{-6}(mol/Kg).[22] Detailed descriptions of the construction method are well published in the literature.[21, 23, 24] As the potential depends on the activity of dissolved species, it is customary to select four activities 1, 10^{-2}, 10^{-4}, and 10^{-6} in molar concentration (mol/Liter) or molal concentration (mol/Kg). Pourbaix diagrams offer a framework for kinetic interpretation, but they do not provide information on corrosion rates. Moreover, they are not a substitute for kinetic studies.

2.2.2 Construction of the Pourbaix diagram at high temperatures

In the previous section, the basic principle for the construction of a Pourbaix diagram was presented. The construction of a Pourbaix diagram is straightforward at room temperature in the sense that most thermodynamic data are readily available in the literature. However, high temperature thermodynamic data to construct Pourbaix diagrams are very limited and are not available in most cases, especially for ionic species. In the case of pure substances, i.e. solids, gases, and liquids, we can obtain reasonably accurate free energy change at high temperature from heat capacity data available in the literature. However, in the case of ionic species, the heat capacity data are not usually available. In this section, a theoretical methodology to obtain high temperature thermodynamic data for ionic species is presented.

In electrochemical thermodynamics, the standard hydrogen electrode is defined as the zero potential at all temperatures (i.e. $\mu^0_{H^+}(T) = 0$). By using the relation $\Delta G^0 = -nFE^0$, the standard electrode potential of any half-cell reaction at any temperature T can be referred to its standard value at 25°C by the using the thermodynamic relation

$$\left(\frac{\partial \Delta H}{\partial T}\right)_P = T\left(\frac{\partial \Delta S}{\partial T}\right)_P = \Delta C_P \qquad (2.19)$$

where ΔH is the enthalpy change, ΔS is the entropy change, and ΔC_P is the heat capacity change of the reaction as a function of temperature T (degree K) at constant pressure. Using equation (2.19), we can obtain the following thermodynamic relation by integration

$$\Delta G^0_{T_2} = \Delta H^0_{T_2} - T_2 \Delta S^0_{T_2} = \Delta H^0_{T_1} + \int_{T_1}^{T_2} \Delta C_P dT - T_2 \Delta S^0_{T_1} - T_2 \int_{T_1}^{T_2} \frac{\Delta C_P}{T} dT$$

$$= \Delta G^0_{T_1} + \int_{T_1}^{T_2} \Delta C_P dT - T_2 \int_{T_1}^{T_2} \frac{\Delta C_P}{T} dT - \Delta T \Delta S^0_{T_1} \qquad (2.20)$$

where T_1 is reference temperature and $\Delta T = T_2 - T_1$. The C_P data required for equation (2.20) are not available for most ionic species.[25] However, Criss and Cobble have devised a method for solving this equation by the "Entropy Correspondence Principle."[26-29] The absolute entropy of the hydrogen ion at 25°C, $S^0_{25}(H^+)$, is estimated to be –5.0 eu. Criss and Cobble normalized all of the literature values of the ionic entropy at 25°C to the absolute scale by the following relationship:

$$S^0_{25}(i, abs) = S^0_{25}(i, conventional) - 5.0z \qquad (2.21)$$

where $S^0_{25}(i, abs)$ is absolute entropy of i at 25°C, z is ionic charge with sign, and the conventional scale is based on $S^0(H^+) = 0$ at any temperature. Criss and Cobble showed that equation (2.21) is valid for any temperature, T_2:

$$S^0_{T_2}(i, abs) = S^0_{T_2}(i, conventional) - S^0_{T_2}(H^+, abs)z\,. \qquad (2.22)$$

Criss and Coble have related $S^0_{T_2}(i, abs)$ to $S^0_{25}(i, abs)$ by using the following relationship, which is called the "Correspondence Principle of Ionic Entropy":

$$S^0_{T_2}(i,abs) = a(T_2) + b(T_2)S^0_{25}(i,abs)\,. \qquad (2.23)$$

The basis of equation (2.23) rests on the analysis of the available experimental data in the literature by Criss and Cobble. For each temperature T_2, only one assigned value of $S^0_{T_2}(H^+,abs)$ can be used in equation (2.22) to give a linear relationship between $S^0_{T_2}(i,abs)$ and $S^0_{25}(i,abs)$ for every ion type. To calculate values of $\Delta G^0_{T_2}$ from equation (2.20) using the Correspondence Principle, the average value of the heat capacity over a given, extended temperature interval is used by the following relation:

$$\overline{C}_P\Big|_{T_1}^{T_2} = \frac{\int_{T_1}^{T_2} C_P dT}{\int_{T_1}^{T_2} dT} \qquad (2.24)$$

where $\overline{C}_P\Big|_{T_1}^{T_2}$ is the average value of the heat capacity. By equation (2.24), we can approximate equation (2.20) as

$$\Delta G^0_{T_2} = \Delta G^0_{T_1} - \Delta T \Delta S^0_{T_1} + \overline{\Delta C}_P\Big|_{T_1}^{T_2}\left(\Delta T - T_2 \ln\frac{T_2}{T_1}\right). \qquad (2.25)$$

For nonionic species, entropy and heat capacity values are available for a wide range of temperatures. For ionic species, the average heat capacity is calculated from the entropy data of Criss and Cobble with the following relation:

$$\overline{C}_P\Big|_{T_1}^{T_2} = \frac{S^0_{T_2} - S^0_{T_1}}{\ln(T_2/T_1)}. \qquad (2.26)$$

The $\Delta G^0_{T_2}$ value calculated at T_2 would then be converted to $E^0_{T_2}$ by using the Nernst equation. If T_2 is greater than 200°C, the right-hand side of equation (2.25) will have accumulative error due to averaging of heat capacity. To minimize this error, the ΔG^0 value for 200°C is calculated, and 200°C is used as the base temperature T_1 for further extrapolation. Due to limited availability of thermodynamic data of ionic species at high temperature, the Entropy Correspondence Principle established by Criss and Cobble is frequently used to obtain high temperature thermodynamic data. Although this

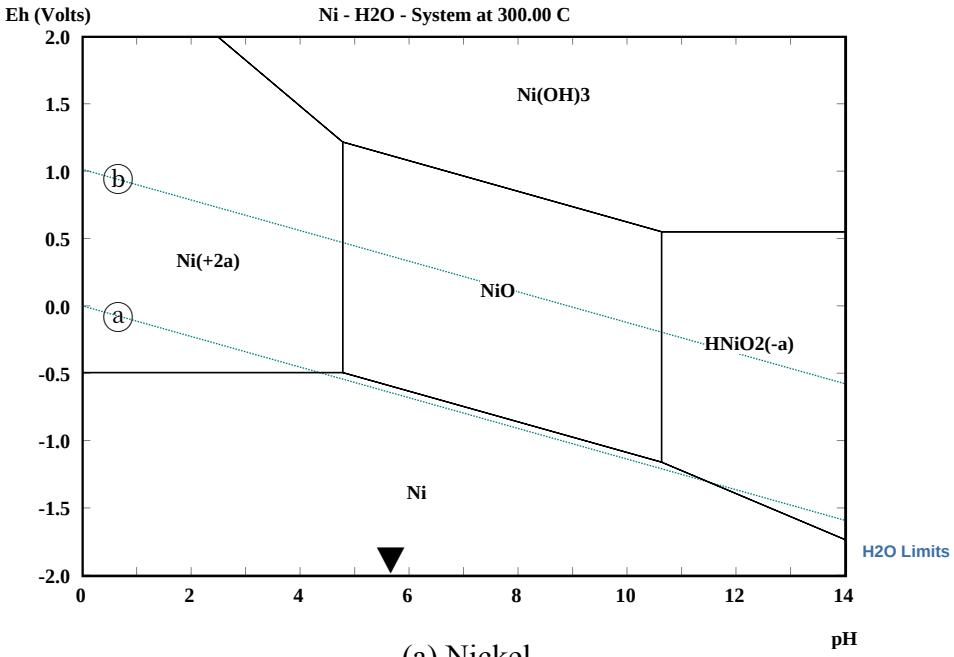

(a) Nickel

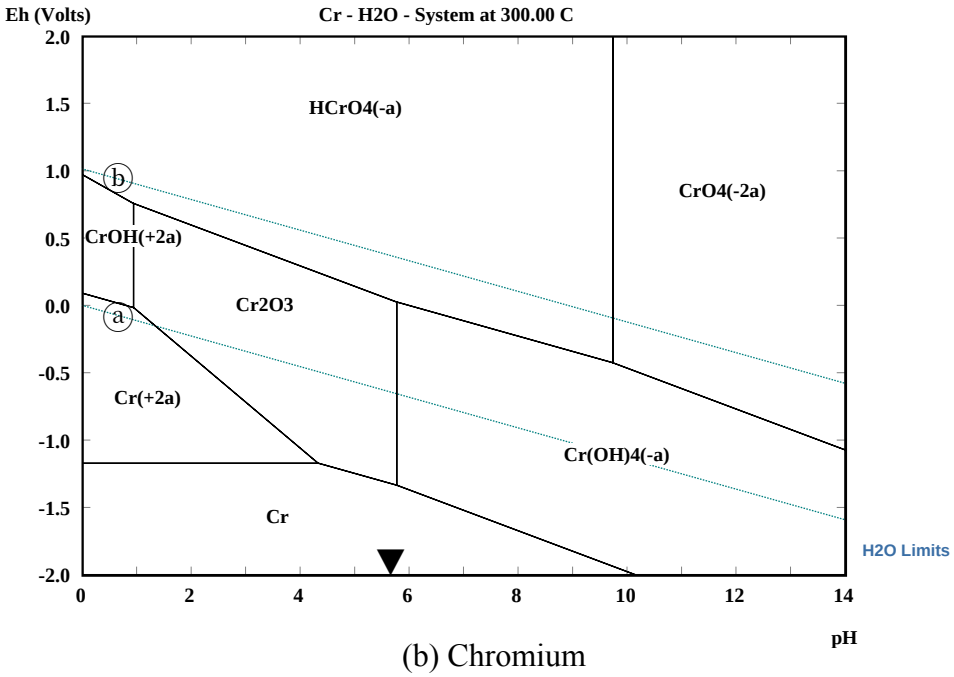

(b) Chromium

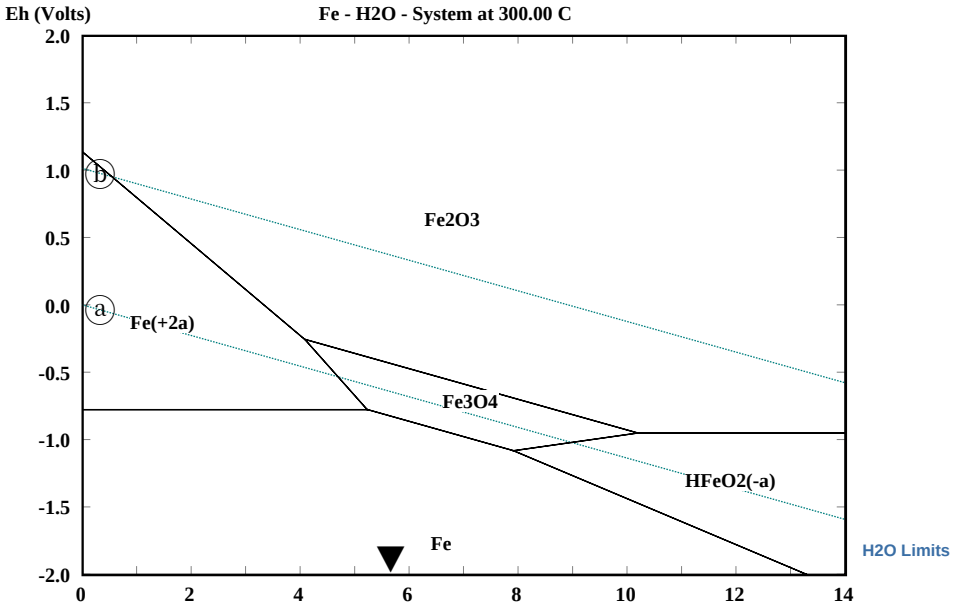

(c) Iron

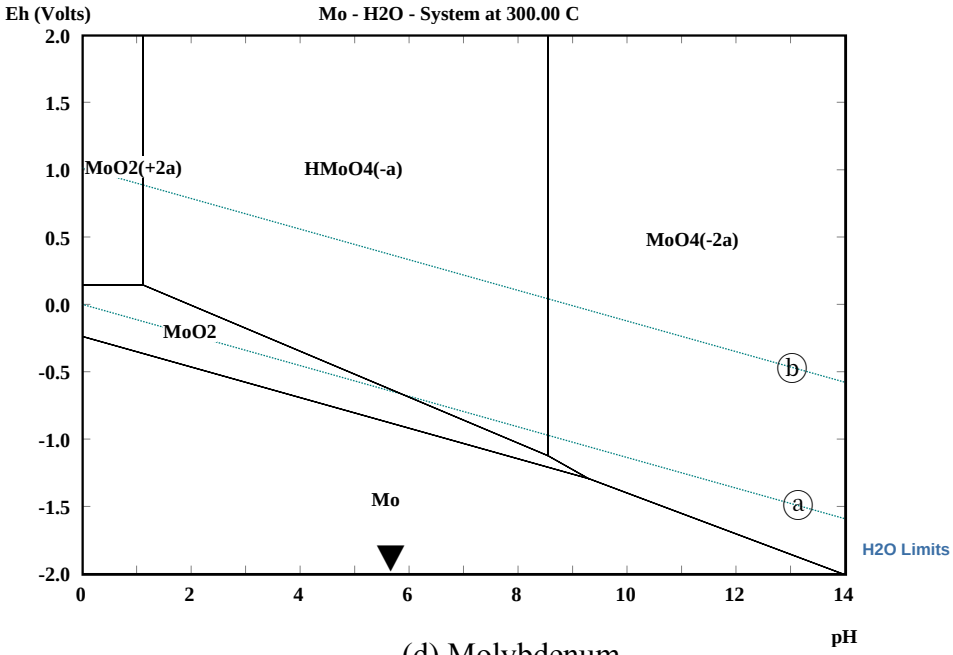

(d) Molybdenum

Figure 2.6 E-pH diagram for Ni, Cr, Fe and Mo at T=300℃ and P=84.63bar (saturated vapor pressure) with an assigned molality of 10^{-6}. The stability line of water is indicated by ⓐ, ⓑ in each diagram. Neutral pH is indicated by ▼ with a numeric value of 5.65 at 300℃ and 84.63 bar.

methodology has a somewhat theoretical basis, it is basically extrapolation of low temperature thermodynamic data to higher temperatures. Furthermore, in equation (2.20) the free energy contribution caused by the change of pressure is not considered. However, this change in equilibrium pressure can produce an additional free energy change:

$$\Delta G = \int_{P_1}^{P_2} V dP \qquad (2.27)$$

The change in pressure will also change the activity coefficients of dissolved species and partial molal volume, both leading to the free energy change of the system.[26] Criss and Cobble have shown that these effects are important, but that they can be ignored up to 300°C since the magnitude of the errors introduced are within the limited accuracy of the data used to formulate the Correspondence Principle. The agreement between this method and experiments is very accurate up to 300°C and suggests that it is reasonable to use for calculating E^0 values of electrochemical reactions in aqueous solutions at elevated temperatures. Pourbaix diagrams of Ni, Cr, Mo, and Fe at 300°C are presented in Figure 3.6 by using commercial HSC software[22] and its thermodynamic databases, which extrapolate the low temperature data with the Entropy Correspondence Principle of Criss and Cobble. Each diagram shows regions of stable states as solids or ions for each element.

2.3 Review of nickel-base alloys[24, 30-32]

Nickel-base alloys are vitally important to modern industry because of their ability to withstand a wide variety of severe operating conditions involving corrosive environments, high temperature, high stresses, and combinations of these factors. There are several reasons for these capabilities. Pure nickel is ductile and tough because it possesses a face-centered cubic structure up to its melting point (1453°C). Therefore, nickel and nickel-base alloys offer freedom from the ductile-to-brittle transition behavior of other metals and alloys such as steels. Nickel also has good resistance to corrosion in the normal atmosphere, in natural fresh water, and deaerated nonoxidizing acids, and it has excellent resistance to corrosion by caustic alkalies. Therefore, nickel offers very useful corrosion resistance, and it is an excellent base to develop specialized alloys. Among many types of nickel-base alloys, alloys that contain Cr, Mo, and Fe as major alloying elements have been selected due to their practical importance in high temperature applications.

Table 2.3 Effects of alloying elements on the corrosion resistance of nickel-base alloys.[31]

Element	Effect
Ni	Improves high-temperature strength, resistance to oxidation, nitridation, carburization, and halogenation, metallurgical stability, resistance to reducing acids and caustic, resistance to stress corrosion cracking. Detrimental to sulfidation.
Cr	Improves oxidation and sulfidation resistance, aqueous corrosion resistance.
Mo	Improves high temperature-strength, resistance to pitting and crevice corrosion, resistance to reducing acids. May reduce oxidation resistance
Fe	Improves economy of alloys
C	Improves high temperature strength.
Al	Improves resistance to oxidation and sulfidation.
Rare earth	Improves adherance of oxide layer.
Cu	Improves resistance to reducing acids and salts, resistance to sulfuric acid.
Nb	Improves high-temperature strength, resistance to pitting. Carbide stabilization component, Age-hardening component.
S	Improves machinability.
Si	Improves resistance to oxidation and carburization
Co	Improves high temperature strength and oxidation resistance.
N	Can improve high-temperature strength by precipitation of stable nitrides. Improve pitting and crevice corrosion and metallurgical stability by acting as an austenizer.
Ti	Detrimental to oxidation due to titanium oxides disrupting primary oxide scale. Age-hardening component, Carbide stabilization component.
W	Improves resistance to pitting and crevice corrosion and high temperature strength
Yttrium oxide	Improves high-temperature strength, grain size control and resistance to oxidation

Chromium additions impart improved resistance to oxidizing media such as nitric (HNO_3) and chromic (H_2CrO_4) acids. Chromium also improves resistance to high temperature oxidation and to attack by hot sulfur bearing gases. Although alloys have been formulated up to 50%Cr, alloying additions are usually in the range of 15 to 30%.

Iron is typically used in nickel-base alloys to reduce costs, not to promote corrosion resistance. However, iron does provide nickel with improved resistance to H_2SO_4 in concentrations above 50%. Iron also increases the solubility of carbon in nickel, which improves resistance to high-temperature carburizing environments. Molybdenum in nickel substantially improves resistance to nonoxidizing acids. Commercial alloys containing up to 28% Mo have been developed for severe nonoxidizing solutions of HCl, H_3PO_4, and HF, as well as in H_2SO_4 in concentrations below 60%. Molybdenum also markedly improves the pitting and crevice corrosion resistance of nickel-base alloys. In addition, Mo is an important alloying element for imparting strength in metallic materials designed for high-temperature service.[24] In nickel-base alloys, other minor alloying elements also have specific effects on the corrosion resistance and bulk properties of alloys. The effects of important alloying elements in nickel-base alloys are summarized in Table 2.3.[31] These effects of minor alloying elements come from experimental observation in general. As specific environmental effects can easily change the beneficial effects of minor alloying elements, careful selection of materials and consideration of the material performance under specific chemical environments are usually required. These nickel-base alloys have specific applications depending on their alloying elements and corresponding properties. Due to their high temperature strength and resistance to corrosion at high temperature, these materials are usually applied to high temperature applications such as engine and power generation systems.

Bibliography

1. Zemansky, M.W. and R.H. Dittman, *Heat and Thermodynamics, 7th edition*. 1997: McGraw-Hill.
2. Sengers, J.M.H.L., *Supercritical Fluids: Their Properties and Applications*, in *Supercritical Fluids: Fundamentals and Applications*, C.J. Peters, Editor. 2000, Kluwer Academic Publishers: Boston. p. 1-29.
3. Meyer, C.A., et al., *ASME Steam Tables: Thermodynamic and transport properties of Steam*. 6th ed. 1993: ASME PRESS.
4. Wagner, W. and A. Kruse, *Properties of Water and Steam*. 1998: Springer.
5. Haar, L., J. Gallagher, S., and K.G. S., *NBS/NRC Steam Tables*. 1984: Hemisphere Publishing Coorporation.
6. Bockris, J.O.M. and A.K.N. Reddy, *Modern Electrochemistry, an Introduction to an Interdisciplinary Area, Vol. 1*. 1970. 622 pp.
7. Postorino, P., et al., *The Interatomic Structure of Water at Supercritical*

Temperatures. Nature, 1993. **366**(6456): p. 668-670.

8. Postorino, P., M.A. Ricci, and A.K. Soper, *Water above Its Boiling-Point - Study of the Temperature and Density-Dependence of the Partial Pair Correlation-Functions .1. Neutron-Diffraction Experiment.* Journal of Chemical Physics, 1994. **101**(5): p. 4123-4132.
9. Bellissent-Funel, M.-C., *Structure of supercritical water.* Journal of Molecular Liquids, 2001. **90**(1-3): p. 313-322.
10. Nakahara, M., et al., *Structure and dynamics of water: from ambient to supercritical.* Journal of Molecular Liquids, 2001. **90**(1-3): p. 75-83.
11. Gorbaty, Y.E. and A.G. Kalinichev, *Hydrogen-Bonding in Supercritical Water .1. Experimental Results.* Journal of Physical Chemistry, 1995. **99**(15): p. 5336-5340.
12. Tester, J.W., et al., *Supercritical Water Oxidation Technology - Process-Development and Fundamental Research.* ACS Symposium Series, 1993. **518**: p. 35-76.
13. Connolly, J.F., *Solubility of hydrocarbons in Water Near the Critical Solution Temperatures.* Journal of chemical And Engineering Data, 1966. **11**(1): p. 13-16.
14. Bischoff, J.L. and P.K. S., *Liquid-Vapor Relations for the system NaCl-H2O: Summary of the P-T-x Surface from 300[deg]C to 500[deg]C.* American Journal of Science, 1989. **289**: p. 217-248.
15. Rebert, C.J. and W.B. Kay, *The phase behavior and solubility.* A.I.Ch.E. Journal, 1959. **5**(3): p. 285-289.
16. Japas, M.L. and E.U. Franck, *High Pressure Phase Equilibria and PVT-Data of the Water-Oxygen System Including Water-Air to 673 K and 250MPa.* Ber. Bunsenges. Phys. Chem., 1985. **89**: p. 1268-1275.
17. Japas, M.L. and E.U. Franck, *High Pressure Phase Equilibria and PVT-Data of the Water-Nitrogen System to 673K and 250 MPa.* Ber. Bunsenges. Phys. Chem., 1985. **89**: p. 793-800.
18. Seward, T.M. and E.U. Franck, *The system Hydrogen - Water up to 440[deg]C and 2500bar Pressure.* Ber. Bunsenges. Phys. Chem., 1981. **85**: p. 2-7.
19. Tester, J.W. and J.A. Cline, *Hydrolysis and Oxidation in Subcritical and Supercritical Water: Connecting Process Engineering Science to Molecular Interactions.* Corrosion, 1999. **55**(11): p. 1088-1100.
20. Martynova, O.I., *Solubility of Inorganic Compounds in Subcritical and Supercritical Water*, in *High Temperature High Pressure Electrochemistry in Aqueous Solutions*, R.W. Staehle, Editor. 1973, National Association of Corrosion Engineers: Houston. p. 131-138.

21. Jones, D.A., *Principles and Prevention of Corrosion, 2nd Edition*. 1996: Prentice-Hall.
22. *HSC chemistry, 5.11*. 2002, Outokumpu.
23. Pourbaix, M., *Atlas of Electrochemical Equilibria in Aqueous Solutions*. 1974, Houston: National Association of Corrosion Engineers.
24. *Metals Handbook. 9th deition. Corrosion*. Vol. 13. 1987: ASM International.
25. Cowan, R.L. and S.R. W., *The Thermodynamics and Electrode Kinetic Behavior of Nickel in Acid Solution in the Temperature Range 25 [deg]C to 300 [deg]C.* J. Electrochem. Soc., 1974. **118**(4): p. 557-568.
26. Criss, C.M. and J.W. Cobble, *The Thermodynamic Properties of High Temperature Aqueous Solutions. VI. Applications of Entropy correspondence Principle to Thermodynamics and Kinetics.* J. Am. Chem. Soc., 1964. **86**: p. 5394-5401.
27. Criss, C.M. and J.W. Cobble, *The Thermodynamic Properties of High Temperature Aqueous Solutions. I. Standard Partial Molal Heat Capacities of Sodium Chloride and Barium Chloride from 0 to 100 [deg]C.* J. Am. Chem. Soc., 1961. **83**: p. 3223-3228.
28. Criss, C.M. and J.W. Cobble, *The Thermodynamic Properties of High Temperature Aqueous Solutions. IV. Entropies of the Ions up to 200 [deg]C and the Correspondence Principle.* J. Am. Chem. Soc., 1964. **86**: p. 5385-5390.
29. Criss, C.M. and J.W. Cobble, *The Thermodynamic Properties of High Temperature Aqueous Solutions. V. The Calculation of Ionic Heat Capacities up to 200[deg]C. Entropies and Heat Capacities above 200[deg]C.* J. Am. Chem. Soc., 1964. **86**: p. 5390-5393.
30. Heubner, U., *Nickel Alloys*. 1998, New York: Marcel Dekker, Inc. 309.
31. Davis, J.R., ed. *Nickel, Cobalt, and Their Alloys*. ASM Specialty Handbook. 2000, ASM International: Materials Park, OH.
32. Lai, G.Y., *High-Temperature Corrosion of Engineering Alloys*. 1990, Materials Park: ASM International. 231.

Chapter 3: Experiments and results

3.1 Experimental procedure

To investigate the corrosion mechanisms in SCWO systems, a test facility has been developed to expose various materials to the supercritical and subcritical temperature ranges at a constant pressure. The system shown in Figure 3.1 draws from three feed-carbuoys, two of which contain deionized water (DW), and the third, dilute aqueous hydrochloric acid (pH 1.65 under ambient conditions). System pressure is developed by a continuously-running two-head piston-type HPLC feed pump (Eldex, model AA-100-s) at the system's upstream end and a back-pressure regulator (BPR) (Tescom, model 26-1722-24-090) at the downstream. System pressure is measured by transducers (Omega engineering, model PX613-5KG5V), and is maintained at approximately 24.1 MPa (3500 psi) throughout the system after a thermal steady state has been achieved. The feed to one pump head is switchable between the HCl(aq) and DW containers so that a thermal steady-state can be achieved without aggressive species such as proton and chloride. The system temperature is developed by means of a preheater coil inside a ceramic heater (Omega engineering, model CRFC-66/240-A), and the air temperature inside the ceramic heater, insulated by a ceramic fiber blanket, is set as 660°C. The pressurized DW-only stream flows through the preheater coil to bring the fluid to a supercritical temperature, after which it proceeds to an insulated mixing tee, where it is mixed with the room-temperature acid or DW stream from the other pump head. At the volumetric flow ratio of 4.6:1.6 (water:acid), the fluid exits the mixing tee as an HCl solution at pH 2 (under ambient conditions). From the mixing tee, the flow enters the reaction vessel, which is a tube which is instrumented with five Type K thermocouples (Omega engineering, model KMQSS-020-U-12) starting at the hot end. Each thermocouple is wrapped around and cemented to the tube using high temperature metallic adhesive (Aremco products, Pyro-putty 2400). These five thermocouples in all are used to monitor the temperatures of the reaction vessel. After passing through the reaction vessel, the flow proceeds to a shell-and-tube heat exchanger where it is cooled to room temperature. The cooled stream then passes through the back-pressure regulator (BPR) and then to effluent storage. Pressure is measured just upstream of the BPR, as well as in each feed stream. For safety, the system is shielded by high strength Lexan panels, three rupture disks are placed in the pressurized parts of the system and the system is controlled by LABVIEW software.

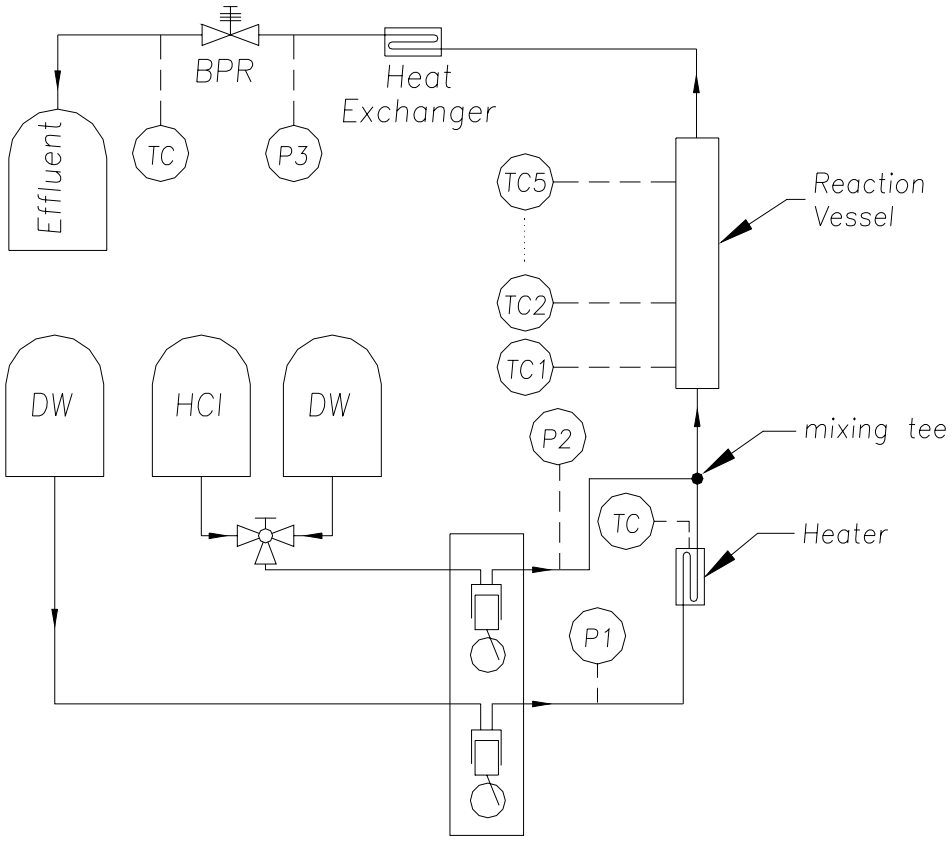

Figure 3.1 Schematic diagram of testing facility for exposure tests. P represents the transducer position and TC represents the thermocouple position.

With the exceptions of the snubbers on the pressure transducers and the downstream fittings of the test section, which are made from 316 stainless steel, the system components at high temperature sections are made out of Inconel 625 due to its high temperature strength and corrosion resistance against HCl(aq). A preheater coil made from Inconel 625 was annealed in a vacuum furnace at 1037℃ for 15 minutes and cooled by an argon fan to relieve the residual stress caused by bending. All the system components and samples were cleaned by acetone and DW before test.

3.2 Acidic environment testing results

To expose various nickel-base alloys (wires) to the acidic SCWO environment, a

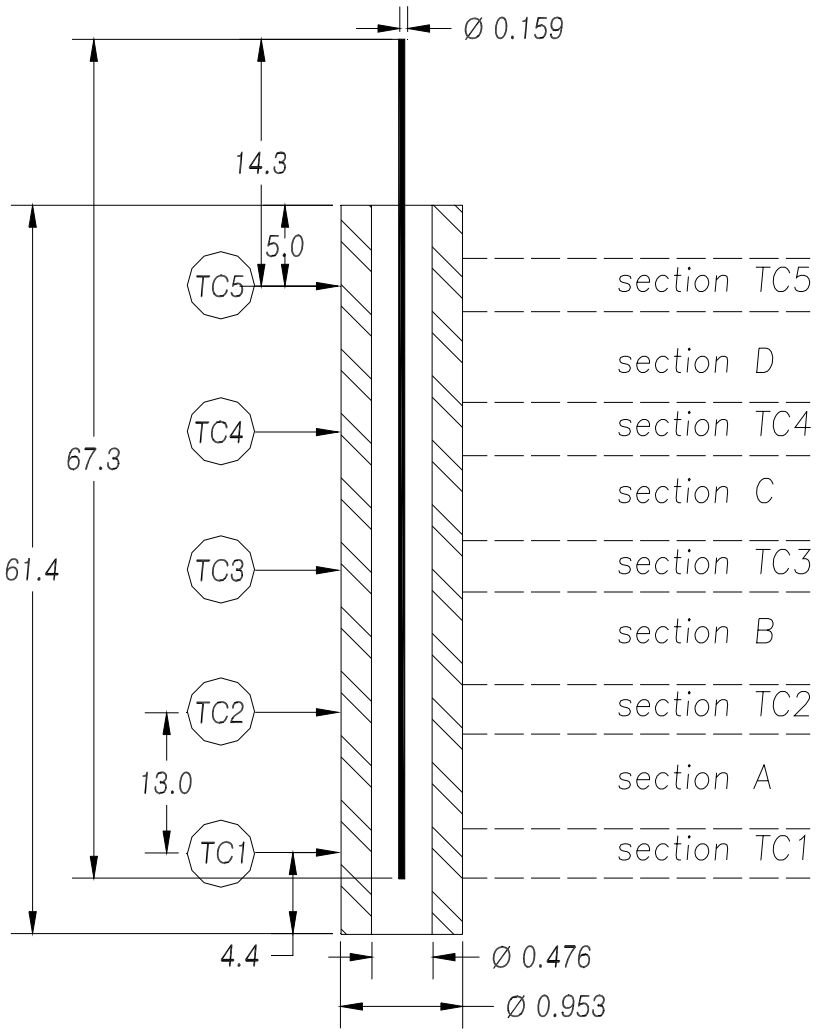

Figure 3.2 Detailed schematic of reaction vessel for acidic environment testing. Nickel-base wires are inserted in the Inconel 625 reaction vessel tube. Each wire and tube section indicated (right-hand) is cut for analysis after the exposure test. Flow direction is from bottom to top. Dimensions are in centimeters.

reaction vessel tube with the dimension of 9.53㎜ (3/8") in outer diameter (OD), 4.76㎜ (3/16") in inner diameter (ID) and 61.4㎝ in length is used to place the nickel-base wires. The flow rate of the system is 6.2㎖/min, with 4.6㎖/min from the DW stream and 1.6㎖ /min from the acid stream. The reaction vessel is made out of Inconel 625 for its corrosion resistance and strength at high temperature. The chemical compositions of nickel-base alloys and 316L stainless steel are provided in Table 3.1. Each nickel-base alloy in the shape of a cylinder with the diameter of 1.59㎜ (1/16") and length of 67.3㎝ is placed inside the reaction vessel as shown in Figure 3.2. For each run, temperatures measured by five thermocouples wrapped around the reaction vessel every 13㎝ are

averaged for each thermocouple. The average temperature and exposure time are given in Table 3.2. The temperatures from the first two thermocouples are beyond the critical point of pure water and the others are below the critical point.

Table 3.1 Nominal chemical composition (wt%) of nickel-base alloys and 316L stainless steel.

Element / Alloy	Ni	Cr	Mo	Fe	C	Others
Inconel 625	64.04	22.03	8.99	0.89	0.01	0.03Co, 3.48NbTa, 0.08Si, 0.01Mn, 0.004P, 0.001S, 0.02Cu, 0.21Ti, 0.21Al
Hastelloy C-22	55.4	21.1	14.2	4.3	0.002	3.0W, 1.43Co, <0.1NbTa, 0.024Si, 0.38Mn, 0.008P, 0.002S. 0.08Cu, 0.06V
Hastelloy C-276	57.0	15.5	16	5.5	0.01	4.0W, 0.08Si
Hastelloy C-2000	57.9	22.83	16.8	0.44	0.003	0.08W, 0.09Co, 0.02NbTa, 0.024Si, 0.19Mn, 0.004P, 0.004S, 1.65Cu, 0.01V
Alloy 59	60.31	22.8	15.55	0.73	0.002	0.03Co, 0.034N, 0.04Si, 0.15Mn, 0.004P, 0.002S, 0.01Cu, 0.12Al
Alloy 33	30.6	32.6	1.59	33.10	0.008	0.04Co, 0.410N, 0.25Si, 0.64Mn, 0.011P, 0.002S, 0.56Cu, 0.06Al
Alloy 671	55.37	44.22	-	0.2	0.03	0.16Si, 0.02Mn, 0.001S, 0.071Cu, 0.084Al, 0.88Ti, 0.88Mg
Hastelloy G-30	43.0	30.0	5.5	15.0	0.03	2.5W, 5.0Co, 1.5NbTa, 1.0Si, 1.5Mn, 2.0Cu
Hastelloy B-2	69.85	0.68	26.70	1.81	0.005	0.04Co, 0.003N, 0.57 Mn, 0.002P, 0.002S, 0.01Cu, 0.260Al
MC	54.7	44.4	0.9	-	-	-
316L SS	12.29	16.84	2.08	Bal	0.018	0.29Si, 1.18Mn, 0.034P, 0.008S

It is noted that in Table 3.2, the MC (Run#6 and Run#9) and the MC* (Run#12) alloy developed by Mitsubishi Materials Corporation have the same chemical composition and differ only by processing procedures. MC had unspecified processing errors during the surface treatment and MC* was newly provided for testing under the same conditions. From the X-ray mappings and back-scattered electron images of these two alloys, MC shows homogeneous phase (FCC) and MC* shows two phases composed of the primary

Ni-rich phase (face-centered cubic, FCC) and the secondary Cr-rich phase (body-centered cubic, BCC). This finding is confirmed further by X-ray diffraction patterns. Although MC has a high chromium concentration, comparable to alloy 671 (Run#5), MC shows the worst corrosion and alloy 671 the least. This difference occurs because the MC alloy has ubiquitous deep surface cracks (tens of micrometers into the core) and large voids in the substrate generated during the processing. These cracks provide direct penetration of the acidic subcritical water into the substrate. MC* shows comparable corrosion resistance to alloy 671. To stress the importance of the processing of the materials and surface treatment, MC and MC* testing results are presented in the following sections.

Table 3.2 Exposure time and average temperature (℃) at each thermocouple position for nickel-base wire experiments.

Run#	Alloy	Test time (Hour)	Temperature (℃)				
			TC1	TC2	TC3	TC4	TC5
1	Inconel 625	23.5	423	385	355	350	299
2	C-22	6	426	385	357	355	304
3	C-22	24	425	380	357	354	304
4	Alloy 59	23	425	380	355	355	295
5	Alloy 671	20	428	383	353	353	290
6	MC	24	424	380	354	352	290
7	Alloy33	24	424	380	352	349	290
8	C-2000	24	425	380	353	351	295
9	MC	6	425	382	352	349	286
10	B2	24	428	383	353	349	268
11	G30	6	435	380	349	336	240
12	MC*	6	408	373	368	352	278

3.2.1 Nickel-base alloys in an acidic environment (wires)

After each exposure test, each wire sample is cut for analysis. In each wire, the sections where temperature is measured by five thermocouples are cut in 2㎝ lengths centered around the thermocouple position and cold-mounted using epoxy resin (Buehler, Epoxide Resin No. 20-8130-128), and hardener (Buehler, Epoxide Hardener No. 20-

8132-032) with a mass ratio of 5:2 (epoxy: hardener). These sections are indicated by TC numbers (TC#) as TC1, TC2, TC3, TC4, and TC5, respectively. These TC# sections are ground and polished with SiC paper and water, down to 1200 grit, and then with 6μm and 1μm diamond pastes. The remaining sections, indicated by A, B, C, D in Figure 3.2, are cut in 1.5cm lengths for analysis without metallographic sample preparation.

Some important observations made by the naked eye are summarized in this paragraph. First, most of the oxide scales formed in both the supercritical and subcritical temperature ranges are adherent to the metal substrate with several exceptions. Second, the colors of the oxides at the supercritical temperature and at the high subcritcal temperature are different from each other. The colors of the oxides grown in the high subcritical temperature range are deep dark black. The colors of the oxides grown in the supercritical temperature range are semi-transparent bluish, except for the B-2 alloy with whitish color. Third, the oxide scale formed on alloy 33 (which contains 33wt%Fe) in the high subcritical temperature range is detached from the substrate, indicating that high iron concentration is not beneficial in forming an adherent oxide. The oxide scale on alloy 33 in the supercritical temperature range is adherent. Finally, the oxide formed on B-2 (27.70wt% Mo) in the supercritical temperature range is powder-like and is easily removed. The oxide formed on B-2 in the high subcritical temperature range is also easily removed.

The sections indicated by TC# are analyzed by an environmental scanning electron microscope (ESEM, FEI/Phillips XL30 FEG ESEM) with energy dispersive spectrometry (EDS) analysis. The images obtained from each TC# and the corresponding X-ray mappings of elements are shown in Figure 3.3 for the Inconel 625 wire sample. The images obtained from other alloys have similar features and are presented in Appendix A. From these images and X-ray mappings for all nickel-base alloys, it is observed that the most aggressive attack occurs in the high subcritical temperature ranges in accordance with the previous work.[1] In the supercritical temperature range, only thin oxide whose length is not resolvable by ESEM (much less than 1μm) forms on the surface. From the X-ray mappings in the subcritical temperature range, it is observed that nickel is depleted and oxygen and chromium are enriched in the distinctive surface layer relative to the metal substrate (refer to TC3 section image in Figure 3.3). Severe corrosion in the subcritical temperature range is always accompanied by selective dissolution of nickel into the water and formation of stable chromium oxide. In the subcritical temperature range, it is found that molybdenum forms a stable oxide like chromium and iron, like nickel, is selectively dissolved into the solution. The results of the semi-quantitative (standardless) analysis on the dealloyed oxide phase by the EDS are given in Table 3.3.

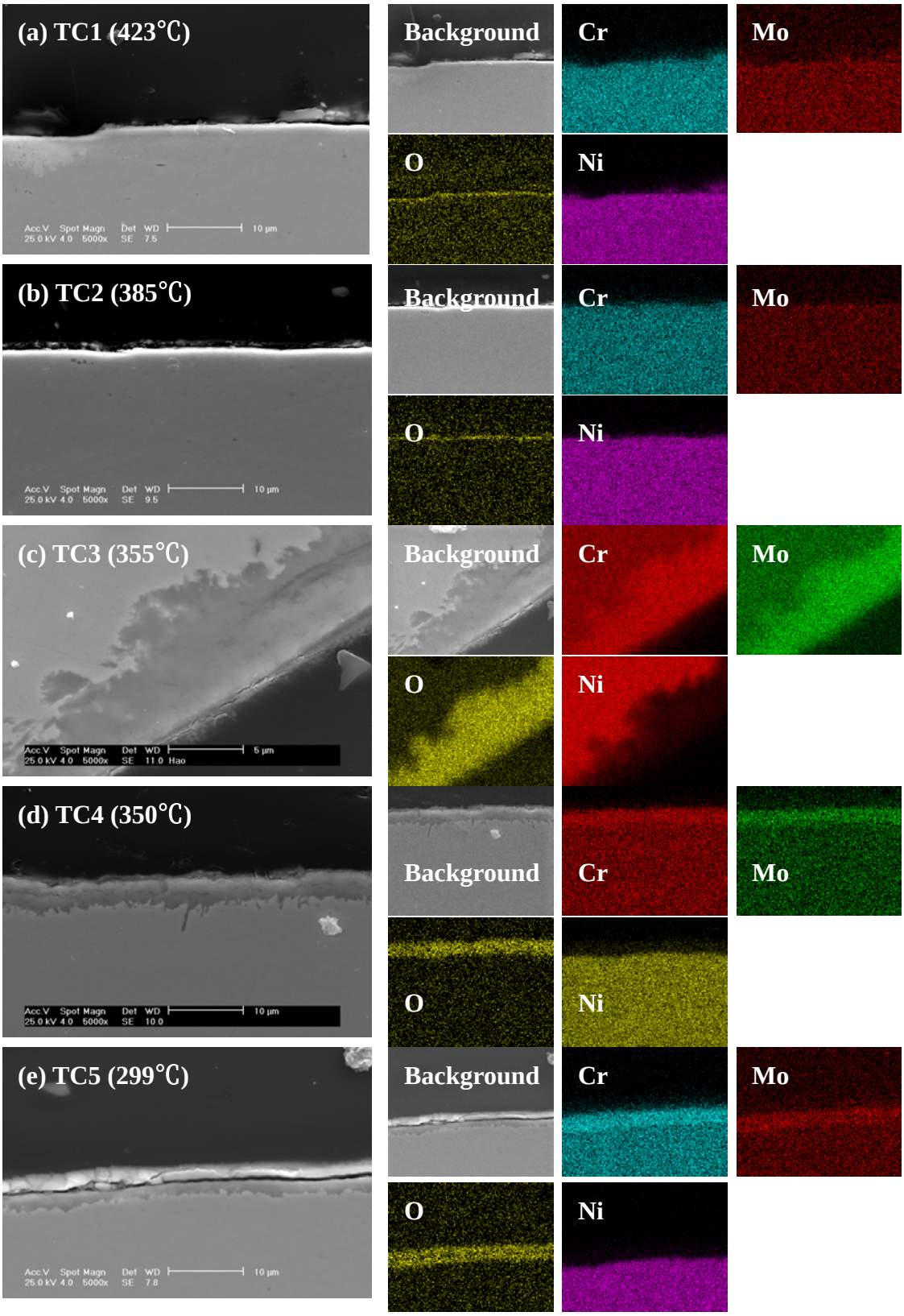

Figure 3.3 ESEM images and X-ray mappings for Run#1 (Inconel 625).

Table 3.3 Semi-quantitative (standardless) chemical analysis on the dealloyed oxide layer of wire samples by EDS.

		Composition (At%)					Composition (Wt%)				
Run#	**Position**	**Cr**	**Mo**	**Ni**	**O**	**Others**	**Cr**	**Mo**	**Ni**	**O**	**Others**
6	**TC4**	36.05	1.33	1.98	60.63	-	60.68	4.14	3.77	31.41	-
7	**TC4**	37.27	1.41	0.63	60.62	0.08Fe	62.83	4.38	1.19	31.45	0.15
8	**TC2**	24.53	10.31	8.30	56.86	-	34.84	27.02	13.30	24.85	-
8	**TC3**	23.12	5.99	3.30	67.60	-	39.39	18.82	6.34	35.45	-
9	**TC4**	35.55	1.44	1.56	61.46	-	60.38	4.51	2.99	32.12	-
10	**TC3**	-	21.24	12.12	66.65	-	-	53.41	18.65	27.95	-

Table 3.4 Thickness of the dealloyed oxide layer measured from the ESEM image. Maximum uniform thickness is measured in all cases.

	Thickness of the dealloyed oxide layer (㎛)				
Run#	**TC1**	**TC2**	**TC3**	**TC4**	**TC5**
1	-	-	7.5	5	4.3
2	-	-	4.3	4	-
3	-	2.2	7	7	2
4	-	0.75	3	3.6	1.8
5	-	-	-	1.3	0.6
6	-	-	33.5	32	-
7	-	-	5.7	6.8	3.6
8	-	2	5	6.91	3.9
9	-	-	15	15.8	10
10	-	5.5	19.2	18	5.4
11	-	-	3.6	-	-
12	-	-	-	-	-

From the chemical analysis of the attacked surface layer in subcritical temperatures, selective dissolution of iron and nickel and formation of chromium and molybdenum oxide are identified to be the major corrosion mechanisms. It is seen that the corrosion processes in the subcritical and supercritical temperature ranges are quite different from each other. Although each nickel-base alloy has shown different penetration rates depending on its chemical composition and metallurgical conditions, formation of the dealloyed oxide layer at the subcritical temperature and formation of thin oxide at the supercritical temperature are common to nickel-base alloys tested in this work.

From the ESEM images, the thickness of the dealloyed oxide layer is measured to compare the penetration depths of different alloys in Table 3.4 and plotted as a function of temperature in Figure 3.4. In each measurement, the maximum thickness of the uniform dealloyed oxide layer has been measured for each section, indicated by TC#. Figure 3.4 shows that the most aggressive attack occurs in the high subcritical temperature range and no severe corrosion occurs in the supercritical temperature range. To compare the performance of different nickel-base alloys, penetration rates of alloys in the high subcritical temperature range are plotted in Figure 3.5 as a function of the major alloying element (chromium) concentration. Because the kinetics of oxidation is not linear with respect to time, runs close to the 24 hours of exposure are only considered for comparison except Run#6 (the MC with the processing error).

Figure 3.5 shows that the penetration rate decreases as the chromium concentration increases. As the chromium concentration increases, more dense chromium oxide forms with less dealloying of nickel within the dealloyed oxide layer and as a result, restricts the diffusion of ionic species required for further dealloyed oxide layer formation. In this figure, alloy33 (33wt% Fe, 32.6wt% Cr) shows a greater penetration rate with a higher chromium concentration than alloys of 625, C-22, C-2000, and 59. This fact occurs because the iron is also dealloyed from the substrate together with Ni and the dealloyed oxide layer formed has no good adhesion to the alloy33 metal substrate. For alloys with a similar amount of chromium concentration (about 22Wt%Cr), slight dependence on molybdenum concentration is observed. C-22, C-2000, and alloy 59 have similar molybdenum concentrations and show some decrease in the penetration rate relative to that of Inconel 625. Because molybdenum also forms a stable oxide in the dealloyed oxide layer, it may decrease the penetration rate with more dense oxide formation. However, alloy B2, which contains nickel and molybdenum with little chromium, does not give suitable corrosion resistance, indicating that molybdenum itself without chromium does not provide suitable protection against the SCWO environments in the supercritical and subcritical temperature ranges.

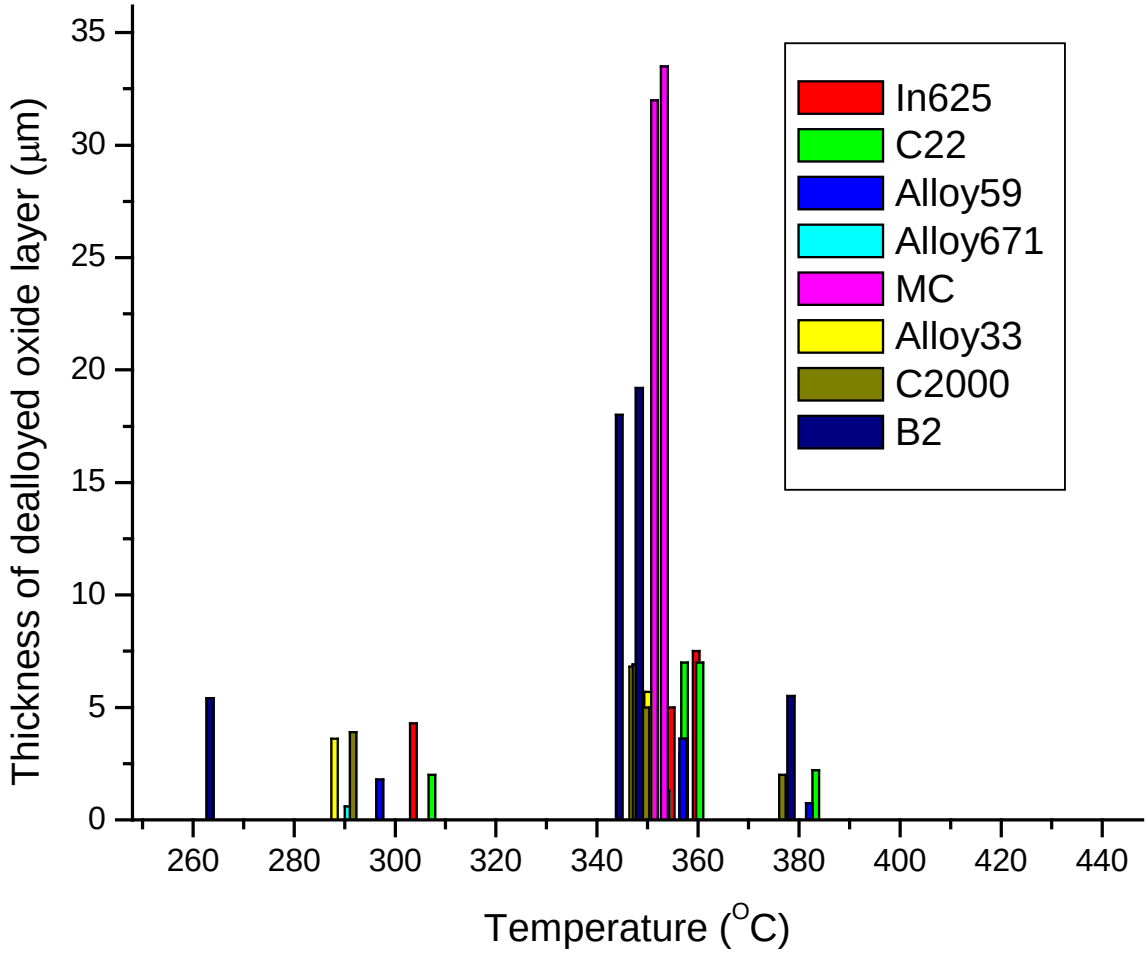

Figure 3.4 Thickness of dealloyed oxide layer vs. temperature for various nickel-base alloys from Table 3.4.

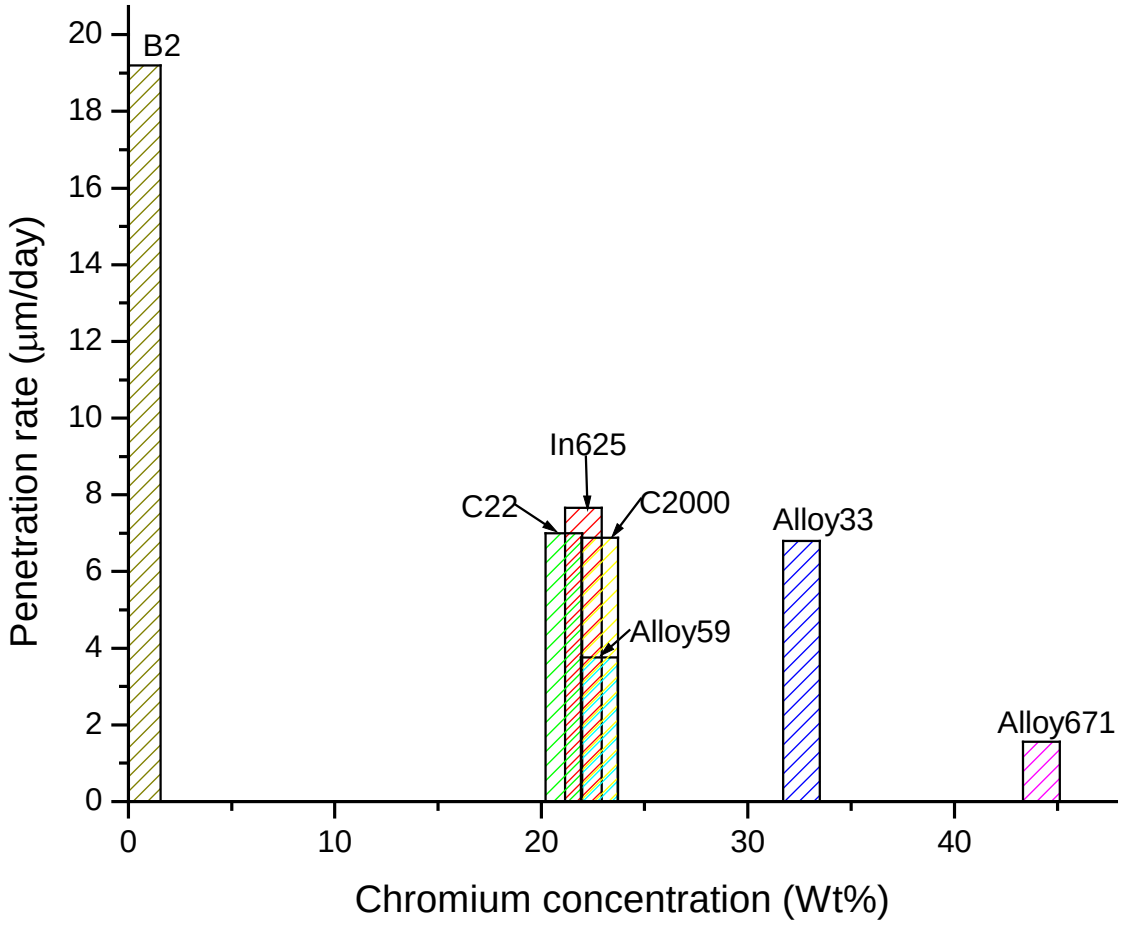

Figure 3.5 Penetration rate vs. chromium concentration for Run# 1, 3, 4, 5, 7, 8, 10.

The sections of the wires indicated by A, B, C, and D (refer to Figure 3.2) are cut to characterize the surface oxide layer as exposed (without metallographic sample preparation) and analyzed by ESEM, X-ray diffractometer (XRD, Rigaku 185㎜ X-ray diffractometer, copper anode) and X-ray photoelectron spectroscopy (XPS, Kratos AXIS Ultra Imaging X-ray Photoelectron Spectrometer, monochromated Al Kα). Although temperatures for these sections are not measured directly, we can obtain approximate temperature ranges from the measured temperatures of TC#. Section A is in the supercritical temperature range between TC1 and TC2. Section B is both above and below the critical temperature between TC2 and TC3. Section C is in the high subcritical temperature range between TC3 and TC4. Section D is in the subcritical temperature range between TC4 and TC5. The ESEM images of the surface oxide morphology for sections A and C are shown in Figures 3.6 for the Inconel 625 wire sample. Images obtained from other alloys are presented in Appendix B. Images of the surface oxides are given at high and low magnifications with original sample images for comparison. The oxide phase morphologies between the supercritical and the high subcritical temperature ranges are quite different from each other, supporting the fact that the oxidation mechanisms on the surface differ. In the supercritical temperature range, each constituent element contributes to the thin oxide formation without selective dissolution of nickel and iron. However, in the high subcritical temperature range, the nickel and iron are selectively dissolved from the metal substrate and the oxygen from the solution penetrates into the dealloyed metal substrate to form the dealloyed oxide layer.

X-ray diffraction (XRD) patterns are obtained from the surfaces of sections A, B, C, D and unexposed samples to characterize the structure of the surface oxide layer and listed in Figures 3.7-3.8 for the Inconel 625 and B-2 wire samples. Additional XRD patterns obtained from other alloys are presented in Appendix C. All the nickel-base alloys tested in this work have a face-centered cubic (FCC) crystal structure in their original condition and their lattice constants differ depending on the chemical composition, and so their unexposed samples are analyzed together to facilitate peak identification. In all cases with the exception of B-2, the diffraction pattern from sections A (in the supercritical temperature range) coincides with the diffraction pattern from the unexposed samples. This result occurs because the thickness of oxide is too thin and/or the oxide can be hydroxide with amorphous phase. In contrast to the diffraction patterns from sections A, diffraction patterns from sections C (in the high subcritical temperature range) indicate that the crystalline oxide phase has grown. The dealloyed oxide layer grows by dissolving the nickel and iron from the substrate and is composed of chromium and molybdenum oxides with a residual amount of nickel and iron. For this reason, oxides with complete

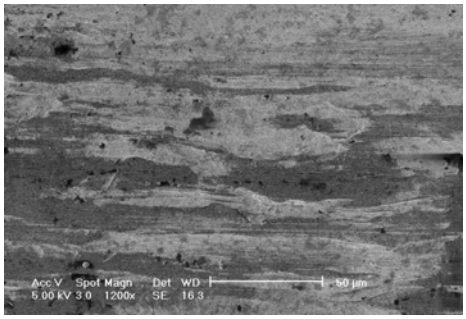

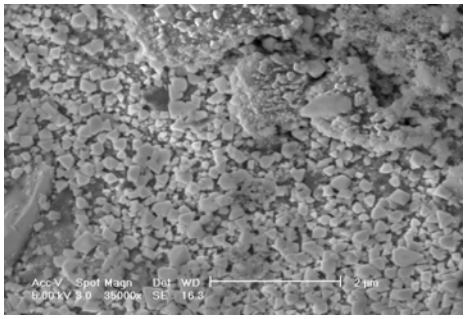

(a) Run#1-A (supercritical temperature)

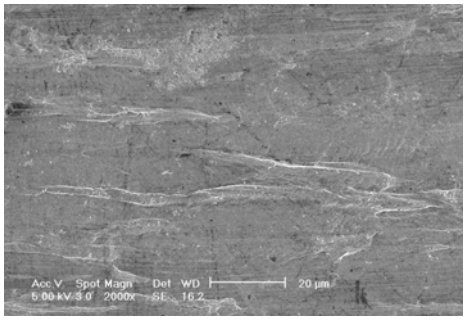

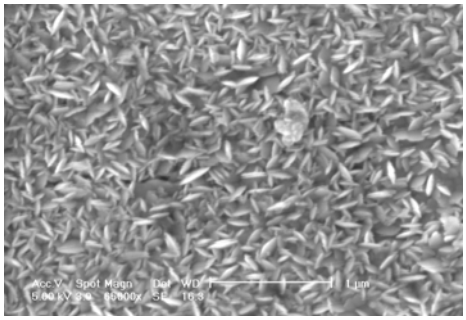

(b) Run#1-C (subcritical temperature)

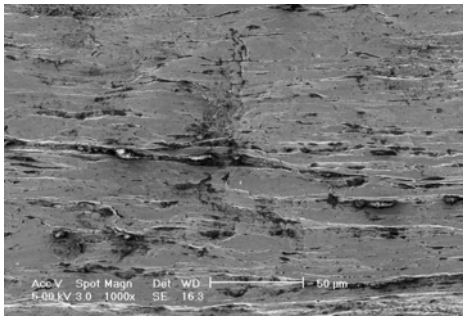

(c) Inconel 625 wire surface (as received)

Figure 3.6 ESEM images on surface oxides for Run#1 (In625). The left-hand images are in low magnification and the right-hand images are in high magnification.

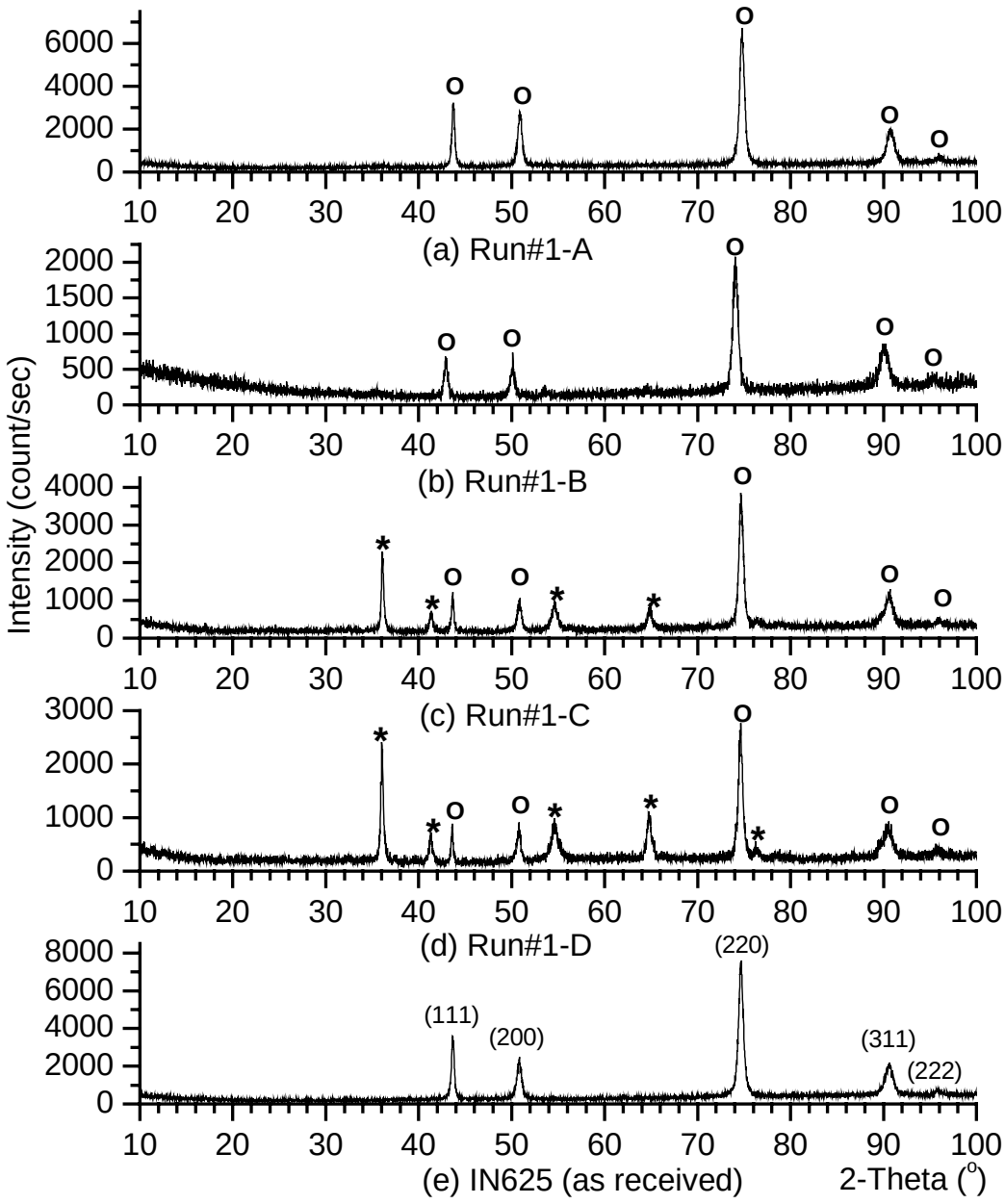

Figure 3.7 XRD patterns for Run#1 (Inconel 625). (e) FCC-phase peaks are indicated by Miller indices. Peaks are indicated by *o* when they match the peak position from (e). Peaks are indicated by * when they are generated from the oxide phase.

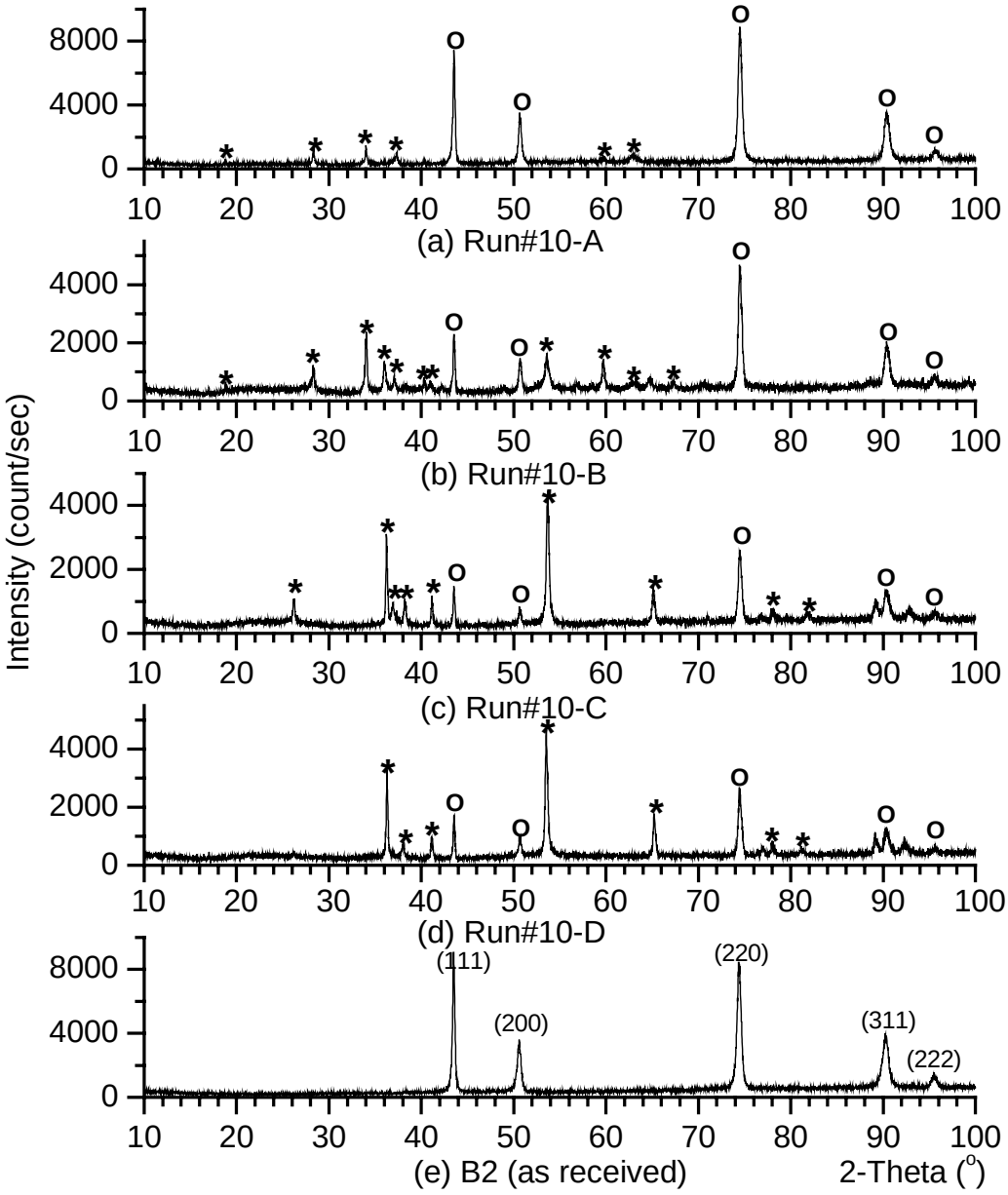

Figure 3.8 XRD patterns for Run#10 (B-2). (e) FCC-phase peaks are indicated by Miller indices. Peaks are indicated by *o* when they match the peak position from (e). Peaks are indicated by * when they are generated from the oxide phase.

crystal structures cannot grow due to the spatial restriction imposed by the substrate crystal structure (FCC) and relatively low temperature. As the oxide layer is mainly composed of the chromium oxide, the oxide peaks best match those of the crystalline Cr_2O_3 oxide with a corundum structure. Comparison between the diffraction patterns of Run#2 (C-22, 6 hours exposure) and Run#3 (C-22, 24 hours exposure) in Figures C.1-C.2 shows that the oxide phase grown for 6 hours has an amorphous phase mainly relative to the oxide phase grown for 24 hours. This fact may indicate that the oxide may grow in an amorphous structure in the initial stage of the dealloyed oxide layer formation. In contrast, Run#11 (G-30, 6 hours) and Run#12 (MC*, 6 hours) in Figures C.9-C.10 have no oxide phase peak at any temperatures, indicating that a high chromium concentration reduces the penetration depth. The MC* alloy (refer to XRD patterns in Figure C.10) has two phases (Ni-rich FCC phase and Cr-rich BCC phase) due to its high chromium concentration relative to other nickel-base alloys and, as a result, diffraction patterns have primary FCC peaks with secondary BCC crystalline peaks (indicated by + in Figure C.10). Although alloy 671 has a similar chromium concentration, this alloy is found to have FCC phase only. This could be due to the effects of various minor alloying elements in the alloy 671 (refer to Table 3.1 for chemical compositions of MC and alloy 671) and heat treatment. B-2 is, essentially, a binary alloy composed of nickel and molybdenum. The composition analysis of the B-2 alloy by EDS in Table 3.3 indicates that the dealloyed oxide layer contains a significant amount of nickel in the dealloyed oxide layer relative to other Ni-Cr alloys. XRD patterns from Run#10 (B2, 24 hours) in Figure 3.8 could not be identified whether the peaks are from either MoO_2 or MoO_3 because the peaks from each molybdenum oxide overlap considerably and the contribution from nickel oxide cannot be resolved definitely.

XPS spectra (by monochromated Al Kα, E=1486.6eV) are obtained from the surface of sections A (supercritical temperature) and C (high subcritical temperature) to characterize the chemical state of the surface oxide layer and shown in Figure 3.9 for Inconel 625 and C-22 wire samples. Additional survey spectra for other alloys are presented in Appendix D. From the survey spectra (intervals of 1.0eV binding energy), the semi-quantitative (standardless) chemical composition of the surface oxide layer is calculated in Table 3.5. Since XPS measurement provides information from only a few upper surface layers, the oxygen concentration measured by XPS is higher than that measured by EDS. This difference occurs because the oxygen atoms can adsorb on the surface oxide layer during the exposure to the air and the surface oxide layer was in direct contact with the solution, which is an oxygen-containing medium during the exposure tests. XPS survey spectra and composition analysis also support the fact that selective

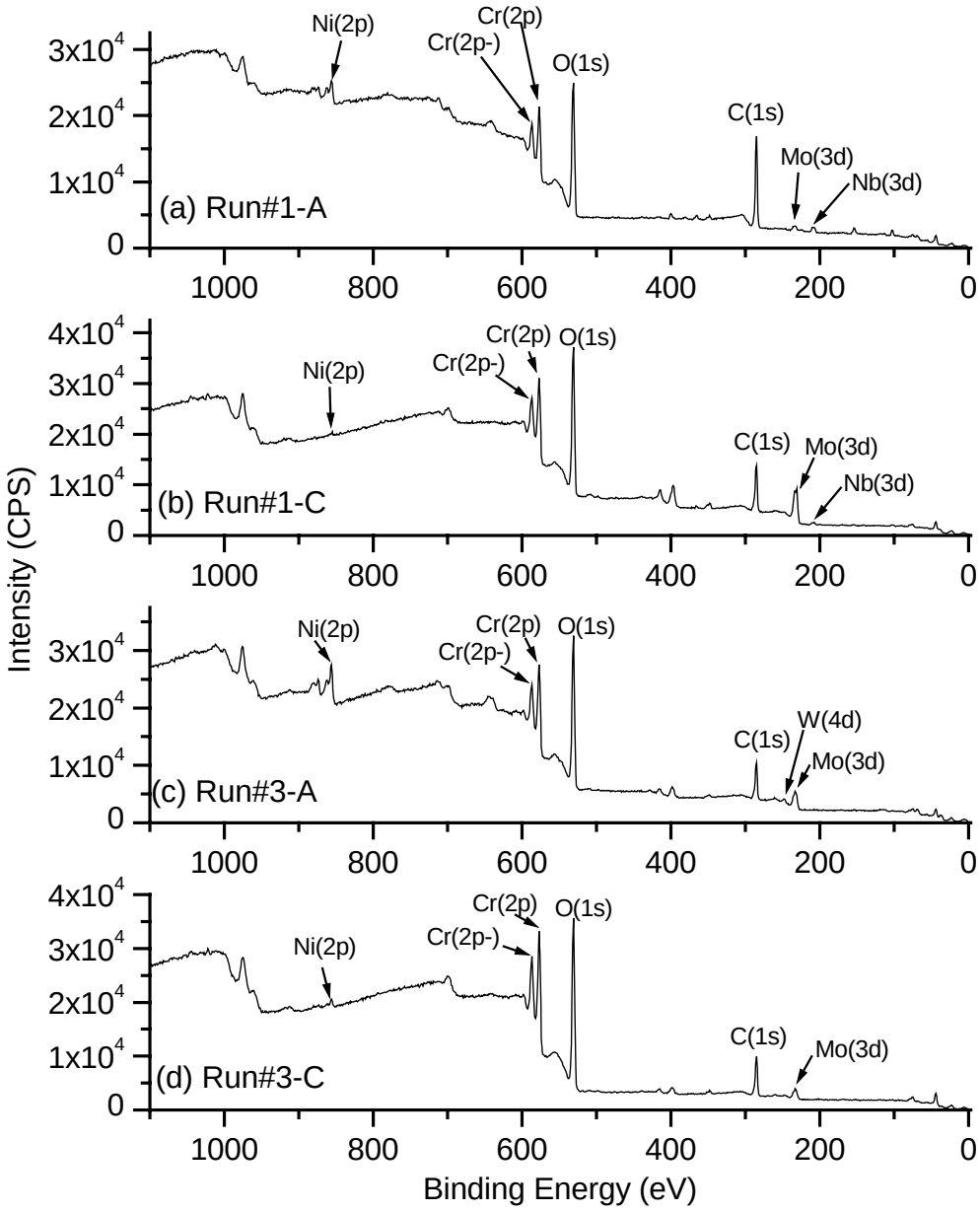

Figure 3.9 XPS survey spectra for Run#1 (Inconel 625) and Run#3 (C-22). Run # -A is at a supercritical temperature. Run#-C is at a high subcritical temperature. Spin-orbit splitting of Cr is represented by Cr(2p-) for Cr($2p_{1/2}$), and Cr(2p) for Cr($2p_{3/2}$).

Table 3.5 Semi-quantitative (standardless) chemical analysis on the surface oxides of wire samples by XPS.

		Composition (At%)					Composition (Wt%)				
Run#	**Position**	**Cr**	**Mo**	**Ni**	**O**	**Others**	**Cr**	**Mo**	**Ni**	**O**	**Others**
1	**A**	18.01	0.85	5.82	74.31	1Nb	35.45	3.09	12.94	45.01	3.51Nb
1	**C**	21.64	5.73	0.26	71.95	0.42Nb	39.06	19.07	0.53	39.96	1.37Nb
3	**A**	20.13	2.67	8.8	67.48	0.93W	34.1	8.34	16.83	35.18	5.54W
3	**C**	25.68	1.38	1.69	71.24		49.33	4.9	3.67	42.1	
4	**A**	14.46	0.82	8.37	76.35		29.56	3.1	19.32	48.02	
4	**C**	23.69	5.77	0.36	70.18		42.05	18.89	0.73	38.33	
5	**A**	11.38	0.58	4.06	78.04	5.94Fe	23.99	2.25	9.66	50.63	13.46Fe
5	**C**	21.07	0.98	0.39	77.56		44.65	3.82	0.94	50.59	
6	**A**	16.84	0.55	9.91	70.04	2.67Fe	31.5	1.9	20.92	40.31	5.37Fe
6	**C**	28.76	1.92	1.89	67.43		52.11	6.43	3.87	37.59	
7	**A**	7.43	0.63	6.46	78.52	6.96Fe	15.63	2.43	15.36	50.85	15.73Fe
7	**C**	29.39	1.33	1.59	66.37	1.32Fe	52.98	4.42	3.23	36.81	2.56Fe
8	**A**	10.58	1	11.51	73.96	2.95Fe	20.6	3.6	25.3	44.33	6.17Fe
8	**C**	30.05	1.89	1.85	65.33	0.87Fe	53.02	6.15	3.69	35.47	1.66Fe
10	**A**	3.72	4.38	24.55	67.35		6.18	13.42	46	34.4	
10	**C**	5.81	14.15	7.89	72.15		9.22	41.42	14.13	35.23	

dissolution of nickel and the formation of stable chromium oxide are dominant corrosion mechanisms in the high subcritical temperature range. In the supercritical temperature range, the oxide shows no indication of dealloying of nickel and each constituent element contributes to stable oxide formation. For the identification of the chemical states of the elements, high-resolution spectra (intervals of 0.1eV binding energy) are obtained for the major elements, Cr, Ni, and Mo in Figures 3.10-3.12. All the high-resolution data are acquired using the same photon source as the survey. As the surface oxide might be insulating to some degree, these spectra are charge-corrected to adventitious hydrocarbon at 285.0eV. These high–resolution spectra are compared to the reference peak positions in the literature[2] and the chemical states of chromium agree well with the Cr in Cr_2O_3 both at the high subcritical temperature and at the supercritical temperature as shown in Figure 3.10. The chemical shift between Cr_2O_3 and CrOOH, where Cr in both cases is in

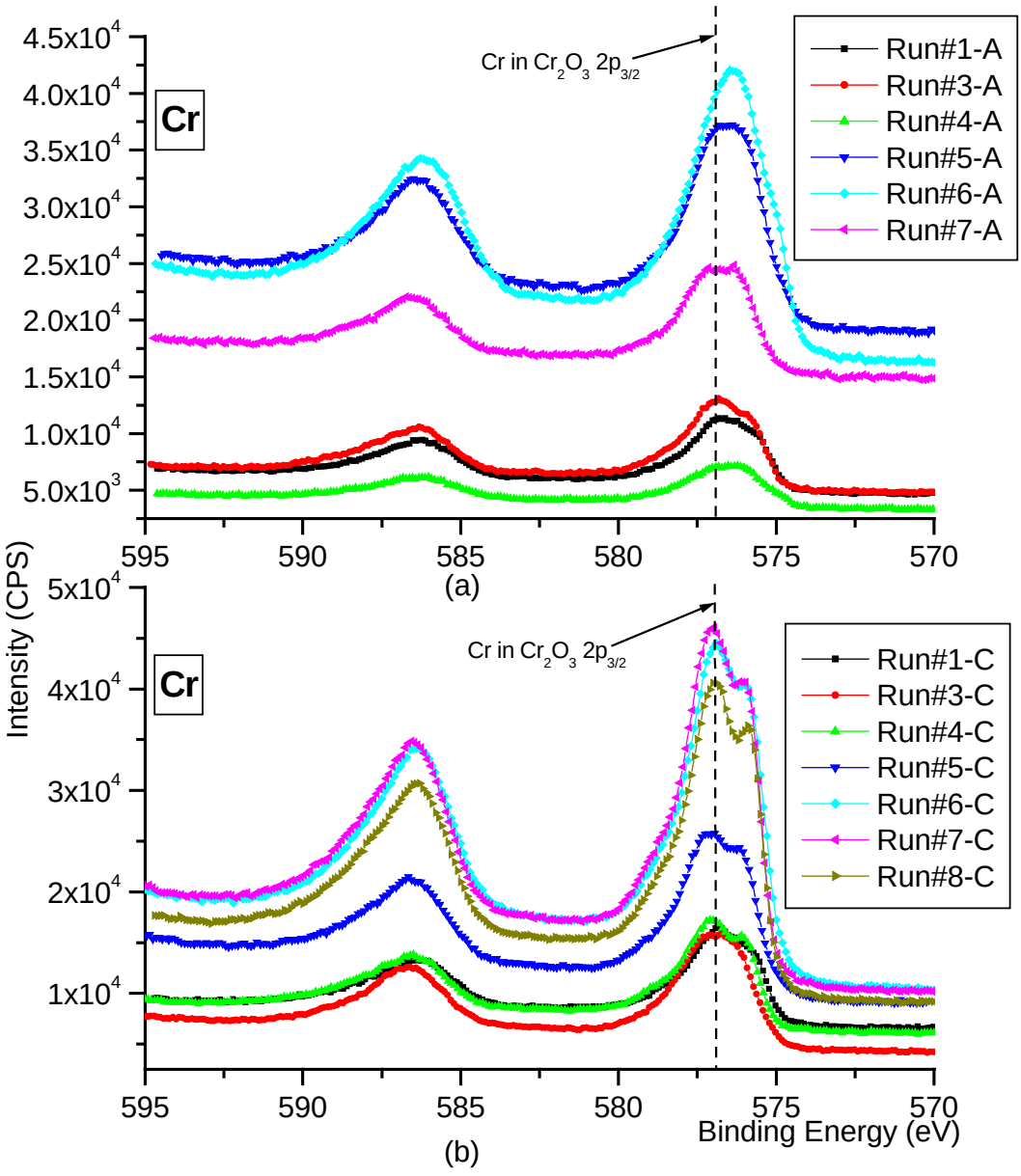

Figure 3.10 XPS high-resolution spectra for chromium, charge-corrected to adventitious hydrocarbon at 285.0eV.

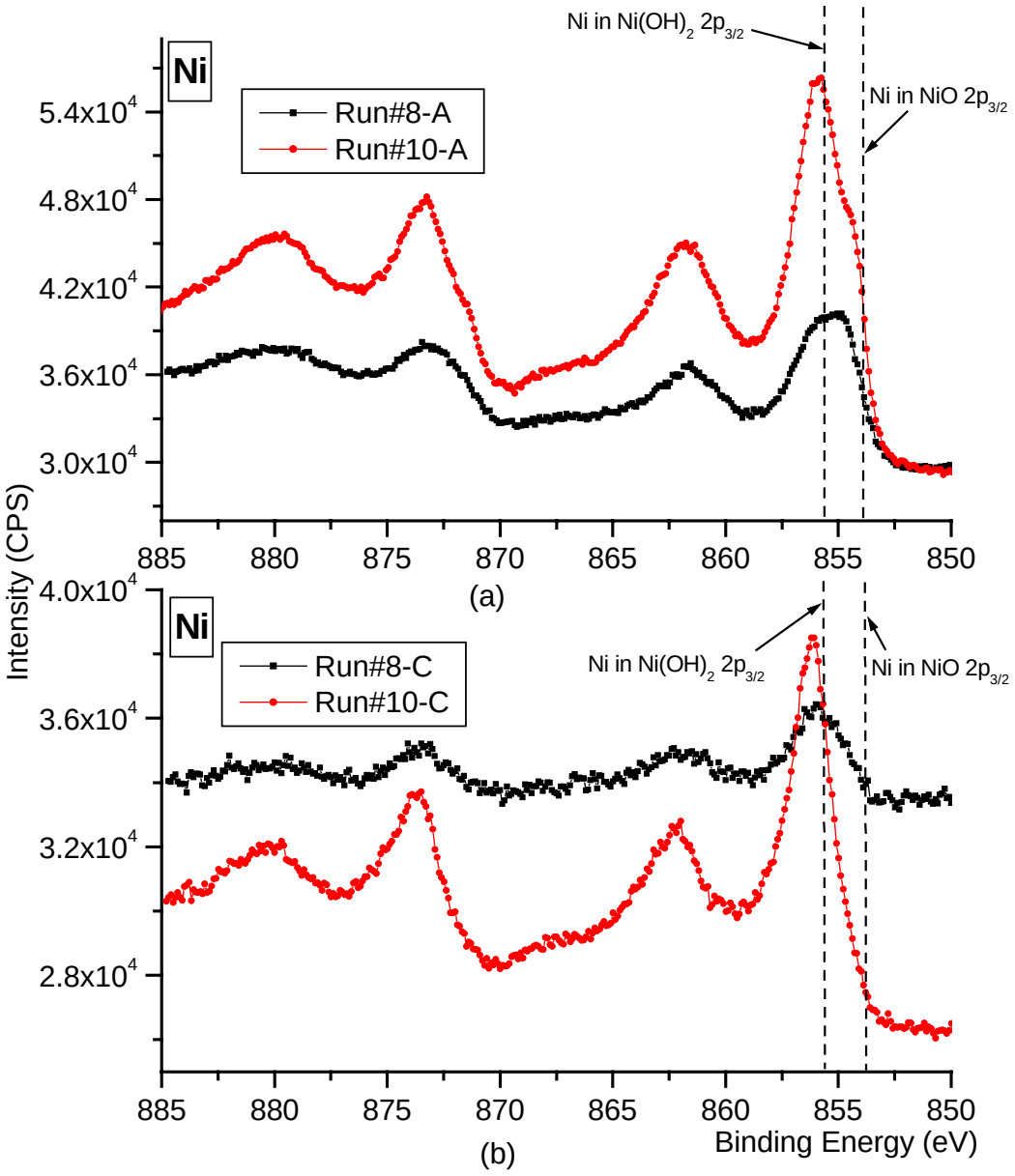

Figure 3.11 XPS high-resolution spectra for nickel, charge-corrected to adventitious hydrocarbon at 285.0eV.

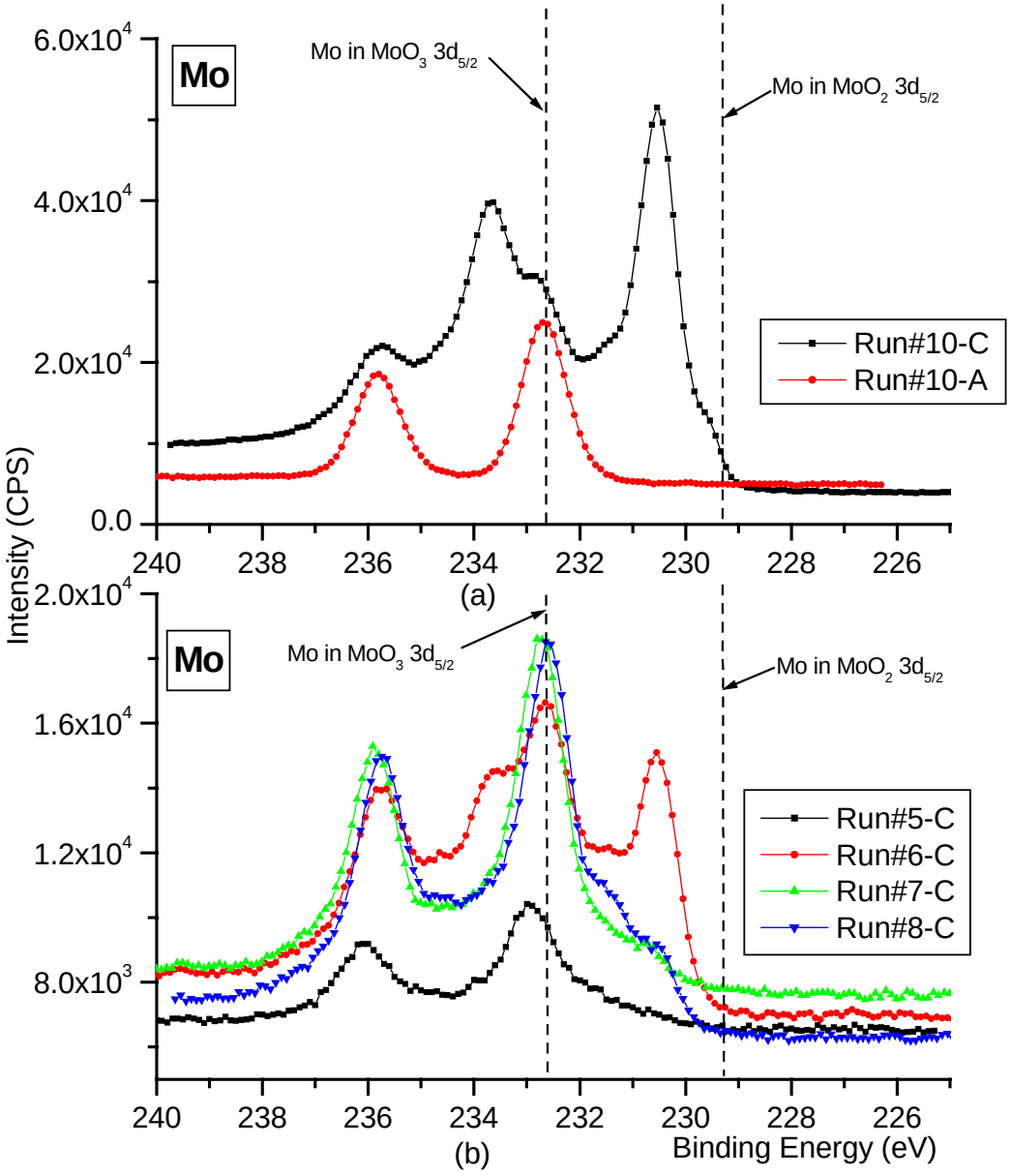

Figure 3.12 XPS high-resolution spectra for molybdenum, charge-corrected to adventitious hydrocarbon at 285.0eV.

the chemical state of Cr^{3+}, is so small that the definite chemical state of chromium cannot be resolved. However, the chromium high-resolution XPS spectra together with the X-ray diffraction patterns for sections C (high subcritcal temperature) confirm that the chromium oxide in the dealloyed oxide layer is Cr_2O_3. The chemical states of nickel at the supercritical temperature are in good agreement with those of the $Ni(OH)_2$ shown in Figure 3.11 (a). On the other hand, the chemical states of nickel at the high subcritical temperature are located between the $Ni(OH)_2$ and Ni_2O_3 in Figure 3.11 (b) and this might be due to the two following reasons. Firstly, because nickel is depleted from the substrate and oxygen penetrates into the dealloyed layer to form a chromium oxide (Cr_2O_3), the residual amount of nickel inside the Cr_2O_3 can, in the environment of high oxygen activity, have the chemical state of Ni_2O_3. Secondly, because the metal surface is in direct contact with the solution, nickel can form a hydroxide, $Ni(OH)_2$, at the surface and, in the environment of high oxygen activity, yield high oxidation state energy locally.

Considering that the XPS spectra obtain signals from several surface layers, the characterized surface oxide chemistry can be different from that of the bulk dealloyed oxide layer. Due to uncertainties in characterizing the chemical state of Ni in the dealloyed oxide layer by XPS spectra, the nickel is assumed to form the oxide of NiO inside the dealloyed oxide layer in developing the kinetic model in Chapter 4. This assumption partly comes from the consideration that the water molecules may not easily penetrate into the dealloyed oxide layer due to their larger size relative to the oxygen anions.

The interpretation of molybdenum is much more complicated and uncertain relative to Cr and Ni. The spectra in Figure 3.12 (b) are obtained for Ni-Cr base alloys in the high subcritical temperature range. Spectra of section C from Run #5 and Run #7 show that molybdenum is in the chemical state of MoO_3 and spectra of section C from Run#6 and Run#8 show that molybdenum might have two chemical states, MoO_2 and MoO_3. The spectra obtained from alloy B-2 (Ni-Mo) in Figure 3.43 (a) show that molybdenum in section A (supercritical temperature) is in the chemical state of MoO_3 and in section C (high subcritical temperature) might have two chemical states, MoO_2 and MoO_3. The peak positions of Mo in Figure 3.12 are not clearly matched with reference peak positions and they might be affected by complex chemistry in the dealloyed oxide layer.

Analytical results consistently indicate that the most aggressive corrosion occurs in the high subcritcal temperature range with dealloying of nickel and iron and oxidation of chromium in an acidic environment (pH 2 under ambient conditions).

3.2.2 The Inconel 625 Reaction vessel in an acidic environment

After the various nickel-base alloy tests up to Run #11, the Inconel 625 reaction vessel was disassembled and filled with the epoxy resin and hardener to protect the oxide scales before cutting. The tube was cut into five sections, with each section having a thermocouple at the center. These sections, identified by TC#, were ground and polished. The temperature and total exposure time are summarized in Table 3.6. The temperature is a time-weighted average from the 11 nickel-base wire tests shown in Table 3.2.

Table 3.6 Average temperature (time-weighted averaged from Table 3.2) at each thermocouple position for Inconel 625 reaction vessel and uniform dealloyed oxide layer thickness. (Total exposure time = 204.5 hours)

	TC1	TC2	TC3	TC4	TC5
Temperature (℃)	426	381	353	351	290
Uniform dealloyed oxide layer thickness (㎛)	-	33.0	35.9	37.9	18.3

The images obtained from each TC# by ESEM are presented in Figures 3.13-16 for each temperature with X-ray mappings of elements. Note that the nickel-based wires are located inside the reaction vessel and the system pressure of 24.1 MPa acts as a compressive stress along the tangential direction of the wire. In the reaction vessel, the system pressure acts as a tensile stress along the tangential direction of the tube. In addition, for both cases of wires and the reaction vessel, there may be a significant amount of residual stress developed during the fabrication of the alloy as a wire and a tube. Figure 3.13 (TC1, supercritical temperature) clearly shows that stress corrosion cracking (SCC) occurs at the supercritical temperature for extended exposure time in the presence of the tensile component of system pressure. However, the development of SCC at the supercritical temperature involves no dealloying. The maximum crack length is about 60㎛.

Slight dealloying of nickel inside the crack in Figure 3.13 (a) comes from the thermal cycles between different alloy tests. The acidic supercritical water inside the crack is trapped, and during the cool-down of the system it passes through the subcritical temperature range where the dealloying of nickel occurs as shown in X-ray mappings (left-side of the image) in Figure 3.13 (a). X-ray-mappings in Figure 3.13 (a) for two different regions indicate that the local chemistry inside the crack can be changed significantly. Near the middle of the crack (left-side of the image) shows dealloying of

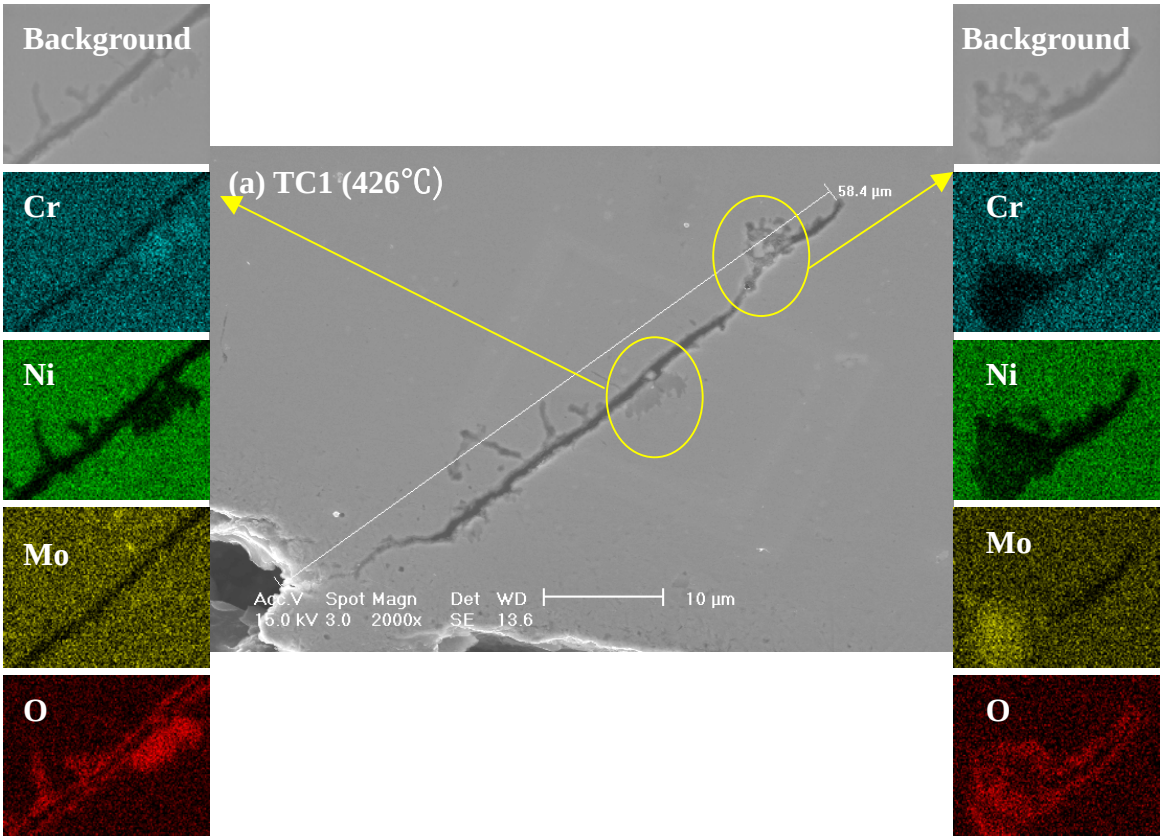

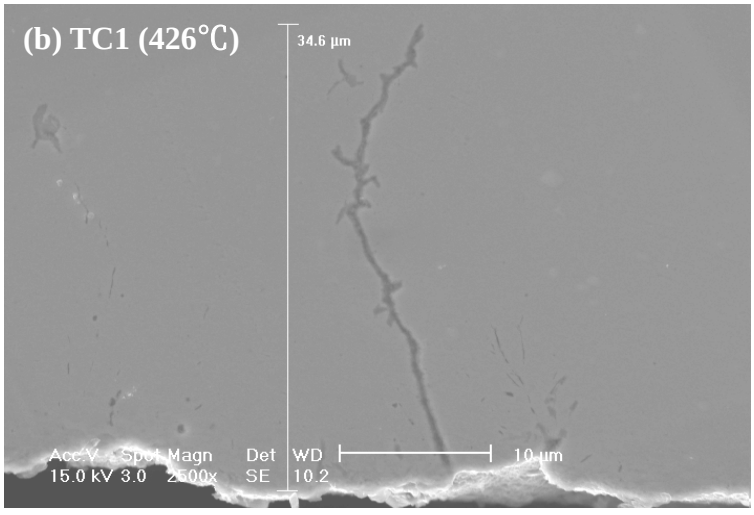

Figure 3.13 ESEM images and X-ray mappings of the Inconel 625 reaction vessel tube at section TC1.

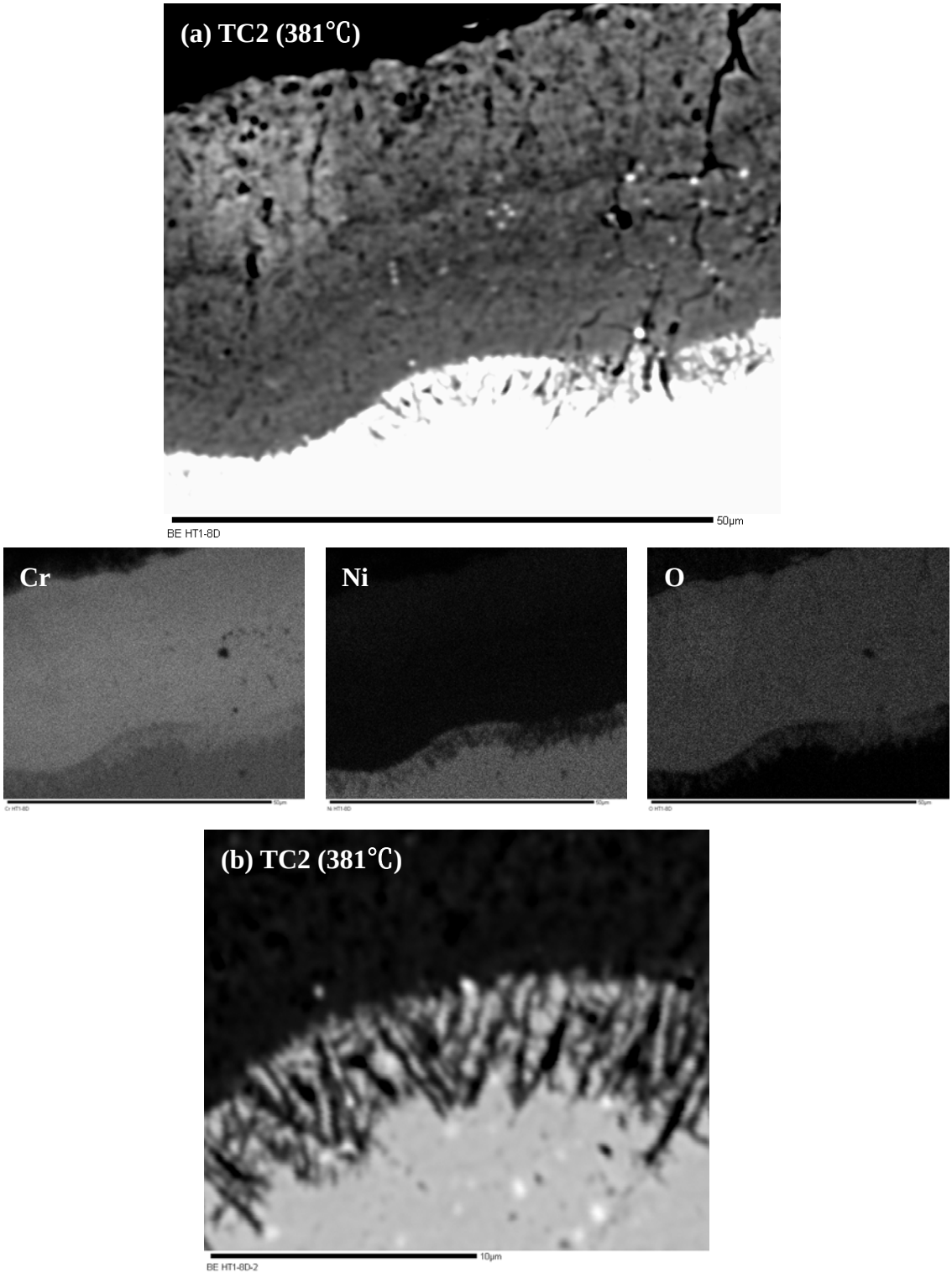

Figure 3.14 SEM images and X-ray mappings of the Inconel 625 reaction vessel tube at section TC2. (b) High magnification near the metal-oxide interface.

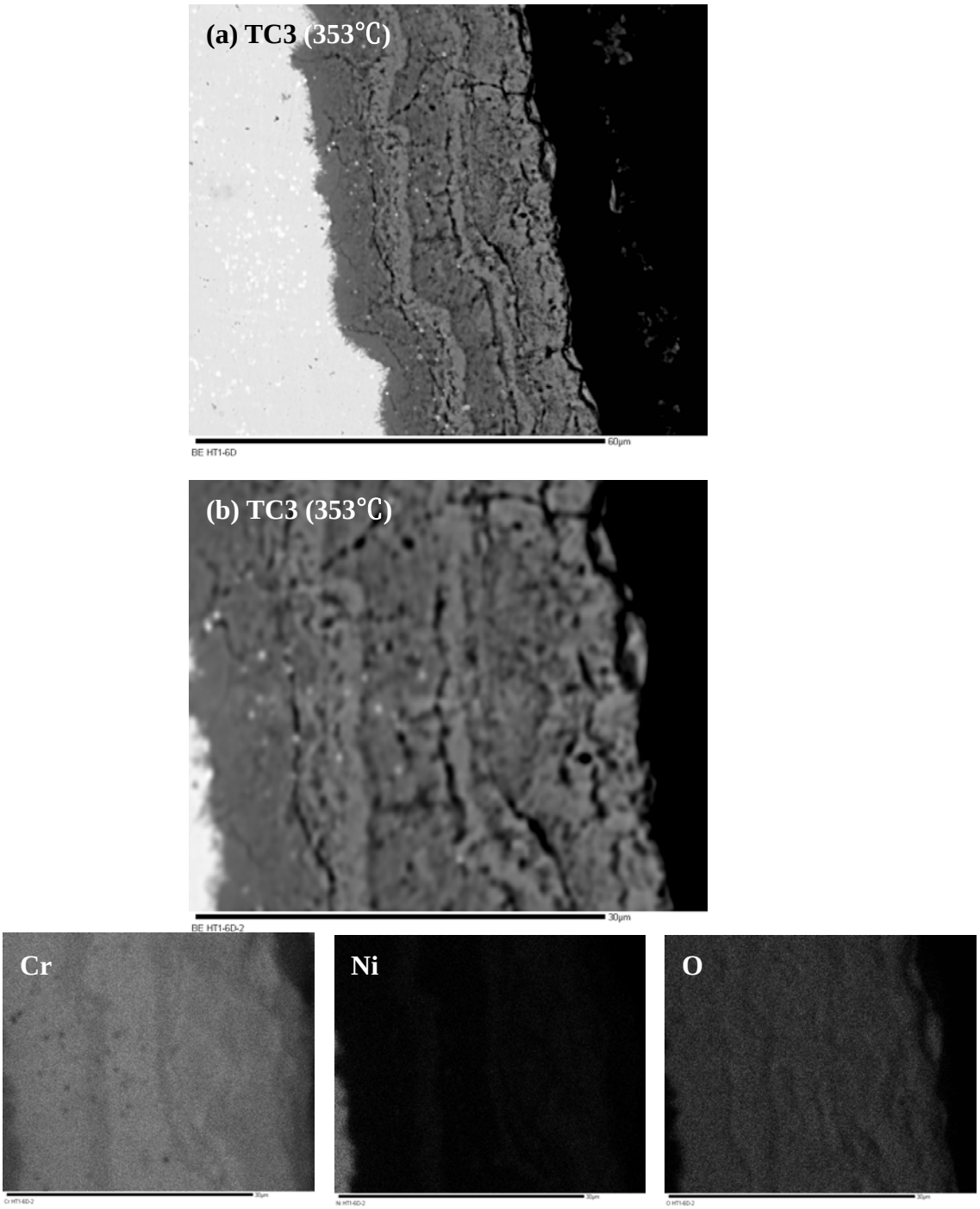

Figure 3.15 SEM images and X-ray mappings of the Inconel 625 reaction vessel tube at section TC3. (b) High magnification.

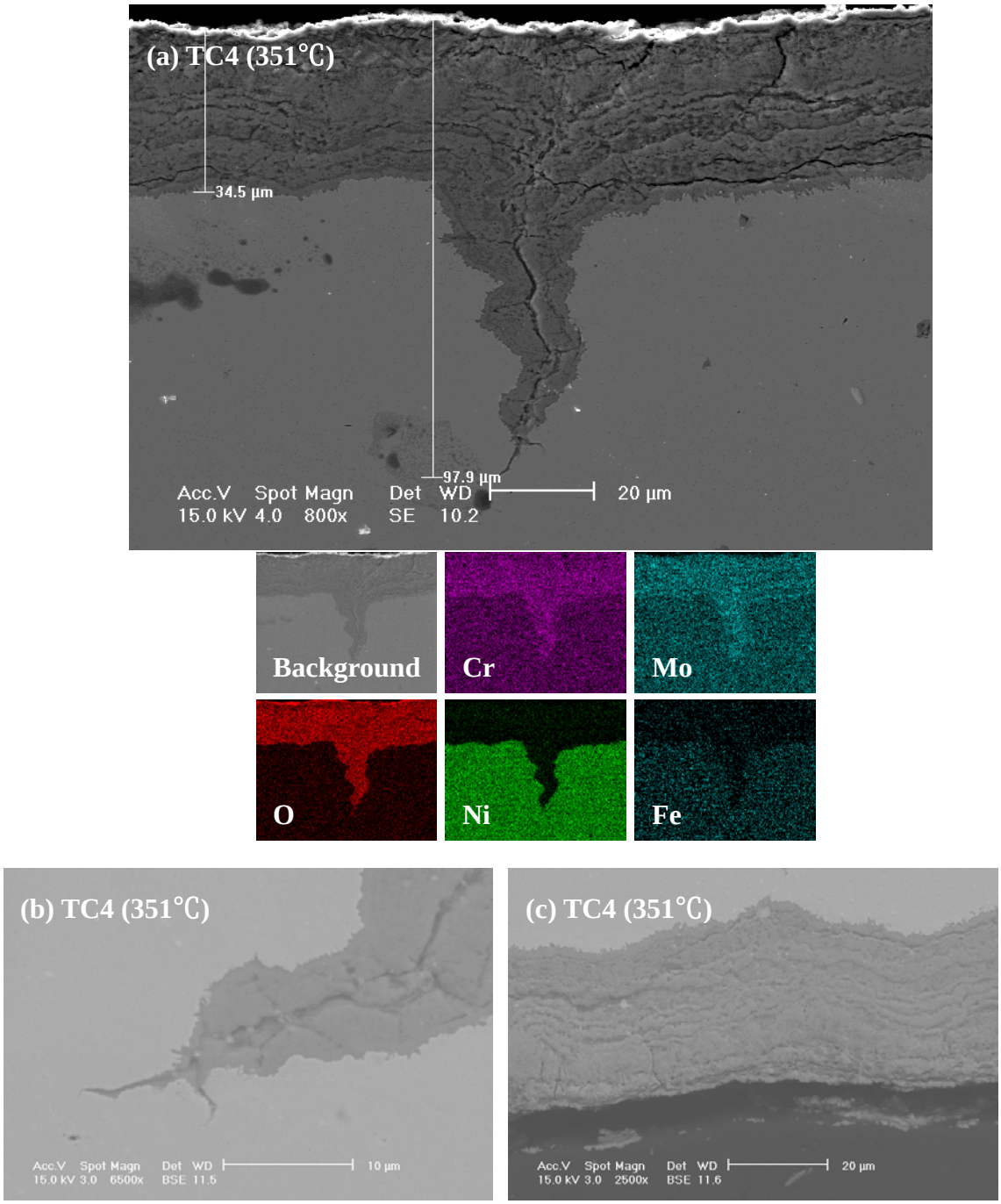

Figure 3.16 ESEM images and X-ray mappings of the Inconel 625 reaction vessel tube at section TC4. (b) High magnification at the tip of intrusion. (c) Uniform dealloyed oxide layer.

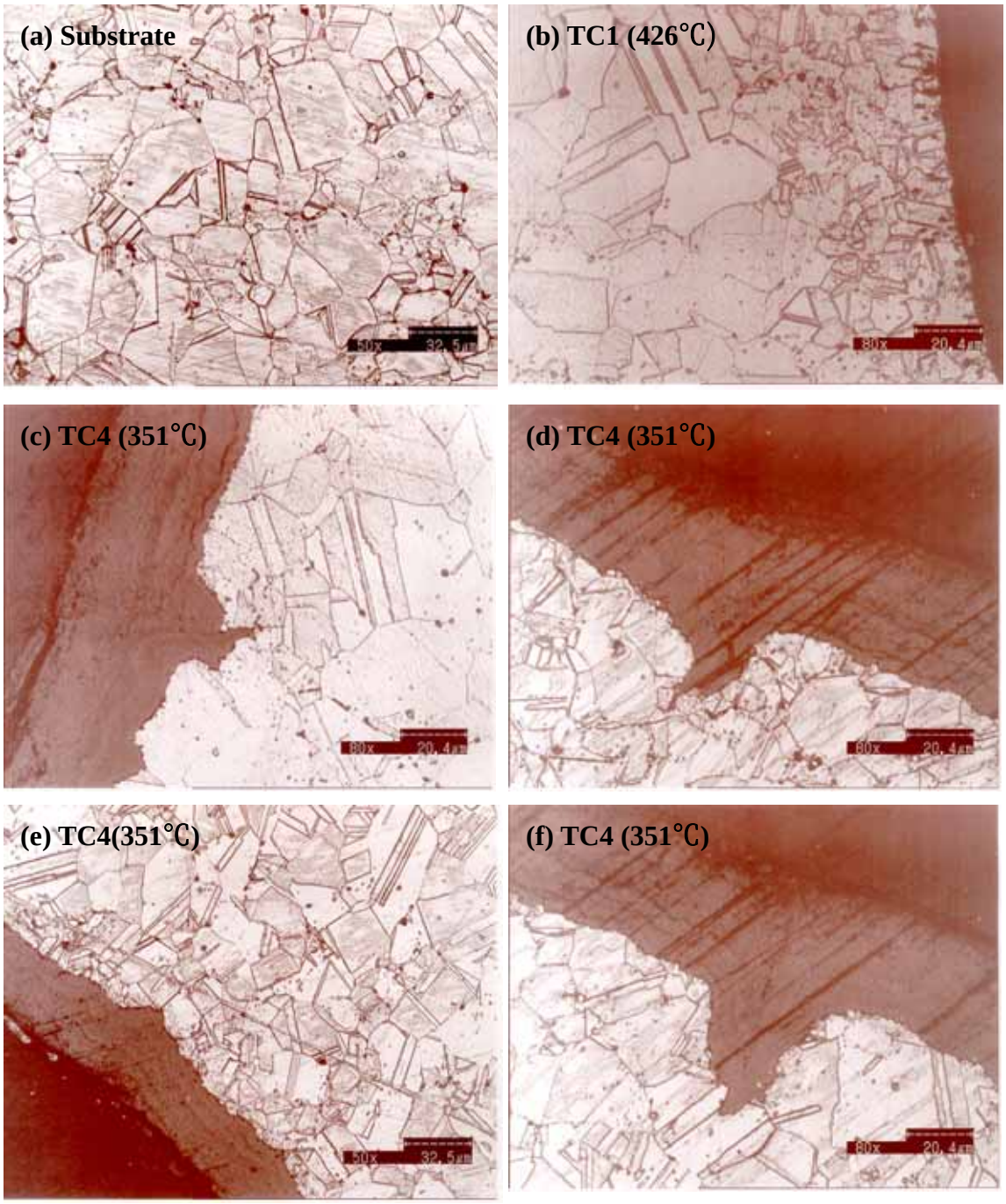

Figure 3.17 Laser microscope images of etched samples of the Inconel 625 reaction vessel tube. (a) Substrate image away from the surface. (b) Image obtained from TC1 (supercritical temperature). (c)-(f) Images obtained from TC4 (subcritical temperatures).

nickel. Near the bottom of the crack (right-side of the image), X-ray mapping shows that even the chromium is depleted and only molybdenum forms a stable oxide. This fact might occur because the local chemistry inside the crack can be altered significantly, usually is more acidified, and as a result even chromium experiences dealloying during the thermal cycles. Whether the crack path is intergranular or transgranular is uncertain. Because cold-work during the alloy fabrication is concentrated on the surface regions and surface regions have smaller grain size relative to the regions away from the surface, the etching image does not distinguish the crack path (refer to Figure 3.17 (a) and (b)).

Images obtained from the samples exposed at subcritical temperatures (Figures 3.14-16) show similar features with those of nickel-base wires. Also, dealloying of nickel and iron and formation of stable chromium and molybdenum oxide are the dominant corrosion mechanisms in the subcritical temperature range. The images in Figure 3.14 (a) indicate that nickel-base alloys exposed at a temperature slightly above the critical temperature also experience considerable nickel dealloying. Figure 3.14 (b) shows that the interface between the dealloyed oxide layer and the metal consists of many thin, hair-like projections. The banded structure in Figure 3.15 is thought to come from the operational (thermal and chemical) cycles to which the reaction vessel is exposed. The maximum uniform thickness of the dealloyed oxide layer has been measured in Table 3.6 at each thermocouple position. Also, the dealloyed oxide layer thickness has the maximum value at the high subcritical temperature range.

Unlike the wire samples, which are in compressive stress along the tangential direction and show a relatively uniform dealloyed oxide layer in the high subcritical temperature range, the reaction vessel tube in the high subcritical temperature range shows a localized intrusion where the dealloyed oxide layer grows sharply into the metal substrate with an accelerated rate as seen in Figure 3.16. To verify the acceleration path of the localized intrusion, the samples are etched and images are obtained by a confocal laser microscope (Lasertec Corporation, Confocal Laser Scanning Microscope 1LM21W). The etchant was prepared freshly and consisted of 15㎖ of concentrated hydrochloric acid, 10㎖ of glacial acetic acid, 5㎖ of concentrated nitric acid, and 2 drops of glycerol.[3] After exposure for 3.5 minutes, the samples were rinsed with distilled water. After etching, the samples verify that the intrusion follows the grain boundaries as shown in Figure 3.17 (c)-(f).

The presence of the tensile component of stress along the tangential direction accentuates and accelerates dealloyed oxide layer formation along the grain boundaries. Because the grain boundaries have more open structure relative to the bulk lattice, the diffusion of ions along the grain boundaries is faster than in lattice diffusion. As a result,

dealloying of nickel and penetration of oxygen accelerate along the grain boundaries. A crack can easily initiate and propagate along localized intrusions, which are brittle, defective and porous relative to the metal substrate as indicated in Figure 3.16. The length of intrusions ranges up to three times that of the uniform dealloyed oxide layer thickness. These intrusions act as a precursor to SCC in the presence of tensile stress in the high subcritical temperature range.

Table 3.7 Average concentration of elements in the dealloyed oxide layer and the metal substrate from EPMA analysis for the Inconel 625 reaction vessel tube. (Averaged from the individual data points of Figure 3.19)

		Cr	Mo	Nb	Ta	Fe	Ni	O
Oxide	**Wt%**	43.69	13.09	6.53	0.06	0.45	4.46	31.71
Substrate		22.57	9.11	4.63	0.96	3.69	59.04	0
Oxide	**At%**	27	4.39	2.26	0.01	0.26	2.45	63.63
Substrate		26.21	5.73	3.02	0.32	3.99	60.72	0

The semi-quantitative (standardless) chemical composition profile in the dealloyed oxide layer is analyzed by Auger electron spectroscopy (AES, Physical Electronics, Model 660 Scanning Auger Microscope). The concentration profile in the dealloyed oxide layer is given in Figure 3.18. The concentration profile is obtained along the position number in Figure 3.18 (a) for the TC 4 section. Note that, like XPS, AES obtains information from only a few upper surface layers, and as a result, the oxygen concentration obtained in this figure is increased due to the adsorbed oxygen atoms during exposure to the air. The oxygen concentration at the metal substrate is about 8 At% due to the adsorbed oxygen atoms on the surface layer. The concentration profile of each element in the dealloyed oxide layer is relatively constant, with high chromium and oxygen concentrations and a residual amount of nickel.

More accurate analysis by an electron probe microanalyzer (EPMA, JEOL, JXA-733 Superprobe) on the dealloyed oxide layer also supports the fact that the concentration profile along the dealloyed oxide layer is essentially constant as shown in Figure 3.19. In EPMA, the intensities of the X-rays are measured by wavelength dispersive spectrometry (WDS) for a quantitative analysis of elements. Standard X-ray intensities of the elements to be measured are obtained and calibrated prior to quantitative analysis, with a spatial resolution of approximately 2 microns.

Concentration profiles are obtained along the red line in Figure 3.19 (a) every two-

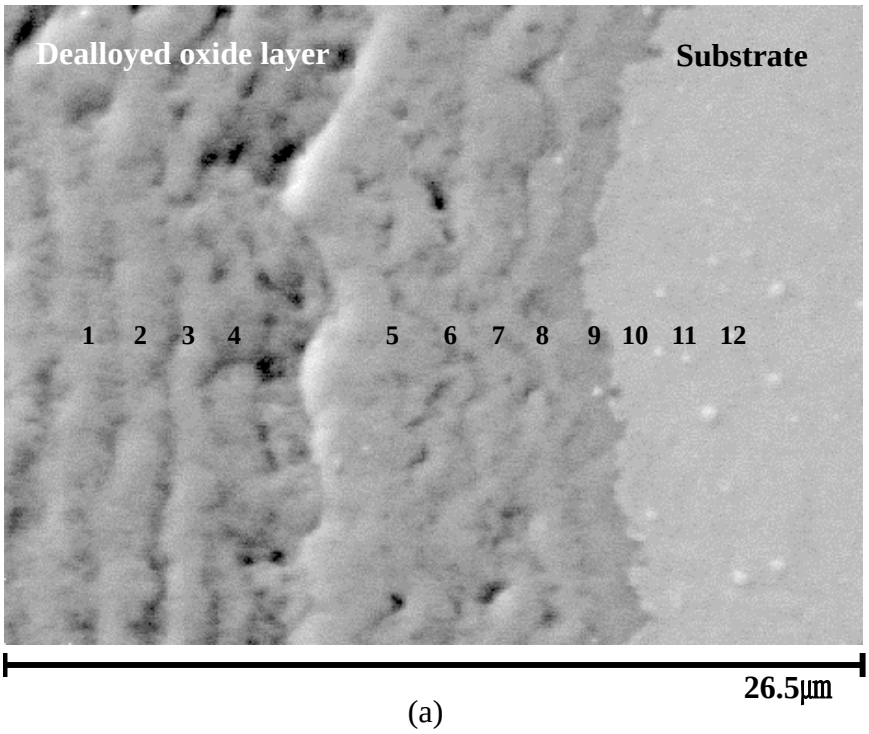

(a)

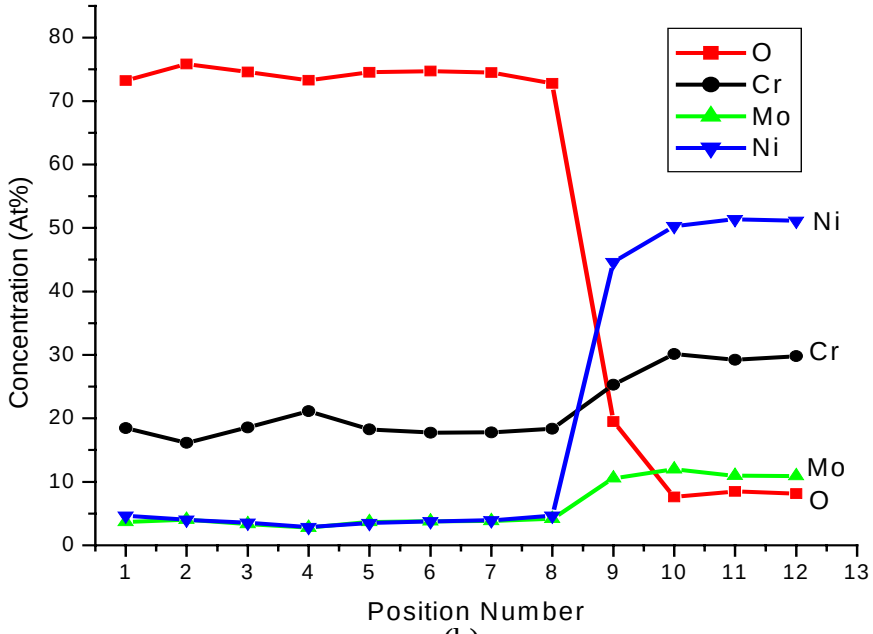

(b)

Figure 3.18 Concentration profile of elements along the position numbers indicated in SEM image (a) by AES on the TC4 section (351℃) of the Inconel 625 reaction vessel tube.

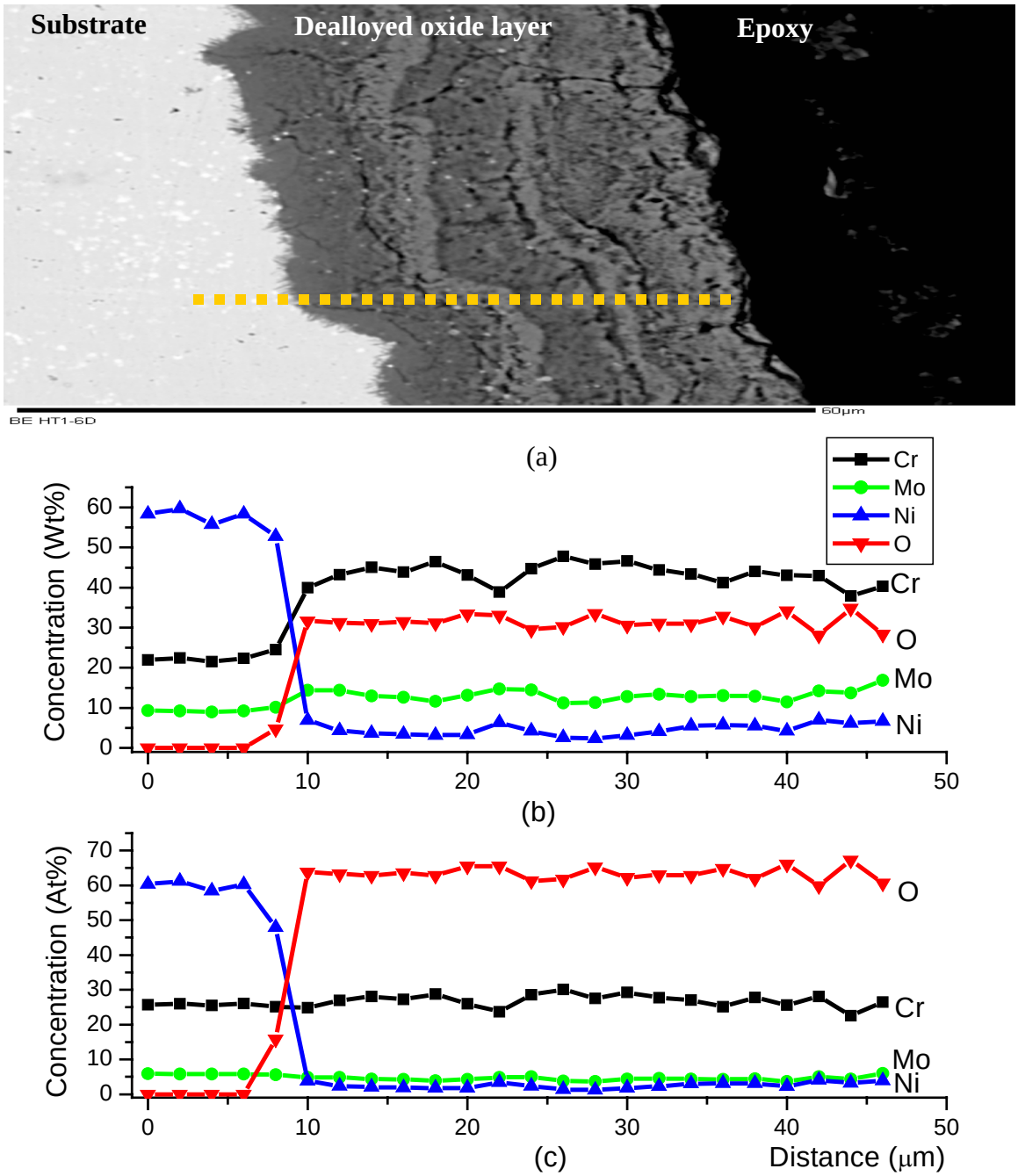

Figure 3.19 Concentration profile of elements along the dotted line in SEM image (a) by EPMA on the TC3 section (353℃) of the Inconel 625 reaction vessel tube.

micron step, and are plotted in Figure 3.19 (b) and (c). It is verified that the concentration profiles of the elements in the dealloyed oxide layer are relatively constant and the quantification analysis on the substrate also agrees well with the nominal composition of Inconel 625 given in Table 3.1. Although the concentration profiles of elements are constant in the dealloyed oxide layer, near the metal-oxide interface there might be a sharp concentration gradient that cannot be measured by EPMA due to its spatial resolution. The average concentrations of the elements in the dealloyed oxide layer and the Inconel 625 substrate are listed in Table 3.7. The average atomic concentration (At%) of elements in the dealloyed oxide layer also supports the fact that chromium oxide is likely to be Cr_2O_3 from the stochiometric analysis. When the oxides of Cr, Mo, Ni, Nb, Ta and Fe are assumed to be Cr_2O_3, MoO_3, NiO, Nb_2O_5, Ta_2O_5 and Fe_2O_3, repectively, the oxygen concentration is estimated to be 62.19 At%. This oxygen concentration is very close to the experimental analysis of 63.63 At% in Table 3.7.

3.3 Neutral environment testing results

Until this point, nickel-base alloys have been tested in an acidic environment in the supercritical and the subcritical temperature ranges. The dealloyed oxide layer has been identified in the subcritical temperature range, and thin oxide film has formed on the surface in the supercritical temperature range. To contrast the results of the acidic environment (pH=2 aqueous HCl under ambient conditions) with a neutral environment (pH=7 under ambient conditions), the reaction vessel is replaced by 316L stainless steel and Inconel 625 tube samples.

The testing sections of the tube samples are schematically drawn in Figure 3.20. The five thermocouples are wrapped around the tube samples every 12㎝. The acidic feed stream is turned off, and only DI water flows throughout the system. The flow rate is adjusted and measured to be 2.3 ㎖/min to obtain the highest temperature reading from the first thermocouple. For each run, the temperatures measured by the five thermocouples wrapped around the tube sample are averaged for each thermocouple. The average temperature and exposure time are given in Table 3.8. The temperature from the first thermocouples is beyond the critical point of pure water, and others are below the critical point. The tube is filled with epoxy resin and hardener to protect the oxide scales prior to sectioning. Each section identified by TC# is cut, cold mounted using epoxy and hardener, and polished in the same way as described in section 3.2.1.

Images from each TC section appear in Figures 3.21 and 3.22. The section indicated by TC0, whose temperature is not directly measured, is at a slightly higher temperature than

TC1. When the inlet stream contains only DW, material degradation is not significant for the innocuous feed stream up to the exposure test time of 240hrs. In all temperature ranges, thin surface oxidation is identified, and there is no indication of dealloying of elements and SCC up to 240 hours. Oxides of Ni, Cr, Fe, and Mo at all temperature ranges are stable in a neutral environment and might form a protective scale against the innocuous DW feed stream. It is noted that due to the sample geometry being tubular in shape, the identification of localized pitting cannot be performed.

Table 3.8 Exposure time and average temperature at each thermocouple position for tube experiments in a neutral environment.

Run#	Alloy	Test time (Hour)	Temperature (℃)				
			TC1	TC2	TC3	TC4	TC5
A	**316L SS**	192	395	348	342	300	250
B	**In625**	240	419	365	357	342	300

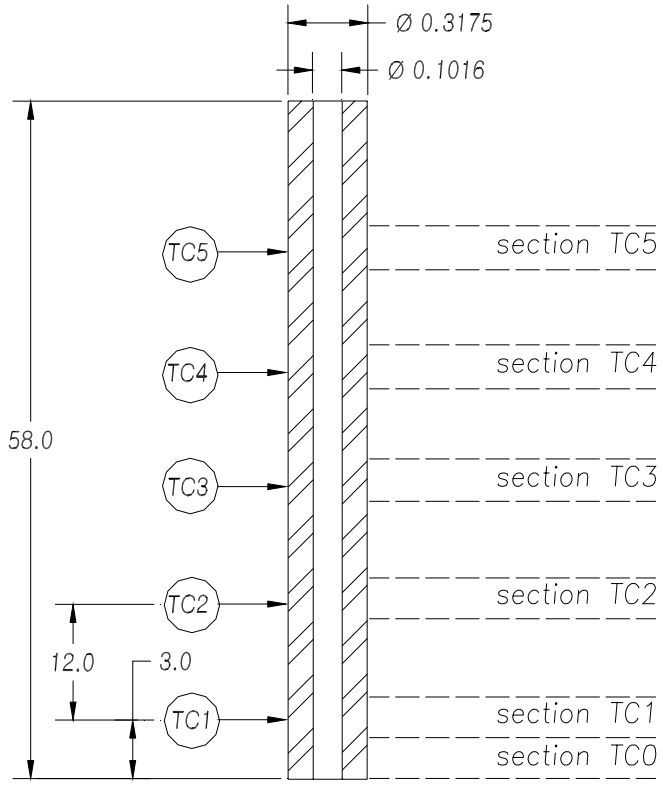

Figure 3.20 Detailed schematic of a reaction vessel tube for neutral environment testing. Each tube section indicated (right-hand) is cut for analysis after the exposure test. Flow direction is from bottom to top. Dimensions are in centimeters.

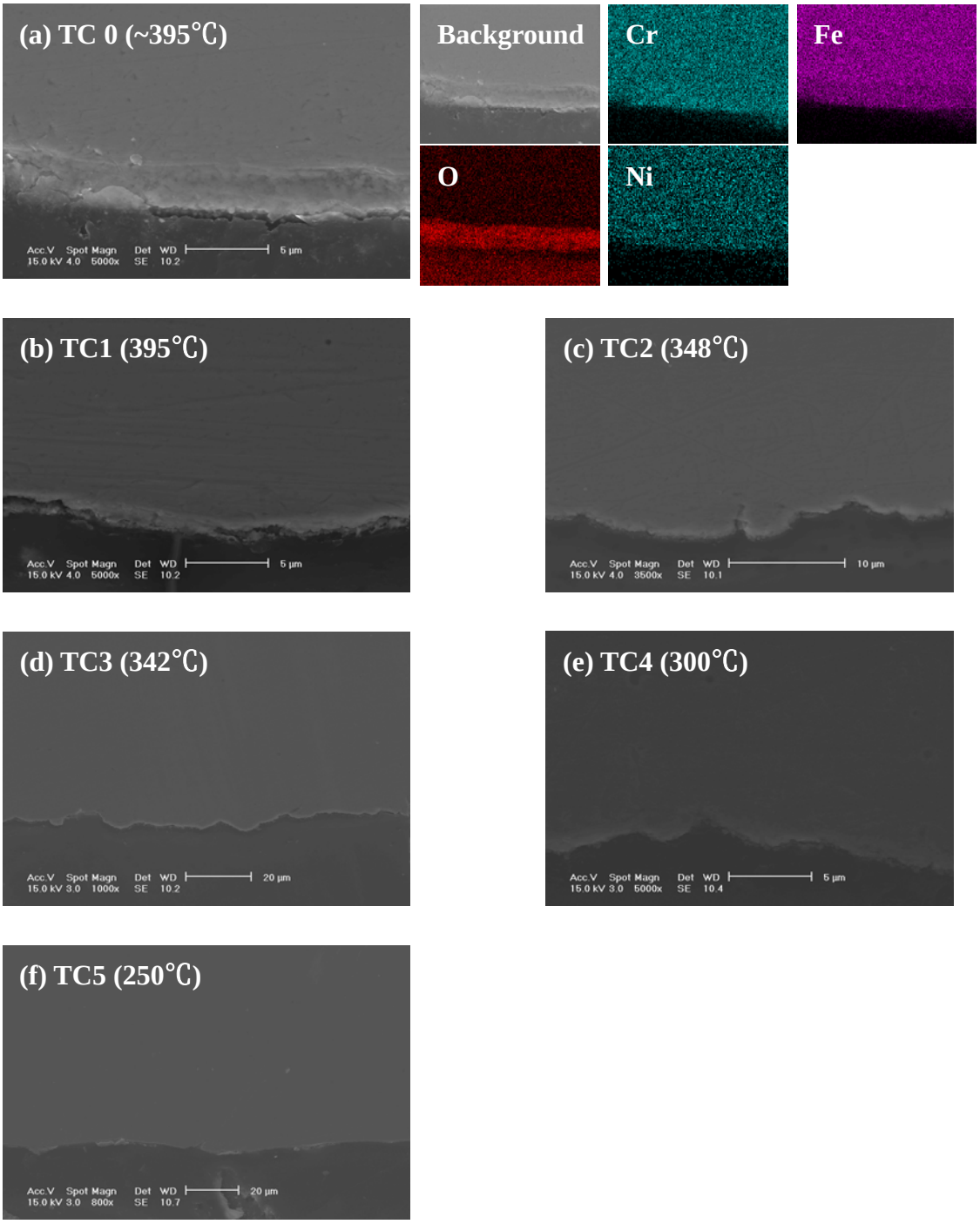

Figure 3.21 ESEM images and X-ray mappings for Run#A (316L Stainless Steel).

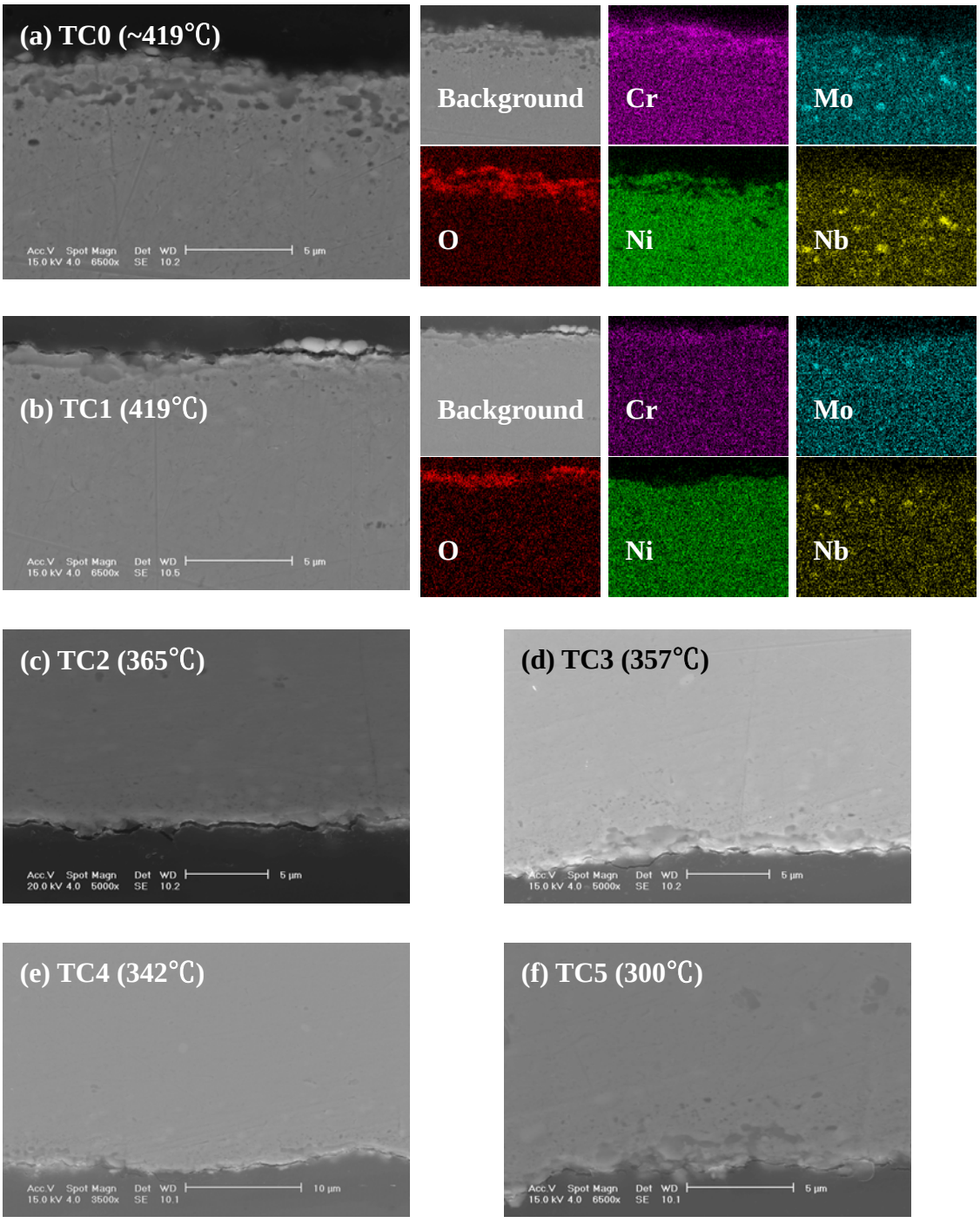

Figure 3.22 ESEM images and X-ray mappings for Run#B (In625).

3.4 Electrochemical cell for pH measurement (Penn State University)

At the Center for Advance Materials in Penn State University, a flow-through electrochemical cell was developed to measure in-situ pH and electrochemical potential (ECP) at the high subcritical temperature. The detailed system configuration is well published in the literature.[4-6] It is noted that their system configuration is modified to induce corrosion of nickel-base alloy inside the cell and to measure the pH and ECP in-situ. A Hastelloy C-276 tube with dimensions of 6.35㎜ (1/4") in OD and 0.889㎜ (0.035") in wall thickness is located inside the cell, while the test solution enters through the test tube into the cell. System pressure is measured to be 27.3 MPa, and because the tube is located inside the cell, there is no pressure difference between the inside and the outside of the C-276 tube. The temperature inside the cell is controlled constantly and measured to be 350℃, which corresponds to the high subcritical temperature. The first test was performed in a neutral environment for 70 hours with the test solution of 0.1m NaCl. The second test was performed in an acidic environment for 53 hours with the test solution of 0.1m NaCl and 0.1m HCl. The pH value of the second test corresponds to pH 1 under ambient conditions. The experimental condition and results are summarized in Table 3.9 (or Appendix E). The pH values are in molal scale for convenience at high temperatures. After in-situ pH and ECP measurements, tested C-276 tubes were analyzed at MIT. Samples were cold-mounted using epoxy resin and hardener to protect oxide scales, cut and polished for analysis, and etched using the same etchant as described in section 3.2.2.

Table 3.9 Experimental conditions and measurement of pH and ECP for the C-276 tube tested at Penn State University.

Test#	1	2
Alloy	C-276	C-276
Temperature (℃)	350	350
Pressure (MPa)	27.3	27.3
Test time (hour)	70	53
Test solution	0.1m NaCl	0.1m NaCl + 0.1m HCl
Measured pH	4.36	0.48
Theoretical pH	5.84	1.96
Electrochemical Potential	440 mV (vs. Ag/AgCl)	-35 mV (vs. Ag/AgCl)

Several observations made with the naked eye are summarized as follows. First, the tube sample from Test#1 is covered with semi-transparent oxide films. Second, the tube sample from Test#2 is covered with thick black oxide scales, and the surface is very rough relative to that from Test#1.

Images obtained by ESEM and a laser confocal microscope appear in Figure 3.23. When the test solution is neutral (Test#1), a thin surface oxide film is observed as shown in Figure 3.23 (a). However, when the test solution is acidic (Test#2), SCC is observed along the grain boundaries as in Figure 3.23 (b)-(g). All the cracks develop from the outer surface, and their penetration depth reaches more than half of the wall thickness (~0.5㎜). The inward crack propagation may occur due to the instability of the pressure between the outside and inside of the C-276 tube through which the test solution enters into the electrochemical cell. From the X-ray mappings of elements in Figure 3.23 (e), the most stable element in the oxide layer is identified as molybdenum, and the selective dissolution of nickel and iron is observed. From the X-ray mapping image of chromium in Figure 3.23 (e), it is observed that chromium is not enriched in the dealloyed oxide layer, unlike the previous results from the acidic environment (pH 2 under ambient conditions), where chromium is highly enriched in the dealloyed oxide layer to form a stable chromium oxide (Cr_2O_3). In a more acidified feed stream (pH 1 under ambient conditions), chromium also dissolves significantly. The X-ray mappings obtained from the cracks show the same feature as Figure 3.23 (e), indicating that nickel, iron, and chromium are depleted and that stable molybdenum oxide has formed. To obtain chemical concentrations of elements, EPMA analysis is performed in the oxide inside the crack. The elemental composition is quantified by WDS for accuracy, and the results are summarized in Table 3.10. From this analysis, it is determined that chromium does not form a stable oxide and that it dissolves significantly relative to the previous results in Table 3.5. It is noted that although chromium is depleted, the degree of the dissolution is not as severe as that of nickel and iron.

Table 3.10 Average concentration of elements in dealloyed oxide layer and substrate (C-276) for Test#2 by EPMA.

		Cr	Mo	W	Co	Fe	Ni	O
Oxide	**Wt%**	16.06	37.26	8.45	0.06	0.18	1.61	36.38
Substrate		16.25	15.83	3.46	1.53	5.83	57.11	0
Oxide	**At%**	10.13	12.75	1.51	0.04	0.11	0.9	74.57
Substrate		19.54	10.32	1.18	1.62	6.53	60.82	0

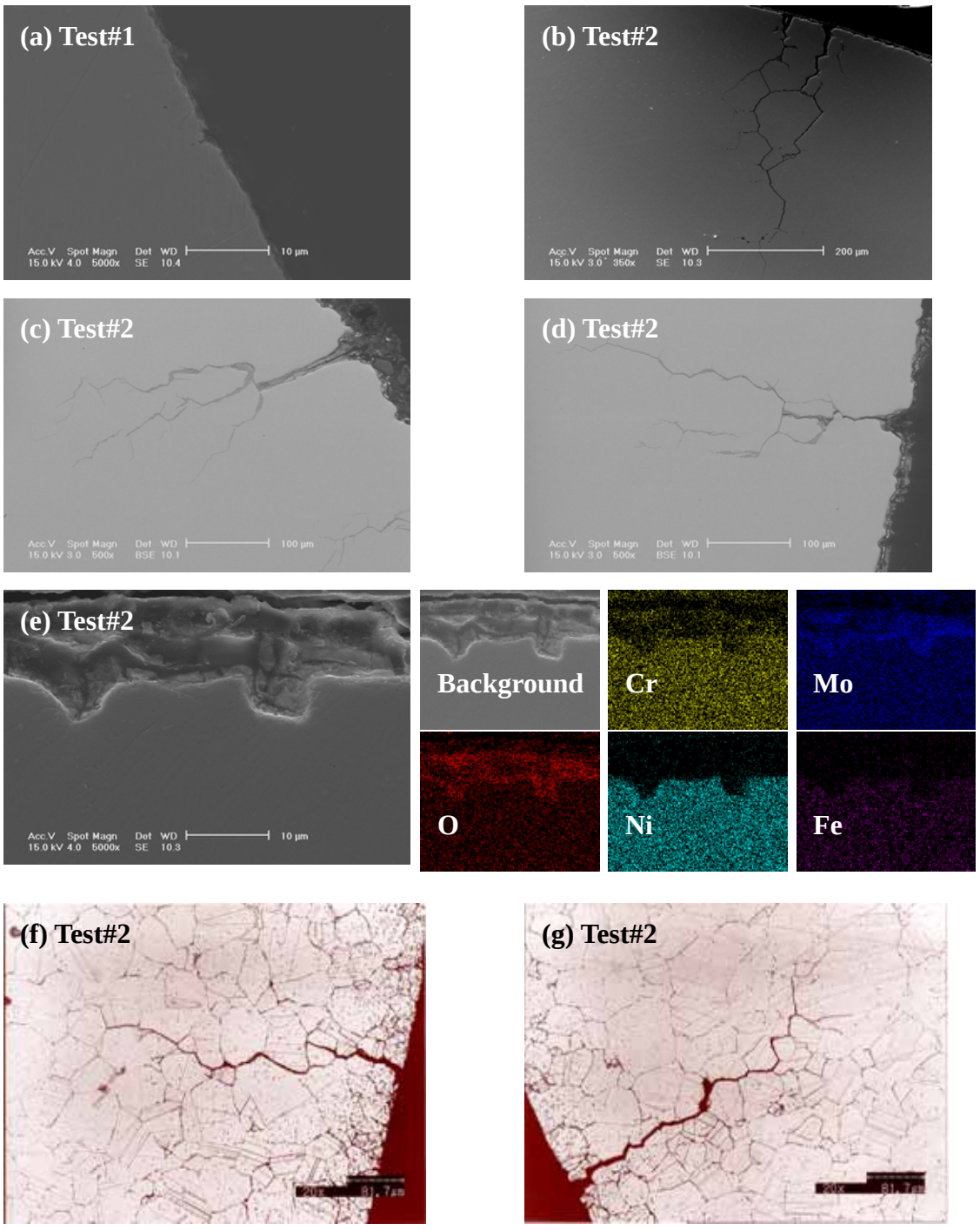

Figure 3.23 Images obtained by ESEM and laser microscope for C-276 tube tested at Penn State University. (a) ESEM image of Test#1. (b)-(e) ESEM images and X-ray mappings of Test#2. (f)-(g) Laser microscope images of etched sample of Test#2.

3.5 Summary of experimental results

From various exposure tests and analyses, the following facts are observed.

First, when the feed stream is in a neutral pH range, no significant material degradation other than thin oxide formation from various constituent elements of the alloy is observed at any temperature ranges.

Second, when the feed stream is at a pH of 2 (under ambient conditions), nickel and iron are selectively dissolved, and chromium and molybdenum form a stable oxide to form a dealloyed oxide layer in the subcritical temperature range. This dealloyed oxide layer in the presence of tensile components of system pressure grows along the grain boundary at an accelerated rate to form intrusions, which are precursors to the intergranular SCC in the high subcritical temperature range. In the supercritical temperature range, a thin oxide film from various constituent elements of the alloys develops on the surface, and there is no dealloying of elements. However, SCC is observed in the presence of tensile stress induced by system pressure when the test time is extended to about 205 hours in the supercritical temperature range.

Finally, when the feed stream is at a pH of 1 (under ambient conditions) in the high subcritical temperature, even chromium is dissolved though to a lesser degree than nickel and iron. The most stable element in the oxide layer is molybdenum. In addition, severe intergranular SCC is observed.

Bibliography

1. Cline, J.A., *Experimental and Ab Initio Investigation into the Fundamentals of corrosion, in the Context of Supercritical Water Oxidation Systems*, in *Department of Chemical Engineering*. 2000, MIT.
2. Moulder, J.F., et al., *Handbook of X-ray Photoelectron Spectroscopy : A Reference Book of Standard Spectra for Identification and Interpretation of XPS Data*. 1992: Physical Electronics, Inc.
3. Davis, J.R., ed. *Nickel, Cobalt, and Their Alloys*. ASM Specialty Handbook. 2000, ASM International: Materials Park, OH.
4. Zhou, X.Y., et al., *Quantitative evalution of general corrosion of Type 304 stainless steel in subcritical and supercritical aqueous solution via electrochemical noise analysis.* Corrosion Science, 2002. **44**: p. 841-860.
5. Macdonald, D.D. and L.B. Kriksunov, *Probing the chemical and electrochemical properties of SCWO systems.* Electrochemica Acta, 2001. **47**: p. 775-790.

6. Lvov, S.N., X.Y. Zhou, and D.D. Macdonald, *Flow-through electrochemical cell for accurate pH measurements at temperatures up to 400 [deg]C]*. Journal of Electroanalytical Chemistry, 1999. **463**: p. 146-156.

Chapter 4: Discussion

This chapter begins by considering the thermodynamics of a metal-water system to explain the experimental observations in Chapter 3. Based on the thermodynamics of a metal-water system, the kinetic model for the dealloyed oxide layer is developed and the detailed corrosion mechanisms are discussed in this chapter.

4.1 Thermodynamics of a metal-water system

Pourbaix diagrams summarize thermodynamic relationships in metal-water systems and give useful information about thermodynamically possible reactions and the stability of various species over a wide range of pH and potential. The general methodology used to build high temperature Pourbaix diagrams has been reviewed in section 2.2.2, and Pourbaix diagrams of Ni, Cr, Fe, and Mo at 300℃ have been presented in Figure 2.6. Recall that these constituent elements are the most important in nickel-base alloys for high temperature strength and corrosion resistance, as described in section 2.3. To identify the stability of each element in nickel-base alloy systems in aqueous media, each Pourbaix diagram of pure elements is superposed.

It is worthwhile to note the well-known limitations of this type of diagram. First, it refers to pure, defect-free, unstressed metals in pure water, does not consider the interactions among constituent elements in an alloy and assumes ideal behavior of the elements in the alloy. Second, although these diagrams reveal the reactions which are thermodynamically possible and stable regions of species in E-pH domains, they do not indicate the rate at which these reactions may take place. Even with these apparent limitations, however, the composite diagrams from each element can provide valuable information on the stability of each element in an alloy.[1]

Due to the complexity of a composite diagram of four elements (see Figure 4.1(c)), this diagram is split into two diagrams as shown in Figure 4.1 (a) and (b) for simplicity. Figure 4.1 (a) is a composite diagram of chromium and molybdenum, which form stable oxides in the subcritical temperature range in the acidic environment of pH 2 (under ambient conditions). Figure 4.1 (b) is a composite diagram of nickel and iron, which are unstable and selectively dissolved from the substrate into the water phase in the subcritcal temperature range in the acidic environment of pH 2 (under ambient conditions). Both Figures 4.1 (a) and (b) focus on stable solid species of the metal and the oxide, while stable regions of ionic species can be found in Figure 2.6. It is important to note that the pH scale in these diagrams is not in the conventional molar scale (molarity, mol per unit volume of aqueous solution, mol/Liter) but molal scale (molality, mol per unit mass of

solvent (water), mol/kg). The relationship between these two pH scales is expressen in equation 4.8. The molal scale is chosen for convenience because molality does not depend on the density of the solution and, hence, does not vary with temperature. Under ambient conditions, defined by the standard state of 1 atm and 25°C, the molal pH and molar pH are essentially the same. The neutral pH value in the molal scale is calculated from the ionic dissociation constant of pure water at 300°C and 84.63 bar (saturated vapor pressure) and has a numeric value of 5.65 (indicated by ▼ in each diagram). Note that this neutral pH value varies as a function of temperature as reviewed in section 2.1 (ionic dissociation constant of pure water).

The acidic solution used for exposure tests of various nickel-base alloys (Run#1-12 and the Inconel 625 reaction vessel) has a pH value of 2 under ambient conditions. This pH value of 2 is obtained from the fact that the solution contains 0.01 molal concentration of HCl as associated molecules and that it is a strong acid. Most of the associated HCl molecules dissociate in water and exist as protons (H^+) and chloride (Cl^-). Even though we use the molal pH scale, which is independent of temperature, the change in properties of water may change the dissociation constant of HCl molecules in water. This change is investigated in section 4.2.1, and the result shows that the molal pH value remains at 2 until the temperature increases above 300°C and increases rapidly near the critical point of pure water (see Figure 4.2 (c)). Therefore, we can assume that the molal pH of the acidic solution remains approximately 2 up to the high subcritical temperature range.

The experimental results from an acidic environment indicate that nickel and iron are selectively dissolved (dealloying) and that chromium and molybdenum form stable oxides in the high subcritical temperature range. The crosshatched region in Figure 4.1 at a pH value of 2 is drawn to identify the region where chromium is stable as solids, and nickel and iron are stable as aqueous ions. Because we do not have information on the potential range during the corrosion process, the crosshatched region is extended along the potential (y-axis in the diagram). This area of the figure corresponds to the region where the chromium forms an oxide as Cr_2O_3, and the nickel and iron exist as dissolved species of Ni^{2+} and Fe^{2+}, respectively. For molybdenum, the thermodynamic data for MoO_3 are not available at elevated temperatures and are not included in the construction of Pourbaix diagram. Since the test solution is saturated by air and SCWO systems generally have a highly oxidizing environment, the constituent alloying elements may exist as oxide instead of metal.

When the solution is neutral, the experimental results (Run#A with 316L SS and Run#B with Inconel 625) show that thin oxides form and no dealloying of nickel and iron is observed at either the supercritical or subcritical temperature ranges. These thin oxides

in the supercritical temperature range consist of oxides of constituent alloying elements, which is readily observed from the composite diagrams in Figure 4.1, where the neutral pH of 5.65 is indicated by ▼. All elements have oxide stability over a wide range of potential near the neutral pH.

The validity of the composite Pourbaix diagram is also supported by the experimental results obtained from Penn State University (Test#1 and Test#2). The pH scale represented in Table 3.9 is defined by the molality of hydrogen ion in the same way as described earlier. The theoretical pH value of Test#1 (neutral condition of 0.1m NaCl, pH = 5.84) is directly calculated using the ionic dissociation constant of pure water. However, the theoretical pH value of Test#2 (acidic condition of 0.1m NaCl and 0.1m HCl, pH=1.96) is calculated by using the dissociation equilibrium constants of pure water and HCl (at 350℃ and 27.3 MPa) as well as the equations of electroneutrality and mass balance without taking into account any corrosion process. The methodology used in this calculation is described in section 4.2.1 in detail.

It is noted that the measured pH value is significantly different from the theoretical calculation, which does not take into account the corrosion processes as shown in Table 3.9 (or Appendix E). This may be due to the fact that in the presence of corrosion, the solution is contaminated by dissolved species from the metal substrate. These dissolved species in the water phase at the high subcritical temperature (350℃) can interact with water molecules to change the water chemistry locally near the metal substrate. Charged dissolved species such as Ni^{2+}, Fe^{2+}, and Cr^{3+} (or $CrOH^{2+}$) may stabilize themselves in aqueous high pressure environments by decreasing their charge/radius ratio through hydrolysis (e.g. $Ni(OH)^{+}$, $Fe(OH)_2^{+}$, etc.) or by forming complex ions with anions in the solution (e.g. $FeCl^{+}$).[2] Through these reactions, the local environment can be acidified and as a result, the measured pH value of the corroding metal can be lower than the theoretical calculation.

In the case of the neutral test solution, the experimental results from Test #1 show that thin oxide films incorporating each of the constituent elements develop in accordance with the neutral environment testing results from Run#A and Run#B. Although the detailed experimental conditions are different from the conditions of composite Pourbaix diagrams, we can assume that the composite Pourbaix diagrams at 300℃ do not change their shapes significantly up to 350℃. The electrochemical potential is 0.44V vs. Ag/AgCl, which corresponds to 0.662 V vs. SHE. The measured pH value is 4.36 in contrast to the theoretical neutral pH value of 5.84. The measured pH and electrochemical potential are indicated by ◆ in Figure 4.1, which corresponds to the region where iron is stable as Fe_2O_3, nickel is stable as Ni^{2+}, chromium is stable as $HCrO_4^{-}$, and

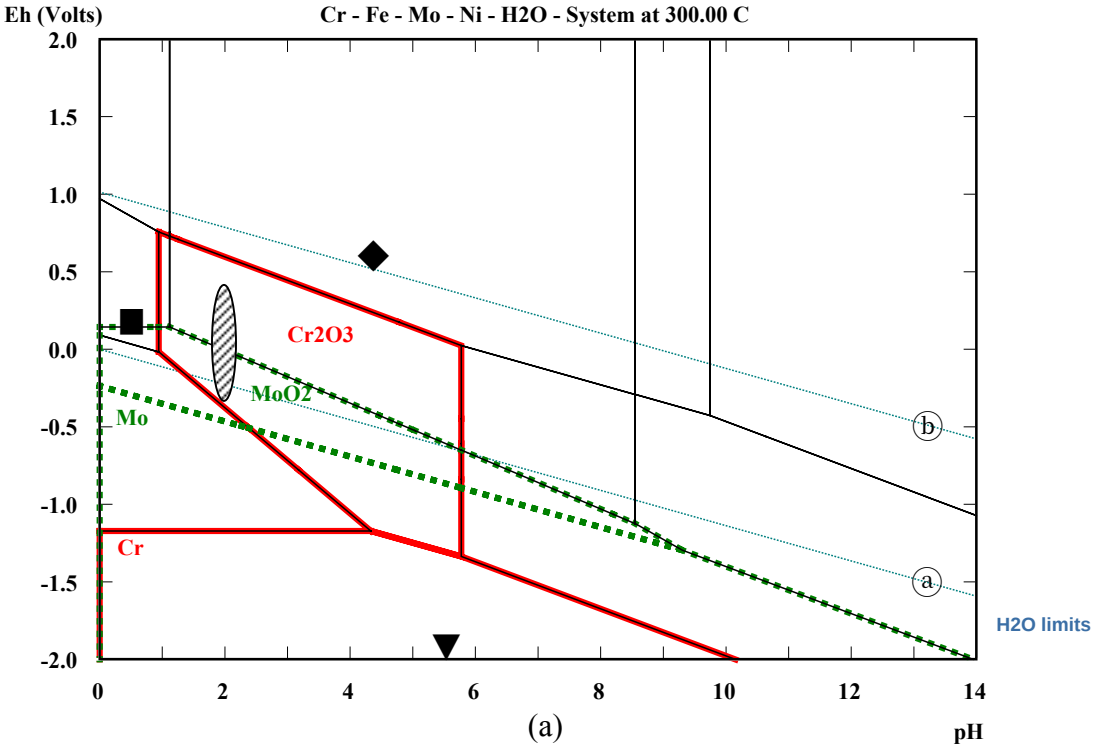
Eh (Volts)
Cr - Fe - Mo - Ni - H2O - System at 300.00 C
2.0
1.5
1.0
0.5
0.0
-0.5
-1.0
-1.5
-2.0
0
2
4
6
8
10
12
14
pH
Cr2O3
MoO2
Mo
Cr
b
a
H2O limits

(a)

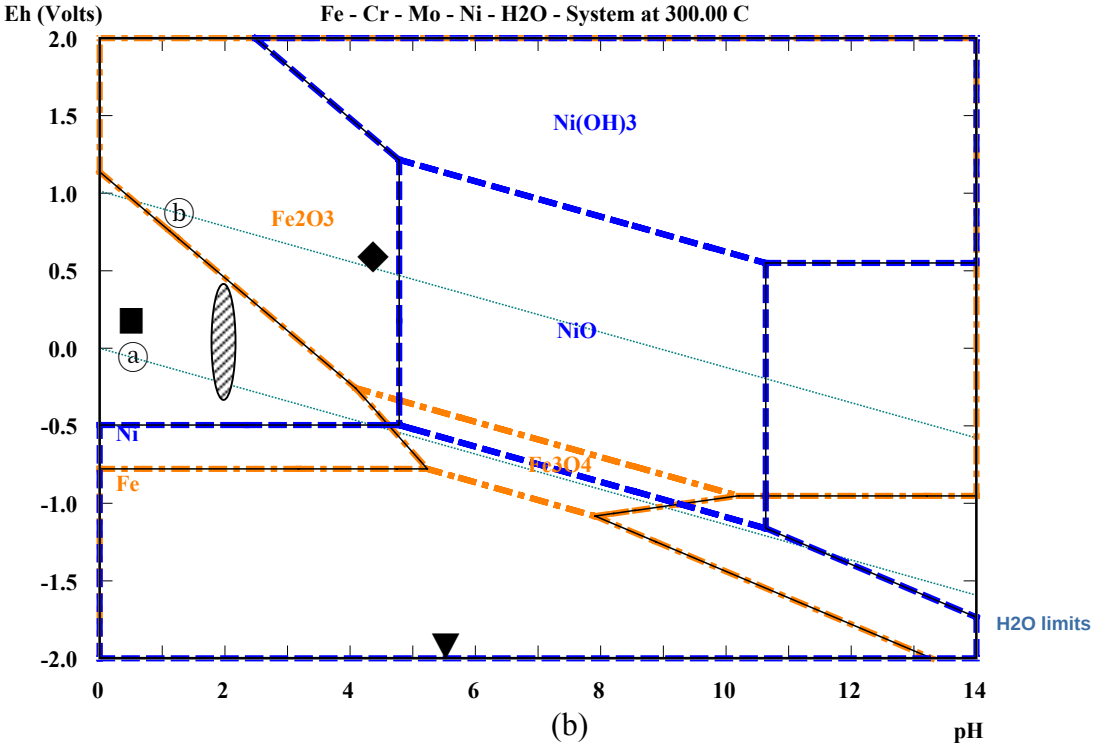
Eh (Volts)
Fe - Cr - Mo - Ni - H2O - System at 300.00 C
2.0
1.5
1.0
0.5
0.0
-0.5
-1.0
-1.5
-2.0
0
2
4
6
8
10
12
14
pH
Ni(OH)3
Fe2O3
NiO
Ni
Fe
Fe3O4
b
a
H2O limits

(b)

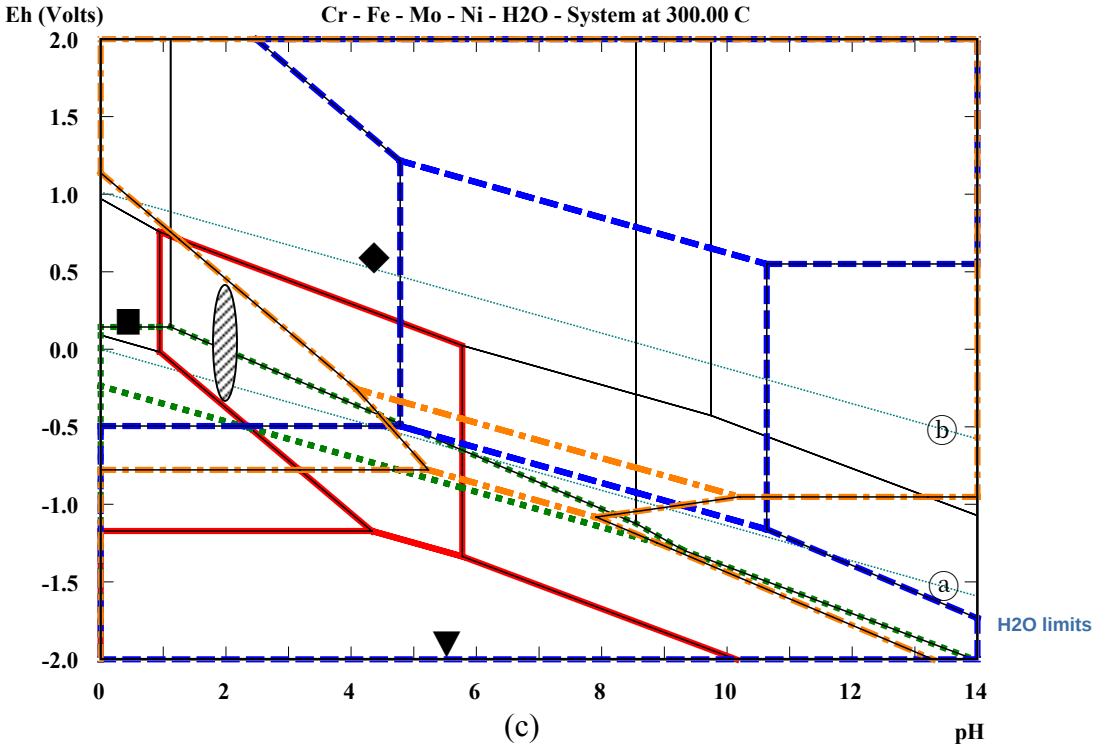

Figure 4.1 Composite E-pH diagram Ni, Fe, Mo, and Cr at T=300℃ and P=84.63 bar (saturated vapor pressure) with an assigned molality of 10^{-6}. (a) composite diagram of Cr (solid line in red) and Mo (dotted line in green), (b) composite diagram of Ni (dash line in blue) and Fe (dash-dot line in orange), (c) composite diagram of Cr, Mo, Ni and Fe. Stability line (dash) of water is indicated by ⓐ, ⓑ in each diagram. Neutral pH is indicated by ▼ with a numeric value of 5.65 at 300℃ and 84.63 bar.

molybdenum is stable as $HMoO_4^-$. Note that only the iron oxide is stable as a solid phase, while all the other elements are stable as dissolved ionic species at the indicated point (◆). However, the uncertainties in thermodynamic data for the construction of Pourbaix diagrams and their apparent limitations as noted earlier may apply in this case along with the uncertainties in experimental measurement. Even though only iron forms an iron oxide and other elements are dissolved as ions from a thermodynamic viewpoint, Pourbaix diagrams do not indicate the rate at which these reactions may take place and do not consider the interactions between elements in an alloy.

When the test solution is acidic with an ambient pH value of 1 (Test#2), the experimental results show a discrepancy from the results of Run#1-12 and the Inconel 625 reaction vessel. The nickel and iron are selectively dissolved in the same way; however, the chromium is not enriched in the dealloyed oxide layer, indicating that chromium is also dissolved from the metal substrate to a lesser degree than nickel and iron (refer to Figure 3.23(e)). Only molybdenum is identified to form a stable oxide in a more acidified environment. The measured pH value is 0.48 in contrast to the theoretical calculation, while the electrochemical potential is –0.035V vs. Ag/AgCl and 0.187 vs. SHE. The measured pH and potential is indicated by ■ in Figure 4.1, which corresponds to the region where iron is stable as Fe^{2+}, nickel is stable as Ni^{2+}, chromium is stable as $CrOH^{2+}$, and molybdenum is stable as MoO_2^{2+}. All the elements exist as dissolved species at this pH and potential range. The composite Pourbaix diagrams properly explain the experimental observations that even the chromium is dissolved like nickel and iron. However, the oxide formation of Mo is not clearly understood from thermodynamics. The experimental observation that molybdenum forms a stable oxide may come from the lack of thermodynamic data and apparent limitations of the Pourbaix diagram as described at the beginning of this section. The thermodynamic data for MoO_3 at high temperatures are not available and so are not included in the Pourbaix diagram of molybdenum. The Pourbaix diagram of molybdenum at 25℃ in Figure 2.5(d) indicates the presence of stable molybdenum oxide as MoO_3 in an acidic environment.

4.2 Kinetics of corrosion in an acidic environment

The thermodynamics of a metal-water system have been used in the previous section to describe dealloyed oxide layer formation in the subcritical temperature range in an acidic environment. The experimental results are in considerable agreement with the expectations obtained from the thermodynamic relations. However, thermodynamics does not provide the information on the rate of corrosion. The experimental observations show that the dealloyed oxide layer formation is maximized in the high subcritical temperature range and the dealloyed oxide layer formation is totally suppressed in the supercritical temperature range; in contrast, thin oxide is formed in the supercritical temperature range. This observation is investigated first in section 4.2.1 using a phenomenological model; the kinetic model for the dealloyed oxide layer is developed in section 4.2.2.

4.2.1 Phenomenological model

The experimental results show that maximum corrosion occurs in the high subcritical

temperature range in an acidic environment. The phenomenological model originally developed by L.B. Kriksunov et al.[3] is modified for the experimental conditions of the pH 2 (under ambient conditions) aqueous solution to explain the degradation of nickel-base alloys in the high subcritical temperature range. This model primarily considers the physical property changes of water over a wide range of temperature, and their effects on corrosion of nickel-base alloys are obtained qualitatively.

An electrochemical system runs on the basis of charge-transfer reactions at the metal-electrolyte interfaces. These reactions involve ions or molecules which are constituents of the electrolyte. Thus, the transport of particles to or away from the interface becomes an essential condition for the continued electrochemical transformation of reactants at the interface. Corrosion on the metal surface can be regarded as a heterogeneous chemical reaction at the metal surface in the initial stage. From the experimental results, dealloying of nickel and chromium oxidation are considered to be dominant corrosion reactions in the high subcritical temperature range. These chemical reactions are written as follows:

$$Ni \rightarrow Ni^{2+} + 2e^{-} \text{ (Anodic reaction)} \tag{4.1}$$

$$\tfrac{1}{2}O_2 + 2H^{+} + 2e^{-} \rightarrow H_2O(\ell) \text{ (Cathodic reaction)} \tag{4.2}$$

$$Ni + \tfrac{1}{2}O_2 + 2H^{+} \rightarrow Ni^{2+} + H_2O(\ell) \text{ (Overall reaction)} \tag{4.3}$$

$$2Cr + \tfrac{3}{2}O_2 \rightarrow Cr_2O_3 \text{ (Chromium oxidation)} \tag{4.4}$$

From a chemical kinetic viewpoint, the rate of corrosion depends on the concentration of reacting species. From the above reactions, the reacting species in the corrosion processes are oxygen molecules (O_2) and hydrogen ions (H^+). Assuming first order reaction kinetics, the reaction rate can be written as follows:

$$R_S = k_S C_{O_2} C_{H^+} = k_{S0} C_{O_2} C_{H^+} \exp(-\frac{E_a}{RT}) \tag{4.5}$$

where R_S is a heterogeneous reaction rate, k_S is a heterogeneous reaction rate constant having a temperature dependence based on the Arrhenius equation, k_{S0} is the reference reaction rate constant, E_a is an activation energy for the corrosion reaction, and C_{O_2} and C_{H^+} are the molar concentrations of oxygen and hydrogen ions, respectively. The relative reaction rate can be expressed by dividing the expression by the reference temperature (T_0) reaction rate, indicated by superscipt 0, as follows:

$$\left(\frac{R_S}{R_S^0}\right)=\left(\frac{C_{O_2}}{C_{O_2}^0}\right)\left(\frac{C_{H^+}}{C_{H^+}^0}\right)\exp\left(-\frac{E_a}{RT}+\frac{E_a}{RT_0}\right) \tag{4.6}$$

$$\log\left(\frac{R_S}{R_S^0}\right)=\log\left(\frac{C_{O_2}}{C_{O_2}^0}\right)+\log\left(\frac{C_{H^+}}{C_{H^+}^0}\right)+\left(-\frac{E_a}{RT}+\frac{E_a}{RT_0}\right)\cdot\frac{1}{2.303}. \tag{4.7}$$

As the concentration of each species is expressed in molar concentration, it has a temperature dependence caused by the density change of an aqueous solution. The molar concentration and molal concentration dependence has a relationship expressed as

$$C_i=\frac{m_i\rho}{1+m_iM_i}, \tag{4.8}$$

where C_i is molar concentration of the species, m_i is molal concentration, ρ is the density of the solution and M_i is the molar mass of the species. In case of dilute solutions the expression can be approximated as

$$C_i\approx m_i\rho. \tag{4.9}$$

The relative reaction rate can, therefore, be expressed in molal concentrations of the species as follows:

$$\log\left(\frac{R_S}{R_S^0}\right)=2\log\left(\frac{\rho}{\rho^0}\right)+\log\left(\frac{m_{O_2}}{m_{O_2}^0}\right)+\log\left(\frac{m_{H^+}}{m_{H^+}^0}\right)+\left(-\frac{E_a}{RT}+\frac{E_a}{RT_0}\right)\cdot\frac{1}{2.303}. \tag{4.10}$$

This expression incorporates the effects of the density changes of water, the effects of the change in the oxygen concentration, and the effects of changes in the concentration of hydrogen ions due to the change in the dissociation constant of HCl and H_2O. The last term represents the exponential effect of temperature on the rate constant. In the case of oxygen, its molal concentration can be assumed to be constant throughout the system if the system operates in a steady state inside the reaction vessel, and this fact simplifies equation (4.10) to

$$\log\left(\frac{R_S}{R_S^0}\right)=2\log\left(\frac{\rho}{\rho^0}\right)+\log\left(\frac{m_{H^+}}{m_{H^+}^0}\right)+\left(-\frac{E_a}{RT}+\frac{E_a}{RT_0}\right)\cdot\frac{1}{2.303}. \tag{4.11}$$

The molal concentration of hydrogen ion can be obtained from the equilibrium dissociation reactions of HCl and water as follows:

$$HCl(aq)\leftrightarrow H^+ + Cl^- \tag{4.12}$$

$$H_2O(\ell)\leftrightarrow H^+ + OH^- \tag{4.13}$$

For these two reactions, the dissociation constants are expressed

$$K_d = \frac{m_{H^+} m_{Cl^-} \gamma_{\pm}^2}{m_{HCl} \gamma_{HCl}} \tag{4.14}$$

$$K_W = m_{H^+} m_{OH^-} \gamma_{\pm}^2 \tag{4.15}$$

where K_d is the dissociation constant of HCl and K_W is the ionic dissociation constant of pure water, m_{HCl} is the molality of HCl as associated molecules, m_{Cl^-} is the molality of chloride, $\gamma_{\pm}$ is the mean molal activity coefficient and γ_{HCl} is the activity coefficient of associated HCl molecules. Mass balance of species and the charge neutrality condition of the solution give the following relations:

$$m_{HCl}^0 = m_{Cl^-} + m_{HCl} \tag{4.16}$$

$$m_{H^+} = m_{Cl^-} + m_{OH^-} \tag{4.17}$$

where m_{HCl}^0 is the total molal concentration of HCl in solution before dissociation. The mass balance equation in (4.16) shows that the total amount of HCl before dissociation is equal to the sum of associated HCl molecules and one of the dissociated species (H^+ or Cl^-) in water. From equations (4.14)–(4.17), we can obtain the molal concentrations of hydrogen ions (H^+) over a wide temperature range. The number of unknowns in these equations, K_d, K_W, m_{H^+}, m_{OH^-}, m_{HCl}^0, m_{Cl^-}, m_{HCl}, $\gamma_{\pm}$ and γ_{HCl}, are nine in total. However, as will be shown later in detail, the actual number of unknowns to be solved can be reduced to four, m_{H^+}, m_{OH^-}, m_{Cl^-}, and m_{HCl}. The dissociation constants, K_d, and ionic dissociation constants of water, K_W, are available in the literature. The total molal concentration of HCl, m_{HCl}^0, is readily determined from the ambient pH value, 2 in this case, and so m_{HCl}^0 is equal to 0.01.

The activity coefficient of associated HCl molecules, γ_{HCl}, is assumed to be 1, while the mean molal activity coefficient, $\gamma_{\pm}$, is calculated using the Debye-Hückel limiting law, which is valid at very low electrolyte concentrations. In the case of HCl, the limiting law is accurate up to 0.01 molal concentration at room temperature[4]. This limiting law may also be acceptable at higher temperatures since the ionic concentration drops due to

the decrease of the dissociation constant of HCl. The mean activity coefficient is expressed as follows:

$$\log \gamma_{\pm} = -|z_{+} z_{-}| A\sqrt{I} \tag{4.18}$$

$$A = \frac{F^3}{4\pi N_A \ln 10}\left(\frac{\rho}{2\varepsilon^3 R^3 T^3}\right)^{1/2} \tag{4.19}$$

$$I = \frac{1}{2}\sum_i m_i z_i^2 \tag{4.20}$$

where z_i is the charge number of the ions i (positive for cations and negative for anions), F is Faraday's constant, N_A is Avogardo's number, ε is the dielectric constant of the medium, R is the gas constant and T is the temperature in Kelvin[5]. The constant A has a numerical value of 0.509 for aqueous solution at 25℃. The constant I represents ionic strength of the solution, which can be expressed as follows for an aqueous HCl solution

$$I = \frac{1}{2}\sum_i m_i z_i^2 = \frac{1}{2}(m_{H^+} + m_{OH^-} + m_{Cl^-}). \tag{4.21}$$

According to the charge neutrality condition presented in equation (4.17), the ionic strength is further simplified to

$$I = m_{H^+}. \tag{4.22}$$

By inserting equation (4.22) into (4.18) with corresponding charge numbers, the mean activity coefficient becomes

$$\log \gamma_{\pm} = -A\sqrt{m_{H^+}}. \tag{4.23}$$

To solve equations (4.14)-(4.17) in terms of equation (4.23), the physical constants of an HCl solution, such as ε and ρ, are required in estimating the constant A over a wide temperature range in equation (4.19). Assuming the solution is sufficiently dilute, the values of pure water can be used instead.

In recent years, there have been comprehensive efforts to obtain the dissociation constant of HCl, K_d, because of its importance in geological chemistry.[6-13] More comprehensive experimental methods and results on the dissociation constant of HCl are reviewed in the literature[7, 9-13]. In this calculation, the empirical relationship obtained by Frantz et al.[7] is adopted to solve equations (4.14)-(4.17). The dissociation constant of HCl in water is defined by molal concentration and expressed as follows:

$$\log K_d = -5.405 + \frac{3874.9}{T[^O K]} + 13.93 \log \rho_{H_2O} \qquad (4.24)$$

where ρ_{H_2O} is the density of pure water. This relation was obtained by the conductance measurements of an HCl solution over a wide range of temperature, pressure, and concentrations of hydrochloric acid solutions.

One limitation of this is that when equation (4.24) is extrapolated to ambient conditions, the dissociation constant of HCl has an error of approximately one logarithmic unit. This error occurs because equation (4.24) was obtained under conditions of high temperature, high pressure, and high water density. Another limitation of this empirical relation is the fact that the dissociation constants continuously decrease as temperature increases as shown in Figure 4.2 (a) at constant pressure of 25 MPa. More accurate experimental results show that the dissociation constants increase as the temperature approaches ~100°C, after which they decrease continuously as the temperature increases.[13] Although the dissociation constants of HCl increase up to ~100°C, the molality of the hydrogen ion is not changed significantly, which is verified by HCl being a very strong acid at low temperatures and HCl molecules dissociating strongly at this low temperature range. The rapid decrease of dissociation constants of HCl also indicates that the ionic species are not preferred in supercritical water, just like the solvation property changes of supercritical water (section 2.1.3).

With the relations and data up to this point, equations (4.14)-(4.17) and (4.23)-(4.24) are solved numerically using MATLAB (The Mathworks, MATLAB 6.5), included in Appendix F. The physical properties of water used in this calculation are obtained from the literature[14-16] and tabulated in Appendix F with the numerical results. The properties of water are obtained assuming a constant pressure of 25MPa, close to the experimental condition of 24.1MPa. Numerical results are ploted as a function of temperature in Figure 4.2, which shows that the dissociation constants of HCl decrease as temperature increases, more rapidly near the critical point of pure water. From the calculated molal concentrations of the species in Figure 4.2 (b)-(c), it is shown that near the critical point of water the molal concentration of hydrogen ions (H^+) decreases rapidly and the molal concentration of associated HCl molecules increases rapidly. The decrease of molal concentration of hydrogen ion (H^+) leads to the increase in molal pH near the critical point of water. As a result, the molal pH in the supercritical temperature range approaches that of a neutral solution. This fact has important consequences in corrosion processes in SCWO systems.

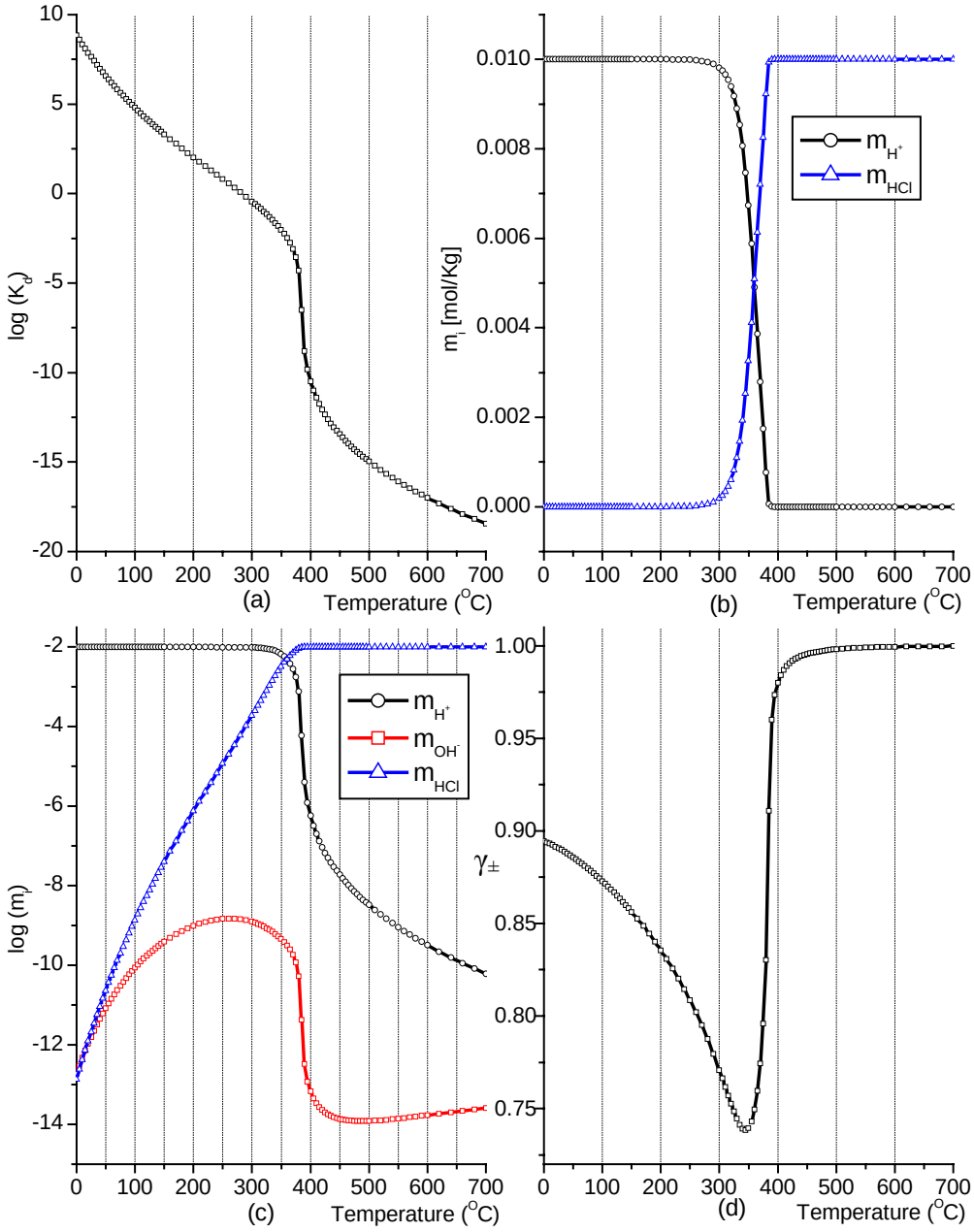

Figure 4.2 The molal concentration change of various species over a wide range of temperature up to 700℃ at constant pressure (25MPa) with $m^0_{HCl} = 0.01$. (a) Dissociation constant of HCl, (b) molal concentration of H^+ and associated HCl molecules (c) molal concentration of H^+, OH^-, and associated HCl molecules (d) mean activity coefficient, $\gamma_{\pm}$.

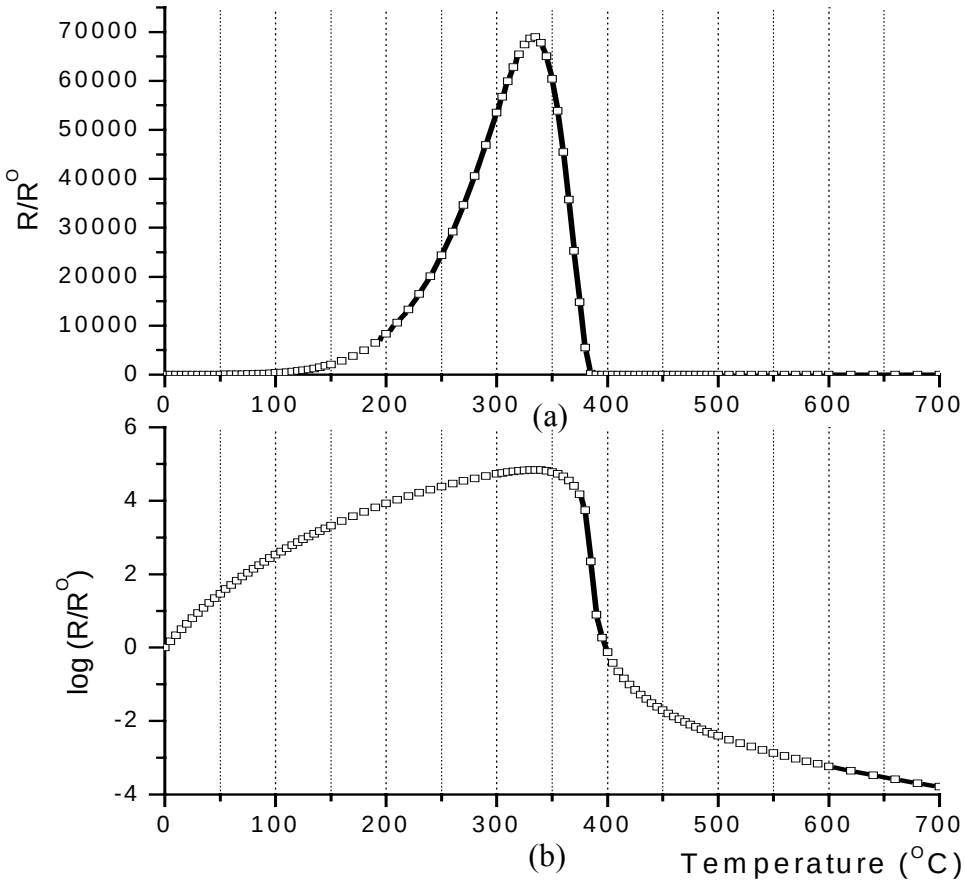

Figure 4.3 Relative corrosion rate (R/R^0) over a wide range of temperature up to 700℃. (a) linear scale, R/R^0 (b) logarithmic scale, $\log(R/R^0)$.

The phenomenological model properly explains the experimental results; the formation of the dealloyed oxide layer occurs because of high concentration of the hydrogen ions in the subcritical temperature range and thermodynamic stability of elements in that environment. The formation of thin oxide from various constituent elements might occur in the supercritical temperature range due to significant decrease of hydrogen ion concentration in the supercritical temperature range.

The corrosion rate in equation (4.11) considers the effects of ionic concentration changes of species and density change. From the calculated molal concentrations, the relative corrosion rate is calculated and plotted in Figure 4.3 from 0℃ to 700℃. The reference is arbitrarily chosen as 0℃. To obtain the relative corrosion rate, it is assumed that the activation energy of the corrosion process is 50 KJ/mol. This value is chosen because it is an intermediate value between that of diffusion control and activation

control. The corrosion process can be diffusion controlled and/or activation controlled from the aqueous solution. Figure 4.3 shows that the relative corrosion rate is maximized in the high subcritical temperature range. The relative corrosion rate around 400°C is similar to that of the reference temperature, T_0=0°C. These findings are in excellent agreement with the experimental observations in that the dealloyed oxide layer thickness is maximized in the high subcritical temperature range. While the ambient pH value of 2 in molal scale remains almost constant up to 300°C, the pH values in the supercritical temperatures shift towards the neutral pH. With very low hydrogen ion concentrations in the supercritical temperature range, the constituent elements may form a stable oxide. It should be stressed that this model only considers that the ionic species of hydrogen ion and oxygen cause corrosion reactions on the surface of the metal substrate. Although this model correctly predicts that the dealloyed oxide layer formation is maximized at the high subcritical temperature and minimal corrosion in the supercritical temperature range, it does not take into account the detailed corrosion mechanisms in the metal substrate. Even with low hydrogen ion concentration and a low corrosion reaction rate at supercritical temperatures, SCC was observed in the Inconel 625 reaction vessel. This may be due to the high concentration of associated HCl molecules that might attack the base metal and/or thin oxides formed in the supercritical temperature range.

In developing the phenomenological model in this section, we did not consider the detailed kinetic mechanisms inside the metal substrate. The detailed mechanism of dealloyed oxide layer formation in the high subcritical temperature range is developed and discussed in the following section.

4.2.2 Kinetic model for the dealloyed oxide layer formation

Thermodynamics and the phenomenological model in previous sections provide good descriptions of the corrosion processes in SCWO systems. However, they do not consider detailed mechanisms in the metal substrate and oxide layer. Because the most interesting and important aspects are associated with these detailed mechanisms in the metal substrate and oxide layer, the kinetics of dealloyed oxide layer formation in the high subcritical temperature range is considered in this section. Before getting into the development of the kinetic model, the mechanisms of dealloying in the literature are presented briefly for its relevance.

Mechanisms of dealloying (review)

Dealloying is a corrosion process in which one constituent of an alloy is preferentially removed, leaving behind an altered residual structure. This phenomenon was first

reported by Calvert and Johnson in 1866 on brass alloys.[17] Since that time, dealloying has been reported in a number of copper-base alloy systems as well as in gray iron, noble metal alloys, etc. Although numerous attempts have been made to clarify the mechanisms of dealloying, two theories are most prevalent.

In the first, two metals in an alloy are dissolved, and more noble metal redeposits on the surface. The redeposited metal on the surface can aggregate by surface diffusion and form a porous layer. The solution can then penetrate through the porous layer and attack underlying metal directly without volume diffusion. Because this model assumes redeposition of noble elements on the surface, the structural evolution of the porous surface layer is investigated in the literature in terms of surface diffusion.[18-27]

In the second theory, one metal is selectively dissolved from an alloy by volume diffusion, leaving a porous residue of the more noble species. Mechanisms involving ionization of the less noble metal and movement of both metals in the atomic state by volume diffusion are normally considered inoperable on the basis of diffusivities extrapolated from high temperature measurements. Use of this extrapolation implies that equilibrium concentrations of vacancies (and interstitials) are established at room temperature as at elevated temperatures, and the contribution of diffusion along dislocations and grain boundaries is negligible at room temperature. However, the effective diffusion coefficient at room temperature may be considerably greater than the value of the volume diffusion coefficient obtained by extrapolation of high temperature data. This occurs because short circuit diffusion along the grain boundary and dislocations are dominant at low temperatures. In addition, Pickering and Wagner suggested that the rate-limiting step in the electrolytic dissolution of a binary alloy (Cu-Ag) is the solid state diffusion of the less noble metal element via a divacancy mechanism. Because the diffusivity of monovacancies is insufficient, monovacancies cannot account for the diffusion of copper at room temperature. By considering a diffusivity of monovacancy of 3×10^{-19} cm^2/sec at room temperature and a divacancy at room temperature of 1.3×10^{-12} cm^2/sec, they showed that volume diffusion can be operative via divacancies.[28]

Regardless of the mechanism, however, during dealloying, the metal in the affected area becomes porous and loses much of its strength, hardness, and ductility. Failure may be sudden and unexpected because dimensional changes do not always occur and the corrosion sometimes appears to be superficial, although the selective attack may have left only a small fraction of the original thickness of the part unaffected.[29]

Although there has been much effort to clarify the mechanisms of dealloying, the mechanism of dealloying is not clearly defined and both mechanisms described above are

probable. A majority of the experiments and theories consider noble binary alloys such as Au-Ag or Au-Cu in a stagnant solution without dissolved oxygen to suppress the oxidation of noble elements.

In this work, the situation is more complex for the following reasons. First, the engineering nickel-base alloys contain various minor alloying elements to modify the property of the alloy. Second, dealloying of nickel and iron accompanies the oxidation of remaining elements such as chromium and molybdenum. From the experimental observation, the volume diffusion mechanism seems more reasonable in the present work for the following reasons. (i) The aqueous solution flows throughout the system continuously with oxygen present. (ii) The dimension of the samples remains unchanged after the exposure tests. (iii) The development of intrusions along the grain boundary is not explained by the redeposition mechanism.

Kinetic model

Nickel-base alloys are composed of various alloying elements, and all the minor alloying elements contribute to the properties of nickel-base alloys and also to the corrosion processes. Considering all the alloying elements, however, in developing the kinetic model might not be practical due to its complexity and inefficiency. The most important points in the high subcritical temperature range are the dealloying of nickel and the formation of chromium oxide, both within the dealloyed oxide layer. In this regard, the nickel-base alloys are approximated as a binary alloy composed of chromium and nickel, which are the most important alloying elements both in weight percent and in providing proper corrosion resistance.

In the initial oxidation stage, the oxygen molecules adsorb on the surface to form a chromium oxide, while nickel elements in direct contact with the aqueous environment are selectively dissolved into the aqueous solution. After the formation of the initial dealloyed oxide layer, further growth requires the transport of metal ions from the metal/oxide interface and oxygen ions from the oxide-solution interface.

According to the experimental results in section 3.2.1 (Inconel 625 reaction vessel), the dealloyed oxide layer is composed primarily of chromium oxide and a residual amount of nickel. Figures 3.18-19 support that the compositions of the constituent elements of oxygen, chromium, and nickel are fairly constant throughout the dealloyed oxide layer. Figure 3.19 shows that the oxygen concentration in the metal is zero, within the accuracy of analysis, indicating that no internal oxidation occurs in the metal substrate. From these observations, it is assumed that the major migrating species for further growth of the oxide are nickel cations, oxygen anions, and electrons. The chromium elements are not likely to migrate significantly because they form a stable oxide at the metal-oxide

interface and provide a porous and defective medium for the migration of nickel and oxygen ions. These experimental observations are used as support for the following assumptions in developing the kinetic model for the growth of the dealloyed oxide layer.

(1) Only nickel and chromium are considered to be alloying elements.
(Ni-Cr, binary alloy)

(2) The dealloyed oxide layer is a compact, adherent scale.

(3) The migrating species is assumed to consist of electrons and ions of nickel and oxygen. (Chromium is not considered to be a migrating species.)

(4) The migration of ions or electrons across the oxide scale is the rate controlling process.

(5) Thermodynamic equilibrium is established at both the metal-oxide and oxide-solution interfaces.

(6) The concentrations of species are constant throughout the oxide layer.

(7) Thermodynamic equilibrium is established locally throughout the oxide layer.

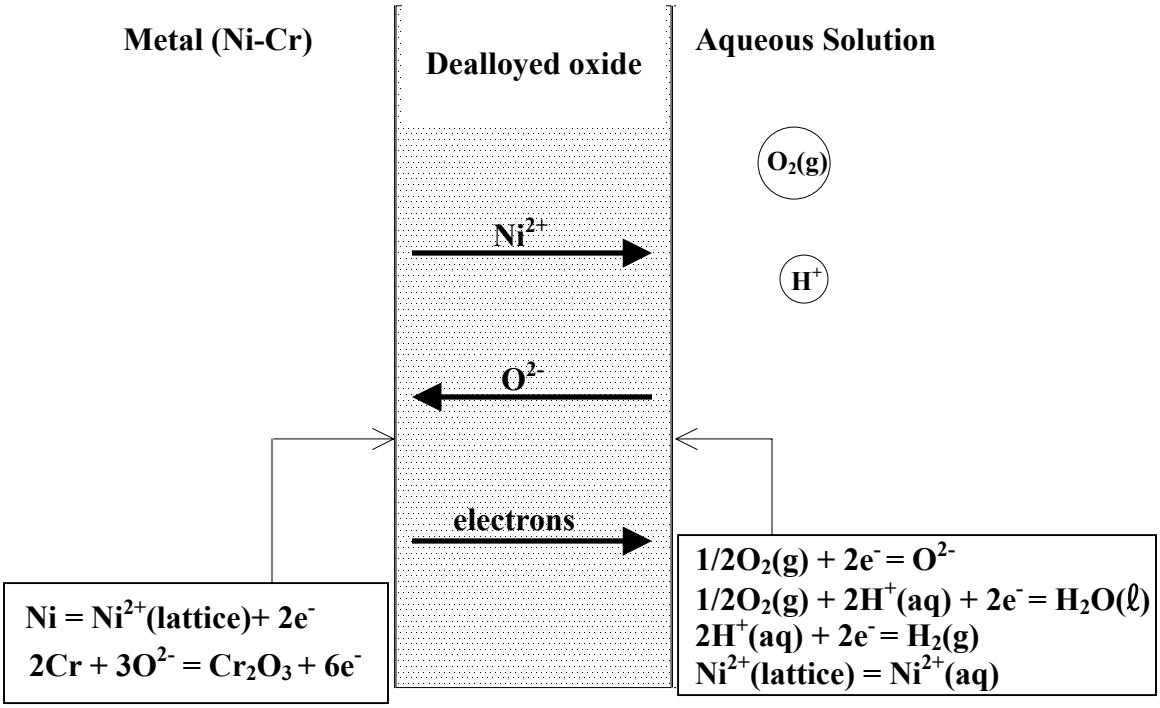

Figure 4.4 Simplified model of transport processes for the formation of the dealloyed oxide layer. Chemical reactions at the interfaces are shown inside the box.

Assumptions (1)-(3) and (6) are supported by experimental results. Other assumptions are made to facilitate the kinetic modeling of the oxide growth. Although these assumptions are essentially similar to those of Wagner's oxidation theory[30-34], the exposed environments are different from each other. In Wagner's oxidation theory, the environment is assumed gaseous oxygen and the oxide scale forms by the migrations of cations and/or anions. In this model, the environment is an aqueous solution which contains dissolved oxygen gas and hydrogen ions. In a stationary state, nickel ions migrate toward the oxide-solution interface and ultimately are transferred to the solution and as a result, selective dissolution of nickel from the metal substrate occurs. Oxygen ions migrate toward the metal-oxide interface through the dealloyed oxide layer and combine with the chromium to form chromium oxide at the metal-oxide interface. Although there might be a mass transfer resistance of nickel ions at the oxide-solution interface, this is neglected and only the migration of ions and electrons is considered as the rate-controlling process. The simplified transport processes of species are schematically drawn in Figure 4.4. Various interfacial reactions considered in this model are also listed in Figure 4.4. These interfacial reactions are not considered to be the rate controlling process and as a result, their kinetics are neglected as well.

As the ions and electrons are charged, they respond to both chemical and electrical potential gradients, which together provide the net driving force for their migration. The migration rates of cations, anions, and electrons are different from each other and cause an electric field to be established across the scale. A particle, i, carrying a charge, z_i, is acted on by a force, f, given by

$$f = -\frac{1}{N_A}\left(\frac{\partial \mu_i}{\partial x} + z_i F \frac{\partial \phi}{\partial x}\right) \quad \text{[J/cm/particle]} \tag{4.25}$$

where F is the Faraday constant, $\partial \mu_i / \partial x$ is the chemical potential gradient and $\partial \phi / \partial x$ is the electrical potential gradient. When ions are subjected to a directed force, they acquire a directed component of velocity (the drift velocity, v_d) under the assumption that the various particles migrate independently of each other. This drift velocity is in the direction of and proportional to the force:

$$v_d = -\frac{B_i}{N_A}\left(\frac{\partial \mu_i}{\partial x} + z_i F \frac{\partial \phi}{\partial x}\right) \quad \text{[cm/sec]} \tag{4.26}$$

where B_i is defined as the absolute mobility of an ion, i. The flux of the ion, i, acted on by the force given in equation (4.25), is

$$j_i = c_i v_d = -\frac{c_i B_i}{N_A}\left(\frac{\partial \mu_i}{\partial x} + z_i F \frac{\partial \phi}{\partial x}\right) \quad \text{[particle/cm}^2\text{/s]}. \tag{4.27}$$

where c_i is the concentration of the ion, i, in particles/cm^3.[30] In molar units,

equation (4.27) is written as

$$j_i = -\frac{c_i B_i}{N_A^2}\left(\frac{\partial \mu_i}{\partial x} + z_i F \frac{\partial \phi}{\partial x}\right) \quad [\text{mol/cm}^2/\text{s}] \,. \tag{4.28}$$

The relationship between the absolute mobility and its partial conductivity can be derived from the definition of conductivity.

$$I_i \equiv -\sigma_i \frac{\partial \phi}{\partial x} \tag{4.29}$$

$$I_i = (z_i F)\cdot j_i\big|_{\partial \mu_i / \partial x = 0} = -\frac{c_i B_i}{N_A^2}(z_i F)^2\left(\frac{\partial \phi}{\partial x}\right) \tag{4.30}$$

where I_i is the conduction current induced by an electric field, and σ_i is the partial conductivity of species i. From equations (4.29)-(4.30), the relationship between mobility and conductivity is obtained as

$$c_i B_i = \frac{\sigma_i}{z_i^2 e^2} \,. \tag{4.31}$$

Using equation (4.31), the flux of species i is expressed as

$$j_i = -\frac{\sigma_i}{z_i^2 F^2}\left(\frac{\partial \mu_i}{\partial x} + z_i F \frac{\partial \phi}{\partial x}\right) . \tag{4.32}$$

As the migrating ions are the nickel cation (Ni^{2+}), oxygen anion (O^{2-}), and electrons (e^-), the flux of the charged particles is as follows, respectively

$$j_c = -\frac{\sigma_c}{z_c^2 F^2}\left(\frac{\partial \mu_c}{\partial x} + z_c F \frac{\partial \phi}{\partial x}\right) \tag{4.33}$$

$$j_a = -\frac{\sigma_a}{z_a^2 F^2}\left(\frac{\partial \mu_a}{\partial x} + z_a F \frac{\partial \phi}{\partial x}\right) \tag{4.34}$$

$$j_e = -\frac{\sigma_e}{z_e^2 F^2}\left(\frac{\partial \mu_e}{\partial x} + z_e F \frac{\partial \phi}{\partial x}\right) \tag{4.35}$$

where subscripts c, a, and e represent Ni^{2+}, O^{2-}, and e^-. Because no net current flows through the dealloyed oxide layer during the stationary state, the electrical neutrality condition is imposed as

$$z_c j_c + z_a j_a + z_e j_e = 0 \,. \tag{4.36}$$

Before we proceed, it is convenient to define the transference number (or transport numbers), t_i of species i. The transference numbers are defined by the fractions of the current carried by charged species as

$$t_i = \left(\frac{I_i}{I_t}\right)_{\partial \mu_i / \partial x = 0} = \frac{I_i}{I_c + I_a + I_e} = \frac{\sigma_i}{\sigma_c + \sigma_a + \sigma_e} = \frac{\sigma_i}{\sigma_t} \tag{4.37}$$

$$\sum t_i = t_c + t_a + t_e = 1 \tag{4.38}$$

where I_t is the total current of an electrical potential gradient when there is no chemical potential gradient and σ_t is the total conductivity.[35] With the definition of the transference number, we can get the expression for the electrical potential gradient from equations (4.33)-(4.36) as

$$\frac{\partial \phi}{\partial x} = -\frac{1}{F}\left(\frac{t_c}{z_c}\frac{\partial \mu_c}{\partial x} + \frac{t_a}{z_a}\frac{\partial \mu_a}{\partial x} + \frac{t_e}{z_e}\frac{\partial \mu_e}{\partial x} \right). \tag{4.39}$$

By substituting equation (4.39) into equations (4.33)-(4.35), the flux of each species is obtained as

$$j_c = \frac{\sigma_c}{z_c F^2}\left(\frac{(t_c - 1)}{z_c}\frac{\partial \mu_c}{\partial x} + \frac{t_a}{z_a}\frac{\partial \mu_a}{\partial x} + \frac{t_e}{z_e}\frac{\partial \mu_e}{\partial x} \right) \tag{4.40}$$

$$j_a = \frac{\sigma_a}{z_a F^2}\left(\frac{t_c}{z_c}\frac{\partial \mu_c}{\partial x} + \frac{(t_a - 1)}{z_a}\frac{\partial \mu_a}{\partial x} + \frac{t_e}{z_e}\frac{\partial \mu_e}{\partial x} \right) \tag{4.41}$$

$$j_e = \frac{\sigma_e}{z_e F^2}\left(\frac{t_c}{z_c}\frac{\partial \mu_c}{\partial x} + \frac{t_a}{z_a}\frac{\partial \mu_a}{\partial x} + \frac{(t_e - 1)}{z_e}\frac{\partial \mu_e}{\partial x} \right). \tag{4.42}$$

Assuming local equilibrium is established inside the dealloyed oxide layer, we can further simplify the flux of charged particles. In view of the chemical equilibrium, it is assumed that local equilibrium exists between ions, electrons, and electrically neutral atoms as

$$Ni = Ni^{2+} + 2e, \qquad \mu_{Ni} = \mu_{Ni^{2+}} + 2\mu_e \tag{4.43}$$

$$O = O^{2-} - 2e, \qquad \mu_O = \mu_{O^{2-}} - 2\mu_e \tag{4.44}$$

where μ_{Ni} and μ_O are the chemical potentials of the electrically neutral reactants. Although the nickel is selectively dissolved from the metal substrate, the dealloyed oxide layer contains a residual amount of nickel with a constant concentration profile throughout the oxide layer. The residual amount of nickel is assumed to form a nickel oxide, NiO, which is also assumed to be in local equilibrium as follows:

$$NiO = Ni + O, \qquad \mu_{NiO} = \mu_{Ni} + \mu_O. \tag{4.45}$$

As the concentration of nickel is approximately constant throughout the dealloyed oxide layer (see Figures 3.18-19), it is assumed that the chemical potential of nickel oxide (NiO) is approximately constant throughout the dealloyed oxide layer in equation (4.45).

By taking the spatial derivative of the chemical potential we can obtain the following relations:

$$\frac{\partial \mu_{Ni}}{\partial x} = \frac{\partial \mu_{Ni^{2+}}}{\partial x} + 2\frac{\partial \mu_e}{\partial x} \tag{4.46}$$

$$\frac{\partial \mu_O}{\partial x} = \frac{\partial \mu_{O^{2-}}}{\partial x} - 2\frac{\partial \mu_e}{\partial x} \tag{4.47}$$

$$\frac{\partial \mu_{NiO}}{\partial x} = \frac{\partial \mu_{Ni}}{\partial x} + \frac{\partial \mu_O}{\partial x} = 0\,. \tag{4.48}$$

From local equilibrium, we can assign the charge number of migrating species to be $z_c = 2$, $z_a = -2$, and $z_e = -1$. By substituting equations (4.46)-(4.48) into equations (4.40)-(4.42) with assigned charge numbers, the following simple expressions for the particle flux are obtained as

$$j_c = \frac{t_e \sigma_c}{4F^2}\left(\frac{\partial \mu_O}{\partial x}\right) = -\frac{t_e \sigma_c}{4F^2}\left(\frac{\partial \mu_{Ni}}{\partial x}\right) \tag{4.49}$$

$$j_a = -\frac{t_e \sigma_a}{4F^2}\left(\frac{\partial \mu_O}{\partial x}\right) = \frac{t_e \sigma_a}{4F^2}\left(\frac{\partial \mu_{Ni}}{\partial x}\right) \tag{4.50}$$

$$j_e = -\frac{(t_e - 1)\sigma_e}{2F^2}\left(\frac{\partial \mu_O}{\partial x}\right) = \frac{(t_e - 1)\sigma_e}{2F^2}\left(\frac{\partial \mu_{Ni}}{\partial x}\right). \tag{4.51}$$

These expressions show that the flux of charged particles is proportional to their chemical potential gradient and conductivity.

The developments of a thick dealloyed oxide layer at the high subcritical temperatures and thin oxide at the supercritical temperatures imply that the thick dealloyed oxide can grow with the dealloying of nickel from the metal substrate. In order for the metal-oxide interface to shift toward the metal substrate, nickel at the metal-oxide interface should be ionized and leave the lattice site in the direction of oxide-solution interface, leaving behind vacancies at the metal-oxide interface. By the ionization and migration of nickel, new extra vacancies are generated at the metal-oxide interface, and via these vacancies, oxygen anions can migrate and form a new chromium oxide at the metal-oxide interface. These two steps seem to occur in order during the growth of the dealloyed oxide layer. Further, this is supported by the experimental result that no internal oxidation inside the metal substrate occurs (see Figure 3.19 and Table 3.7). Because the ionization and migration of nickel precedes the formation of the dealloyed oxide layer, the growth rate of the dealloyed oxide layer is controlled by the migration of nickel. The assumption that the migration of ions is the rate-controlling process implies that the interfacial reaction (ionization of nickel) is not the rate controlling process. As the growth of the dealloyed oxide layer is controlled solely by the migration of the nickel cation, the cation flux in

equation (4.49) is further considered in detail. Equation (4.49) represents the cationic flux at any place in the dealloyed oxide layer, where the partial conductivities and the chemical potential gradient are the instantaneous values at that place. Since all of these values may change with the position in the scale, it is necessary to integrate equation (4.49) in order to define j_c in terms of the scale thickness, x, and the measurable metal chemical potentials, $\mu_{Ni}^{'}$ (at the metal-oxide interface) and $\mu_{Ni}^{''}$ (at the oxide-solution interface), respectively, i.e.

$$j_c = -\frac{t_e \sigma_c}{4F^2}\left(\frac{\partial \mu_{Ni}}{\partial x}\right) \cong -\frac{1}{4F^2 x}\int_{\mu_{Ni}^{'}}^{\mu_{Ni}^{''}} t_e \sigma_c d\mu_{Ni} \quad [\text{mol/cm}^2\text{/s}]. \tag{4.52}$$

If the concentration of nickel in the oxide scale is C_{Ni} [mol/cm^3], the flux of nickel cations is also expressed as

$$j_c = C_{Ni}\frac{dx}{dt}. \tag{4.53}$$

From equations (4.52)-(4.53), we obtain the parabolic rate law for the dealloyed oxide layer growth as

$$\frac{dx}{dt} = -\frac{1}{4F^2 x C_{Ni}}\int_{\mu_{Ni}^{'}}^{\mu_{Ni}^{''}} t_e \sigma_c d\mu_{Ni} = \frac{k^{'}}{x} \quad [\text{cm/s}] \tag{4.54}$$

$$k^{'} = -\frac{1}{4F^2 C_{Ni}}\int_{\mu_{Ni}^{'}}^{\mu_{Ni}^{''}} t_e \sigma_c d\mu_{Ni} \qquad [\text{cm}^2\text{/s}] \tag{4.55}$$

$$x^2 = 2k^{'}t \tag{4.56}$$

where $k^{'}$ is the parabolic rate constant. In general, it is found that the transport number of electrons is close to unity, compared with which the transport numbers of cations or anions are negligibly small.[30, 32, 33] The transport number of electrons in equations (4.54)-(4.56) is set as unity in the following equations. The mobility, B_i, and diffusion coefficient of a species, D_i, are related by the Einstein equation

$$D_i = B_i kT \qquad [\text{cm}^2\text{/sec}] \tag{4.57}$$

where k is the Boltzmann constant and T is absolute temperature. From equation (4.31), the diffusion coefficient of nickel cation is expressed as

$$D_{Ni} = \frac{\sigma_c RT}{4F^2 C_{Ni}} \quad . \tag{4.58}$$

The resulting parabolic rate constant in equation (4.55) becomes

$$k^{'} = -\frac{1}{RT}\int_{\mu_{Ni}^{'}}^{\mu_{Ni}^{''}} D_{Ni} d\mu_{Ni}. \tag{4.59}$$

It is also assumed that the diffusion coefficient of nickel in the dealloyed chromium oxide layer is approximately constant for the chemical potential change. The chemical

potentials of nickel in chromium oxide in the high subcritical temperature range are not available in the literature and so they are approximated by assuming that the dealloyed oxide layer is an ideal solid solution of Cr-Ni-O. With these assumptions, the parabolic rate constant in equation (4.59) is approximated as

$$k' \approx -\frac{D_{Ni}}{RT}\left(\mu''_{Ni} - \mu'_{Ni}\right) \approx D_{Ni} \ln\left(\frac{X'_{Ni}}{X''_{Ni}}\right) \tag{4.60}$$

$$\mu_{Ni} = \mu^0_{Ni} + RT \ln(a_{Ni}) \approx \mu^0_{Ni} + RT \ln(X_{Ni}) \tag{4.61}$$

where X'_{Ni} is the mole fraction of nickel at the metal-oxide interface and X''_{Ni} is the mole fraction of nickel at the oxide-solution interface. Although the Inconel 625 reaction vessel is a complex alloy system, we approximate it as a binary Ni-Cr alloy, and the experimental results are used to estimate the diffusion coefficient of nickel in the dealloyed oxide layer. The self-diffusion coefficient of nickel in the literature in this temperature range is not appropriate in evaluating equation (4.60) because its value is too low in the high subcritical temperature range and the diffusion processes are occurring throughout the dealloyed oxide layer with a high concentration of defects. To estimate the diffusion coefficient of nickel in the dealloyed oxide layer, the Inconel 625 reaction vessel results are used.

If the chemical compositions of nickel and chromium from Inconel 625 (Table 3.7 for the substrate) are considered and normalized in atomic concentration, the resulting mole fractions of nickel and chromium are 0.7 and 0.3, respectively. The mole fraction of nickel, 0.7, is assigned to X'_{Ni}.

If the atomic concentrations of nickel, chromium, and oxygen in the dealloyed oxide layer are considered and normalized from Table 3.7, the resulting mole fractions are 0.026, 0.29 and 0.684, respectively. The mole fraction of nickel, 0.026, is assigned to X''_{Ni}.

Finally, the thickness of the dealloyed oxide layer, x, is determined by the measurement of the dealloyed oxide layer thickness in the high subcritical temperature range from Table 3.6 as 37.9 μm with the exposure time of 204.5 hours. It is noted that the kinetics model is being developed for plate sample geometry but experimental measurements of the dealloyed oxide layer thickness are measured using tubular geometry. This can be justified by the fact that the thickness of the dealloyed oxide layer

is quite small relative to the thickness of the tube, at a ratio of approximately 1/62. When the values obtained from experimental measurements are used to estimate the diffusion coefficient of nickel in the dealloyed oxide layer, it is estimated to be 3.0×10^{-12} cm^2/sec at 350°C, which is very high considering the system temperature of 350°C. Unfortunately, the actual measurement data for the diffusion coefficient of nickel in the dealloyed oxide layer are not available in the literature and data associated with similar systems of nickel migration in chromium oxide are also not available. Even with these limitations, the measured diffusivity data of the self-diffusion of nickel in NiO at high temperature are extrapolated to 350°C for a qualitative comparison.[33, 36-39]

It is noted that the self-diffusion coefficient of nickel in NiO was measured in the gaseous environment for a limited temperature range by the tracer technique. The diffusivity of Ni in NiO and the surface diffusivity of Ni on nickel are presented in Figure 4.5. When compared to the self-diffusion coefficient of nickel ion in NiO, the estimated diffusivity of nickel is about three orders of magnitude higher than the grain boundary diffusivity (Ni in NiO) at 350°C and about three orders of magnitude lower than the surface diffusivity of nickel (Ni on Ni surface). The surface diffusivity of Ni may provide an upper limit in estimating and comparing the diffusivity of Ni in the dealloyed oxide layer.

The high diffusivity in the dealloyed oxide layer may have several causes. First, the diffusion processes of nickel in the dealloyed oxide layer (primarily chromium oxide layer) are accelerated due to a high concentration of defects generated by the selective dissolution of nickel and formation of chromium oxide. Selective dissolution of nickel generates a high vacancy concentration in the oxide layer, and highly defective and somewhat amorphous dealloyed chromium oxide may contain a very high concentration of defects. The diffusivity of Ni in NiO in Figure 4.5 does not take into account the effect of severe dealloying of nickel from the metal substrate. Second, the electric field potential built throughout the dealloyed oxide layer, along with the defective structure, is thought to lower the activation energy for the diffusion of nickel significantly. Third, the high vacancy generated due to the selective dissolution of nickel can also generate di-vacancy which significantly increases the diffusivity of diffusing elements as indicated by Pickering and Wagner.[28] Fourth, the cold-working process of the Inconel 625 tube can increase the diffusivity of elements by forming finer grains near surface, and generating defects such as dislocations and voids. These finer grains with a high defect concentration in the cold-worked surface region provide easy diffusion paths.[40] Finally, the tensile stress along the tangential (hoop) direction may accelerate the diffusivity of nickel in the dealloyed oxide layer.

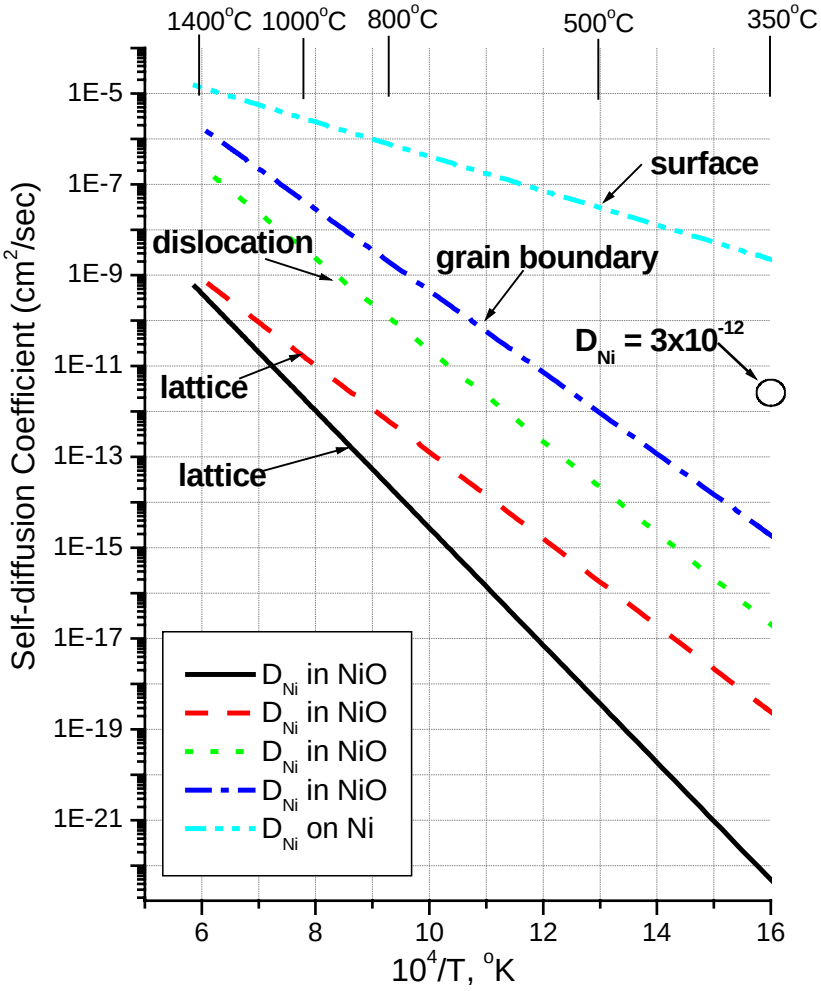

Figure 4.5 Reported values of self-diffusion of Ni in NiO. The hollow black circle is the estimated diffusion coefficient of Ni in dealloyed oxide layer at the high subcritical temperature. All the diffusivity is measured by the tracer technique with the exception of the calculated surface diffusivity.

Diffusivity in lattice (solid line): Atkinson and Taylor. 522-1400℃[38]

Diffusivity in lattice (dash line): Shim and Moore. 1000-1400℃[41]

Diffusivity in dislocation (dot line): Atkinson and Taylor. 522-800℃[38]

Diffusivity in grain boundary (dash-dot line): Atkinson and Taylor, 500-800℃[39]

Surface diffusivity (dash-dot-dot line): Agrawal et al.[37]

From the estimated diffusion coefficient of nickel in the dealloyed oxide layer, the growth rate is plotted as a function of time in Figure 4.6. Although we developed a simple parabolic growth rate of the dealloyed oxide layer, we cannot decide whether this parabolic law is accurate due to lack of the experimental data (only one data point as a function of time for the Inconel 625 reaction vessel). For this reason, the experimental data obtained from nickel-base wires are compared instead. Thus, the thickness data of Run#1-3 from Table 3.4 are superposed in Figure 4.6, which indicates that the growth rate of the Inconel 625 reaction vessel is faster than that of the wire samples of Run#1-3. This result comes from the system pressure, which acts as a tensile stress in the reaction vessel and acts as a compressive stress in the wire samples along the tangential direction, and the operational (chemical, thermal and mechanical) cycles of the system. The tensile stress stretches the lattice to facilitate the diffusion process while compressive stress may hinder the diffusion process. The result of C-22 wire sample in Figure 4.6 shows that the rate is fast at the initial stage, and then decreases at later stages. This result partly supports the validity the growth rate of the dealloyed oxide layer.

The simplified model described here implies that the nickel-base alloy can be more corrosion-resistant by increasing the chromium concentration, resulting in a more compact oxide layer. This occurs because the diffusivity of nickel in the more compact oxide layer is lowered due to a relatively low defect concentration and higher activation energy for the diffusion process. In the same way, molybdenum can be conducive to forming a more compact oxide to increase the corrosion resistance.

This model is characterized by a simple parabolic rate law, derived from assumptions at the beginning of this section. It is worthwhile to note the validity of these assumptions in brief. We assumed that particles migrate independently of each other and local equilibria exist within the dealloyed oxide layer. These assumptions might be valid in a limiting case, and in a detailed treatment it is necessary to use general transport equations of irreversible thermodynamics as a basis.[31, 33, 42] However, due to the limited thermodynamic data and the complexity of the alloy and oxide system, it appears that this simplified model gives an adequate description of the dealloyed oxide layer in the high subcritical temperature range within the accuracy of the experimental results.

In the supercritical temperature range, both nickel and chromium form stable oxides without dealloying. Due to the relatively low temperature, the growth rate of the oxide is slow. In addition, various alloying elements may participate in the formation of the oxide. Although the temperature is higher than the high subcritical temperature, the absence of dealloying seems to make the oxidation kinetics sluggish relative to that of the subcritical temperatures. A large number of theories and models such as a point defect model[43-50]

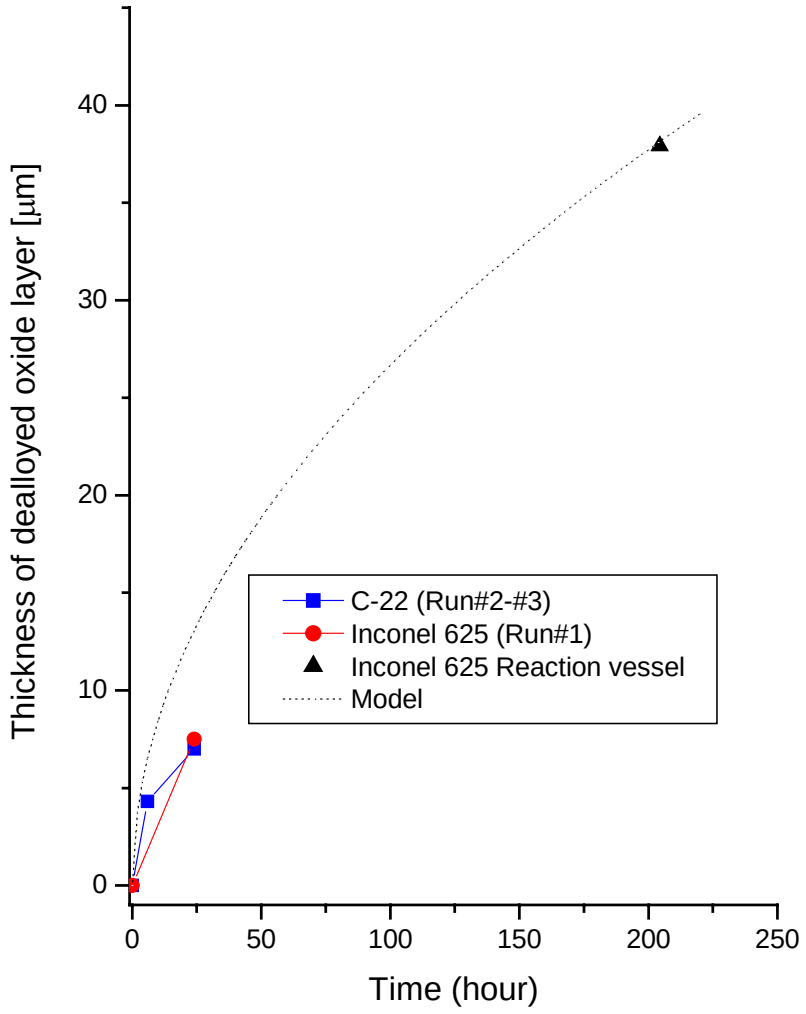

Figure 4.6 Comparison between dealloyed oxide layer growth rates of Run#1-3 and Inconel 625 reaction vessel. The dotted line is obtained from the modeling of the Inconel 625 reaction vessel with single data point designated by ▲. Data points obtained from Run#1 (Inconel 625 wire) are designated by the red circle. Data points obtained from Run#2-3 (C-22) are designated by the blue square.

have been put forward to explain the kinetics of low temperature oxidation of metals and particularly the logarithmic oxidation behavior. In many cases it is difficult and even impossible to verify the validity and the correctness of the various models and the parameters involved in the equations derived. Most of the theories also assume the existence and formation of uniform oxide films, but this is not always a generally acceptable assumption. The detailed chemical composition (deviating from

stoichiometry) of oxide films and the nature of defects in the films are not easily studied and are not well known, and these factors may also be a function of surface orientation, surface preparation, impurities etc. As thin film formation at low temperatures involves rapidly changing systems under conditions in which thermal diffusion is slow, thermodynamic calculations of the defect concentration in oxides are also questionable. For these reasons and because of the experimental difficulties involved, low temperature oxidation is still not well understood.[33]

4.3 Stress development

In SCWO systems, the stress might develop from several sources: the residual stress during the fabrication of alloys, stress from the operating system pressure, thermal stresses, and stress developed during oxide formation. Thermal stresses can develop from the temperature gradient in the reaction vessel during the system operation and from the thermal cycles (heating and cooling down) of the system. Although the residual stress is important in causing SCC, it is difficult to analyze accurately, namely because the residual stress depends on the processing history of the alloy in various shapes, including the heat treatment, cold work, welding etc. The detailed processing history of the alloy is not provided and the analysis of the stress developed from these processes is highly complex and uncertain. Nevertheless, the residual component of stress is considered as a potential source in causing SCC of alloys. Other sources of stress, operating system pressure, growth stresses, and thermal stress are analyzed to estimate the amount of stress in detail.

4.3.1 Stress from operating system pressure

Stress generated from the operating system pressure can be estimated from its tubular geometry with an operating system pressure of 24.14 MPa (3500psi). The geometry of the reaction vessel and the components of stress are shown in Figure 4.7 (a). From the theory of elasticity, each component of stress in the reaction vessel is derived in the literature[51] as

$$\sigma_r = \frac{a^2 b^2 (p_o - p_i)}{b^2 - a^2} \frac{1}{r^2} + \frac{p_i a^2 - p_o b^2}{b^2 - a^2} \tag{4.62}$$

$$\sigma_\theta = -\frac{a^2 b^2 (p_o - p_i)}{b^2 - a^2} \frac{1}{r^2} + \frac{p_i a^2 - p_o b^2}{b^2 - a^2} \tag{4.63}$$

where σ_r is the radial stress, σ_θ is the tangential stress, a is the inner radius of the cylinder, b is the outer radius of the cylinder, r is the distance from the center of the

cylinder, p_o is the external pressure, and p_i is the internal pressure of the cylinder. The stress distribution for the geometry of the Inconel 625 reaction vessel is shown in Figure 4.7, which also shows that the stress component along the tangential direction is tensile and maximized at the inner surface at 39.95 MPa. The stress component along the radial direction is compressive and decreases continuously.

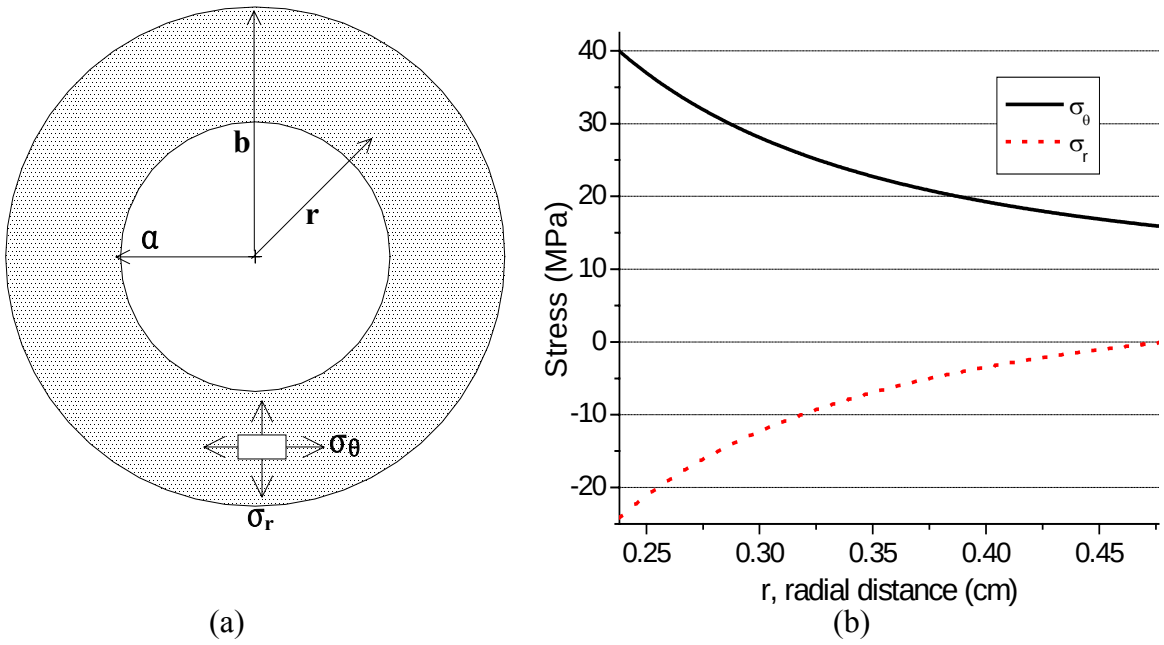

Figure 4.7 Stress of the reaction vessel by the operating system pressure. (a) Inconel 625 reaction vessel cross section, with a=0.238㎝, b=0.476㎝. (b) calculated stress components along the radial distance.

4.3.2 Thermal stress from the temperature gradient

When there exists a temperature gradient in the reaction vessel during the system operation, thermal stress can develop in the reaction vessel. In experiments, the temperature was measured at the outside of the reaction vessel using thermocouples. Although the thermal conductivity of the Inconel 625 is high, there is a temperature gradient along the radial direction of the reaction vessel. Before the thermal stress is analyzed, the temperature gradient along the radial direction is considered with a simple model.

The temperature distribution along the radial direction can be obtained from the energy conservation equation, which considers only thermal effects:

$$\rho C_p \frac{DT}{Dt} = k\nabla^2 T + H_V \tag{4.64}$$

where ρ is the density, C_p is the specific heat capacity, k is the thermal conductivity, and H_V is the heat source term, which represents the rate of energy input from external power sources per unit volume.[52] During steady state system operation, the temperature has no time dependence and no heat source exists in the reaction vessel. Furthermore, the cylindrical geometry of the reaction vessel simplifies the conservation equation because temperature has no dependence on the angle, θ. As a result, the conservation equation in (4.64) simplifies to

$$\frac{1}{r}\frac{\partial}{\partial r}\left(r\frac{\partial T}{\partial r}\right) = 0\,. \tag{4.65}$$

The heat conduction along the z-direction has been neglected due to its uncertainty in this analysis and heat conduction only in the plane of the cross section is considered. To solve this equation, two boundary conditions are imposed as

$$T(r=b) = T_b \tag{4.66}$$

$$q_r(r=b) = -k\nabla T\,|_{r=b} = h(T_b - T_R)\,. \tag{4.67}$$

where b is the outer radius of the tube, as defined in Figure 4.7 (a), T_b is the temperature at the outer surface of the tube, q_r is the heat flux at the outer surface ($r = b$), and h is the heat transfer coefficient of the reaction vessel and assumed to be known. Because thermal steady state is established, the heat flow at any radial position is constant:

$$Q = 2\pi r q_r = \text{constant}. \tag{4.68}$$

The boundary condition in (4.66) is directly measured using thermocouples and assumed to be constant during the steady state operation of the system. The boundary condition in (4.67) is obtained by assuming that heat is transferred to the air by natural convection. With these two boundary conditions, the differential equation in (4.65) is solved as

$$T(r) = T_b + (T_b - T_a)\frac{\ln(r/b)}{\ln(b/a)} \tag{4.69}$$

$$T_a = T_b + Bi(T_b - T_R)\ln(b/a) \tag{4.70}$$

where a is the inner radius of the reaction vessel, T_a is the temperature at the inner surface of the reaction vessel, T_R is the room temperature, and Bi is the dimensionless Biot number, which represents the ratio of the heat transfer resistance within the reaction vessel to that within the surrounding air, defined as

$$Bi \equiv \frac{h \cdot b}{k}. \tag{4.71}$$

To get the temperature distribution in the reaction vessel, the heat transfer coefficient, h, for natural convection is obtained from the literature [53] and has the numeric value of 17.6 (W/m^2/K) approximately. The thermal conductivities of Inconel 625 from the literature are 9.8 (W/m/K) at 21°C and 17.5 (W/m/K) at 538°C.[54] The actual conductivities of Inconel 625 are interpolated linearly from the literature data. Therefore, when the measured temperature is 353°C, the thermal conductivity is 14.74 (W/m/K), the Biot number is 0.0057 and T_a is 354.3°C. In the same way, when the measured temperature is 426°C, the thermal conductivity is 15.83 (W/m/K), the Biot number is 0.0053 and T_a is 427.5°C. Because of a small Biot number, which comes from the high thermal conductivity of Inconel 625 and a small radius of the reaction vessel, the temperature difference between the inner surface and outer surface is not significantly large. Using the temperature distribution in equation (4.69), the thermal stress in the reaction vessel can be estimated.

The stress component developed by the temperature gradient is derived in the literature from the theory of elasticity [51] as

$$\sigma_r = \frac{\alpha E(T_a - T_b)}{2(1-\nu)\ln(b/a)}\left(-\ln(b/r) - \frac{a^2}{b^2-a^2}(1-\frac{b^2}{r^2})\ln(b/a)\right) \qquad (4.72)$$

$$\sigma_\theta = \frac{\alpha E(T_a - T_b)}{2(1-\nu)\ln((b/a)}\left(1-\ln(b/r) - \frac{a^2}{b^2-a^2}(1+\frac{b^2}{r^2})\ln(b/a)\right) \qquad (4.73)$$

where E is the elastic modulus, α is the thermal expansion coefficient, and ν is Poisson's ratio. Equations (4.72)-(4.73) are derived with the plane strain condition (zero axial strain, $\varepsilon_z = 0$), zero axial force, and the temperature at any distance r in equation (4.69). To estimate the stress, the following physical constants are used; Poisson's ratio is 0.278 at 21°C (annealed Inconel 625)[54], the thermal expansion coefficient is 15.21× 10^{-6} at 400°C, and the elastic modulus is 190 GPa at 400°C[55]. The above thermal analysis indicates a temperature difference between two surfaces of about 1.5°C. Based on these conditions, the stress distribution is calculated and shown in Figure 4.8 which indicates that the radial stress is compressive at all points and becomes zero at the inner and outer surfaces of the reaction vessel. Furthermore, the tangential stress has its largest numerical values at the inner and outer surfaces of the reaction vessel and is compressive at the inner surface at -3.7MPa, and tensile at the outer surface at 2.3 MPa.

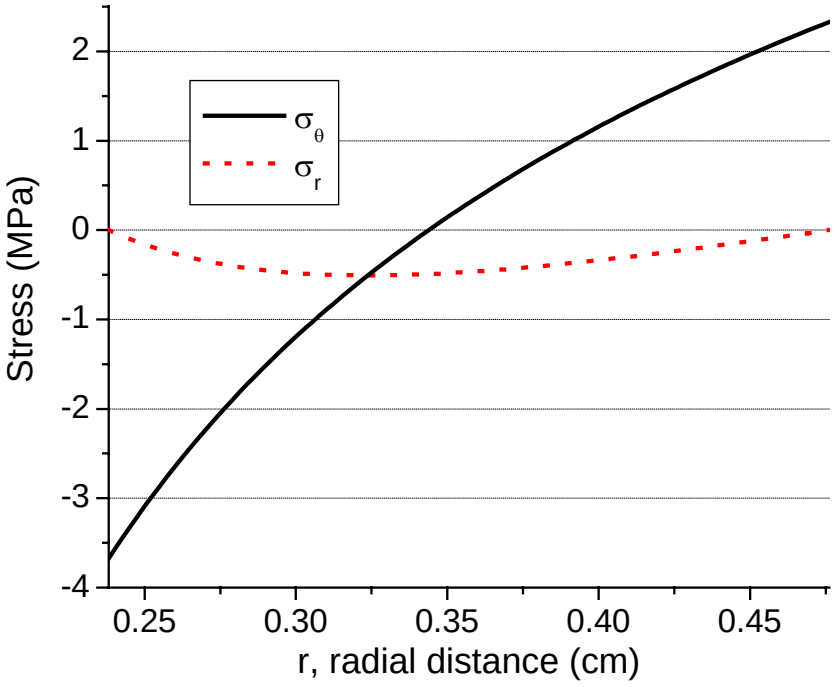

Figure 4.8 Stress of the reaction vessel with respect to a temperature gradient.

4.3.3 Thermal stress from cool-down of the system

When the thick dealloyed oxide layer in the subcritical temperature range develops during the operation of the system in an acidic environment, the oxide phase has different thermal expansion coefficients from the metal substrate. These different thermal expansion coefficients of metal and oxide can induce thermal stress during the cool-down of the system. To derive thermal stresses in an analytical expression from the theory of elasticity, the dealloyed oxide layer is assumed to be uniform and adherent to the metal substrate. We also assume that the dealloyed oxide phase and the metal substrate are isotropic. Plate geometry is first considered for clarity and then tubular geometry is considered as shown in Figure 4.9. When the temperature is in the subcritical temperature range during the operation, no thermal stress is induced initially by neglecting the temperature gradient in the reaction vessel. However, by cooling down the system, the thermal stress is induced due to different thermal expansion coefficients. For the plate geometry in Figure 4.9 (a), the stress-strain relation along the x-axis is obtained using Hooke's law, which is generalized to include thermal effects for isotropic materials, as

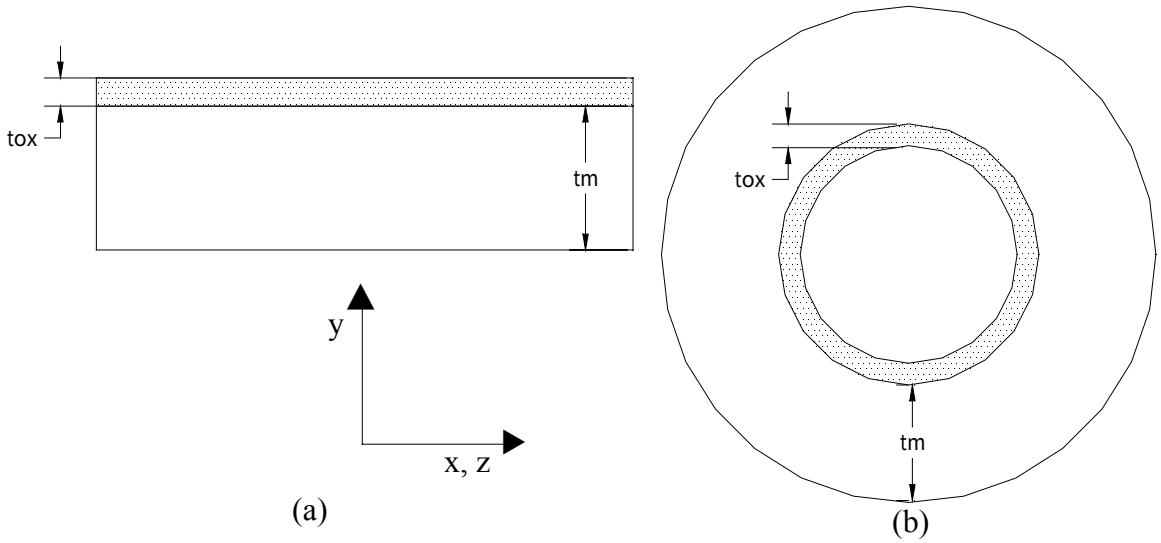

Figure 4.9 Simplified picture for the dealloyed oxide layer formed on the metal substrate. (a) Cartesian coordinates (b) Polar coordinates.

$$\varepsilon_x = \frac{1}{E}\left(\sigma_x - \nu(\sigma_y + \sigma_z)\right) + \alpha\Delta T\,. \tag{4.74}$$

where ΔT is the temperature difference between the initial and final temperature. Assuming that the plate is in an equi-biaxial stress state in the x-z plane and there is no confinement in the y-direction, we obtain

$$\sigma_x = \sigma_z = \sigma\,,\quad \sigma_y = 0\,. \tag{4.75}$$

As a result, the strain in the x-direction simplifies to

$$\varepsilon_x = \frac{1}{E}(1-\nu)\sigma + \alpha\Delta T\,. \tag{4.76}$$

Equation (4.76) holds for both the oxide and the metal substrate. By imposing the isostrain condition for the oxide and the metal substrate for small discrete temperature changes, we can get the following relation:

$$\frac{1}{E_{ox}}(1-\nu_{ox})d\sigma_{ox} + \alpha_{ox}dT = \frac{1}{E_m}(1-\nu_m)d\sigma_m + \alpha_m dT \tag{4.77}$$

where subscript ox represents the oxide, subscript m represents the metal substrate, and the stress represents the stress in the x-direction. The static force balance equation in the x-direction is expressed as

$$d\sigma_{ox}t_{ox}\cdot 1 + d\sigma_m t_m \cdot 1 = 0 \tag{4.78}$$

where t_{ox} is the thickness of the oxide and t_m is the thickness of the metal substrate as

in Figure 4.9(a). Combining equations (4.77)-(4.78), we can obtain the expression of the average stress developed for a small change of temperature as

$$d\sigma_{ox} = -\frac{(\alpha_{ox} - \alpha_m)}{\left(\frac{1-\nu_{ox}}{E_{ox}}\right) + \left(\frac{1-\nu_m}{E_m}\frac{t_{ox}}{t_m}\right)} dT \tag{4.79}$$

$$d\sigma_m = \frac{\alpha_{ox} - \alpha_m}{\left(\frac{1-\nu_m}{E_m}\right) + \left(\frac{1-\nu_{ox}}{E_{ox}}\frac{t_m}{t_{ox}}\right)} dT\,. \tag{4.80}$$

By integrating these equations from T_i to T_f, the average stress developed in the oxide and metal substrate is obtained as

$$\sigma_{ox} = -\int_{T_i}^{T_f} \frac{(\alpha_{ox} - \alpha_m)}{\left(\frac{1-\nu_{ox}}{E_{ox}}\right) + \left(\frac{1-\nu_m}{E_m}\frac{t_{ox}}{t_m}\right)} dT \tag{4.81}$$

$$\sigma_m = \int_{T_i}^{T_f} \frac{\alpha_{ox} - \alpha_m}{\left(\frac{1-\nu_m}{E_m}\right) + \left(\frac{1-\nu_{ox}}{E_{ox}}\frac{t_m}{t_{ox}}\right)} dT\,. \tag{4.82}$$

In the same way, the tangential component of the stress generated by the thermal cooling of the system (refer to Figure 4.9 (b)) is obtained for cylindrical coordinates as

$$\sigma_{ox} = -\int_{T_i}^{T_f} \frac{(\alpha_{ox} - \alpha_m)}{\left(\frac{1}{E_{ox}}\right) + \left(\frac{1}{E_m}\frac{t_{ox}}{t_m}\right)} dT \tag{4.83}$$

$$\sigma_m = \int_{T_i}^{T_f} \frac{\alpha_{ox} - \alpha_m}{\left(\frac{1}{E_m}\right) + \left(\frac{1}{E_{ox}}\frac{t_m}{t_{ox}}\right)} dT\,. \tag{4.84}$$

To obtain the average stress due to the cool-down of the system, the initial temperature and final temperature are assigned as 353℃ and 25℃, respectively and the thickness of the dealloyed oxide layer as 37.9㎛ based on experimental results in Table 3.6. Although the temperature dependence on physical constants of Inconel 625 and the dealloyed oxide layer is not available for a wide temperature range, the temperature dependence on physical constants are reported in the literature for Ni-30Cr alloy and Cr_2O_3.[55] These are listed in Table 4.1 and interpolated linearly to give

Table 4.1 Values of the α and E as a function of temperature for Cr_2O_3 and Ni-30wt%Cr.[55]

T (℃)	α_m (10^{-6}/K)	α_{ox} (10^{-6}/K)	E_m (GPa)	E_{ox} (GPa)
900	18.00	6.77	165	215
800	17.49	6.65	170	225
700	16.92	6.53	175	235
600	16.35	6.40	180	245
500	15.78	6.28	185	255
400	15.21	6.16	190	267
300	14.64	6.03	195	282
200	14.07	5.91	200	297
100	13.50	5.79	205	307
20	13.00	5.70	210	314

$$\alpha_{ox} = 5.67 \times 10^{-6} + 1.23 \times 10^{-9} \cdot T(^oC) \quad (4.85)$$

$$\alpha_m = 12.93 \times 10^{-6} + 5.7 \times 10^{-9} \cdot T(^oC) \quad (4.86)$$

$$E_{ox} = 316.77 - 0.1163 \cdot T(^oC) \quad (4.87)$$

$$E_m = 210.34 - 0.0505 \cdot T(^oC) \quad (4.88)$$

where the elasticity of modulus, E, has units of GPa and linear thermal expansion coefficient, α, has units of $℃^{-1}$ or K^{-1}.

From these data, the resultant average stress developed after cooling to room temperature has a numeric value of –764MPa (compressive) in the oxide phase and 12.4 MPa (tensile) in the metal substrate. Because the metal substrate has a larger thermal expansion coefficient than oxide, the metal substrate is in a tensile stress state and the oxide is in a compressive stress state after cooling to room temperature. It is noted that the stress level we obtained here is the average uniform stress in each phase, which does not consider the stress gradient in the oxide and the metal substrate. From more detailed modeling in the oxide-metal systems using a finite element method, it was found that the local stress at the interface can reach up to nine times the average stress of the metal substrate.[56] In contrast, the stress in the oxide is known to be fairly uniform because the thickness of the oxide is very small relative to that of the metal substrate.[56, 57]

Note that the tensile thermal stress in the metal substrate near the interface can reach up to 111.6 MPa (9×12.4MPa).

4.3.4 Growth stress

The parameter which is commonly invoked as being responsible for the generation of stresses during the oxide growth is the Pilling and Bedworth ratio (PBR). PBR is defined as the ratio of the oxide molar volume to that of the metal which provides the oxide. Pilling and Bedworth assumed that the oxide growth takes place through inward diffusion of oxygen through the oxide scale and thus that the oxide formation take place at the metal/scale interface. If the PBR is smaller than 1, the growth stress in the oxide will be tensile. Furthermore, the oxide will fail to cover the entire metal surface and should accordingly be non-protective. If the PBR is larger than 1, the stresses in the oxide will be compressive, and the oxide can be protective. In particular, at the grain boundary the oxide growth rate is accelerated and volumetric expansion may affect crack growth. Table 4.2 gives values of the oxide to metal volume ratio of some metal-oxygen systems.[33]

In the case of nickel-base alloy systems, the PBR is greater than 1 because the major alloying elements of Ni, Cr, Mo and Fe have PBR values larger than 1. In the case of isotropic materials, the volumetric deformation given by the PBR would be equal to

$$\varepsilon_v = [(PBR)^{1/3} - 1]. \tag{4.89}$$

It was indicated that, in order to calculate reasonable oxide stresses due to the volumetric deformation, it is necessary to add a correction factor w to equation (4.89)[57]:

$$\varepsilon_v = w[(PBR)^{1/3} - 1]. \tag{4.90}$$

Table 4.2 Oxide to metal volume ratios (PBRs) of some metal-oxygen systems.[33]

Oxide	PBR	Oxide	PBR
K_2O	0.45	NiO	1.65
MgO	0.81	FeO	1.7
SiO_2(cristobalite)	2.15	CoO	1.86
ZnO	1.55	Cu_2O	1.64
Al_2O_3	1.28	Ta_2O_5	2.5
Cr_2O_3	2.07	TiO_2	1.73

This correction factor indicates that simple volumetric ratio between the oxide and the metal substrate does not give reasonable stress developing by the oxide growth. The actual growth stress may depend on the detailed oxidation mechanisms, stress relaxation mechanisms and various factors such as surface roughness and geometry of the sample.

The development of compressive stress in the oxide at the supercritical temperatures is quite possible because each element can form a stable oxide at this temperature range. However, the growth stress in the dealloyed oxide layer at the subcritical temperature may not develop in the sense that the oxide formation is always accompanied by the selective dissolution of the nickel from the metal substrate. Although an accurate calculation of PBR is not feasible for the dealloyed oxide layer and the metal substrate, experimental observations support that the growth stress developed in the dealloyed oxide layer might be negligible. Experimental results in Table 3.7 show that the dealloyed oxide layer contains 2.45 at% nickel and 63.63 at% oxygen. Considering that the atomic concentration of nickel is 60.72 in the metal substrate, the oxygen atoms are likely to substitute the position of the nickel atoms and as a result, there seems to be no significant volume expansion in the dealloyed oxide layer.

Table 4.3 Stress analysis of Inconel 625 reaction vessel.

	Subcritical (T~353℃)	**Supercritical (T~426℃)**
Stress by system pressure	39.95 MPa	39.95 MPa
Thermal gradient stress	-3.7 MPa	-3.7 MPa
Thermal cycling stress	9×12.4 MPa = 111.6 MPa	Not considered
Growth stress	Not significant	Might be significant
Residual stress	Not identified	Not identified
Chemical environment	H^+, Cl^-. Dissolved oxygen	Associated HCl molecules. Dissolved oxygen.
Yield strength	490 MPa at 21℃ and 405 MPa at 540℃[54]	
Tensile strength	855 MPa at 21℃ and 745 MPa at 540℃[54]	

4.4 Stress Corrosion Cracking (SCC)

Stress corrosion cracking (SCC) is the brittle failure at relatively low constant tensile stress of an alloy exposed to a corrosive environment. It is thought that three conditions must be present simultaneously to produce SCC: a critical environment, a susceptible

alloy and some component of tensile stress. Experimental results of the Inconel 625 reaction vessel and the C-276 tube at Penn State University show that SCC occurs in both the high subcritical temperature and supercritical temperature ranges of the acidic environment. We discussed the origins of stresses in the SCWO systems and estimated some components of the stresses summarized in Table 4.3. Although SCC is observed both at the supercritical and the high subcritical temperatures, the mechanisms of crack development seem different from each other. The development of SCC at each temperature range is considered in this section.

4.4.1 SCC in the supercritical temperature range

The phenomenological model in 4.2.1 showed that the HCl solution does not dissociate strongly in the supercritical temperature range. The aqueous solution consists of associated HCl molecules in a high concentration with dissolved oxygen at the supercritical temperature. The low value of the dissociation constant of HCl resulted in the low hydrogen ion concentration (high pH) and suppressed the dealloying of nickel from the metal substrate. Consequently, the general corrosion behavior at this temperature range is considered to be thin oxide formation of each constituent element. The facts that SCC is developed in the acidic environment (Figure 3.13) and no SCC is developed in the neutral environment (Figures 3.21-22 (a)) at the supercritical temperature, suggest that low hydrogen ion concentration does not mean the the material is not susceptible to SCC. The associated HCl molecules at the supercritical temperature can attack the metal and/or the oxide directly according to

$$M + 2HCl(associated) = MCl_2 + H_2(g) \qquad (4.91)$$

where M is the metallic element of the substrate.[3] Although accurate stress analysis is difficult due to uncertainties and complexity in the system, the development of the tensile stress is apparent. With no dealloying, the growth stress during the oxidation may be significant at this temperature range along with other components of stresses such as system pressure and residual stress as shown in Table 4.3. The susceptible chemical environment of the supercritical water (associated HCl molecules and oxygen) and the presence of the tensile stress are thought to initiate the crack at the local defect sites of the surface. Because the SCC is developed inside the cold-worked surface region, the crack path is not distinguished between being transgranular or intergranular. Various mechanisms of SCC have been proposed in the literature, however, a satisfactory mechanistic model of SCC has not been developed due to the complex and combined effects between the corrosive environments, susceptible materials, and stresses.

In the present discussion, it is emphasized that once the crack or local defects are

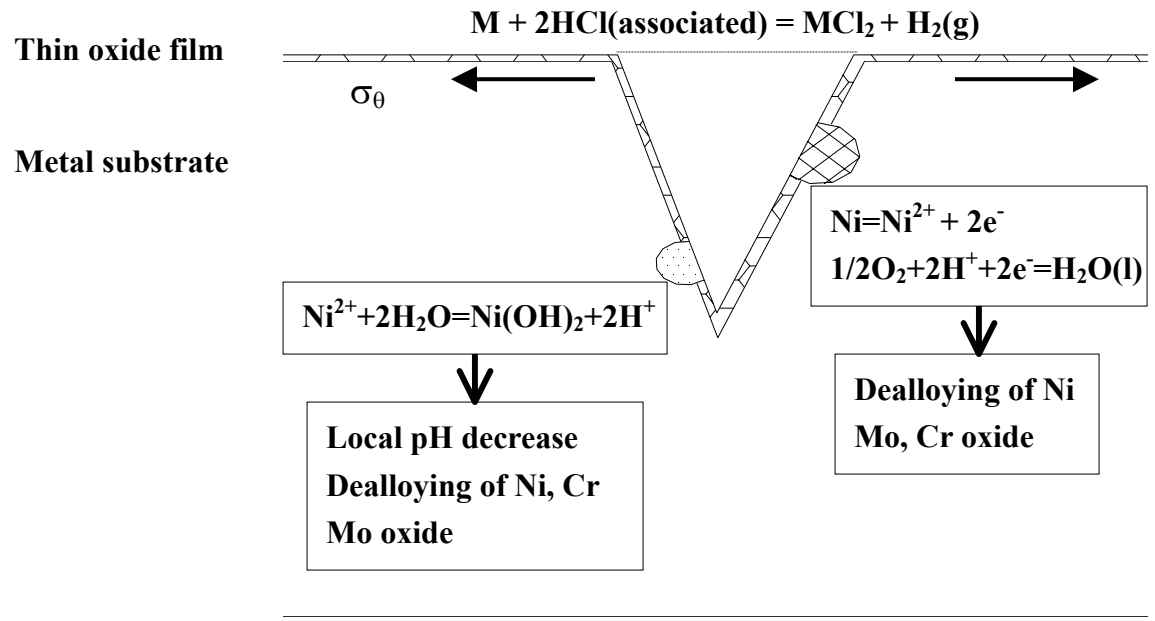

(a) SCC at the supercritical temperature. Local chemistry change is shown.

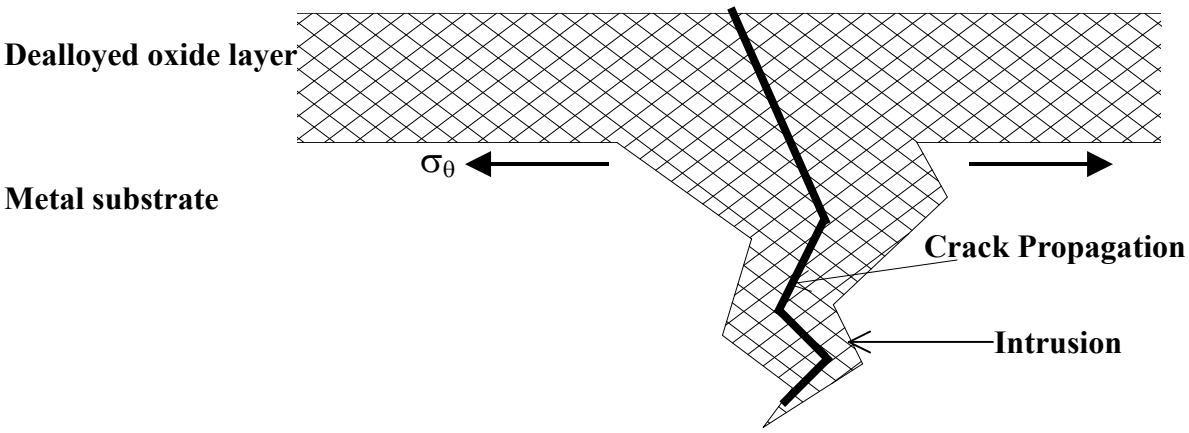

(b) SCC at the high subcritical temperature.

Figure 4.10 SCC in the Inconel 625 reaction vessel (schematic).

initiated at the surface, the local chemistry of the aqueous solution inside the crack can be significantly different from the bulk solution. In the specific example of the Inconel 625 reaction vessel, slight dealloying of nickel is observed inside the crack (left-hand X-ray mappings in Figure 3.13 (a)). This phenomenon occurs because the retained HCl solution at supercritical temperature passes through the subcritical temperature ranges during the thermal cycling of the system, and as a result the associated HCl molecules dissociate strongly and acidify the local chemistry inside the crack. The molal concentration of the hydrogen ion may reach 0.01molality (molal pH 2) after the dissociation reaction of HCl molecules. The reactions involving the dealloying of nickel inside the crack during the thermal cycle are as follows:

$$Ni = Ni^{2+} + 2e^{-} \tag{4.92}$$

$$\tfrac{1}{2}O_2 + 2H^{+} + 2e^{-} = H_2O(\ell)\,. \tag{4.93}$$

The dissolved nickel cation inside the localized crack can react with the water molecules according to the reaction:

$$Ni^{2+} + 2H_2O = Ni(OH)_2 + 2H^{+}\,. \tag{4.94}$$

This reaction shows that the dissolved nickel cation can react with water to form a hydroxide, and as a result acidify the local environment by producing the hydrogen ion. Due to the reaction in (4.94), chromium can also be dissolved in a more acidified environment near the bottom of the crack tip as shown in right-hand X-ray mappings in Figure 3.13 (a). The isolated geometry of the crack and thermal and mechanical cycle of the system can also be factors in accelerating the crack propagation. These processes are schematically drawn in Figure 4.10 (a).

4.4.2 SCC in the high subcritical temperature range

Experimental results in Figure 3.16 show that the development of SCC in the high subcritical temperature range is strongly associated with thick dealloyed oxide layer formation. The phenomenological model in 4.2.1 showed that the HCl solution dissociates strongly in the subcritical temperature range and that the molal pH value is ~2. In other words, the aqueous solution consists of H^{+}, Cl^{-} in a high concentration with dissolved oxygen. Recall that the chemical environment of molal pH ~2 at this temperature range resulted in the formation of the dealloyed oxide layer, which grows along the grain boundary with an accelerated rate to form intrusions. Because the cracks are developed along these intrusions along the grain boundaries, SCC can be termed intergranular stress corrosion cracking (IGSCC). The rudimentary stress analysis of the reaction vessel in section 4.3 is summarized in Table 4.3 for tangential components of

stress. Table 4.3 also shows that the largest tensile component of stress is the stress induced by the operating system pressure (39.95MPa). This stress induced by the temperature gradient in the reaction vessel is –3.7MPa and compressive. In addition, the stress induced by the temperature gradient does not assist in the development of cracks. Although the average tensile stress in the metal substrate induced by thermal cycling of the system is 12.4 MPa and less than the tensile stress by system pressure, the maximum stress at the interface can be nine times higher than the average stress, as discussed in section 4.3.3.[56] As a result, the maximum tensile component of stress by thermal cycling can be 111.6MPa. The total tensile stress is estimated to be 147.9MPa by summation and is about 30% of the yield strength at 21℃ and 37% of the yield strength at 540℃. In estimating total tensile stress, the residual stresses, originating from the processing history of the materials, are not considered. These residual stresses, generated during cold-working, welding etc., are identified to have considerable effect in the SCC in many systems.[29, 58] Because intrusions of the dealloyed oxide grow along the grain boundaries, intrusions are considered to have strongly non-uniform stresses[59, 60] in the presence of the tensile component of stress. As a result, cracks are initiated and propagate along the grain boundaries due to non-uniform stresses around intrusions as schematically shown in Figure 4.10 (b).

It is noted that there can be two possible ways the initiation and propagation of the cracks can occur in the high subcritical temperature range. First, the dealloyed oxide layer grows along the grain boundary deeply into the substrate to form an intrusion. The instability of local stress near the intrusion can initiate and propagate the cracks along the grain boundaries. Second, the dealloyed oxide layer grows uniformly, with a rather rugged morphology at the metal-oxide interface. Then, cracks are initiated along the grain boundaries. If the cracks are initiated along the grain boundaries, the corrosive aqueous solution penetrates into the crack and is in direct contact with the fresh metal surface, and therefore, can attack the fresh metal surface directly. Consequently, the fresh metal surface is attacked by an acidic solution at the high subcritical temperature and the dealloyed oxide layer is formed along the grain boundaries. This dealloyed oxide layer formation may accelerate the propagation of the crack.

Bibliography

1. Mitton, D.B., P.A. Marrone, and R.M. Latanision, *Interpretation of the Rationale for Feed Modification in SCWO systems.* J. Electrochem. Soc., 1996. **143**(3): p. L59-L61.

2. Kriksunov, L.B. and D.D. Macdonald, *Potential-pH Diagrams for Iron in Supercritical Water.* Corrosion, 1997. **53**(8): p. 605-611.
3. Kriksunov, L.B. and D.D. Macdonald, *Corrosion in supercritical water oxidation systems: A phenomenological analysis.* Journal of the Electrochemical Society, 1995. **142**(12): p. 4069-4073.
4. Bockris, J.O.M. and A.K.N. Reddy, *Modern Electrochemistry*. An introduction to an Interdisciplinary Area. Vol. 1. 1970, New York: Plenum Press.
5. Atkins, P.W., *Physical Chemistry, 6th Edition*. 1998. 1014 pp.
6. Mesmer, R.E., et al., *Thermodynamics of Aqueous Association and Ionization Reactions at High Temeratures and Pressures.* Journal of Solution Chemistry, 1988. **17**(8): p. 699-718.
7. Frantz, J.D. and W.L. Marshall, *Electrical Conductances and Ionization-Constants of Salts, Acids, and Bases in Supercritical Aqueous Fluids .1. Hydrochloric-Acid from 100-Degrees-C to 700-Degrees-C and at Pressures to 4000 Bars.* American Journal of Science, 1984. **284**(6): p. 651-667.
8. Frantz, J.D. and E.H. P., *Acid-Base Buffers: Use of Ag+AgCl in the Experimental Control of Solution Equilibria at Elevated Pressures and Temperatures.* American Journal of Science, 1973. **273**: p. 268-286.
9. Marsh, A.R.W. and W.J. McElroy, *The dissociation constant and Henry's law constant of HCl in aqueous solution.* Atmospheric Environment (1967), 1985. **19**(7): p. 1075-1080.
10. Johnston, K.P. and J.B. Chlistunoff, *Neutralization of acids and bases in subcritical and supercritical water: acetic acid and HCl.* Journal of Supercritical Fluids, The, 1998. **12**(2): p. 155-164.
11. Oelkers, E.H. and H.C. Helgeson, *Calculation of dissociation constants and the relative stabilities of polynuclear clusters of 1:1 electrolytes in hydrothermal solutions at supercritical pressures and temperatures.* Geochimica et Cosmochimica Acta, 1993. **57**(12): p. 2673-2697.
12. Pokrovskii, V.A., *Calculation of the standard partial molal thermodynamic properties and dissociation constants of aqueous HCl0 and HBr0 at temperatures to 1000[deg]C and pressures to 5 kbar.* Geochimica et Cosmochimica Acta, 1999. **63**(7-8): p. 1107-1115.
13. Tagirov, B.R., A.V. Zotov, and N.N. Akinfiev, *Experimental study of dissociation of HCl from 350 to 500[deg]C and from 500 to 2500 bars: Thermodynamic properties of HCl[deg](aq).* Geochimica et Cosmochimica Acta, 1997. **61**(20): p. 4267-4280.

14. Meyer, C.A., et al., *ASME Steam Tables: Thermodynamic and transport properties of Steam*. 6th ed. 1993: ASME PRESS.
15. Wagner, W. and A. Kruse, *Properties of Water and Steam*. 1998: Springer.
16. Haar, L., J. Gallagher, S., and K.G. S., *NBS/NRC Steam Tables*. 1984: Hemisphere Publishing Coorporation.
17. Calvert and J. Johnson, J. Chem. Soc., 1866. **19**: p. 436.
18. Wagner, K., et al., *Dealloying below the Critical Potential.* J. Electrochem. Soc., 1997. **144**(10): p. 3545-3555.
19. Vukmirovic, M.B., N. Dimitrov, and K. Sieradzke, *Dealloying and Corrosion of Al Alloy 2024-T3.* J. Electrochem. Soc., 2002. **149**(9): p. B428-B439.
20. Sieradzke, K., et al., *The Relationship Between Dalloying and Transgranular Stress Corrosion Cracking of Cu-Zn and Cu-Al Alloys.* J. Electrochem. Soc., 1987. **134**(7): p. 1635-1639.
21. Sieradzke, K., et al., *The Dealloying Critical Potential.* J. Electrochem. Soc., 2002. **149**(8): p. B370-B377.
22. Sieradzke, K., et al., *Computer simulations of corrosion: selective dissolution of binary alloys.* Philosophical Magazine A, 1989. **59**(4): p. 713-746.
23. Sieradzke, K., *Curvature Effects in Alloy Dissolution.* J. Electrochem. Soc., 1993. **140**(10): p. 2868-2872.
24. Newman, R.C. and K. Sieradzke, *Metallic Corrosion.* Science, 1994. **263**: p. 1708.
25. Dimitrov, N., et al., *Dealloying of Al2CuMg in Alkaline Media.* J. Electrochem. Soc., 2000. **147**(9): p. 3283-3285.
26. Erlebacher, J., et al., *Evolution of nanoporosity in dealloying.* Nature, 2001. **410**: p. 450-453.
27. Forty, A.J., *Corrosion micromorphology of noble metal alloys and depletion gilding.* Nature, 1979. **282**: p. 597-598.
28. Pickering, H.W. and C. Wagner, *Electrolytic Dissolution of Binary Alloys Containing a Noble Metal.* J. Electrochem. Soc., 1967. **114**(7): p. 698-706.
29. *Metals Handbook. 9th deition. Corrosion*. Vol. 13. 1987: ASM International.
30. Birks, N. and G.H. Meier, *Introduction to High Temperature Oxidation of Metals*. 1983, London: Edward Arnold. 198.
31. Wagner, C., *Equations for Transport in Solid Oxides and Sulfides of Transition Metals.* Progress in Solid-State Chemistry, 1975. **10**(Part 1): p. 3-16.
32. Wagner, C., *Diffusion and High Temperature Oxidation of Metals*, in *Atom Movements*. 1951, American Society for Metals: Cleveland. p. 153-173.
33. Kofstad, P., *High Temperature Corrosion*. 1988, London and New York: Elsevier

Applied Science. 558.
34. Khanna, A.S., *Introduction to High Temperature Oxidation and Corrosion*. 2002, Materials Park: ASM International. 324.
35. Bard, A.J. and L.R. Faulkner, *Electrochemical Methods: Fundamentals and Applications, 2nd Edition*. 2001: John Wiley & Sons, Inc. 833.
36. Kofstad, P., *Nonstochiometry, Diffusion, and Electrical Conductivity in Binary Metal Oxides*. 1972: John Wiley & Sons, Inc. 382.
37. Agrawal, P.M., B.M. Rice, and D.L. Thompson, *Predicting trends in rate parameters for self-diffusion on FCC metal surfaces.* Surface Science, 2002. **515**: p. 21-35.
38. Atkinson, A. and R.I. Taylor, *The diffusion of Ni in the bulk and along dislocations in NiO single crystals.* Philosophical Magazine A, 1979. **39**(5): p. 581-595.
39. Atkinson, A. and R.I. Taylor, *The diffusion of Ni along grain boundaries in nickel oxide.* Philosophical Magazine A, 1981. **43**(4): p. 979-998.
40. Caplan, D., M.J. Graham, and M. Cohen, *Effect of Cold Work on the Oxidation of Nickel at High Temeperature.* J. Electrochem. Soc., 1972. **119**(9): p. 1205-1215.
41. Shim, M.T. and W.J. Moore, J. Chem. Phys., 1957. **26**: p. 802.
42. Fronhold, A.T.J., *Theory of Metal Oxidation, Vol. 1, Fundamentals, Vol. 2, Space Charge.* 1980, Amsterdam: North-Holland.
43. Zhang, L. and D.D. Macdonald, *On the transport of point defects in passive films.* Electrochemica Acta, 1998. **43**(7): p. 679-691.
44. Chao, C.Y., L.F. Lin, and D.D. Macdonald, *A point Defect Model for Anodic Passive Films. I Film Growth Kinetics.* J. Electrochem. Soc., 1981. **128**(6): p. 1187-1194.
45. Chao, C.Y., L.F. Lin, and D.D. Macdonald, *A Point Defect Model for Anodic Passive Films. III Impedance Response.* J. Electrochem. Soc., 1982. **129**(9): p. 1874-1879.
46. Lin, L.F., C.Y. Chao, and D.D. Macdonald, *A Point Defect Model for Anodic Passive Films. II Chemical Breakdown and Pit Initiation.* J. Electrochem. Soc., 1981. **128**(6): p. 1194-1198.
47. Macdonald, D.D., *The Point Defect Model for the Passive State.* J. Electrochem. Soc., 1992. **139**(12): p. 3434-3449.
48. Macdonald, D.D., S.R. Biaggio, and H. Song, *Steady-State Passive Films.* J. Electrochem. Soc., 1992. **139**(1): p. 170-177.
49. Macdonald, D.D. and M. Urquido-Macdonald, *Theory of Steady-State Passive Films.* J. Electrochem. Soc., 1990. **137**(8): p. 2395-2402.

50. Zhang, L., et al., *On the kinetics of Growth of Anodic Oxide Films.* J. Electrochem. Soc., 1998. **145**(3): p. 898-905.
51. Timoshenko, S.P. and J.N. Goodier, *Theory of Elasticity*. 3rd edition ed. 1970: McGRAW-HILL.
52. Deen, W.M., *Analysis of Transport Phenomena*. 1998, New York: Oxford University Press. 597.
53. Poirier, D.R. and G.H. Geiger, *Transport Phenomena in Materials Processing*. 1994: TMS. 658.
54. Davis, J.R., ed. *Nickel, Cobalt, and Their Alloys*. ASM Specialty Handbook. 2000, ASM International: Materials Park, OH.
55. Huntz, A.M., et al., *Evidence of stress relaxation in thermally grown oxide layers - experiments and modelling.* Materials Science and Engineering a-Structural Materials Properties Microstructure and Processing, 1998. **248**(1-2): p. 44-55.
56. Barnes, J.J., G.J. G., and D.A. Shores, *A Model for Stress Generation and Relief in Oxide-Metal Systems During a Temperature Change.* Oxidation of Metals, 1989. **32**(5/6): p. 449-469.
57. Huntz, A.M., *Stresses in Nio, Cr2o3 and Al2o3 Oxide Scales.* Materials Science and Engineering a-Structural Materials Properties Microstructure and Processing, 1995. **201**(1-2): p. 211-228.
58. Jones, D.A., *Principles and Prevention of Corrosion, 2nd Edition*. 1996: Prentice-Hall.
59. Evans, H.E., *The Role of Oxide Grain Boundaries in the Development of Growth Stresses During Oxidation.* Corrosion Science, 1983. **23**(5): p. 495-506.
60. Zhdanov, V.P. and P.R. Norton, *Criterion for instability of oxide film growth with respect to formation of cracks.* Surface Science, 1995. **323**: p. L311-L313.

Chapter 5: Conclusions and Future work

5.1 Experiments

When the feed stream is acidic with ambient pH 2, the dealloyed oxide layer forms at the subcritical temperatures and thin oxide forms at the supercritical temperatures. Within the dealloyed oxide layer, the nickel and iron are selectively dissolved from the metal substrate, and chromium and molybdenum form stable oxides. The growth rate of the dealloyed oxide layer is very fast because of the highly defective structure of the dealloyed oxide layer, caused by the selective dissolution of nickel and iron. The suppression of dealloying of nickel at the supercritical temperatures originates from the low hydrogen ion concentration at the supercritical temperatures due to a low dissociation constant of HCl. For the Inconel 625 reaction vessel, SCC is observed both at the supercritical temperatures and at the subcritical temperatures with an exposure time of 204.5 hours. SCC at the subcritical temperatures comes from the thick dealloyed oxide layer formation, while SCC at the supercritical temperature partly comes from the direct chemical attack of associated HCl molecules. The unspecified residual stress might also be a cause of SCC both at the supercritical and subcritical temperatures.

When the feed stream is acidic with an ambient pH of 1, severe SCC is developed at the temperature of 350℃. The dealloyed oxide layer develops at this temperature. Within the dealloyed oxide layer, the nickel and iron are selectively dissolved. In contrast to the experiments at ambient pH 2, even the chromium is also selectively dissolved from the metal substrate to a lesser degree than nickel and iron, and only molybdenum forms a stable oxide.

When the feed stream is neutral, no severe corrosion is observed up to exposure time of 240 hours. Thin oxide forms both at the supercritical and the subcritical temperatures. The thickness of oxide may increase as temperature increases. No dealloying and SCC are observed in a neutral environment.

5.2 Corrosion mitigation methodology

5.2.1 Feed modification

From the experimental results, the corrosion attack of nickel-base alloys comes from the acidic chemical environment and the stability of the elements as solid species under the acidic condition. Pourbaix diagrams indicate that near the neutral pH all the primary elements of nickel-base alloys can form stable oxides. We suggest that pH of the feed

stream needs to be shifted to a region where all the elements can form a stable oxides as shown in Figure 5.1 (along line①).

Dilution

Sufficient dilution of an aggressive feed can potentially reduce the risk of corrosion by lowering the chloride concentration and permit processing by SCWO. However, the required dilution may be so large as to make such a procedure economically unattractive. For example, a dilution of 1000-10000 for wastes high in solvent such as carbon tetrachloride may be required to reduce feeds to acceptable levels.[1]

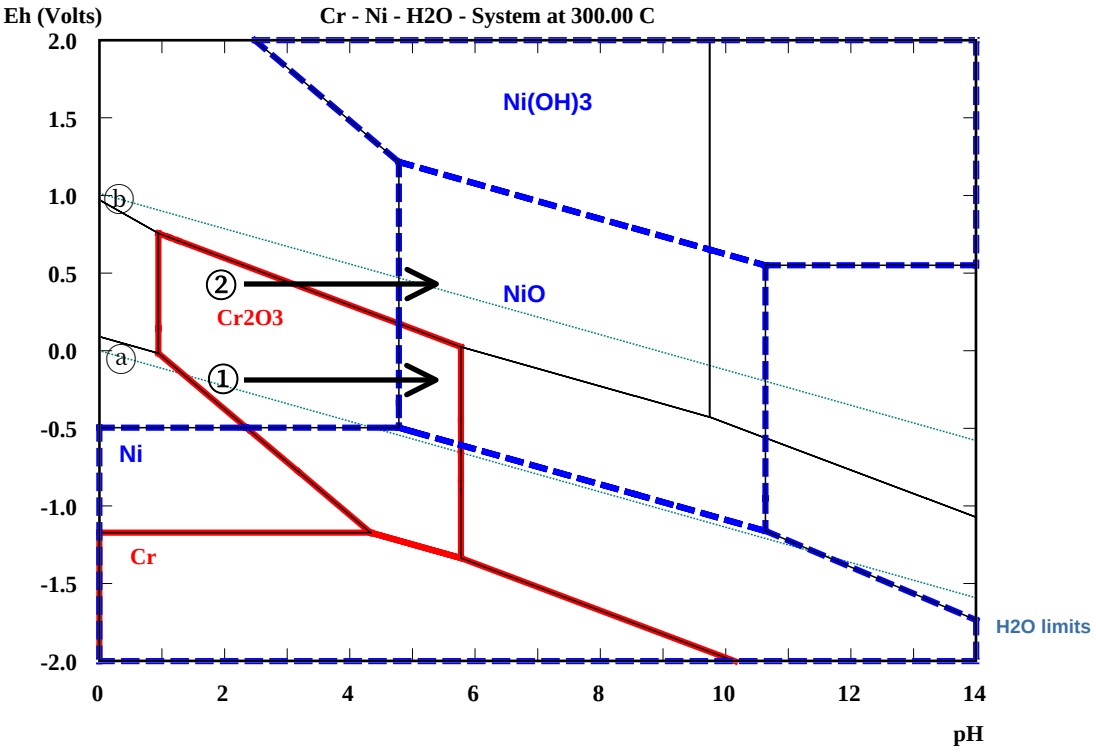

Figure 5.1 Composite E-pH diagram of Ni and Cr at T=300℃ and P=84.63 bar(saturated vapor pressure) with an assigned molality of 10^{-6}.

Neutralization

From the composite Pourbaix diagram in Figure 4.1, near the neutral pH range, major alloying elements of Ni, Cr, Mo and Fe can form stable oxides in the subcriticcal temperature range and in the supercritical temperature range. Although feed neutralization, with NaOH for example, has seen some success in SCWO systems for acidic feeds, it has been carried out without a full understanding of its effect on corrosion.

Typically, feed neutralization involves stoichiometric quantities of neutralizer.[1] To make feed neutralization methodology probable, it may be required to understand the actual pH and potential of the system. As shown in Figure 5.1, there is a limited E-pH region within which the stability of Ni and Cr is thermodynamically favored for high subcritical temperatures (line ① in the diagram) . The effect of added oxidizer such as oxygen and hydrogen peroxide (H_2O_2) should also be carefully considered because the limited E-pH region of stability for Ni and Cr has a dependence on the potential. If the potential range is raised along line ②, the chromium is not stable and may be selectively dissolved from the metal substrate.[2] Namely, the added oxygen may need to be controlled to a level where all these elements can form stable oxides. In this regard, development of high temperature reference electrodes and stable pH sensors is essential to make this methodology possible.

When the feed stream is neutralized, it can contain a superfluous amount of salts and deposit at the supercritical temperatures. So even though the feed stream is neutral, these deposited salts can harbor corrosive species locally and cause localized corrosion such as pitting and crevice corrosion by modifying the local chemistry. These effects need to be studied in more detail.

5.2.2 Corrosion resistant materials

Although all the nickel base alloys have experienced dealloying of nickel and iron from the metal substrate, the depth of penetration varies significantly depending on the alloying composition. In general, the depth of penetration decreases as chromium concentration increases and decreases somewhat as molybdenum concentration increases. Molybdenum without significant amount of chromium does not give suitable corrosion resistance as found from the B-2 alloy. In addition to the concentration of alloying elements, the metallurgical effects such as cold-work and heat treatment and their consequences on the corrosion behavior of materials need to be considered more closely.

Other than nickel-base alloys, titanium alloys (T60 and TA6V) are often found to have better corrosion resistance than nickel-base alloys in an acidic chlorinated feed during the corrosion tests.[3-5] Although there is a report on the through-wall pitting of titanium

liners during the destruction efficiency testing of chlorinated wastes[1], titanium alloys may give suitable corrosion resistance for the specific environment of an acidic chlorinated feed over a limited low temperature range for a specific waste. However, the strength of the titanium alloys at high temperatures decreases significantly[6] and, as a result, these may only be used as liner materials at high temperatures while the strength of nickel-base alloys does not decrease significantly up to ~600°C[6]. At elevated temperatures, potential problems with creep also need to be considered. The applicability of titanium alloys in SCWO systems requires further testing.[1]

5.2.3 Reactor design

Efforts to enhance corrosion resistance of materials as described above should be accompanied by improved reactor design to obtain commercialization of SCWO systems. A number of new or modified reactor designs have emerged over the past two decades and attempted to reduce the problems of corrosion and salt precipitation/solids build up, which can rapidly accumulate on reactor walls or process surfaces and form plugs, causing expensive and frequent downtime of the SCWO systems and more aggressive corrosive environments. These reactor designs include the following: reverse tank reactors with brine pool, transpiring wall reactors, adsorption/reaction on a fluidized solid phase, reverse flow tubular reactors, centrifuge reactors, high velocity flow, mechanical brushing, double wall reactors.[7-10] In brief, several important reactor designs are briefly presented.

Reverse flow, tank reactor with brine pool

The reverse flow tank reactor in Figure 5.2 (a) was originally developed by MODAR. and consists of a vertical pressure vessel with two distinct thermal zones. The upper part of the vessel is kept at a supercritical temperature and is the region where organic species are oxidized, while the lower part of the vessel is kept at a subcritical temperature. The supercritical reaction zone of the vessel functions as a continuous stirred tank reactor (CSTR), with agitation provided by the feed entering the vessel through a nozzle jet which expends into the vessel from the top. Salts which precipitate in the supercritical zones are directed to the bottom of the vessel by gravity, inertia, and forced convection, and redissolve in the subcritical zone, forming a dense brine. The main process effluent flow is withdrawn from the top of the vessel and this produces a recirculation flow pattern in the supercritical zone. As a result, most of the salts are effectively removed from the process flow without impeding the oxidation reaction or any downstream process.[10]

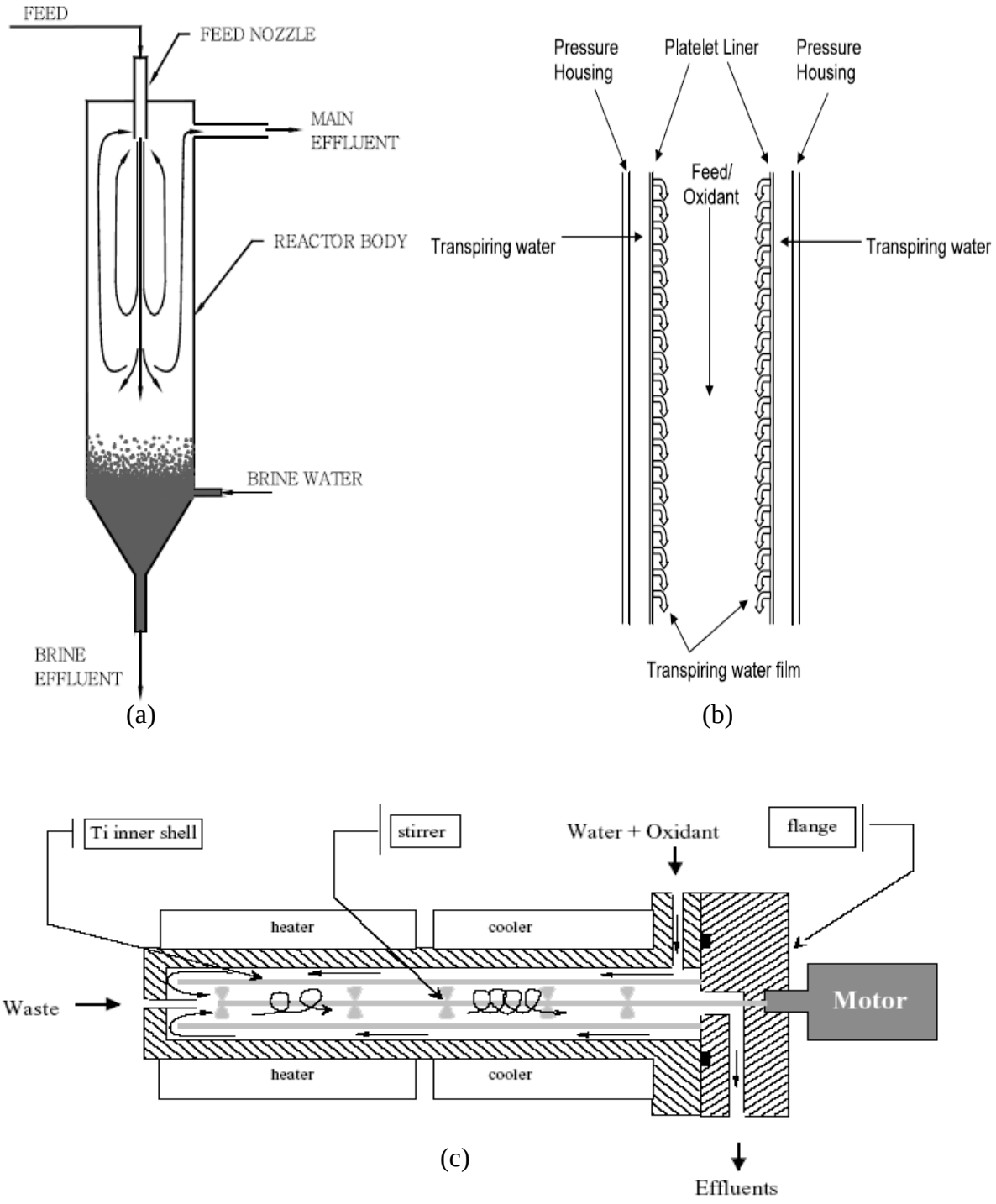

Figure 5.2 Examples of reactor designs. (a) Reverse flow tank reactor with brine pool (adapted from Marrone et al.[10]) (b) Transpiring wall reactor (adapted from Marrone et al.[10]) (c) Double wall reactor (adapted from Calzavara et al.[7])

Transpiring wall reactor

The general concept behind the transpiring wall reactor in Figure 5.2 (b) is to introduce a flow of a solute-free water through a porous reactor liner in order to keep salt particles and corrosive species away from the reactor wall. The cylindrical liner, which fits within a tubular pressure housing, consists of many thin metal layers or platelets bonded together. Each platelet is etched with a specific pattern of indentations such that a three-dimensional network of channels is formed when the platelets are combined to form the liner. The channels are designed to meter and distribute clean water through the liner to its inner surface, which forms the outer boundary of the reaction chamber. The water exits the liner inner surface through pores and forms a thin, protective film on the metal surface. The temperature of the transpiring water can be either subcritical or supercritical, but is usually less than the temperature achieved in the center of the reactor where oxidation takes place. In principle, the continuous film of water prevents any precipitated salts from depositing on to the surface by entraining the solid salt particles and in the flow and/or by redissolving the salts depending on the temperature of the transpiring water. The continuous flow of clean water also prevents or minimizes corrosive species from reaching the metal surface of the liner.[10]

Double wall reactor

The double wall reactor in Figure 5.2 (c) also has been devised to overcome the problems of corrosion and salt plugging. This design has a double shell made from titanium, which prevents corrosion of the reactor. This design also has a stirrer inside the reactor, which creates a turbulent flow in the reactor, prevents the sedimentation of inorganic compounds, and enables better heat transfers.[7]

5.3 Summary and Future work

Although SCWO is an efficient process to treat hazardous organic compounds, the aggressive feed stream of waste stream prevents the successful development of SCWO systems. Due to the highly corrosive nature of the feed stream along with high pressure and high temperature requirements, a material of fabrication universally applicable to all sections of a SCWO system is extremely unlikely.[1] To accomplish the commercialization of SCWO for an aggressive feed streams, corrosion mitigation methodologies such as feed modification, identification of materials and reactor design should all be integrated. A material of good corrosion resistance in a specific environment needs to be identified over a wide temperature range (both at the supercritical and subcritical temperatures) for candidate materials. If a material has good corrosion

resistance against a specific waste stream, the combined consideration of a waste stream and a material can provide a corrosion mitigation methodology for a specific waste stream.

Along with the development of pH and reference electrodes, further corrosion testing needs to be performed at higher temperatures up to 600℃, considering that the actual SCWO reactor temperature reaches this range. The effects of added oxidizers, required in SCWO systems for high efficiency, also considered because the addition of oxidizer can change the potential of the metal surface to an undesired region (Figure 5.1).

The development of SCC at the supercritical temperatures for extended time should be carefully studied due to its localized geometry. They can cause an unexpected catastrophic failure of the system.

The unspecified metallurgical effects of materials need to be studied carefully in constructing the SCWO systems. These metallurgical effects, including heat treatment, cold-work and welding, can be important factors to localized forms of corrosion such as SCC and pitting.

Bibliography

1. Mitton, D.B., J.H. Yoon, and R.M. Latanision, *An overview of Corrosion Phenomena in SCWO systems for Hazardous Waste Destruction.* Zairyo-to-Kankyo, 2000. **49**(3): p. 130-137.
2. Mitton, D.B., P.A. Marrone, and R.M. Latanision, *Interpretation of the Rationale for Feed Modification in SCWO systems.* J. Electrochem. Soc., 1996. **143**(3): p. L59-L61.
3. Botella, P., et al., *Experimental study, via current-potential curves, of the anodic behavior of Alloy C-276 and T60 titanium in chlorinated and oxygenated aqueous media under sub- to supercritical conditions.* The Journal of Supercritical Fluids, 2003. **25**(3): p. 269-278.
4. Botella, P., et al., *Experimental set-up for electrochemical measurements in hydrothermal sub- and supercritical oxidation: polarization curves, determination of corrosion rates and evaluation of the degradability of reactors during hydrothermal treatments of aqueous wastes.* The Journal of Supercritical Fluids, 2003. **26**(2): p. 157-167.
5. Delville, M.H., et al., *Electrochemical study of corrosion in aqueous high pressure, high temperature media and measurements of materials corrosion rates: applications to the hydrothermal treatments of organic wastes by SCWO.* The Journal of Supercritical Fluids, 2003. **26**(2): p. 169-179.

6. *Heat-Resistant Materials*, ed. J.R. Davis. 1997, Materials Park, OH: ASM International. 591.
7. Calzavara, Y., et al., *A new reactor concept for hydrothermal oxidation.* The Journal of Supercritical Fluids. **In Press, Corrected Proof**.
8. Fauvel, E., et al., *A double-wall reactor for hydrothermal oxidation with supercritical water flow across the inner porous tube.* The Journal of Supercritical Fluids, 2004. **28**(1): p. 47-56.
9. Hodes, M., et al., *Salt precipitation and scale control in supercritical water oxidation--Part A: fundamentals and research.* The Journal of Supercritical Fluids. **In Press, Corrected Proof**.
10. Marrone, P.A., et al., *Salt precipitation and scale control in supercritical water oxidation--part B: commercial/full-scale applications.* The Journal of Supercritical Fluids. **In Press, Corrected Proof**.

Appendix A

Additional Experimental Results (Nickel-base alloys, wires)

The images obtained from each alloy (wire sample) in each TC# section are presented.

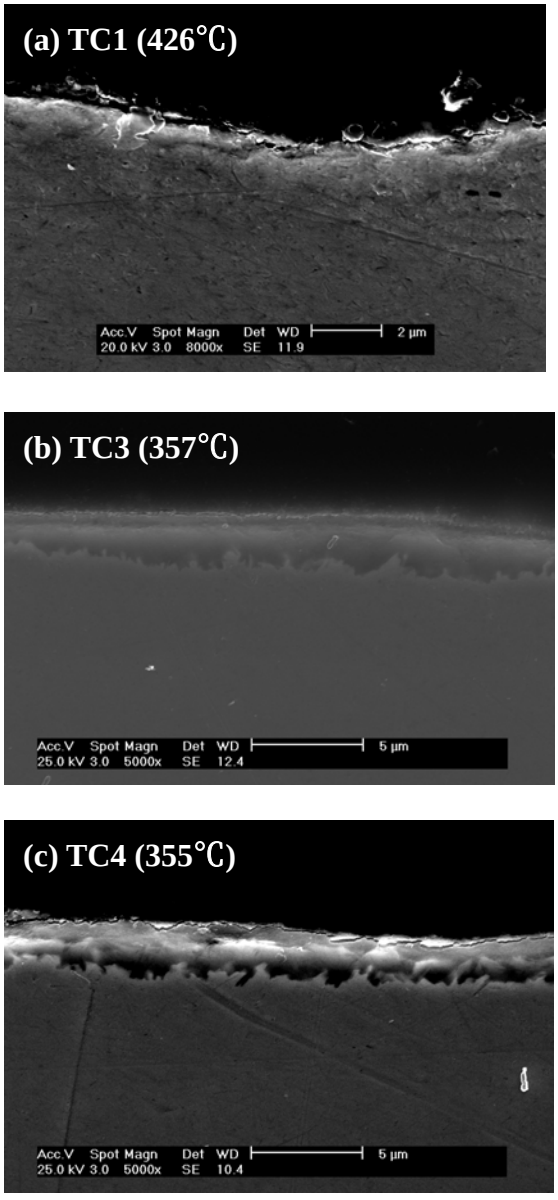

Figure A.1 ESEM images for Run#2 (C-22).

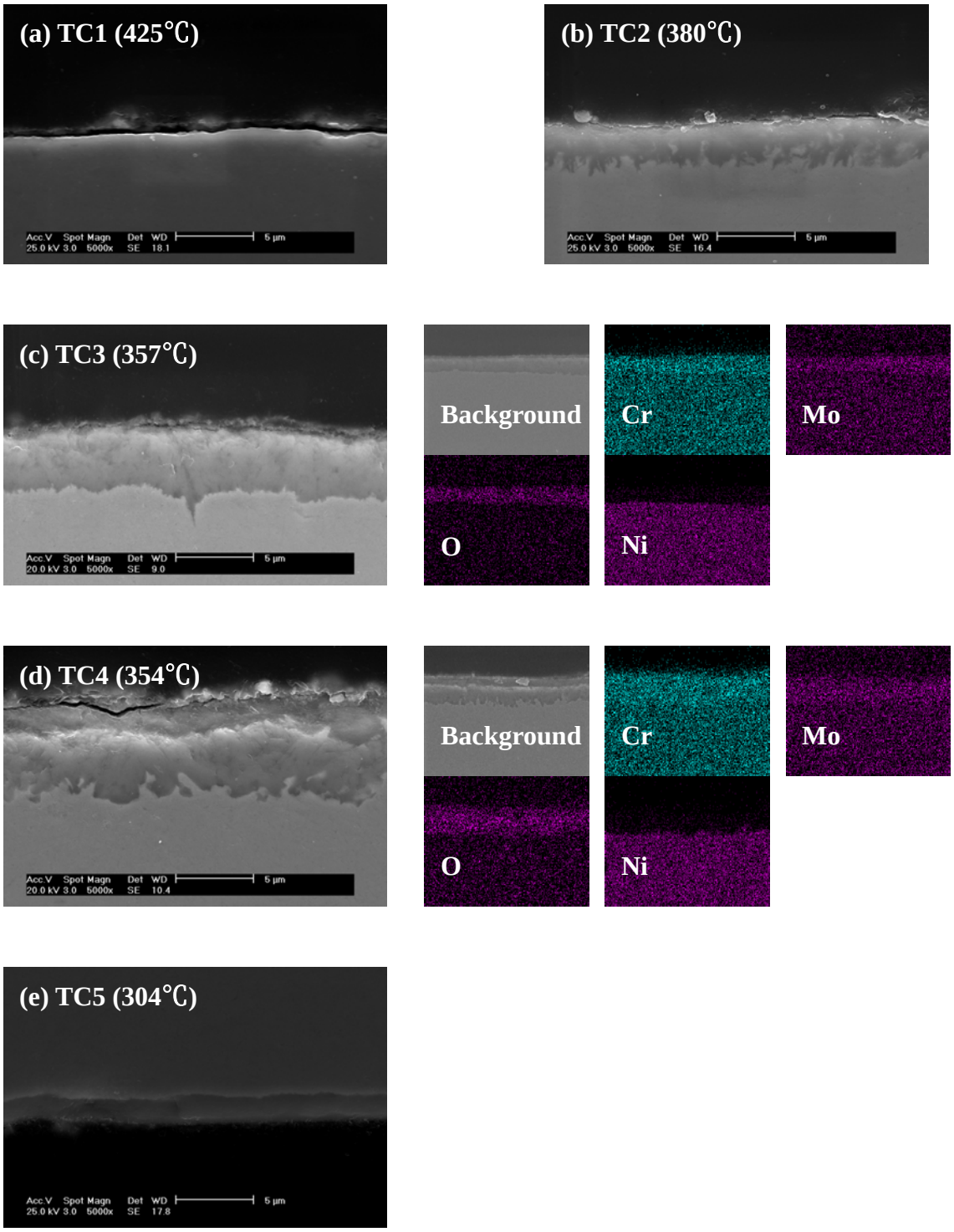

Figure A.2 ESEM images and X-ray mappings for Run#3 (C-22).

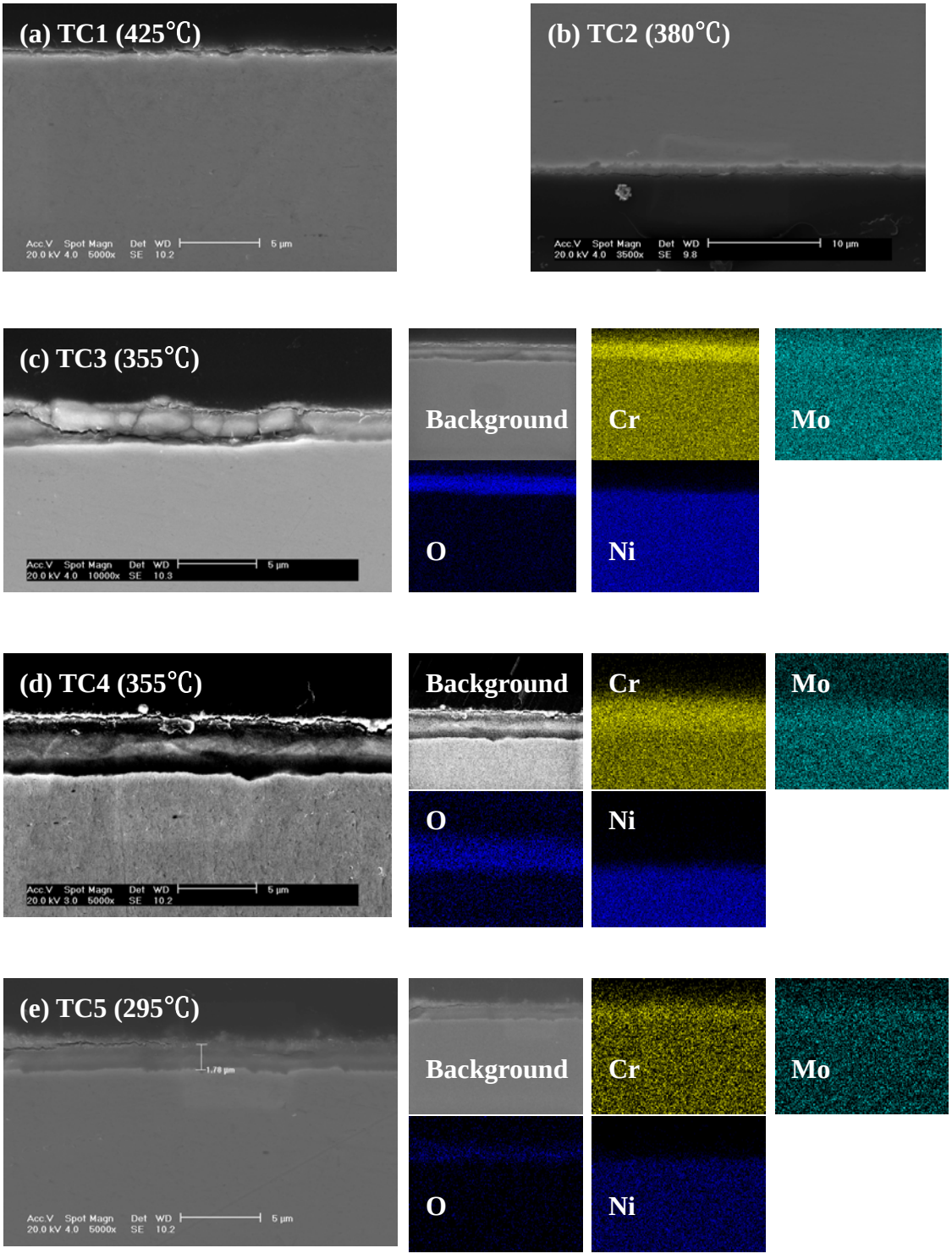

Figure A.3 ESEM images and X-ray mappings for Run#4 (Alloy 59).

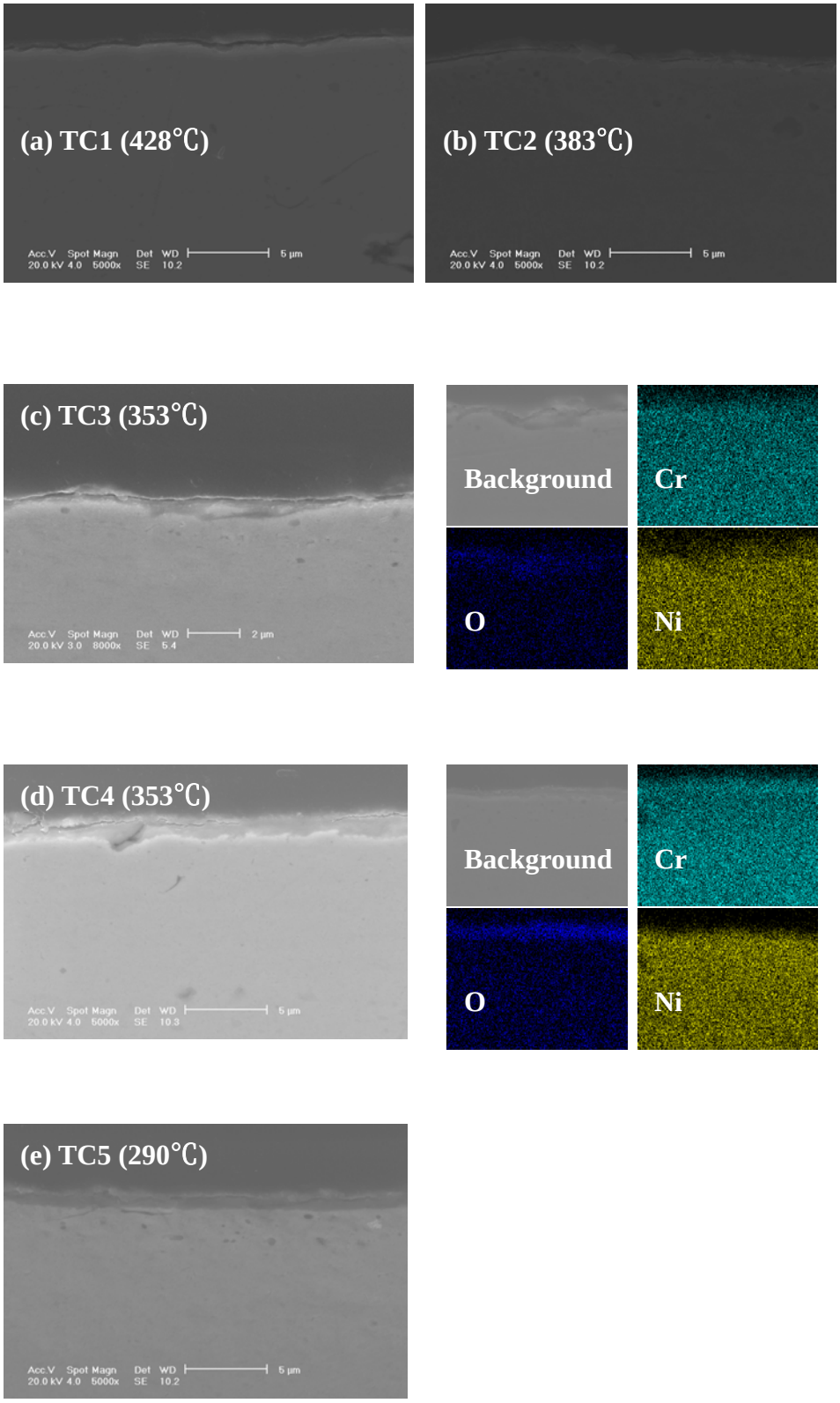

Figure A.4 ESEM images and X-ray mappings for Run#5 (Alloy 671).

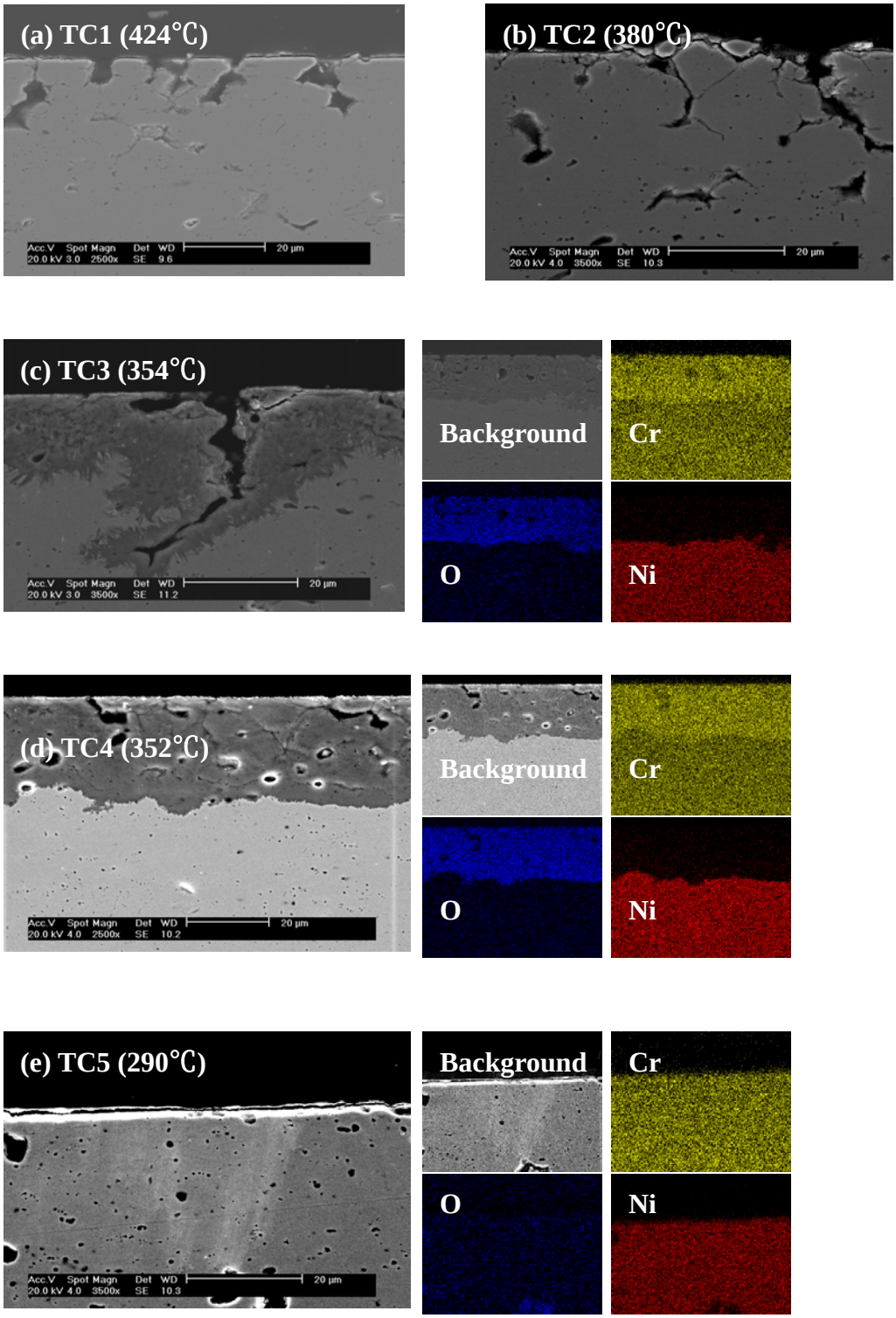

Figure A.5 ESEM images and X-ray mappings for Run#6 (MC).

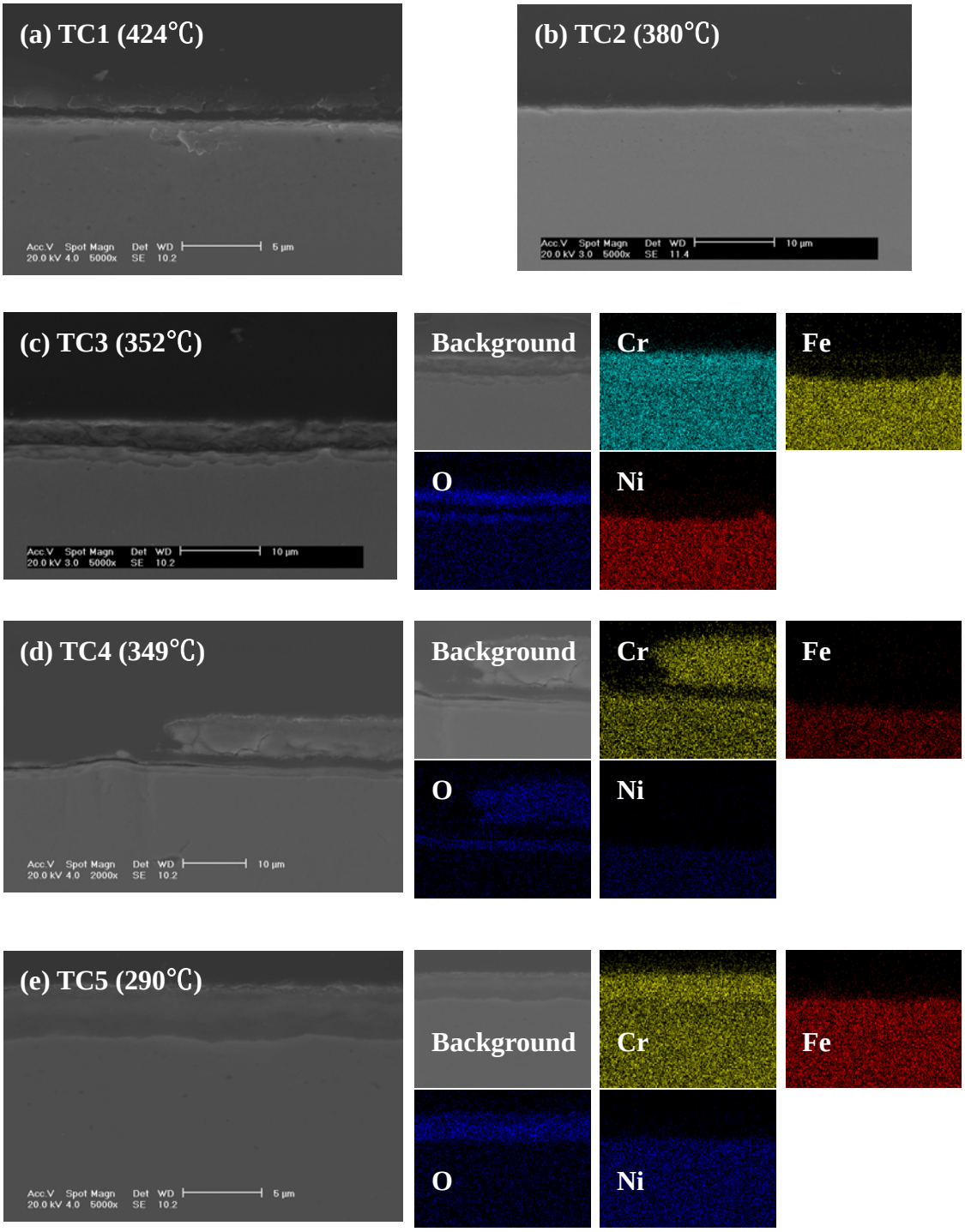

Figure A.6 ESEM images and X-ray mappings for Run#7 (Alloy 33).

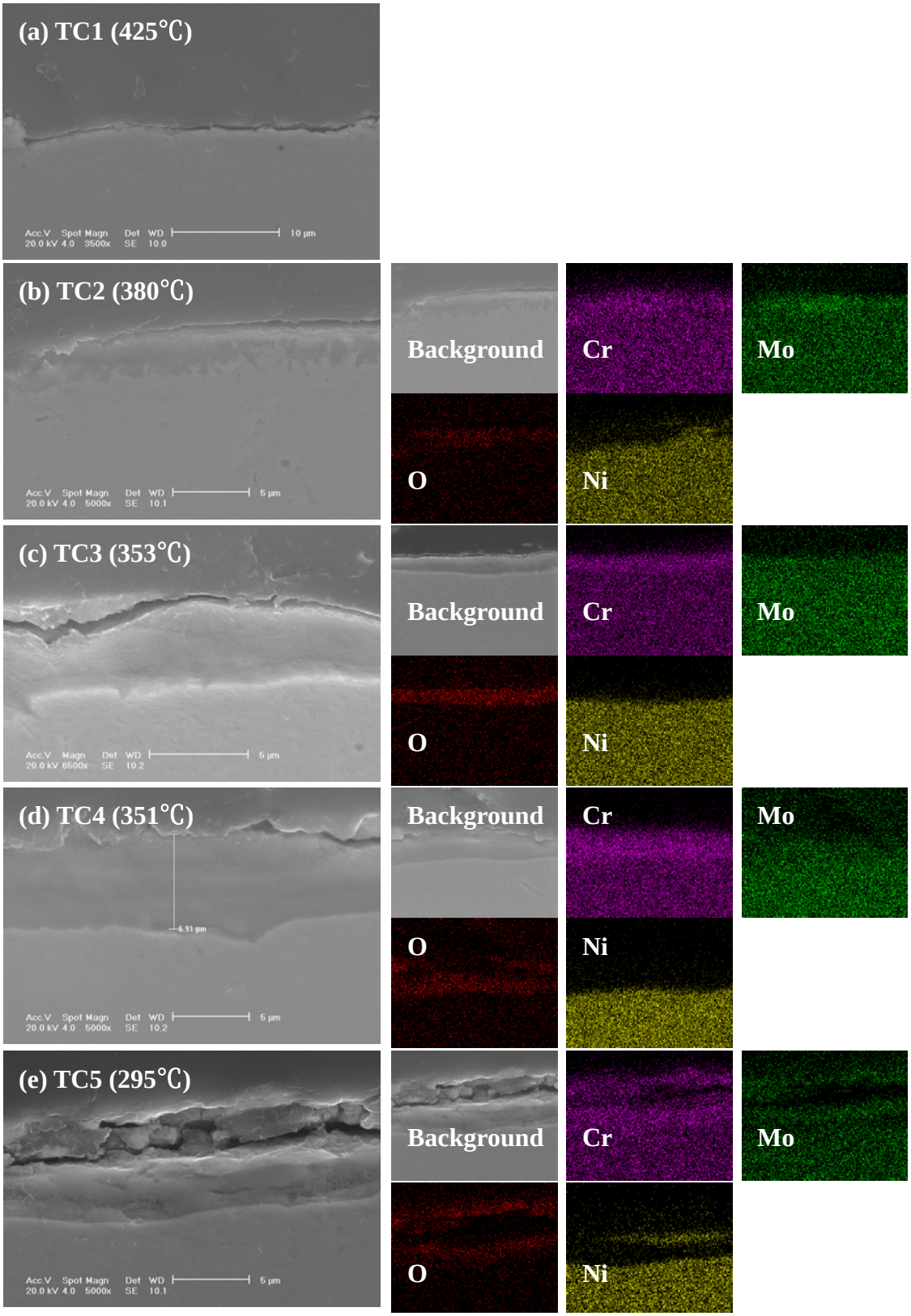

Figure A.7 ESEM images and X-ray mappings for Run#8 (C-2000).

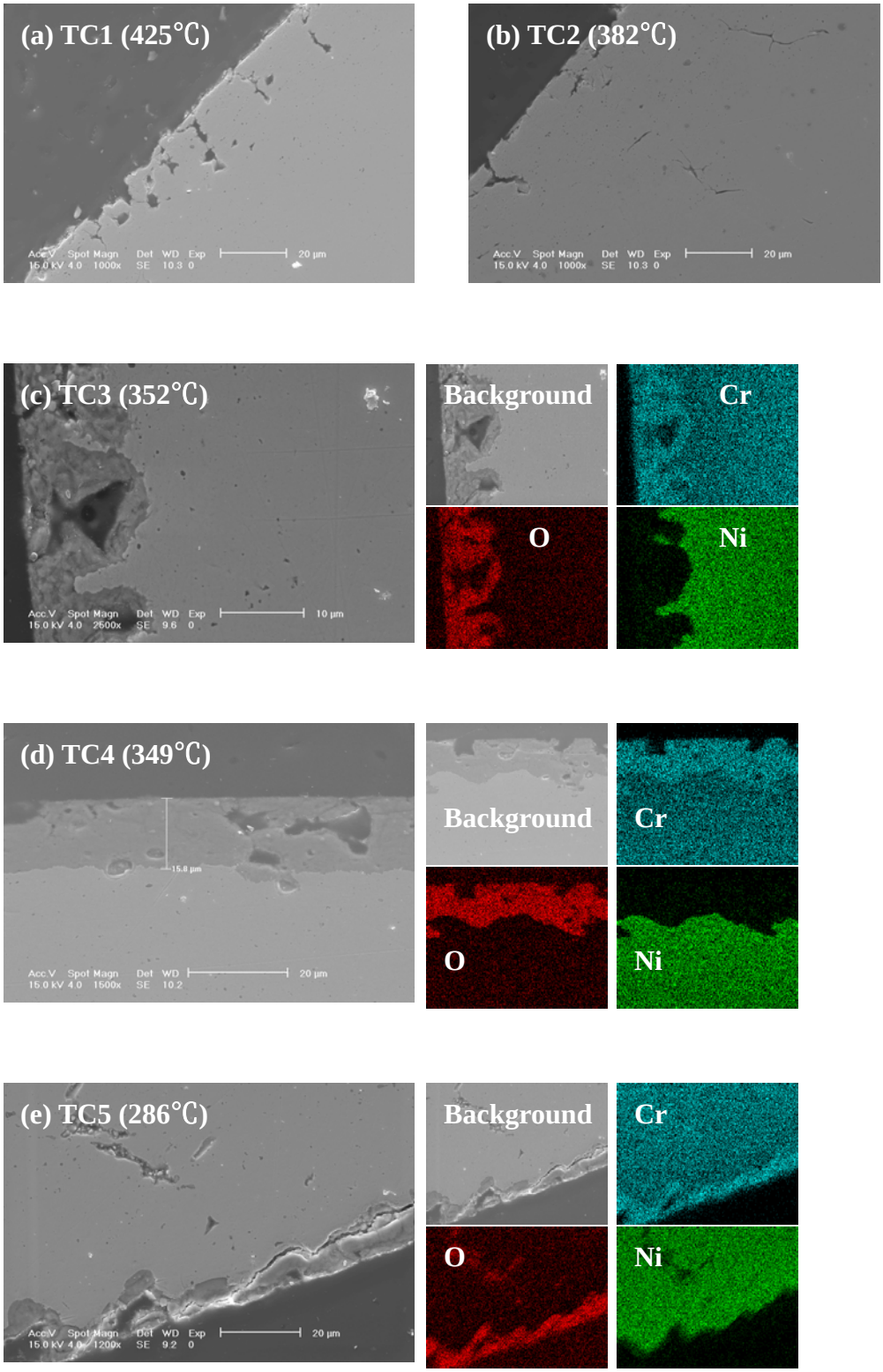

Figure A.8 ESEM images and X-ray mappings for Run#9 (MC).

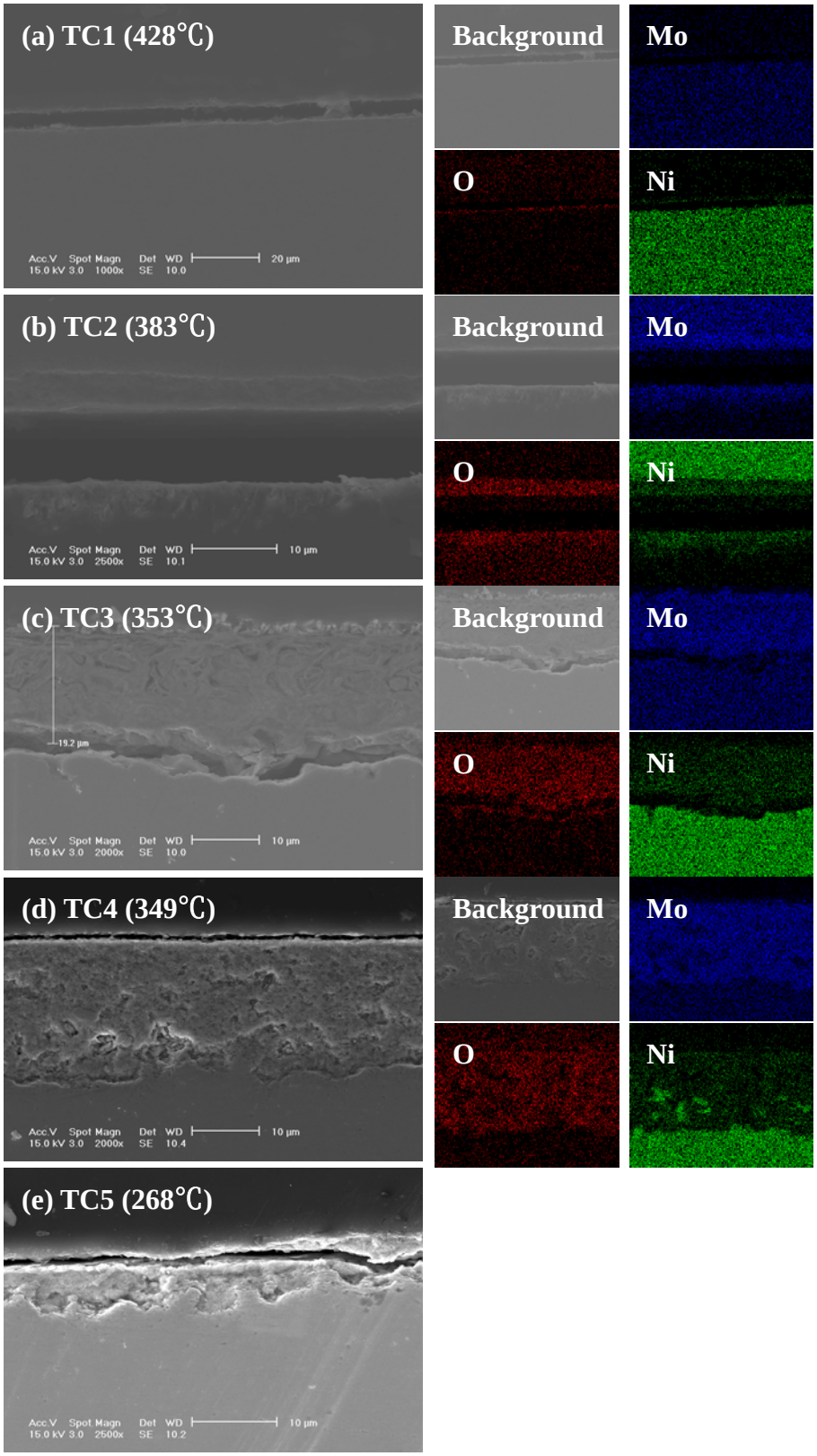

Figure A.9 ESEM images and X-ray mappings for Run#10 (B-2).

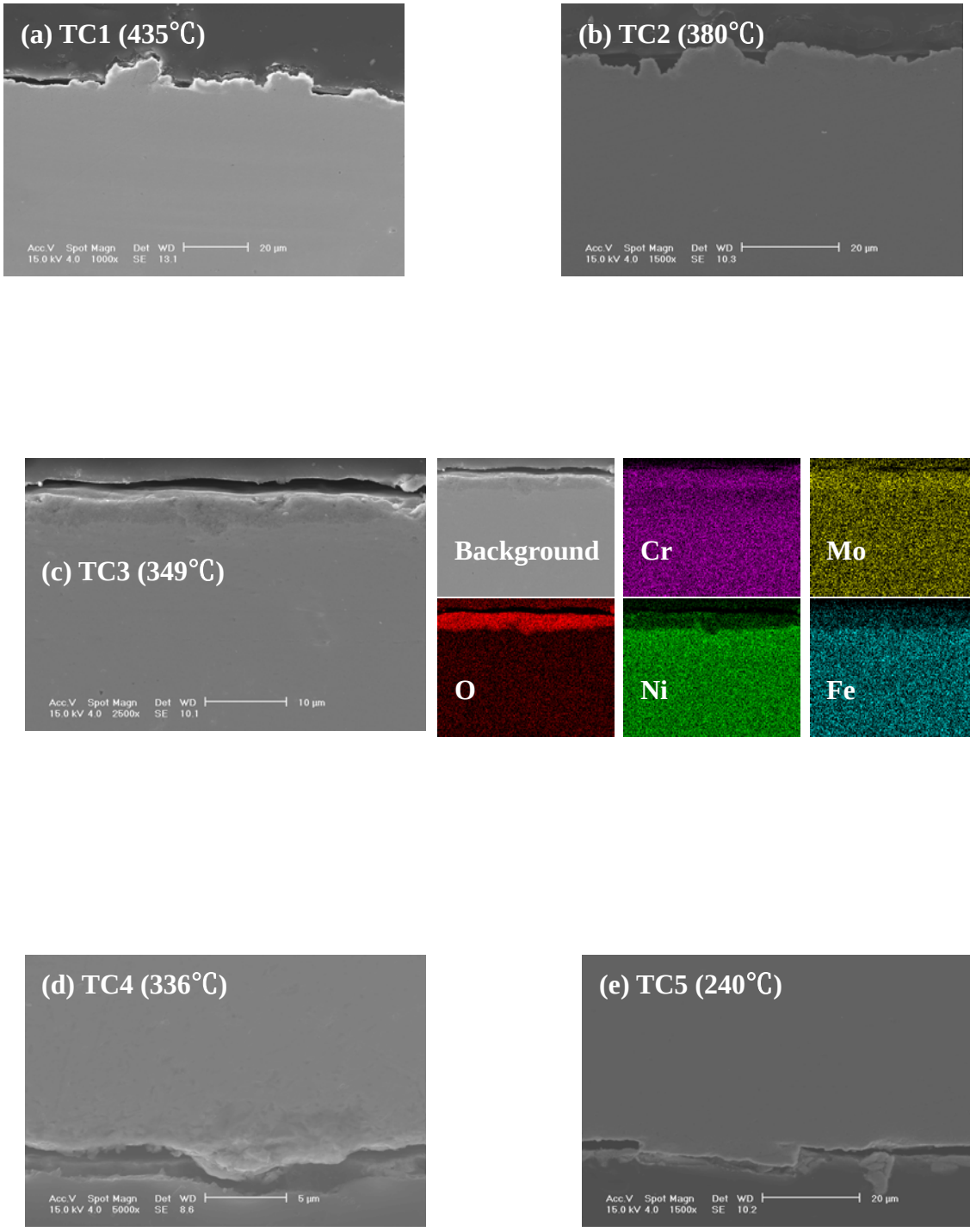

Figure A.10 ESEM images and X-ray mappings for Run#11 (G30).

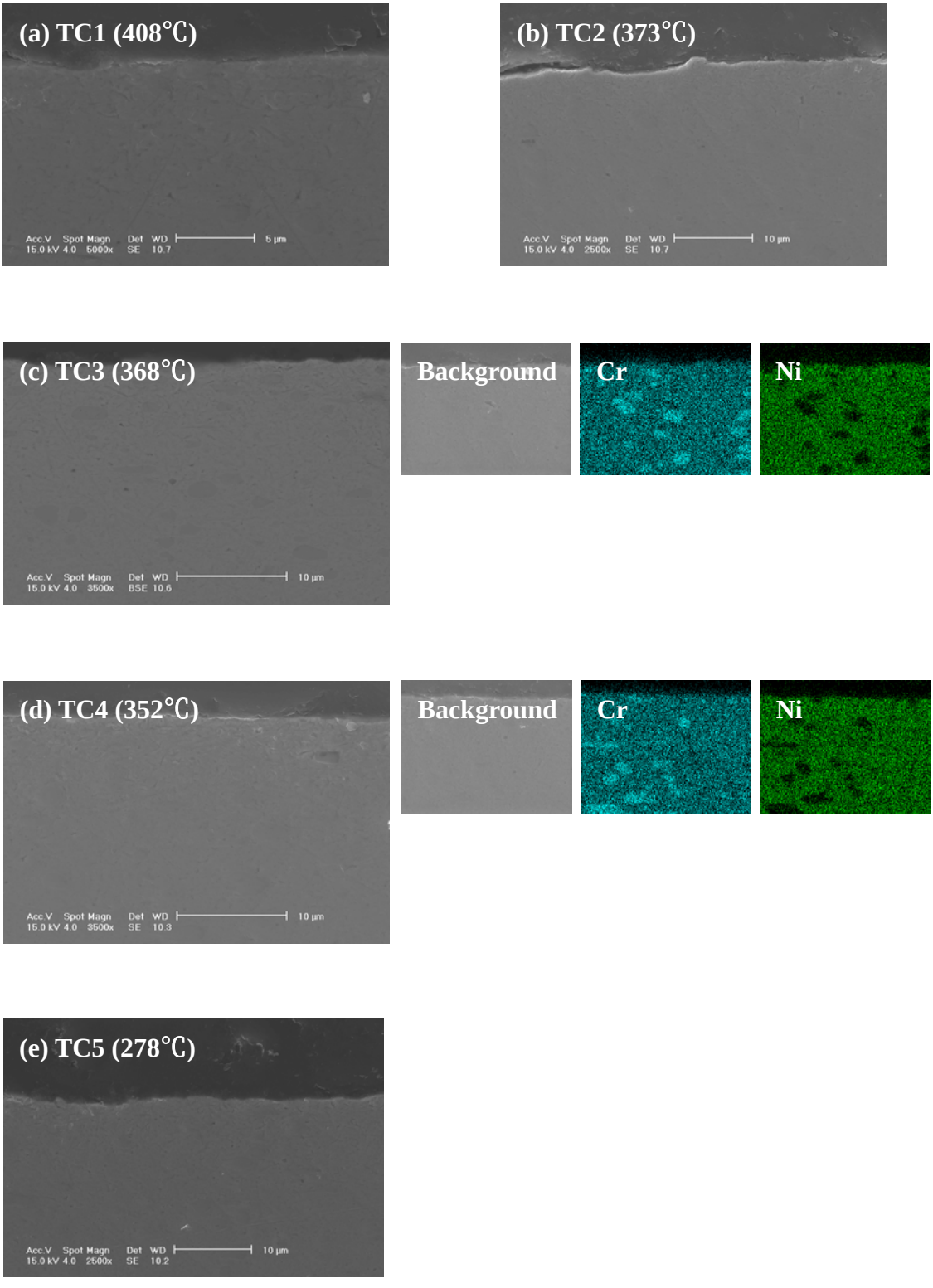

Figure A.11 ESEM images and X-ray mappings for Run#12 (MC*).

Appendix B

Additional Experimental Results (Nickel-base alloys, wires)

The images obtained from each alloy in sections of A, B, C, and D are presented. These images are obtained from the surface of tested wire samples.

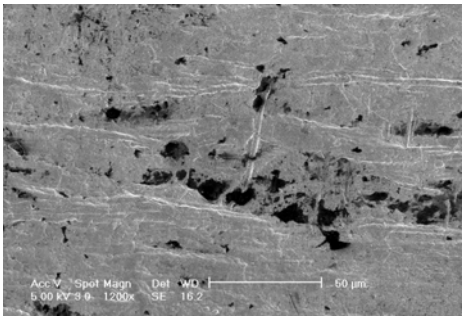
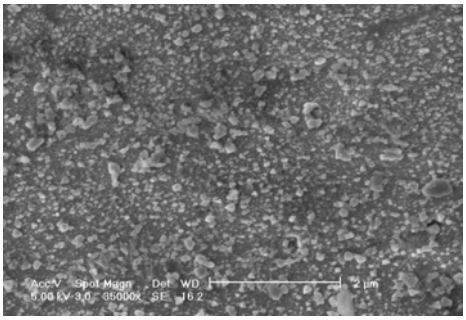

(a) Run#3-A (supercritical temperature)

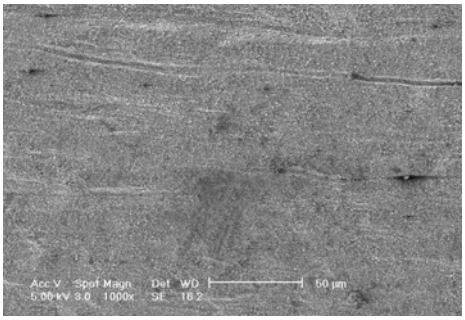
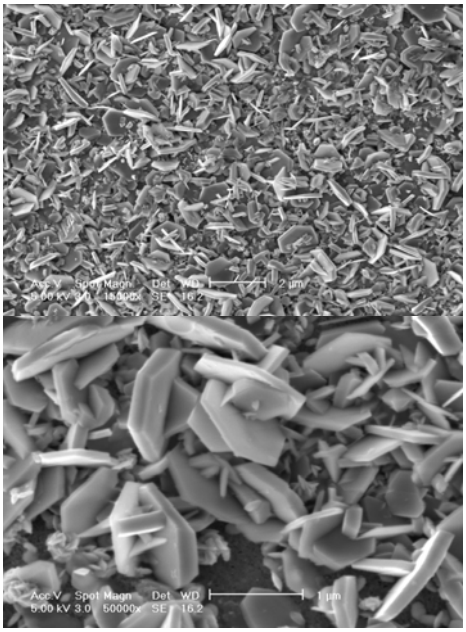

(b) Run#3-C (subcritical temperature)

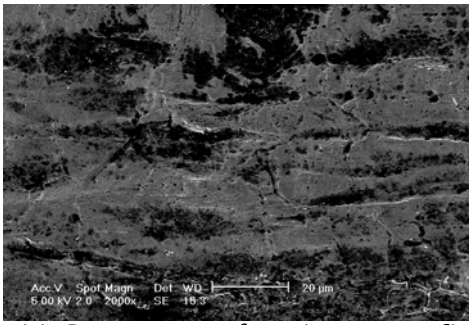

(c) C-22 wire surface (as received)

Figure B.1 ESEM images on surface oxides for Run#3 (C-22). The left-hand images are in low magnification and the right-hand images are in high magnification.

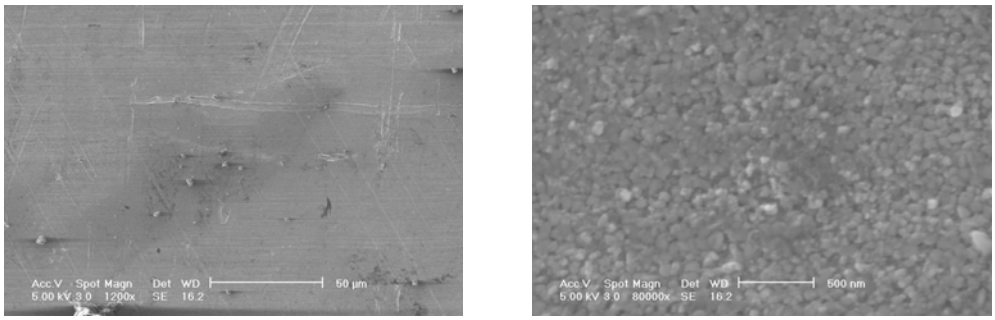

(a) Run#4-A (supercritical temperature)

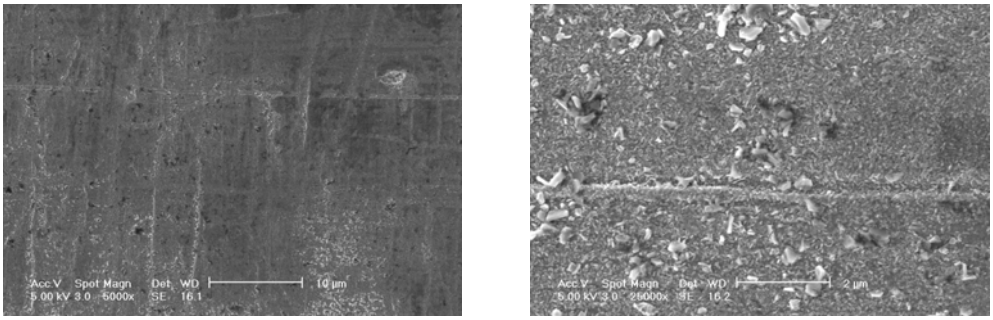

(b) Run#4-C (subcritical temperature)

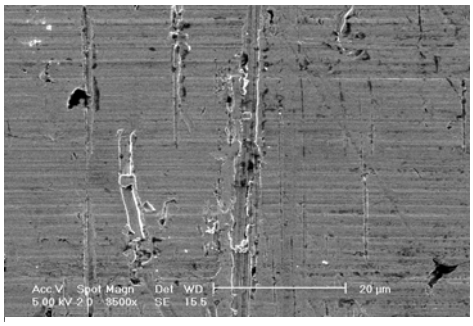

(c) Alloy 59 wire surface (as received)

Figure B.2 ESEM images on surface oxides for Run#4 (Alloy 59). The left-hand images are in low magnification and the right-hand images are in high magnification.

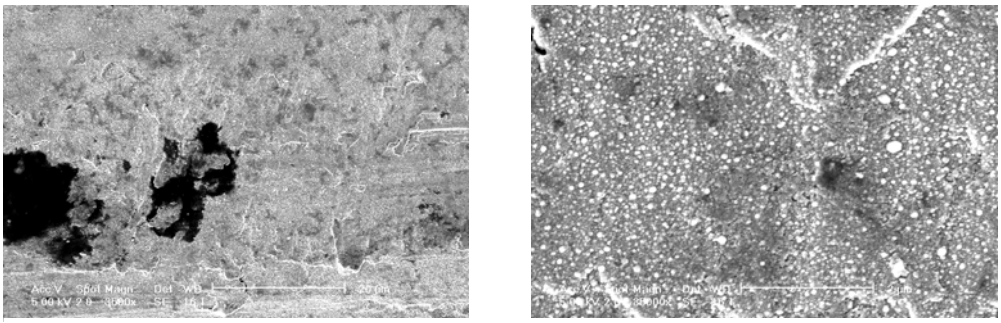

(a) Run#5-A (supercritical temperature)

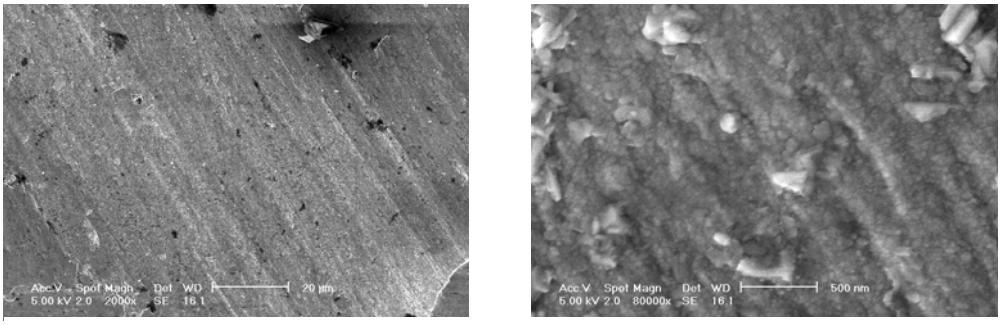

(b) Run#5-C (Supercritical temperature)

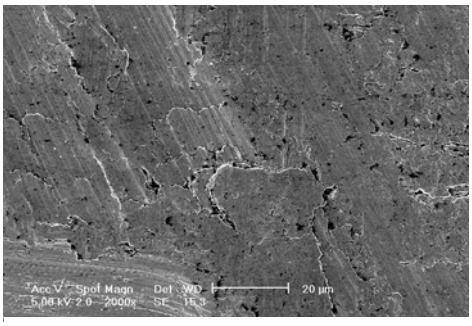

(c) Alloy 671 wire surface (as received)

Figure B.3 ESEM images on surface oxides for Run#5 (Alloy 671). The left-hand images are in low magnification and the right-hand images are in high magnification.

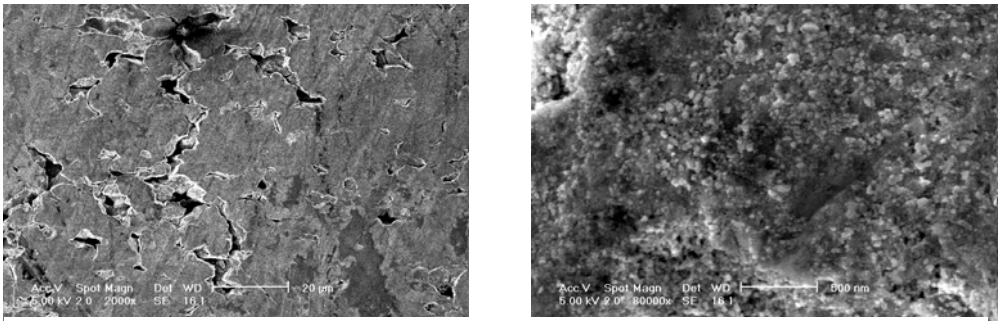

(a) Run#6-A (supercritical temperature)

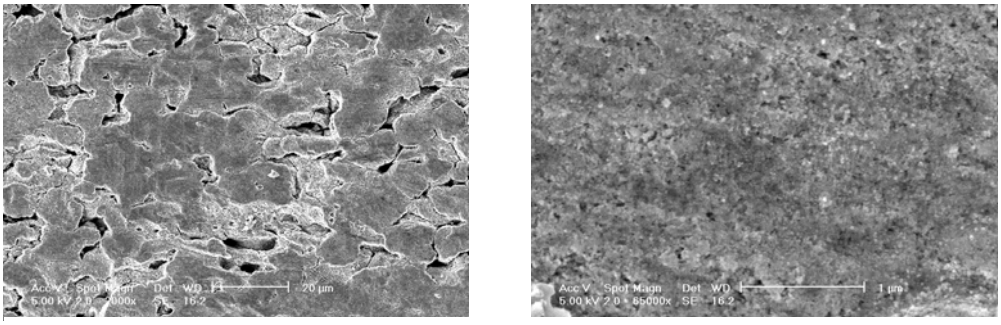

(b) Run#6-C (subcritical temperature)

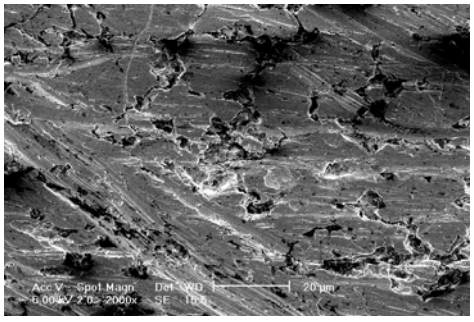

(c) MC wire surface (as received)

Figure B.4 ESEM images on surface oxides for Run#6 (MC). The left-hand images are in low magnification and the right-hand images are in high magnification.

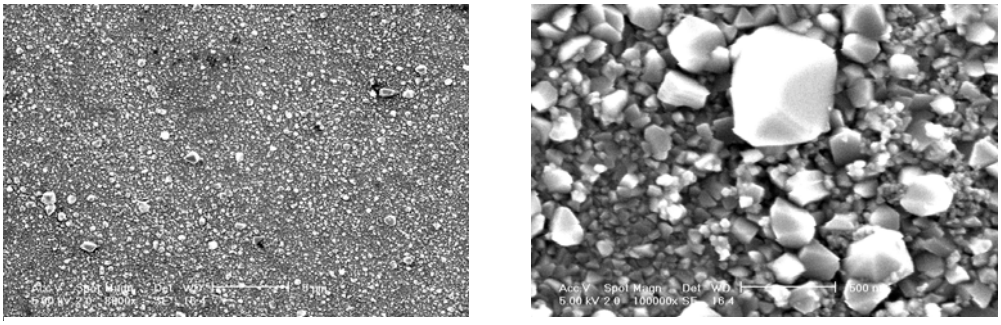

(a) Run#7-A (supercritical temperature)

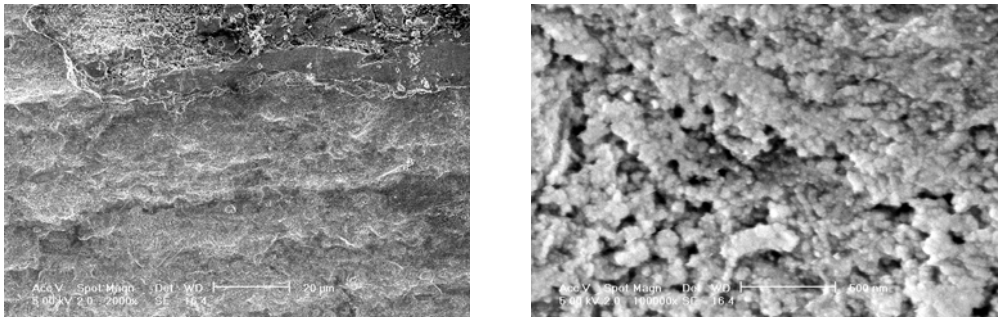

(b) Run#7-C (subcritical temperature)

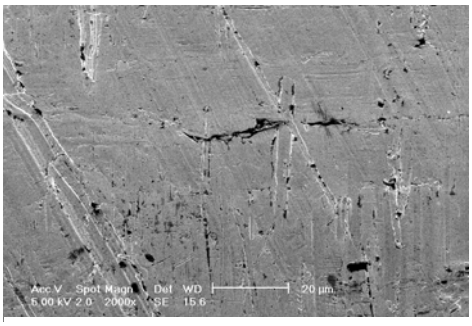

(c) Alloy33 wire surface (as received)

Figure B.5 ESEM images on surface oxides for Run#7 (Alloy 33). The left-hand images are in low magnification and the right-hand images are in high magnification.

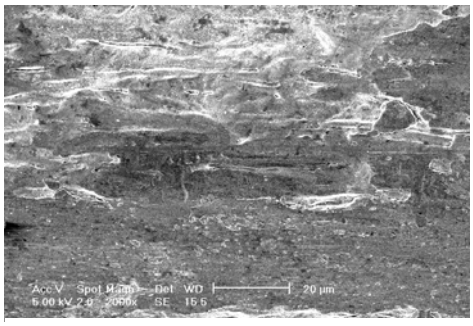
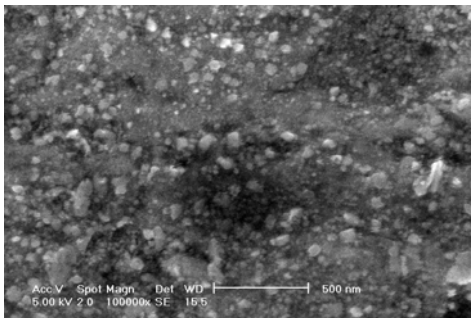

(a) Run#8-A (supercritical temperature)


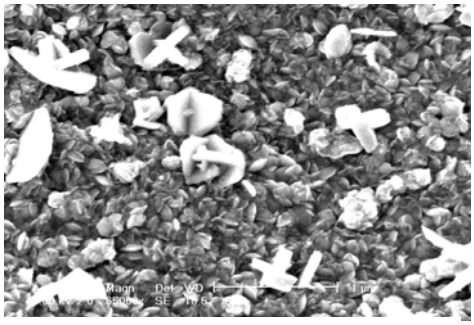

(b) Run#8-C (subcritical temperature)

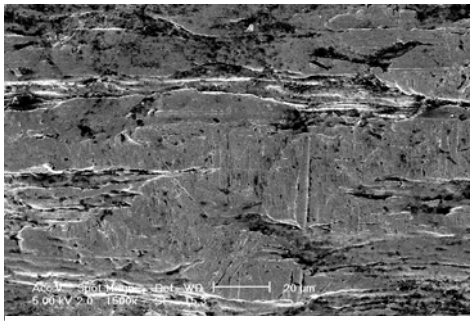

(c) C-2000 wire surface (as received)

Figure B.6 ESEM images on surface oxides for Run#8 (C-2000). The left-hand images are in low magnification and the right-hand images are in high magnification.

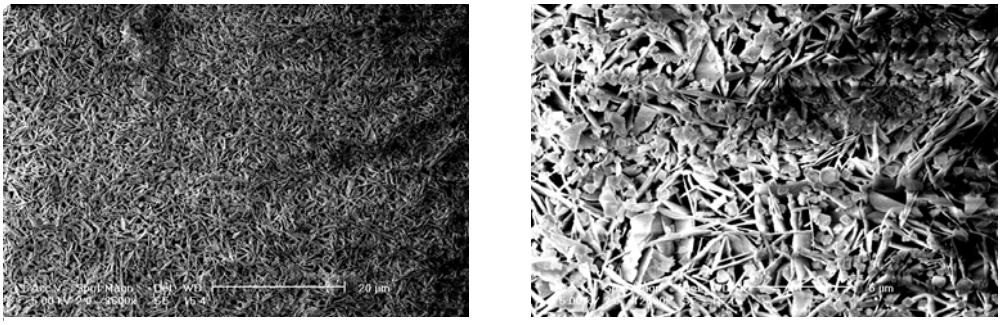

(a) Run#10-A(supercritical temperature)

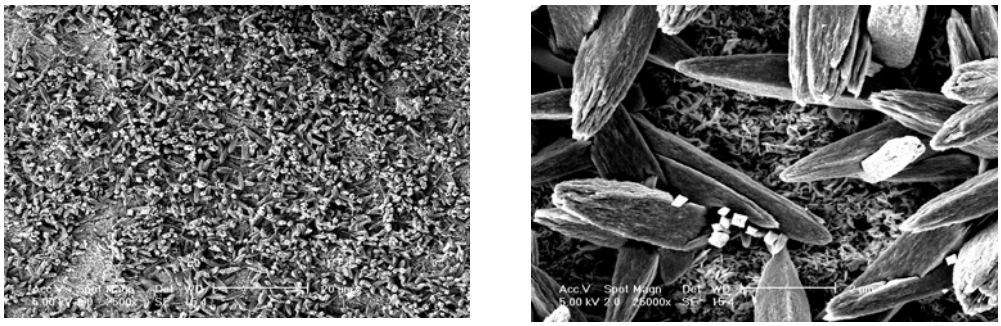

(b) Run#10-C (subcritical temperature)

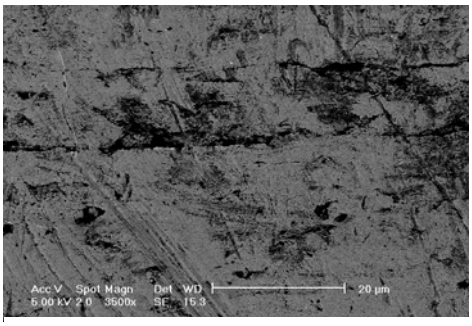

(c) B-2 wire surface (as received)

Figure B.7 ESEM images on surface oxides for Run#10 (B-2). The left-hand images are in low magnification and the right-hand images are in high magnification.

Appendix C

Additional Experimental Results (Nickel-base alloys, wires)

The diffraction pattern obtained from each alloy in sections of A, B, C, and D are presented. These are obtained from the surface of tested wire samples.

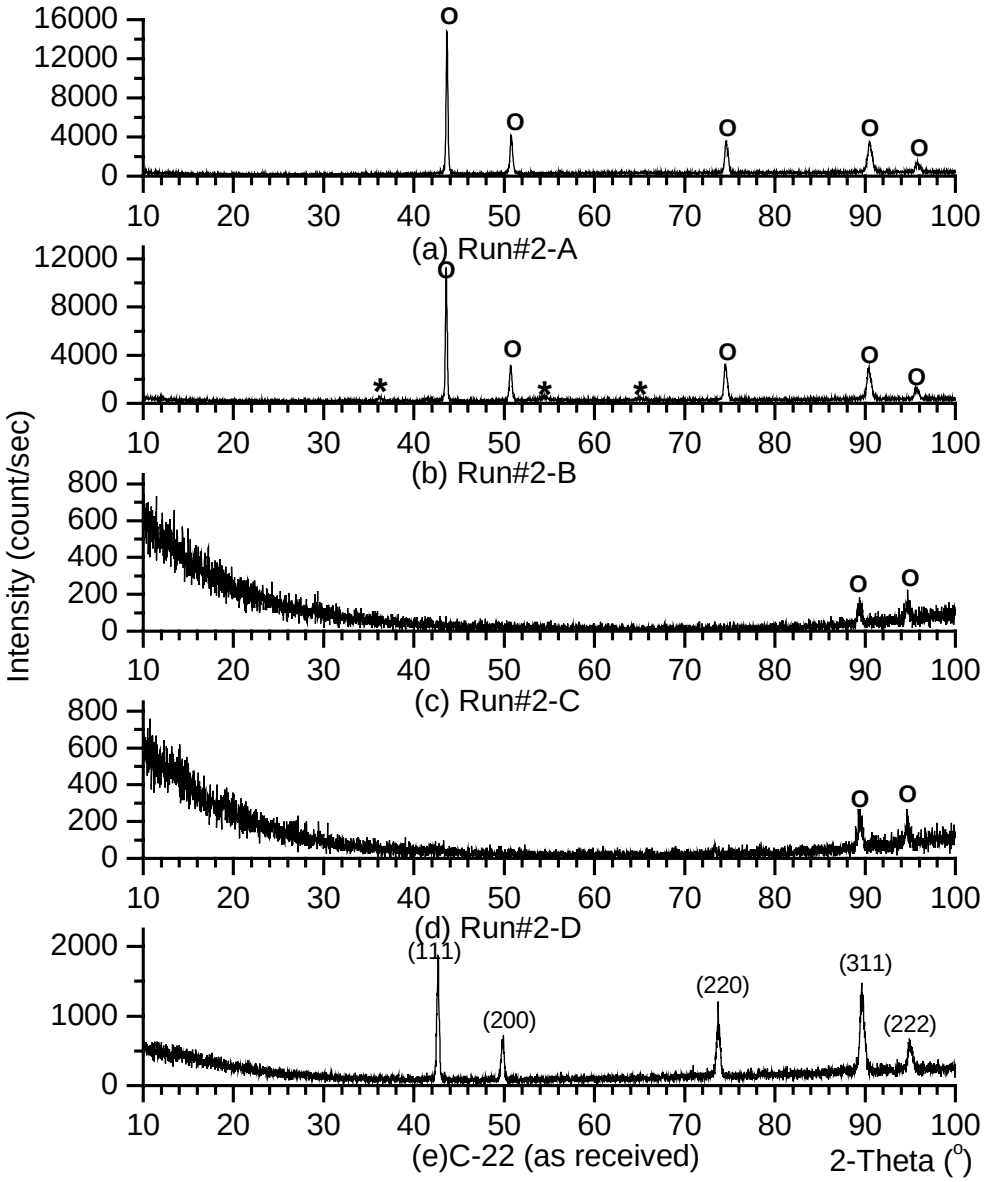

Figure C.1 XRD patterns for Run#2 (C-22). (e) FCC-phase peaks are indicated by Miller indices. Peaks are indicated by *o* when they match the peak position from (e). Peaks are indicated by * when they are generated from the oxide phase.

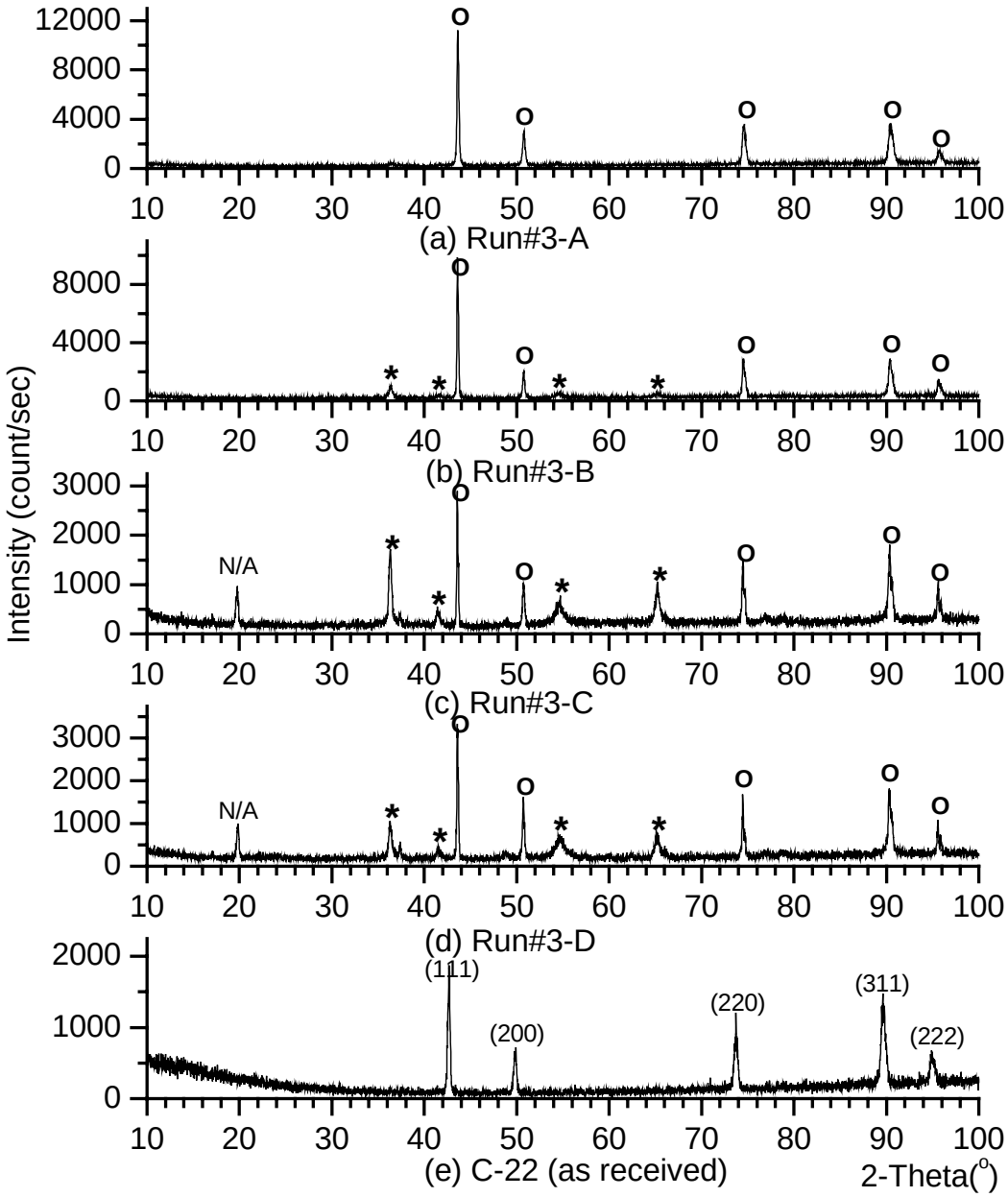

Figure C.2 XRD patterns for Run#3 (C-22). (e) FCC-phase peaks are indicated by Miller indices. Peaks are indicated by *o* when they match the peak position from (e). Peaks are indicated by * when they are generated from the oxide phase. N/A represents peaks from the adhesive tape used for sample mounting.

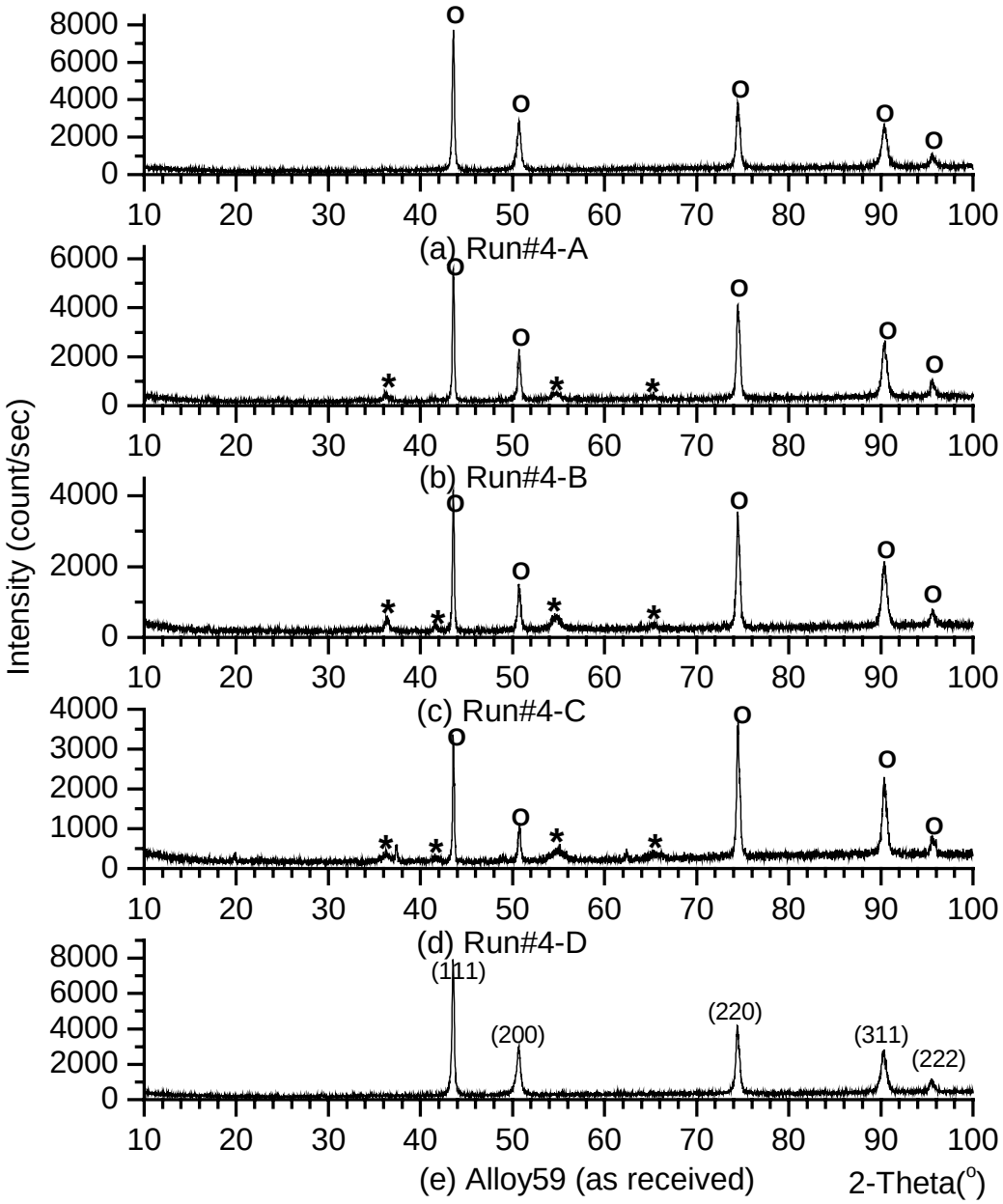

Figure C.3 XRD patterns for Run#4 (Alloy 59). (e) FCC-phase peaks are indicated by Miller indices. Peaks are indicated by *o* when they match the peak position from (e). Peaks are indicated by * when they are generated from the oxide phase.

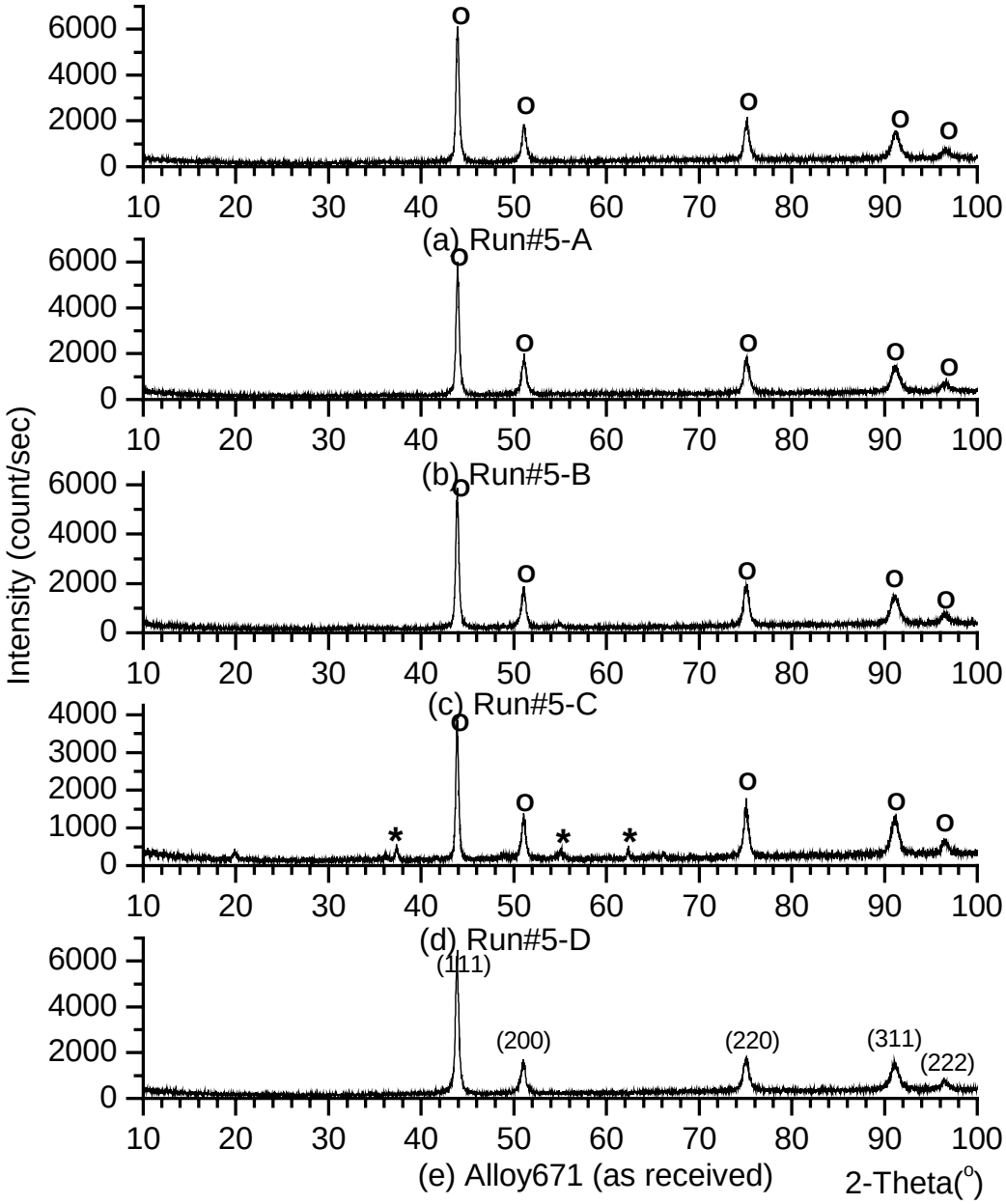

Figure C.4 XRD patterns for Run#5 (Alloy671). (e) FCC-phase peaks are indicated by Miller indices. Peaks are indicated by *o* when they match the peak position from (e). Peaks are indicated by * when they are generated from the oxide phase.

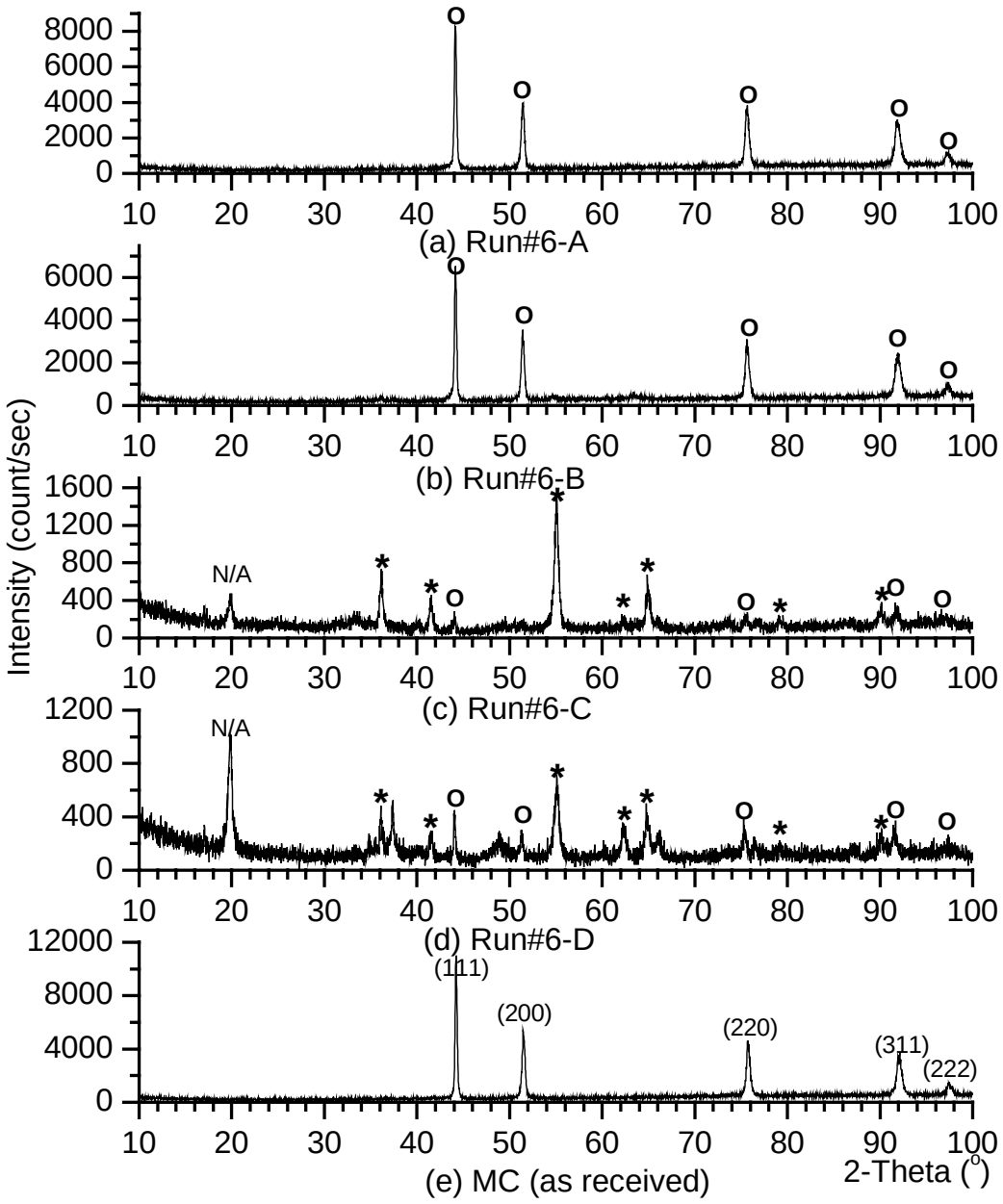

Figure C.5 XRD patterns for Run#6 (MC). (e) FCC-phase peaks are indicated by Miller indices. Peaks are indicated by *o* when they match the peak position from (e). Peaks are indicated by * when they are generated from the oxide phase. N/A represents peaks from the adhesive tape used for sample mounting.

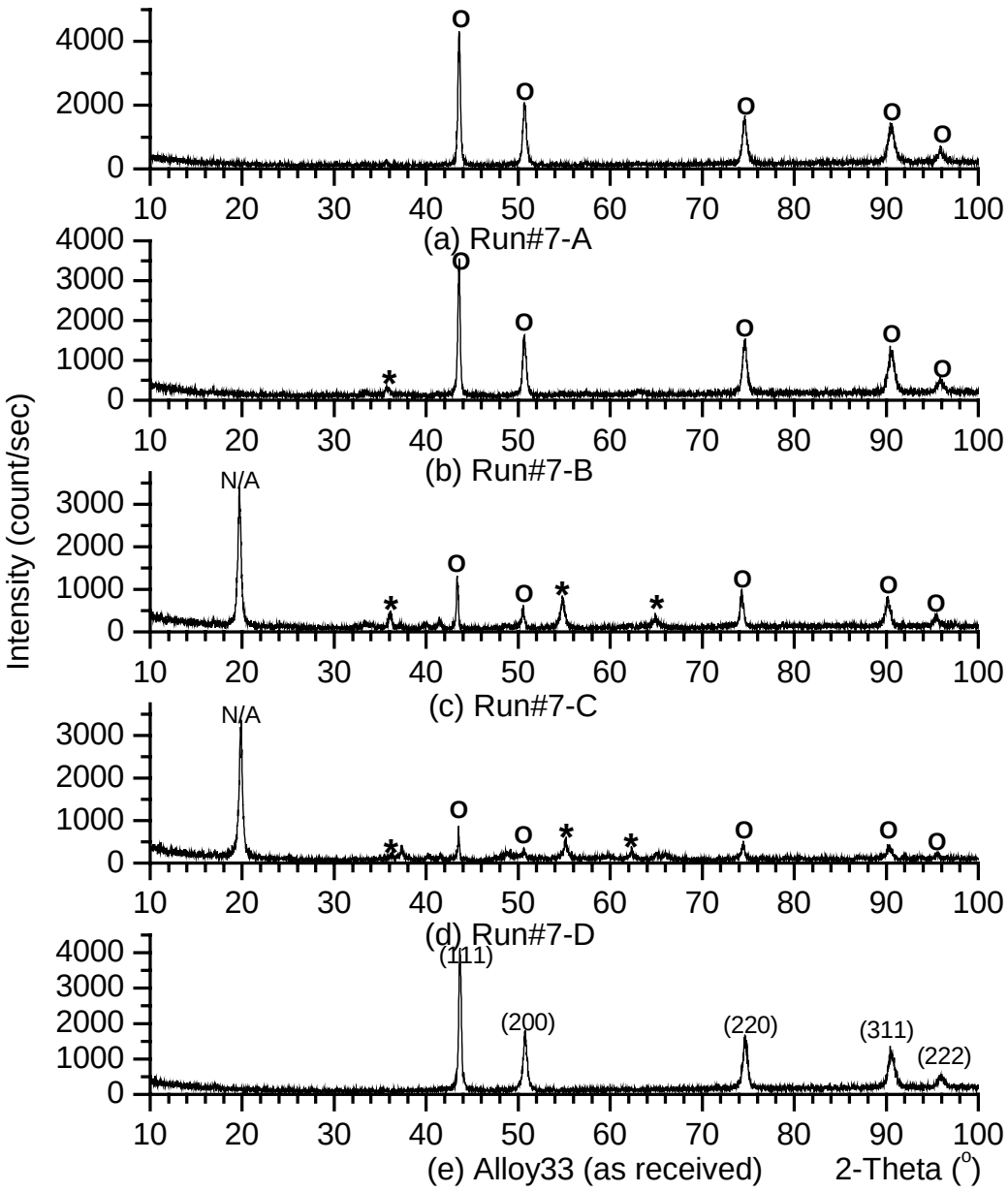

Figure C.6 XRD patterns for Run#7 (Alloy 33). (e) FCC-phase peaks are indicated by Miller indices. Peaks are indicated by *o* when they match the peak position from (e). Peaks are indicated by * when they are generated from the oxide phase. N/A represents peaks from the adhesive tape used for sample mounting.

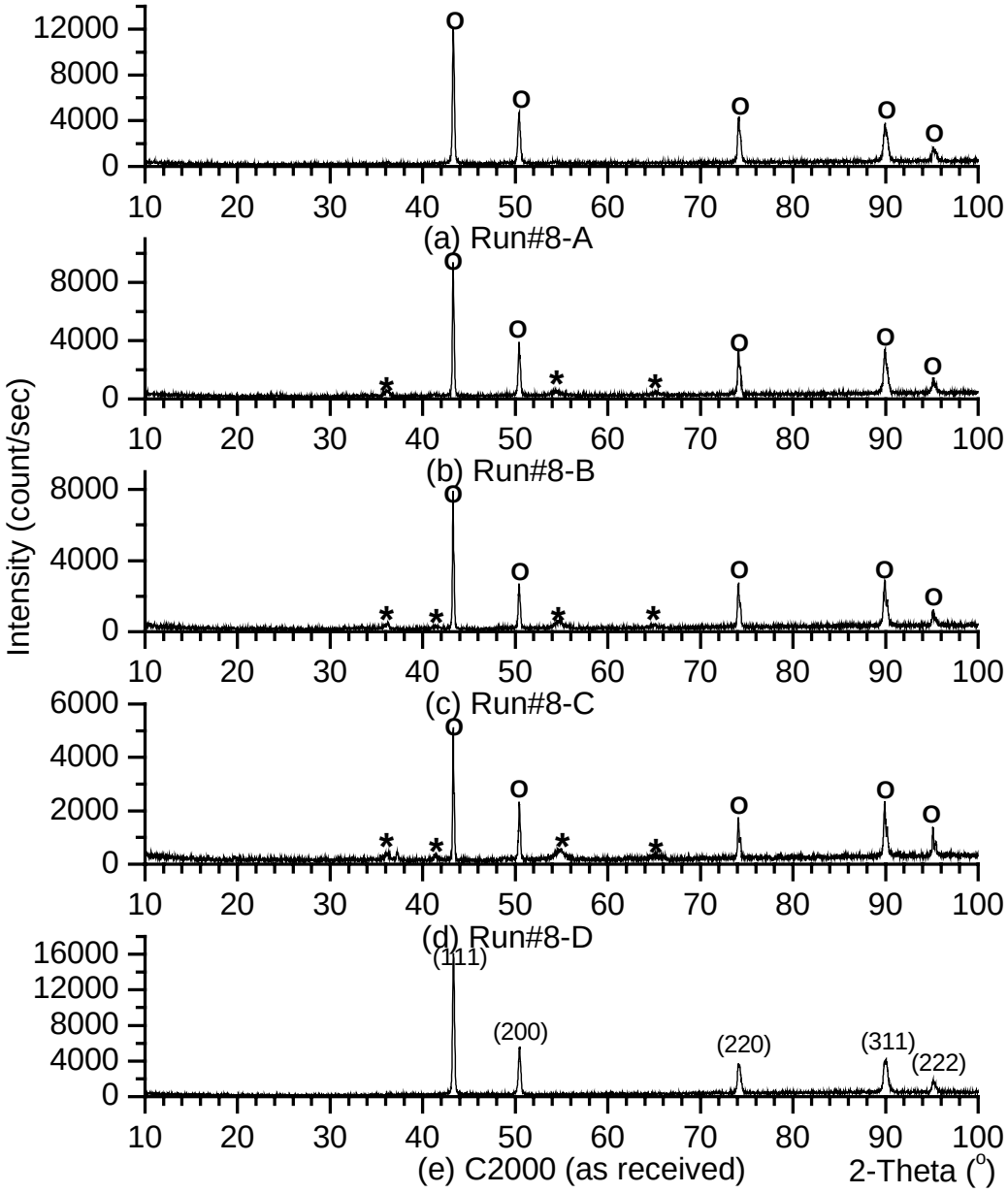

Figure C.7 XRD patterns for Run#8 (C-2000). (e) FCC-phase peaks are indicated by Miller indices. Peaks are indicated by *o* when they match the peak position from (e). Peaks are indicated by * when they are generated from the oxide phase.

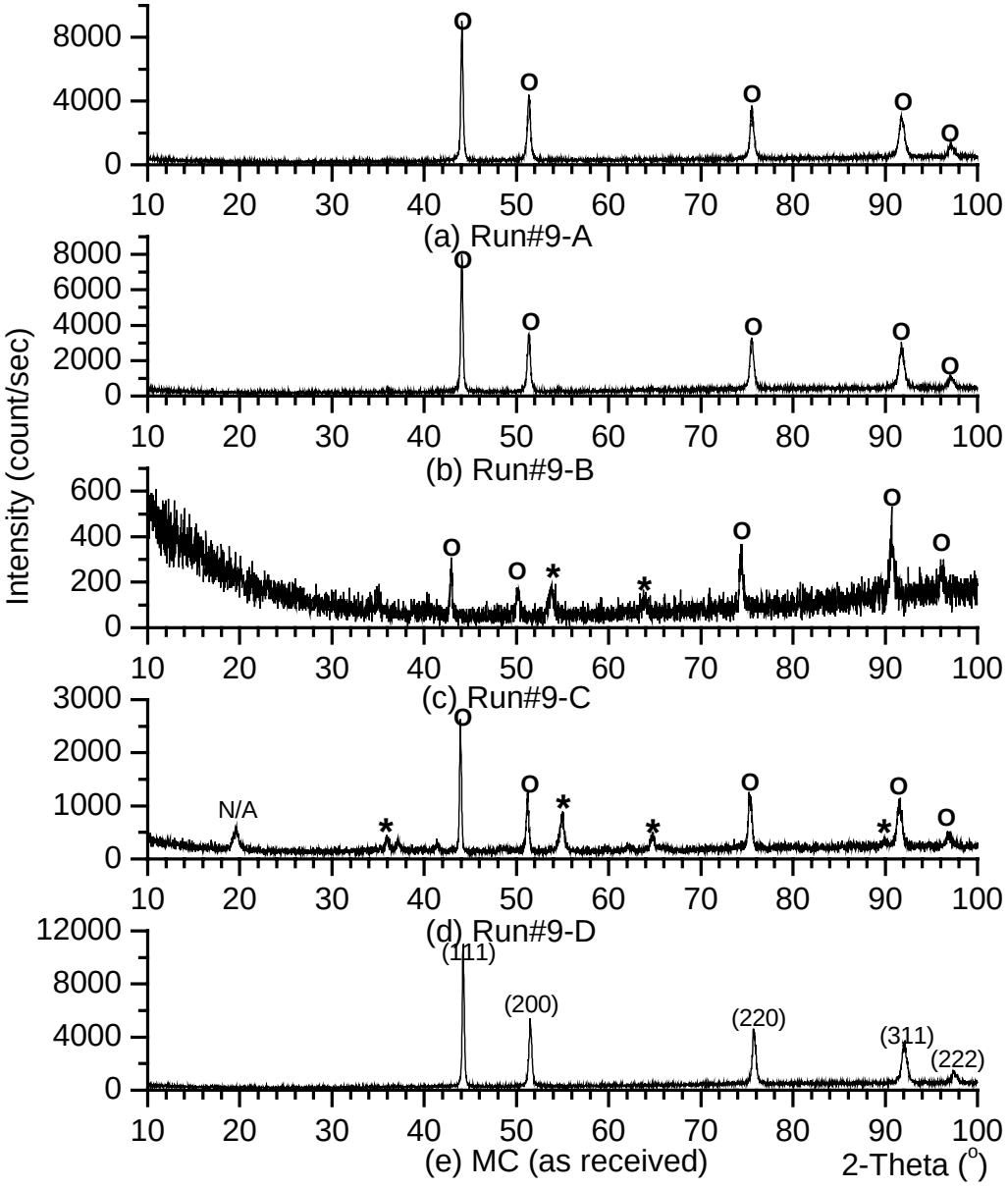

Figure C.8 XRD patterns for Run#9 (MC). (e) FCC-phase peaks are indicated by Miller indices. Peaks are indicated by *o* when they match the peak position from (e). Peaks are indicated by * when they are generated from the oxide phase. N/A represents peaks from the adhesive tape used for sample mounting.

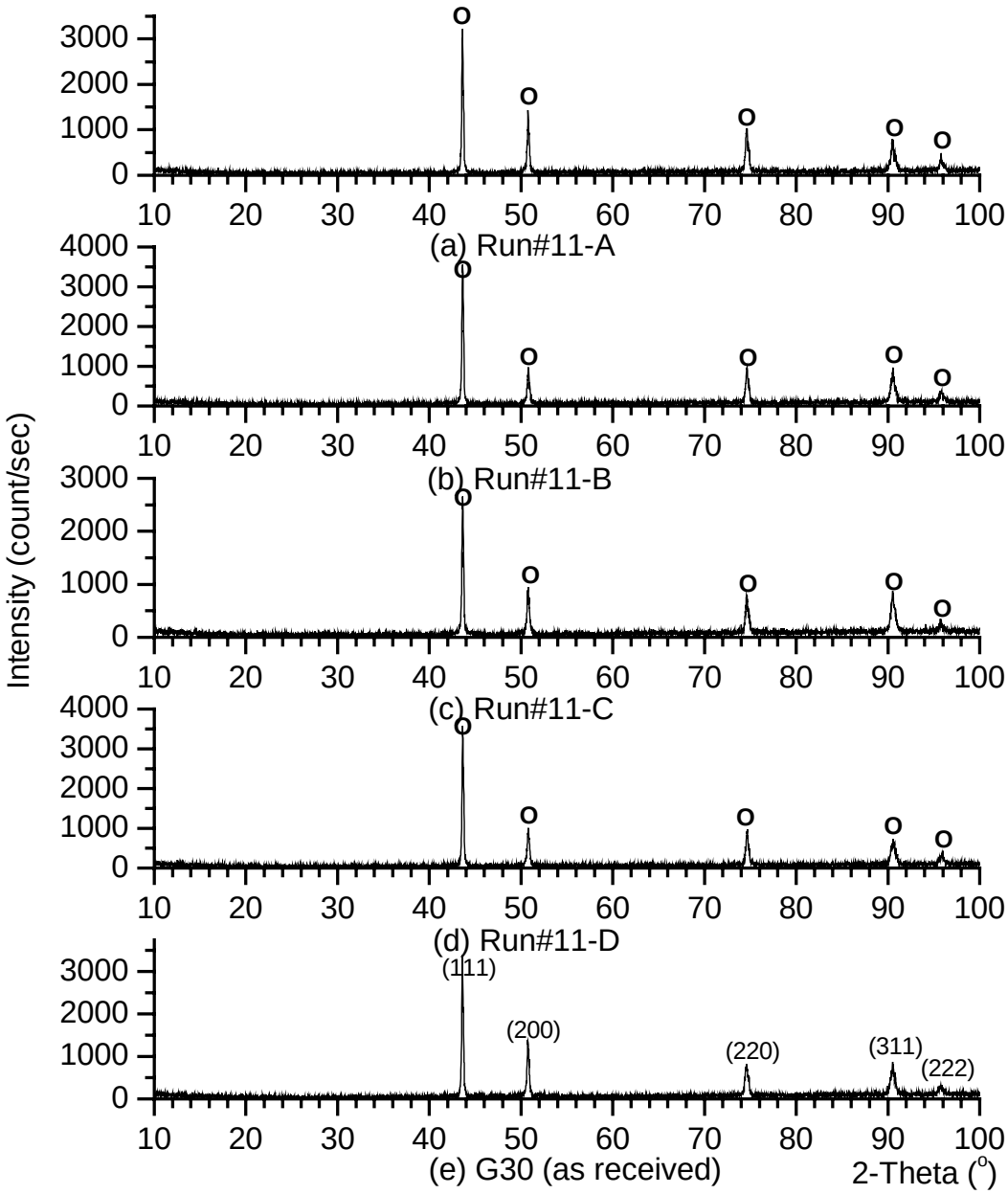

Figure C.9 XRD patterns for Run#11 (G30). (e) FCC-phase peaks are indicated by Miller indices. Peaks are indicated by *o* when they match the peak position from (e). Peaks are indicated by * when they are generated from the oxide phase.

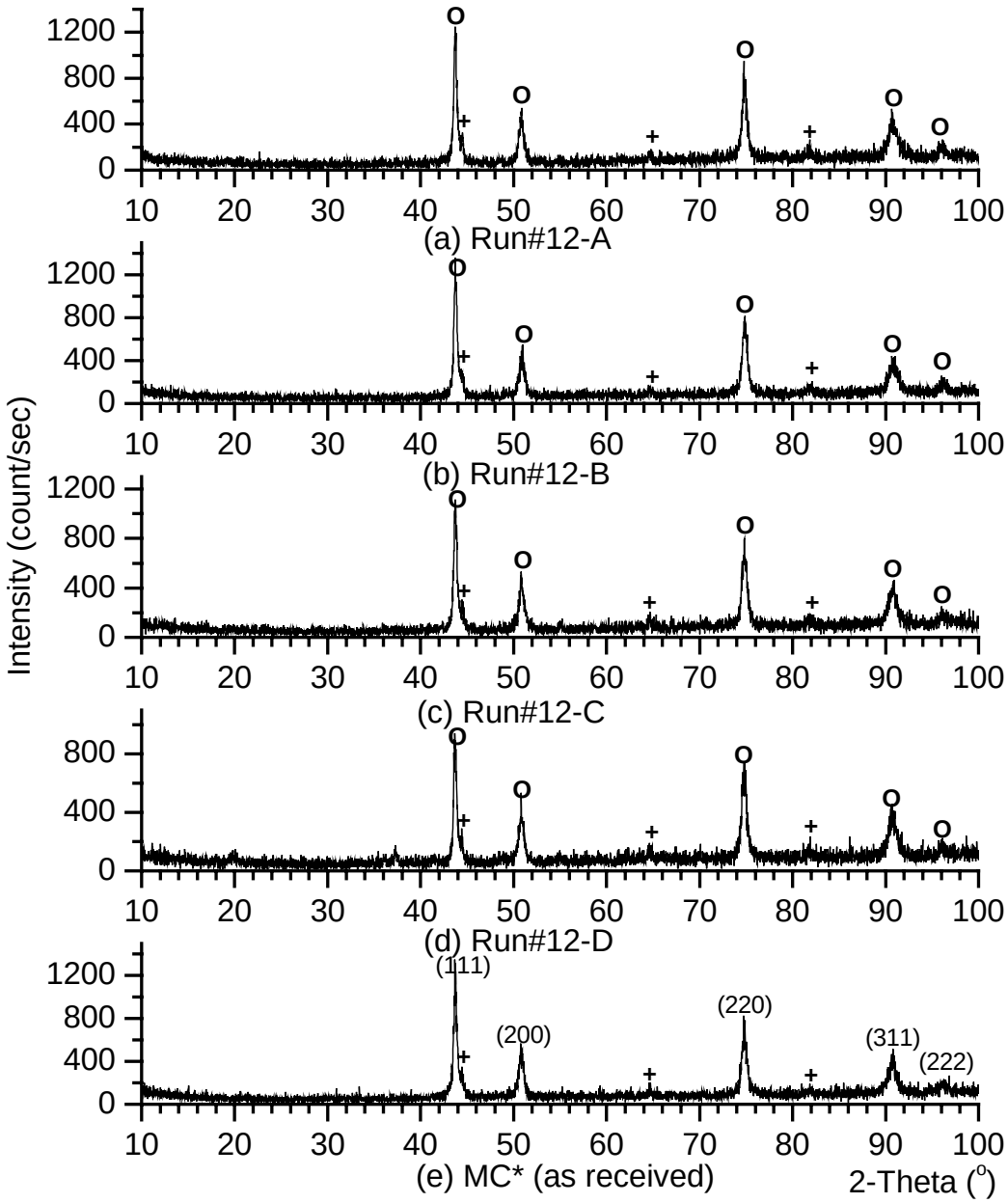

Figure C.10 XRD patterns for Run#12 (MC*). (e) Ni-rich FCC-phase peaks are indicated by Miller indices. Cr-rich BCC-phase peaks are indicated by + in all patterns. Peaks are indicated by *o* when they match the FCC peak position from (e). Peaks are indicated by * when they are generated from the oxide phase.

Appendix D

Additional Experimental Results (Nickel-base alloys, wires)

The XPS survey spectra obtained from each alloy in sections of A, B, C, and D are presented. These are obtained from the surface of tested wire samples.

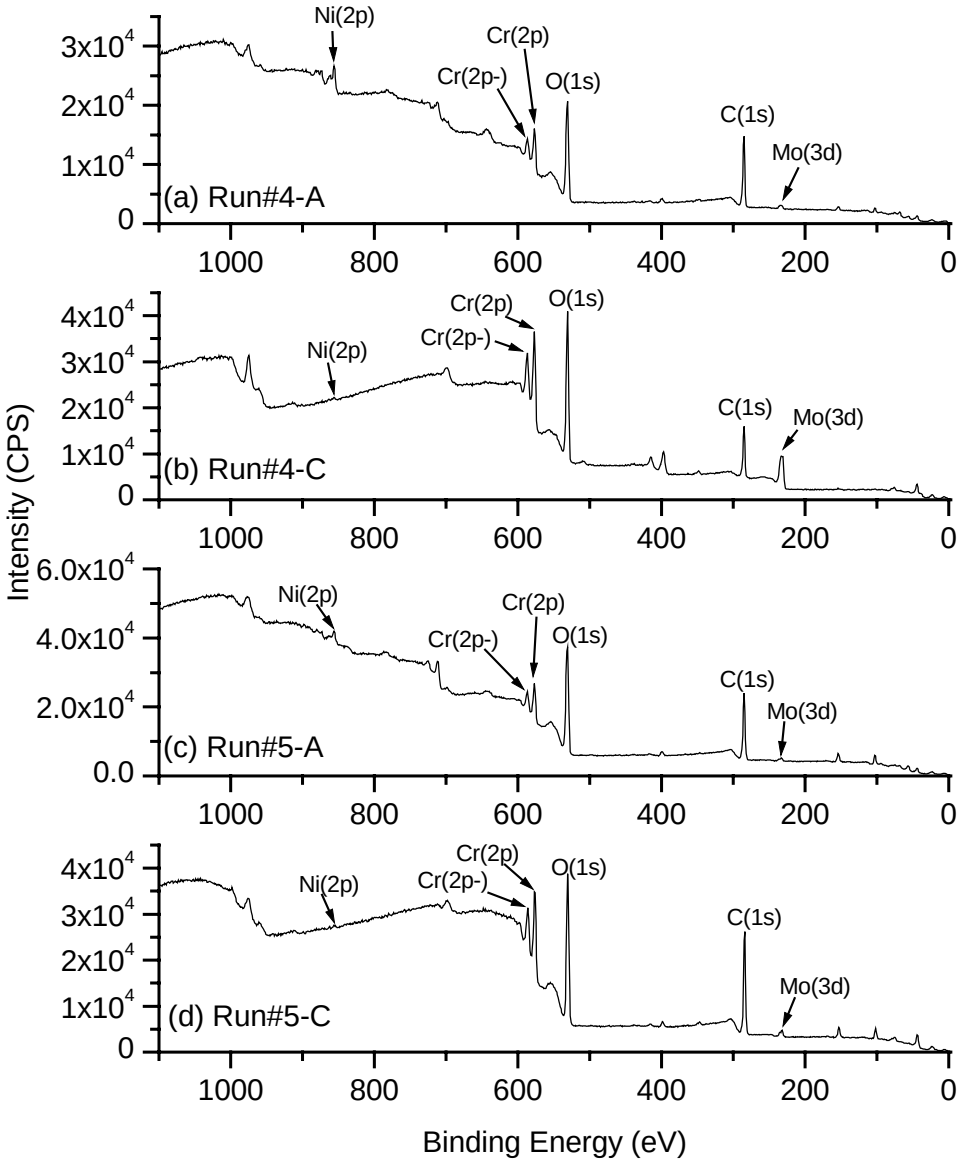

Figure D.1 XPS survey spectra for Run#4 (Alloy 59) and Run#5 (Alloy 671). Run#-A: supercritical temperature. Run#-C: high subcritical temperature. Spin-orbit splitting of Cr is represented by Cr(2p-) for Cr($2p_{1/2}$), and Cr(2p) for Cr($2p_{3/2}$).

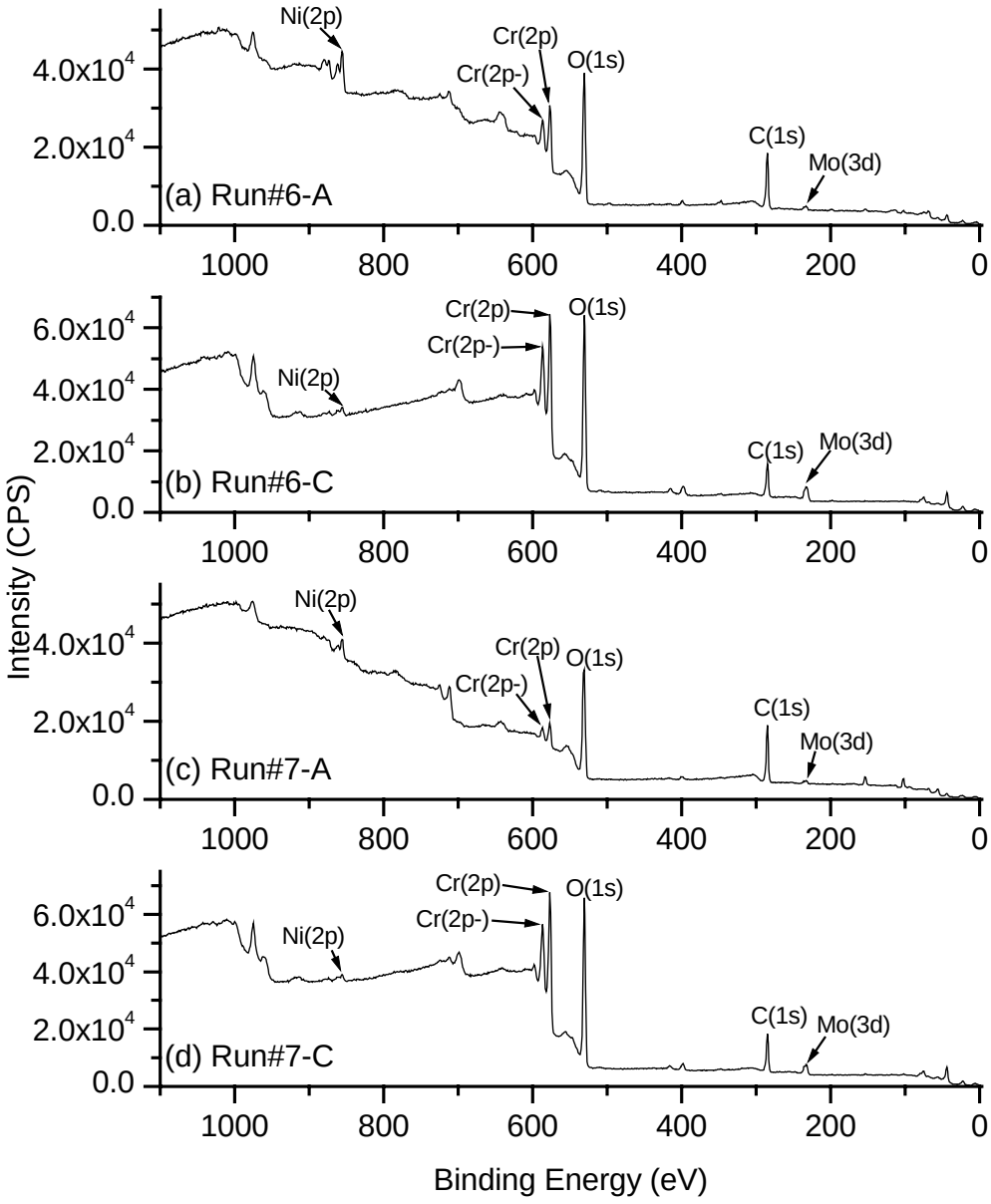

Figure D.2 XPS survey spectra for Run#6 (MC) and Run#7 (Alloy 33). Run#-A: supercritical temperature. Run#-C: high subcritical temperature. Spin-orbit splitting of Cr is represented by Cr(2p-) for Cr($2p_{1/2}$), and Cr(2p) for Cr($2p_{3/2}$).

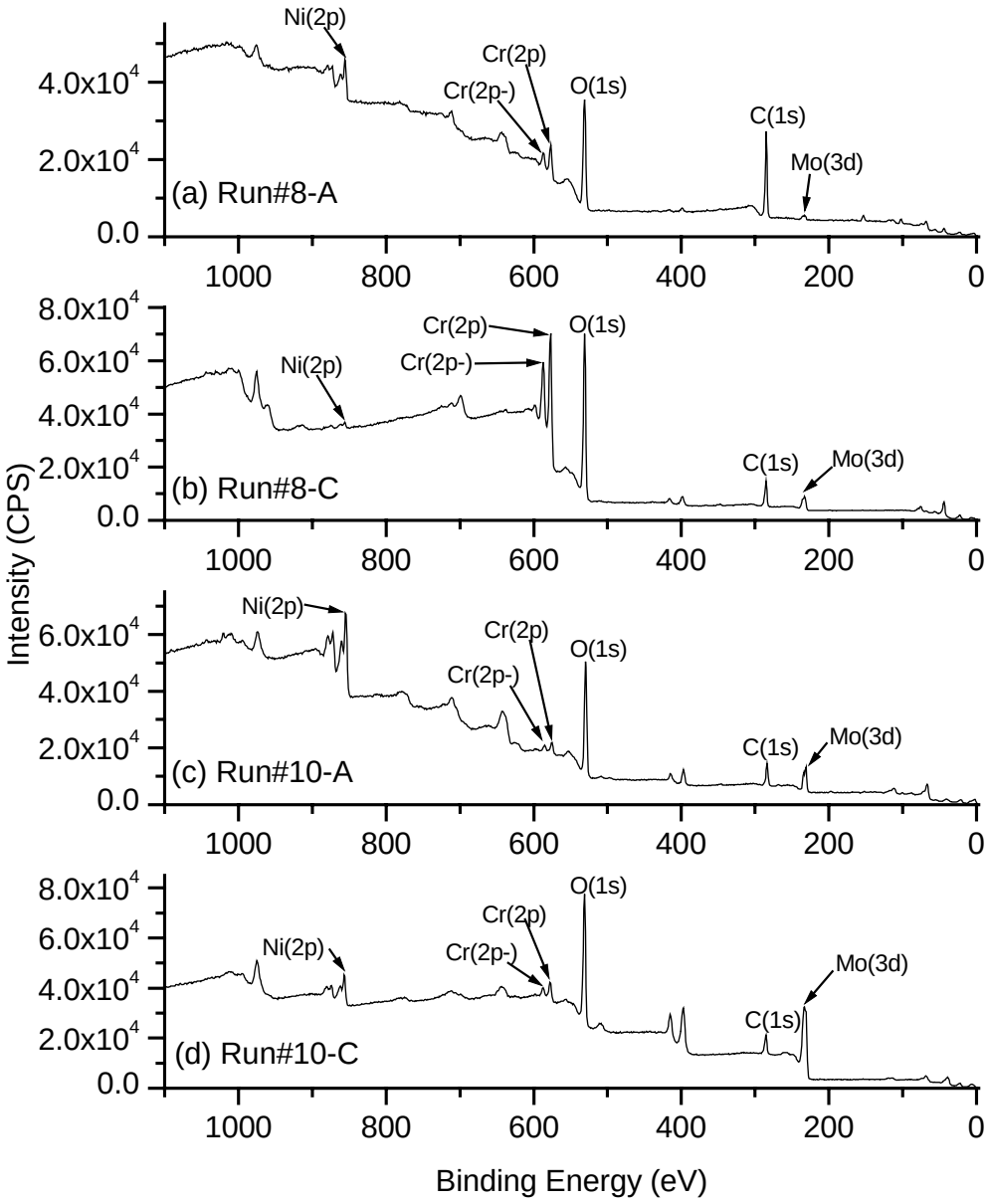

Figure D.3 XPS survey spectra for Run#8 (C-2000) and Run#10 (B-2). Run#-A: supercritical temperature. Run#-C: high subcritical temperature. Spin-orbit splitting of Cr is represented by Cr(2p-) for Cr($2p_{1/2}$), and Cr(2p) for Cr($2p_{3/2}$).

Appendix E

E-pH measurement results at Penn State University

Summary of Experimental tests and calculations at Penn State University is presented as reported.

Table E.1 pH measurements of aqueous solution that were in contact with Hastelloy C-276 tubes at 350℃.

Test#1		**Test#2**	
Duration (hour)	70	**Duration (hour)**	53
Temperature (℃)	350	**Temperature (℃)**	350
Pressure (MPa)	27.3	**Pressure (MPa)**	27.3
Reference solution1	0.01m HCl + 0.1m NaCl	**Reference solution1**	0. 01m HCl + 0.1m NaCl
Reference solution2	0.01m HCl + 0.1m NaCl	**Reference solution2**	0. 001m HCl + 0.1m NaCl
Reference electrode Solution	0.1m NaCl	**Reference electrode Solution**	0.1m NaCl
Test solution	0.1m NaCl	**Test solution**	0. 1m NaCl + 0.1m HCl
E_1 **(mV)**	840	E_1 **(mV)**	530
E_2 **(mV)**	726	E_2 **(mV)**	488
E_x **(mV)**	672	E_x **(mV)**	630
E_{d1} **(mV)**	-0.6	E_{d1} **(mV)**	-0.6
E_{d2} **(mV)**	-0.1	E_{d2} **(mV)**	-0.1
E_{dx} **(mV)**	0.0	E_{dx} **(mV)**	-4.4
pH_1	2.90	pH_1	2.90
pH_2	3.89	pH_2	3.89
pH_x	4.36	pH_x	0.48
$pH_x(cal)$	5.84	$pH_x(cal)$	1.96
ECP	440mV(Ag|AgCl)	*ECP*	-35mV(Ag|AgCl)

Reference solution: the solutions that were used to calibrate the YSZ pH eletrode.

Reference electrode solution: the solution that was in the Ag|AgCl flow-through reference electrode.

Test solution: the solution that was pumped into the Hastelloy C-276 tube; the pH of the solution may change due to corrosion.

E_1: the potential of the YSZ pH electrode vs. the reference electrode for Reference solution 1.

E_2: the potential of the YSZ pH electrode vs. the reference electrode for Reference solution 2.

E_x: the potential of the YSZ pH electrode vs. the reference electrode for test solution.

E_{d1}: the isothermal liquid junction potential between Reference solution 1 and the reference electrode solution.

E_{d2}: the isothermal liquid junction potential between Reference solution 2 and the reference electrode solution.

E_{dx}: the isothermal liquid junction potential between the test solution and the reference electrode solution.

pH_1: pH of Reference solution 1.

pH_2: pH of Reference solution 2.

pH_x: pH of the test solution calculated by:

$$pH_x = pH_1 + (pH_2 - pH_1)\frac{(E_x - E_{dx}) - (E_1 - E_{d1})}{(E_2 - E_{d2}) - (E_1 - E_{d1})} \qquad \text{(E.1)}$$

$pH_x(cal)$: The pH value that was determined by a calculation using the association/dissociation equilibrium constants as well as the equations of electroneutrality and mass balance without taking into account any corrosion process.

ECP: This value was obtained by measuring the electrical potential difference between the Hastelloy C-276 tube and Ag/AgCl electrode, calculating and eliminating the thermal liquid junction potential.

Appendix F

Phenomenological model

The phenomenological model is described in section 4.2.1. Equations (4.14-17) are combined together with respect to the molality of hydrogen ion to give:

$$m_{H^+}^3 + \frac{K_d}{\gamma_\pm^2} m_{H^+}^2 - \frac{(K_d m_{HCl}^0 + K_W)}{\gamma_\pm^2} m_{H^+} - \frac{K_d K_W}{\gamma_\pm^4} = 0 . \qquad \text{(F.1)}$$

By combining equation (F.1) with the obtained expression for the activity coefficient in equation (4.23), we obtain following expression:

$$m_{H^+}^3 + K_d \cdot m_{H^+}^2 \cdot \exp(2 \cdot \ln(10) \cdot A \cdot \sqrt{m_{H^+}} - (K_d m_{HCl}^0 + K_W) m_{H^+} \exp(2 \cdot \ln(10) \cdot \sqrt{m_{H^+}})$$

$$- K_d K_W \exp(4 \cdot \ln(10) \cdot A \sqrt{m_{H^+}}) = 0 \qquad \text{(F.2)}$$

Equation (F.2) is solved numerically using matlab. Matlab programming and numerical results are presented at constant pressure of 25 MPa.

ρ: density of pure water in g/㎤.

ε: static dielectric constant of water.

K_W: ionic dissociation constant of pure water in $(mol/Kg)^2$.

K_d: the dossociation constant of HCl in (mol/Kg).

Matlab programming

……

```
%calculate ionic product constant of HCl
clear all;
load ion_prod; % load K_w, Temp_K, density and dielectric constant of pure water
m0 =    0.01; % initial molality of HCl
format long;
K_d=10.^(-5.405+3874.9./Temp_K + 13.93.*log10(rho_r) ); %ionic dissociation constant of HCl
F = 96485.3; % Faraday constant
Na = 6.022e23; % Avogardo number
R = 8.314; % gas constant
e0 = 8.854e-12; % dielctric constant of vacuum
n= length(K_d);
x0=m0; %initial guess
```

```
options=optimset('tolFun',1e1,'tolX',1e1,'Largescale','on','Display','off');
for i= 1: n
    a=K_d(i); b=K_w(i);
    A(i)=F^3/4/pi/Na/log(10)*sqrt(rho_r(i)*1000/2/(diel(i)*e0)^3/R^3/Temp_K(i)^3);
    c=A(i)*log(10)*2;
    disp(sprintf('%d th case',i))
    x = conti_Newton(a,b,c);
    m(i)=x;
    x_poly=roots([1, a, -(0.01*a+b), -a*b]);
    index=find(x_poly>0);
    m_comp(i)=x_poly(index);
end

%calculate the remaining constant values
coef = 10.^(-A.*sqrt(m)); %activity coefficient by limiting debye-huckel theory
m_OH = K_w./m./coef.^2;
m_Cl = m - m_OH;
m_HCl = 0.01 - m_Cl ;
figure;
subplot(2,2,1);
plot(Temp_K-273.15,log10(K_d)) ;    %hydrogen dissociation constant
xlabel('Temperature[^oC]');
ylabel('log K_d');
subplot(2,2,2);
plot(Temp_K-273.15,log10(m),Temp_K-273.15,log10(m_OH),':',Temp_K-273.15,log10(m_HCl),'--
'); %proton, OH molal concentration(Debye-Huckel)
xlabel('Temperature[^oC]');
ylabel('log m [molality]')
legend('m_H_+','m_O_H_-','m_H_C_l');
subplot(2,2,4);
plot(Temp_K-273.15,coef);
xlabel('Temperature[^oC]');
ylabel('\gamma');
subplot(2,2,3);
plot(Temp_K-273.15,m,Temp_K-273.15,m_HCl,'r--');  %proton,  HCl  molal  concentration(Debye-
Huckel)
```

```
xlabel('Temperature[^oC]');
ylabel('m [molality]')
legend('m_H_+','m_H_C_l');
Rate = (rho_r./rho_r(1)).^2.*(m./m(1)).*exp(-50000/R.*(1./Temp_K-1./Temp_K(1)));% relative corrosion rate
figure;
subplot(2,1,1);
plot(Temp_K-273.15, Rate);
xlabel('Temperature[^oC]');
ylabel('R/R^o');
subplot(2,1,2);
plot(Temp_K-273.15, log10(Rate));
xlabel('Temperature[^oC]');
ylabel('log(R/R^o)');
Export = [Temp_K' rho_r' diel' K_w' K_d' m' m_OH' m_HCl' m_Cl' coef' Rate'];
save export_data Export  -ascii -double -tabs;


function [x,f]=conti_Newton(a,b,c,option)
% CONTI_NEWTON: Newton's method with continuation scheme to solve the concentration problem.
% The main idea of behind this function is to schedule the c value from zero to c, and use the solution to the previous c as the initial condition for the current step.
% Usage: [x,f]=conti_Newton(a,b,c)
if (nargin<4), option='m'; end
% --- Some parameters for the Newton loop. --- %
% Maximum iterations for the inner Newton loop.
max_iter=100;
% Tolerances for the Newton's method.
abs_tol=1e-6;
rel_tol=1e-4;
% Maximum step size.
max_step=0.01*0.1;
% Minimum step size for the continuation scheme.
min_step=1e-12;
% --- Finding the first initial condition. --- %
```

```
% When alpha is zero, f(x;a,b,alpha) reduces to a simple polynomial, and the roots can be easily found.
x_poly=roots([1, a, -(0.01*a+b), -a*b]);
index=find(x_poly>0);
% There should be only one solution.
if (length(index)>1), error('There are more than one solution to the case c=0.'); end
% Set the initial condition for the next step.
x=x_poly(index);
% --- The outer loop is for the continuation scheme. --- %
% Save the previous initial guess.
x_prev=x;
% Set the continuation parameter
alpha=c/100;
dalpha=alpha;
% The loop for continuation scheme.
while (alpha<c)
    % --- The actual Newton method for the given alph starts here. --- %
    % Evaluate the initial function value.
    init_f=func(x,a,b,alpha);
    f=init_f;
    % The Newton loop:
    for iNewton=1:max_iter+1
        % Find the direction.
        dx=-f/dfunc_x(x,a,b,alpha);
        if (abs(dx)>max_step), dx=sign(dx)*max_step; end
        % Move to the new point.
        x=x+dx;
        % Evaluate the new function value and check the convergence criterion.
        f=func(x,a,b,alpha);
        if (abs(f)<(abs_tol+init_f*rel_tol) & abs(dx)<(abs_tol+rel_tol)), break, end
    end
    % --- End of the Newton loop, start scheduling alpha. --- %
    % In case the Newton loop converges,
    if (iNewton<max_iter+1)
        out=sprintf('alpha=%e converged where c=%e',alpha,c);
        % Update the previous initial condition.
```

```
            x_prev=x;
            % Some derivatives at the current point. Used to extrapolate the initial guess.
%             df_x=dfunc_x(x,a,b,alpha);
%             df_alpha=dfunc_alpha(x,a,b,alpha);
            % Increment the step size and move on the the next alpha value.
            dalpha=2*dalpha;
            alpha=alpha+dalpha;
            if (alpha>c), alpha=c; end
            % Extrapolate the initial guess to get a better one.
%             x=x-df_alpha*dalpha/df_x;
            if (option=='v'), disp(sprintf('%s; next alpha is %e.',out,alpha)); end
        else
            % Load the previous initial conditoin.
            x=x_prev;
            % Undo the alpha value and take a smaller step size.
            alpha=alpha-dalpha;
            dalpha=dalpha/2;
            if (dalpha<min_step), error('Step size too small; continuation scheme failed.'), end
            alpha=alpha+dalpha;
            if (option=='v'), disp(sprintf('failed to converge; trying alpha=%e.',alpha)); end
        end
    end % End: while (alpha<c)
    % --- Embedded functions to evaluate the function value and its derivative. --- %
    function y=func(x,a,b,c)
    y=x^3+a*exp(c*sqrt(x))*x^2-(0.01*a+b)*exp(c*sqrt(x))*x-a*b*exp(2*c*sqrt(x));
    function y=dfunc_x(x,a,b,c)
    y=3*x^2+0.5*a*c*exp(c*sqrt(x))*x^(3/2)+2*a*exp(c*sqrt(x))*x...
        -0.5*(0.01*a+b)*c*exp(c*sqrt(x))*sqrt(x)-(0.01*a+b)*exp(c*sqrt(x))-
    a*b*c*exp(2*c*sqrt(x))/sqrt(x);
    function y=dfunc_alpha(x,a,b,c)
    y=a*exp(c*sqrt(x))*x^(5/2)-(0.01*a+b)*exp(c*sqrt(x))*x^(3/2)-2*a*b*exp(2*c*sqrt(x))*sqrt(x);
```

……

Numerical Results

T (℃)	ρ	ε	Log (Kw)	Log(Kd)	Log(m_{H^+})	Log(m_{OH^-})	Log(m_{HCl})	$\gamma_{\pm}$	Log(R/R^0)
0	1.012	88.98	-14.827	8.854	-2.000	-12.730	-12.865	0.894	0.000
5	1.012	87.00	-14.621	8.597	-2.000	-12.523	-12.614	0.894	0.172
10	1.011	85.06	-14.426	8.348	-2.000	-12.328	-12.370	0.893	0.337
15	1.010	83.15	-14.243	8.105	-2.000	-12.144	-12.132	0.892	0.496
20	1.009	81.27	-14.068	7.869	-2.000	-11.969	-11.901	0.892	0.650
25	1.008	79.43	-13.903	7.640	-2.000	-11.803	-11.676	0.891	0.798
30	1.006	77.63	-13.746	7.416	-2.000	-11.645	-11.456	0.890	0.941
35	1.005	75.86	-13.597	7.198	-2.000	-11.495	-11.242	0.889	1.080
40	1.003	74.14	-13.455	6.986	-2.000	-11.352	-11.033	0.888	1.213
45	1.001	72.45	-13.320	6.779	-2.000	-11.215	-10.830	0.887	1.343
50	0.999	70.80	-13.191	6.578	-2.000	-11.085	-10.631	0.886	1.468
55	0.996	69.19	-13.068	6.381	-2.000	-10.961	-10.436	0.885	1.589
60	0.994	67.62	-12.950	6.188	-2.000	-10.842	-10.246	0.883	1.706
65	0.991	66.08	-12.838	6.001	-2.000	-10.729	-10.061	0.882	1.820
70	0.988	64.58	-12.731	5.817	-2.000	-10.621	-9.879	0.881	1.930
75	0.986	63.11	-12.628	5.637	-2.000	-10.517	-9.701	0.880	2.037
80	0.983	61.68	-12.530	5.461	-2.000	-10.417	-9.527	0.878	2.140
85	0.980	60.28	-12.436	5.289	-2.000	-10.322	-9.357	0.877	2.241
90	0.976	58.91	-12.347	5.121	-2.000	-10.232	-9.189	0.876	2.338
95	0.973	57.58	-12.261	4.955	-2.000	-10.144	-9.026	0.874	2.433
100	0.970	56.28	-12.179	4.793	-2.000	-10.061	-8.865	0.873	2.525
105	0.966	55.01	-12.101	4.634	-2.000	-9.981	-8.707	0.871	2.615
110	0.963	53.77	-12.026	4.478	-2.000	-9.905	-8.552	0.870	2.702
115	0.959	52.56	-11.954	4.324	-2.000	-9.832	-8.400	0.868	2.786
120	0.955	51.38	-11.886	4.173	-2.000	-9.762	-8.250	0.867	2.868
125	0.951	50.22	-11.821	4.025	-2.000	-9.695	-8.103	0.865	2.948
130	0.947	49.09	-11.759	3.879	-2.000	-9.631	-7.958	0.863	3.026
135	0.943	47.99	-11.699	3.735	-2.000	-9.570	-7.815	0.862	3.101
140	0.939	46.92	-11.643	3.593	-2.000	-9.512	-7.675	0.860	3.175
145	0.935	45.86	-11.589	3.453	-2.000	-9.456	-7.536	0.858	3.247
150	0.930	44.83	-11.538	3.315	-2.000	-9.404	-7.400	0.856	3.316
160	0.921	42.85	-11.444	3.045	-2.000	-9.305	-7.132	0.853	3.450
170	0.912	40.95	-11.359	2.782	-2.000	-9.216	-6.871	0.849	3.578

180	0.902	39.13	-11.284	2.523	-2.000	-9.137	-6.616	0.844	3.698
190	0.892	37.38	-11.219	2.270	-2.000	-9.068	-6.365	0.840	3.813
200	0.881	35.71	-11.163	2.021	-2.000	-9.007	-6.119	0.836	3.922
210	0.870	34.10	-11.115	1.775	-2.000	-8.954	-5.877	0.831	4.025
220	0.859	32.54	-11.077	1.532	-2.000	-8.910	-5.637	0.826	4.123
230	0.847	31.05	-11.048	1.291	-2.000	-8.875	-5.400	0.820	4.216
240	0.834	29.59	-11.028	1.050	-2.000	-8.850	-5.163	0.815	4.304
250	0.821	28.19	-11.018	0.809	-2.001	-8.833	-4.927	0.809	4.387
260	0.807	26.82	-11.019	0.568	-2.001	-8.826	-4.690	0.802	4.466
270	0.793	25.48	-11.030	0.324	-2.002	-8.829	-4.452	0.795	4.539
280	0.777	24.17	-11.053	0.076	-2.003	-8.843	-4.212	0.788	4.608
290	0.761	22.89	-11.089	-0.177	-2.005	-8.868	-3.969	0.779	4.671
300	0.743	21.61	-11.141	-0.439	-2.008	-8.907	-3.720	0.771	4.728
305	0.734	20.98	-11.173	-0.573	-2.011	-8.930	-3.596	0.766	4.754
310	0.724	20.34	-11.210	-0.711	-2.015	-8.959	-3.469	0.762	4.778
315	0.714	19.70	-11.253	-0.852	-2.020	-8.991	-3.341	0.757	4.798
320	0.704	19.06	-11.300	-0.997	-2.027	-9.026	-3.213	0.753	4.816
325	0.693	18.42	-11.354	-1.147	-2.037	-9.065	-3.086	0.748	4.829
330	0.681	17.77	-11.417	-1.304	-2.051	-9.110	-2.959	0.745	4.837
335	0.669	17.10	-11.488	-1.468	-2.069	-9.159	-2.834	0.741	4.838
340	0.655	16.43	-11.569	-1.640	-2.094	-9.213	-2.712	0.739	4.831
345	0.641	15.73	-11.664	-1.825	-2.127	-9.273	-2.595	0.738	4.813
350	0.626	15.00	-11.773	-2.023	-2.172	-9.339	-2.486	0.740	4.781
355	0.609	14.24	-11.902	-2.240	-2.231	-9.413	-2.385	0.743	4.731
360	0.589	13.43	-12.060	-2.483	-2.309	-9.500	-2.293	0.750	4.658
365	0.567	12.54	-12.255	-2.763	-2.413	-9.604	-2.212	0.760	4.554
370	0.540	11.54	-12.513	-3.104	-2.553	-9.737	-2.143	0.774	4.403
375	0.505	10.32	-12.885	-3.557	-2.758	-9.929	-2.083	0.796	4.171
380	0.450	8.58	-13.551	-4.303	-3.116	-10.274	-2.035	0.830	3.744
385	0.315	5.09	-15.687	-6.509	-4.229	-11.376	-2.003	0.911	2.350
390	0.217	3.17	-17.915	-8.810	-5.394	-12.486	-2.000	0.960	0.891
395	0.185	2.66	-18.851	-9.828	-5.906	-12.921	-2.000	0.973	0.268
400	0.167	2.40	-19.430	-10.490	-6.239	-13.173	-2.000	0.980	-0.124
405	0.154	2.23	-19.849	-10.993	-6.492	-13.343	-2.000	0.984	-0.415

410	0.145	2.10	-20.178	-11.405	-6.699	-13.468	-2.000	0.987	-0.647
415	0.138	2.01	-20.449	-11.758	-6.876	-13.563	-2.000	0.989	-0.840
420	0.132	1.94	-20.677	-12.068	-7.032	-13.638	-2.000	0.991	-1.008
425	0.127	1.87	-20.876	-12.347	-7.171	-13.697	-2.000	0.992	-1.155
430	0.122	1.82	-21.050	-12.601	-7.299	-13.745	-2.000	0.993	-1.286
435	0.119	1.78	-21.205	-12.836	-7.416	-13.784	-2.000	0.994	-1.405
440	0.115	1.74	-21.346	-13.054	-7.525	-13.815	-2.000	0.994	-1.515
445	0.112	1.70	-21.473	-13.258	-7.628	-13.841	-2.000	0.995	-1.615
450	0.109	1.67	-21.589	-13.450	-7.724	-13.861	-2.000	0.995	-1.709
455	0.107	1.64	-21.696	-13.632	-7.815	-13.878	-2.000	0.996	-1.796
460	0.104	1.62	-21.796	-13.806	-7.902	-13.891	-2.000	0.996	-1.878
465	0.102	1.59	-21.888	-13.971	-7.985	-13.901	-2.000	0.997	-1.955
470	0.100	1.57	-21.975	-14.130	-8.064	-13.908	-2.000	0.997	-2.029
475	0.098	1.55	-22.056	-14.282	-8.140	-13.914	-2.000	0.997	-2.098
480	0.096	1.53	-22.132	-14.428	-8.213	-13.917	-2.000	0.997	-2.164
485	0.094	1.52	-22.205	-14.570	-8.284	-13.919	-2.000	0.998	-2.228
490	0.093	1.50	-22.273	-14.706	-8.353	-13.919	-2.000	0.998	-2.288
495	0.091	1.49	-22.338	-14.839	-8.419	-13.918	-2.000	0.998	-2.346
500	0.090	1.47	-22.401	-14.967	-8.483	-13.916	-2.000	0.998	-2.402
510	0.087	1.45	-22.516	-15.213	-8.606	-13.909	-2.000	0.998	-2.508
520	0.085	1.42	-22.622	-15.446	-8.722	-13.899	-2.000	0.999	-2.607
530	0.083	1.40	-22.720	-15.667	-8.833	-13.886	-2.000	0.999	-2.700
540	0.081	1.39	-22.812	-15.879	-8.939	-13.872	-2.000	0.999	-2.788
550	0.079	1.37	-22.898	-16.081	-9.040	-13.856	-2.000	0.999	-2.871
560	0.077	1.35	-22.978	-16.276	-9.138	-13.840	-2.000	0.999	-2.949
570	0.075	1.34	-23.054	-16.463	-9.231	-13.822	-2.000	0.999	-3.025
580	0.074	1.33	-23.126	-16.643	-9.322	-13.804	-2.000	0.999	-3.097
590	0.072	1.32	-23.195	-16.818	-9.409	-13.786	-2.000	0.999	-3.167
600	0.071	1.31	-23.261	-16.987	-9.493	-13.768	-2.000	0.999	-3.233
620	0.068	1.29	-23.385	-17.309	-9.654	-13.730	-2.000	1.000	-3.359
640	0.066	1.27	-23.499	-17.613	-9.806	-13.693	-2.000	1.000	-3.477
660	0.064	1.25	-23.607	-17.900	-9.950	-13.656	-2.000	1.000	-3.588
680	0.062	1.24	-23.709	-18.174	-10.087	-13.621	-2.000	1.000	-3.693
700	0.060	1.23	-23.805	-18.435	-10.218	-13.588	-2.000	1.000	-3.793

Bibliography

1. *www.webelements.com*.
2. *Metals Handbook. 9th deition. Corrosion*. Vol. 13. 1987: ASM International.
3. *Heat-Resistant Materials*, ed. J.R. Davis. 1997, Materials Park, OH: ASM International. 591.
4. *HSC chemistry, 5.11*. 2002, Outokumpu.
5. Agrawal, P.M., B.M. Rice, and D.L. Thompson, *Predicting trends in rate parameters for self-diffusion on FCC metal surfaces.* Surface Science, 2002. **515**: p. 21-35.
6. Atkins, P.W., *Physical Chemistry, 6th Edition*. 1998. 1014 pp.
7. Atkinson, A. and R.I. Taylor, *The diffusion of Ni in the bulk and along dislocations in NiO single crystals.* Philosophical Magazine A, 1979. **39**(5): p. 581-595.
8. Atkinson, A. and R.I. Taylor, *The diffusion of Ni along grain boundaries in nickel oxide.* Philosophical Magazine A, 1981. **43**(4): p. 979-998.
9. Bard, A.J. and L.R. Faulkner, *Electrochemical Methods: Fundamentals and Applications, 2nd Edition*. 2001: John Wiley & Sons, Inc. 833.
10. Barnes, J.J., G.J. G., and D.A. Shores, *A Model for Stress Generation and Relief in Oxide-Metal Systems During a Temperature Change.* Oxidation of Metals, 1989. **32**(5/6): p. 449-469.
11. Bellissent-Funel, M.-C., *Structure of supercritical water.* Journal of Molecular Liquids, 2001. **90**(1-3): p. 313-322.
12. Birks, N. and G.H. Meier, *Introduction to High Temperature Oxidation of Metals*. 1983, London: Edward Arnold. 198.
13. Bischoff, J.L. and P.K. S., *Liquid-Vapor Relations for the system NaCl-H2O: Summary of the P-T-x Surface from 300[deg]C to 500[deg]C.* American Journal of Science, 1989. **289**: p. 217-248.
14. Bockris, J.O.M. and A.K.N. Reddy, *Modern Electrochemistry, an Introduction to an Interdisciplinary Area, Vol. 2*. 1970. 801 pp.
15. Bockris, J.O.M. and A.K.N. Reddy, *Modern Electrochemistry, an Introduction to an Interdisciplinary Area, Vol. 1*. 1970. 622 pp.
16. Botella, P., et al., *Experimental set-up for electrochemical measurements in hydrothermal sub- and supercritical oxidation: polarization curves, determination of corrosion rates and evaluation of the degradability of reactors during hydrothermal treatments of aqueous wastes.* The Journal of Supercritical Fluids,

2003. **26**(2): p. 157-167.
17. Botella, P., et al., *Experimental study, via current-potential curves, of the anodic behavior of Alloy C-276 and T60 titanium in chlorinated and oxygenated aqueous media under sub- to supercritical conditions.* The Journal of Supercritical Fluids, 2003. **25**(3): p. 269-278.
18. Calvert and J. Johnson, J. Chem. Soc., 1866. **19**: p. 436.
19. Calzavara, Y., et al., *A new reactor concept for hydrothermal oxidation.* The Journal of Supercritical Fluids. **In Press, Corrected Proof**.
20. Caplan, D., M.J. Graham, and M. Cohen, *Effect of Cold Work on the Oxidation of Nickel at High Temeperature.* J. Electrochem. Soc., 1972. **119**(9): p. 1205-1215.
21. Chao, C.Y., L.F. Lin, and D.D. Macdonald, *A point Defect Model for Anodic Passive Films. I Film Growth Kinetics.* J. Electrochem. Soc., 1981. **128**(6): p. 1187-1194.
22. Chao, C.Y., L.F. Lin, and D.D. Macdonald, *A Point Defect Model for Anodic Passive Films. III Impedance Response.* J. Electrochem. Soc., 1982. **129**(9): p. 1874-1879.
23. Cline, J.A., *Experimental and Ab Initio Investigation into the Fundamentals of corrosion, in the Context of Supercritical Water Oxidation Systems*, in *Department of Chemical Engineering*. 2000, MIT.
24. Cobble, J.W., *The Thermodynamic Properties of High Temperature Aqueous Solutions. VI. Applications of Entropy Correspondence to Thermodynamics and Kinetics.* J. Am. Chem. Soc., 1964. **86**: p. 5394-5401.
25. Connolly, J.F., *Solubility of hydrocarbons in Water Near the Critical Solution Temperatures.* Journal of chemical And Engineering Data, 1966. **11**(1): p. 13-16.
26. Cowan, R.L. and S.R. W., *The Thermodynamics and Electrode Kinetic Behavior of Nickel in Acid Solution in the Temperature Range 25 [deg]C to 300 [deg]C.* J. Electrochem. Soc., 1974. **118**(4): p. 557-568.
27. Criss, C.M. and J.W. Cobble, *The Thermodynamic Properties of High Temperature Aqueous Solutions. I. Standard Partial Molal Heat Capacities of Sodium Chloride and Barium Chloride from 0 to 100 [deg]C.* J. Am. Chem. Soc., 1961. **83**: p. 3223-3228.
28. Criss, C.M. and J.W. Cobble, *The Thermodynamic Properties of High Temperature Aqueous Solutions. IV. Entropies of the Ions up to 200 [deg]C and the Correspondence Principle.* J. Am. Chem. Soc., 1964. **86**: p. 5385-5390.
29. Criss, C.M. and J.W. Cobble, *The Thermodynamic Properties of High Temperature Aqueous Solutions. V. The Calculation of Ionic Heat Capacities up to*

200[deg]C. Entropies and Heat Capacities above 200[deg]C. J. Am. Chem. Soc., 1964. **86**: p. 5390-5393.

30. Criss, C.M. and J.W. Cobble, *The Thermodynamic Properties of High Temperature Aqueous Solutions. VI. Applications of Entropy correspondence Principle to Thermodynamics and Kinetics.* J. Am. Chem. Soc., 1964. **86**: p. 5394-5401.
31. Davis, J.R., ed. *Nickel, Cobalt, and Their Alloys*. ASM Specialty Handbook. 2000, ASM International: Materials Park, OH.
32. Deen, W.M., *Analysis of Transport Phenomena*. 1998, New York: Oxford University Press. 597.
33. Delville, M.H., et al., *Electrochemical study of corrosion in aqueous high pressure, high temperature media and measurements of materials corrosion rates: applications to the hydrothermal treatments of organic wastes by SCWO.* The Journal of Supercritical Fluids, 2003. **26**(2): p. 169-179.
34. Dimitrov, N., et al., *Dealloying of Al2CuMg in Alkaline Media.* J. Electrochem. Soc., 2000. **147**(9): p. 3283-3285.
35. Erlebacher, J., et al., *Evolution of nanoporosity in dealloying.* Nature, 2001. **410**: p. 450-453.
36. Evans, H.E., *The Role of Oxide Grain Boundaries in the Development of Growth Stresses During Oxidation.* Corrosion Science, 1983. **23**(5): p. 495-506.
37. Fauvel, E., et al., *A double-wall reactor for hydrothermal oxidation with supercritical water flow across the inner porous tube.* The Journal of Supercritical Fluids, 2004. **28**(1): p. 47-56.
38. Forty, A.J., *Corrosion micromorphology of noble metal alloys and depletion gilding.* Nature, 1979. **282**: p. 597-598.
39. Frantz, J.D. and W.L. Marshall, *Electrical Conductances and Ionization-Constants of Salts, Acids, and Bases in Supercritical Aqueous Fluids .1. Hydrochloric-Acid from 100-Degrees-C to 700-Degrees-C and at Pressures to 4000 Bars.* American Journal of Science, 1984. **284**(6): p. 651-667.
40. Frantz, J.D. and E.H. P., *Acid-Base Buffers: Use of Ag+AgCl in the Experimental Control of Solution Equilibria at Elevated Pressures and Temperatures.* American Journal of Science, 1973. **273**: p. 268-286.
41. Fronhold, A.T.J., *Theory of Metal Oxidation, Vol. 1, Fundamentals, Vol. 2, Space Charge.* 1980, Amsterdam: North-Holland.
42. Gorbaty, Y.E. and A.G. Kalinichev, *Hydrogen-Bonding in Supercritical Water .1. Experimental Results.* Journal of Physical Chemistry, 1995. **99**(15): p. 5336-5340.

43. Haar, L., J. Gallagher, S., and K.G. S., *NBS/NRC Steam Tables*. 1984: Hemisphere Publishing Coorporation.
44. Heubner, U., *Nickel Alloys*. 1998, New York: Marcel Dekker, Inc. 309.
45. Hodes, M., et al., *Salt precipitation and scale control in supercritical water oxidation--Part A: fundamentals and research.* The Journal of Supercritical Fluids. **In Press, Corrected Proof**.
46. Huntz, A.M., *Stresses in Nio, Cr2o3 and Al2o3 Oxide Scales.* Materials Science and Engineering a-Structural Materials Properties Microstructure and Processing, 1995. **201**(1-2): p. 211-228.
47. Huntz, A.M., et al., *Evidence of stress relaxation in thermally grown oxide layers - experiments and modelling.* Materials Science and Engineering a-Structural Materials Properties Microstructure and Processing, 1998. **248**(1-2): p. 44-55.
48. Japas, M.L. and E.U. Franck, *High Pressure Phase Equilibria and PVT-Data of the Water-Oxygen System Including Water-Air to 673 K and 250MPa.* Ber. Bunsenges. Phys. Chem., 1985. **89**: p. 1268-1275.
49. Japas, M.L. and E.U. Franck, *High Pressure Phase Equilibria and PVT-Data of the Water-Nitrogen System to 673K and 250 MPa.* Ber. Bunsenges. Phys. Chem., 1985. **89**: p. 793-800.
50. Johnston, K.P. and J.B. Chlistunoff, *Neutralization of acids and bases in subcritical and supercritical water: acetic acid and HCl.* Journal of Supercritical Fluids, The, 1998. **12**(2): p. 155-164.
51. Jones, D.A., *Principles and Prevention of Corrosion, 2nd Edition*. 1996: Prentice-Hall.
52. Khanna, A.S., *Introduction to High Temperature Oxidation and Corrosion*. 2002, Materials Park: ASM International. 324.
53. Kofstad, P., *Nonstochiometry, Diffusion, and Electrical Conductivity in Binary Metal Oxides*. 1972: John Wiley & Sons, Inc. 382.
54. Kofstad, P., *High Temperature Corrosion*. 1988, London and New York: Elsevier Applied Science. 558.
55. Kriksunov, L.B. and D.D. Macdonald, *Corrosion in supercritical water oxidation systems: A phenomenological analysis.* Journal of the Electrochemical Society, 1995. **142**(12): p. 4069-4073.
56. Kriksunov, L.B. and D.D. Macdonald, *Potential-pH Diagrams for Iron in Supercritical Water.* Corrosion, 1997. **53**(8): p. 605-611.
57. Lai, G.Y., *High-Temperature Corrosion of Engineering Alloys*. 1990, Materials Park: ASM International. 231.

58. Lin, L.F., C.Y. Chao, and D.D. Macdonald, *A Point Defect Model for Anodic Passive Films. II Chemical Breakdown and Pit Initiation.* J. Electrochem. Soc., 1981. **128**(6): p. 1194-1198.
59. Lvov, S.N., X.Y. Zhou, and D.D. Macdonald, *Flow-through electrochemical cell for accurate pH measurements at temperatures up to 400 [deg]C]*. Journal of Electroanalytical Chemistry, 1999. **463**: p. 146-156.
60. Macdonald, D.D., *The Point Defect Model for the Passive State.* J. Electrochem. Soc., 1992. **139**(12): p. 3434-3449.
61. Macdonald, D.D., S.R. Biaggio, and H. Song, *Steady-State Passive Films.* J. Electrochem. Soc., 1992. **139**(1): p. 170-177.
62. Macdonald, D.D. and L.B. Kriksunov, *Probing the chemical and electrochemical properties of SCWO systems.* Electrochemica Acta, 2001. **47**: p. 775-790.
63. Macdonald, D.D. and M. Urquido-Macdonald, *Theory of Steady-State Passive Films.* J. Electrochem. Soc., 1990. **137**(8): p. 2395-2402.
64. Marrone, P.A., et al., *Salt precipitation and scale control in supercritical water oxidation--part B: commercial/full-scale applications.* The Journal of Supercritical Fluids. **In Press, Corrected Proof**.
65. Marsh, A.R.W. and W.J. McElroy, *The dissociation constant and Henry's law constant of HCl in aqueous solution.* Atmospheric Environment (1967), 1985. **19**(7): p. 1075-1080.
66. Martynova, O.I., *Solubility of Inorganic Compounds in Subcritical and Supercritical Water*, in *High Temperature High Pressure Electrochemistry in Aqueous Solutions*, D.d.G. Jones and R.W. Staehle, Editors. 1973, National Association of Corrosion Engineers: Houston. p. 131-138.
67. Mesmer, R.E., et al., *Thermodynamics of Aqueous Association and Ionization Reactions at High Temeratures and Pressures.* Journal of Solution Chemistry, 1988. **17**(8): p. 699-718.
68. Meyer, C.A., et al., *ASME Steam Tables: Thermodynamic and transport properties of Steam*. 6th ed. 1993: ASME PRESS.
69. Mitton, D.B., P.A. Marrone, and R.M. Latanision, *Interpretation of the Rationale for Feed Modification in SCWO systems.* J. Electrochem. Soc., 1996. **143**(3): p. L59-L61.
70. Mitton, D.B., J.H. Yoon, and R.M. Latanision, *An overview of Corrosion Phenomena in SCWO systems for Hazardous Waste Destruction.* Zairyo-to-Kankyo, 2000. **49**(3): p. 130-137.
71. Modell, M., *Standard Handbook of Hazardous Waste Treatment and Disposal*.

1989, New York: McGraw-Hill.
72. Moulder, J.F., et al., *Handbook of X-ray Photoelectron Spectroscopy : A Reference Book of Standard Spectra for Identification and Interpretation of XPS Data*. 1992: Physical Electronics, Inc.
73. Nakahara, M., et al., *Structure and dynamics of water: from ambient to supercritical.* Journal of Molecular Liquids, 2001. **90**(1-3): p. 75-83.
74. Newman, R.C. and K. Sieradzke, *Metallic Corrosion.* Science, 1994. **263**: p. 1708.
75. Oelkers, E.H. and H.C. Helgeson, *Calculation of dissociation constants and the relative stabilities of polynuclear clusters of 1:1 electrolytes in hydrothermal solutions at supercritical pressures and temperatures.* Geochimica et Cosmochimica Acta, 1993. **57**(12): p. 2673-2697.
76. Orzalli, J.C., *Preliminary Corrosion Studies of Candidate Materials for Supercritical Water Oxidation Reactor Systems*, in *Department of Materials Science and Engineering*. 1994, MIT: Cambridge.
77. Pickering, H.W. and C. Wagner, *Electrolytic Dissolution of Binary Alloys Containing a Noble Metal.* J. Electrochem. Soc., 1967. **114**(7): p. 698-706.
78. Poirier, D.R. and G.H. Geiger, *Transport Phenomena in Materials Processing*. 1994: TMS. 658.
79. Pokrovskii, V.A., *Calculation of the standard partial molal thermodynamic properties and dissociation constants of aqueous HCl0 and HBr0 at temperatures to 1000[deg]C and pressures to 5 kbar.* Geochimica et Cosmochimica Acta, 1999. **63**(7-8): p. 1107-1115.
80. Postorino, P., M.A. Ricci, and A.K. Soper, *Water above Its Boiling-Point - Study of the Temperature and Density-Dependence of the Partial Pair Correlation-Functions .1. Neutron-Diffraction Experiment.* Journal of Chemical Physics, 1994. **101**(5): p. 4123-4132.
81. Postorino, P., et al., *The Interatomic Structure of Water at Supercritical Temperatures.* Nature, 1993. **366**(6456): p. 668-670.
82. Pourbaix, M., *Atlas of Electrochemical Equilibria in Aqueous Solutions*. 1974, Houston: National Association of Corrosion Engineers.
83. Rebert, C.J. and W.B. Kay, *The phase behavior and solubility.* A.I.Ch.E. Journal, 1959. **5**(3): p. 285-289.
84. Samsonov, G.V., *The Oxide Handbook*. 1973: IFI/Plenum Data Corporation. 524.
85. Sengers, J.M.H.L., *Supercritical Fluids: Their Properties and Applications*, in *Supercritical Fluids: Fundamentals and Applications*, E. Kiran, P.G. Debenedetti, and C.J. Peters, Editors. 2000, Kluwer Academic Publishers: Boston. p. 1-29.

86. Seward, T.M. and E.U. Franck, *The system Hydrogen - Water up to 440[deg]C and 2500bar Pressure.* Ber. Bunsenges. Phys. Chem., 1981. **85**: p. 2-7.
87. Shim, M.T. and W.J. Moore, J. Chem. Phys., 1957. **26**: p. 802.
88. Sieradzke, K., *Curvature Effects in Alloy Dissolution.* J. Electrochem. Soc., 1993. **140**(10): p. 2868-2872.
89. Sieradzke, K., et al., *Computer simulations of corrosion: selective dissolution of binary alloys.* Philosophical Magazine A, 1989. **59**(4): p. 713-746.
90. Sieradzke, K., et al., *The Dealloying Critical Potential.* J. Electrochem. Soc., 2002. **149**(8): p. B370-B377.
91. Sieradzke, K., et al., *The Relationship Between Dalloying and Transgranular Stress Corrosion Cracking of Cu-Zn and Cu-Al Alloys.* J. Electrochem. Soc., 1987. **134**(7): p. 1635-1639.
92. Tagirov, B.R., A.V. Zotov, and N.N. Akinfiev, *Experimental study of dissociation of HCl from 350 to 500[deg]C and from 500 to 2500 bars: Thermodynamic properties of HCl[deg](aq).* Geochimica et Cosmochimica Acta, 1997. **61**(20): p. 4267-4280.
93. Tester, J.W. and J.A. Cline, *Hydrolysis and Oxidation in Subcritical and Supercritical Water: Connecting Process Engineering Science to Molecular Interactions.* Corrosion, 1999. **55**(11): p. 1088-1100.
94. Tester, J.W., et al., *Supercritical Water Oxidation Technology - Process-Development and Fundamental Research.* ACS Symposium Series, 1993. **518**: p. 35-76.
95. Timoshenko, S.P. and J.N. Goodier, *Theory of Elasticity*. 3rd edition ed. 1970: McGRAW-HILL.
96. Vukmirovic, M.B., N. Dimitrov, and K. Sieradzke, *Dealloying and Corrosion of Al Alloy 2024-T3.* J. Electrochem. Soc., 2002. **149**(9): p. B428-B439.
97. Wagner, C., *Diffusion and High Temperature Oxidation of Metals*, in *Atom Movements*. 1951, American Society for Metals: Cleveland. p. 153-173.
98. Wagner, C., *Equations for Transport in Solid Oxides and Sulfides of Transition Metals.* Progress in Solid-State Chemistry, 1975. **10**(Part 1): p. 3-16.
99. Wagner, K., et al., *Dealloying below the Critical Potential.* J. Electrochem. Soc., 1997. **144**(10): p. 3545-3555.
100. Wagner, W. and A. Kruse, *Properties of Water and Steam*. 1998: Springer.
101. Zemansky, M.W. and R.H. Dittman, *Heat and Thermodynamics, 7th edition*. 1997: McGraw-Hill.
102. Zhang, L. and D.D. Macdonald, *On the transport of point defects in passive films.*

Electrochemica Acta, 1998. **43**(7): p. 679-691.
103. Zhang, L., et al., *On the kinetics of Growth of Anodic Oxide Films.* J. Electrochem. Soc., 1998. **145**(3): p. 898-905.
104. Zhdanov, V.P. and P.R. Norton, *Criterion for instability of oxide film growth with respect to formation of cracks.* Surface Science, 1995. **323**: p. L311-L313.
105. Zhou, X.Y., et al., *Quantitative evalution of general corrosion of Type 304 stainless steel in subcritical and supercritical aqueous solution via electrochemical noise analysis.* Corrosion Science, 2002. **44**: p. 841-860.